DoctAir - The Future of Helicopter Emergency Medical Services

Final Report

AE3200: Design Synthesis Exercise

Group 04

Delft University of Technology

TU Delft

DoctAir - The Future of Helicopter Emergency Medical Services

Final Report

by

Group 04

Student Name	Student Number
Marloes van der Zwart	5678439
Frank Olsson	5686466
Rohit Roy Chowdhury	5773407
Swayam Kuckreja	5726549
Simranjeet Singh	5684374
Rimaz Khan	5779235
Maan Pandya	5698537
Valter Somlai	5679427
Fedor Kirillov	5696577
Bram Koelman	5687624

Tutor:	D. Ragni, B. Püroja
Coaches:	P. Ghanoni Bostanabad, C. de Zeeuw
Teaching Assistant:	A. Morland
Project Duration:	22 May, 2025 – 18 June, 2025
Faculty:	Faculty of Aerospace Engineering, Delft

Cover: Final CAD of the design
Style: TU Delft Report Style

TU Delft

Version Control

This section serves to document all the changes made after the initial submission. These changes were made by implementing feedback received from the TA, peer groups, coaches, and tutors.

Executive Overview

- Fixed units in the table

Project Objectives

- Added chapter introduction

Market Analysis

- Added citations

Configuration

- Modified problems with units

Aerodynamics

- Shortened and motivated the assumptions.
- Clarified the general text.
- Added stall angle of attack methodology graphs.

Propulsion System and Power

- Changed ”yield strength” of carbon fiber composite to ”tensile strength” of carbon fiber composite as it doesn’t yield much and instead fractures. Also fixed the unusually low tensile strength of carbon fiber composite to a better value.
- Changed ”carbon fiber” to ”carbon fiber composite” for the propeller blade structure section (as it is not made of only the fibers).
- Clarified the assumption of modeling blade thrust as a point load at 50% of the blade span for bending moment estimation, citing project time constraints and the adequacy of the approximation for first-order analysis.
- Changed battery charging temperature graph to have a point clearly indicating full charge/saturation.
- Added a sentence to clarify the power and energy graph Figure 7.1 so its more clear what it is showing.
- Fixed minor grammar and coherence mistakes.

Structures

- Added subsection about composite layup.
- Modified figure to fit page.

Design Iteration

- Fixed units in the table.

Control and Stability

- Added time to the x axis.
- Clarified several parameters used in equations in Section 10.4.
- Fixed confusion around elevons and elevators.

Sustainability Approach

- Added subsystem and lifecycle sustainability considerations in a table.
- Added reference to Section 13.2 in Chapter 12 when explaining ease of disassembly.

Operation & Logistics

- Added finalized RAMS Analysis with values.

Executive Overview

The provision of Emergency Medical Services (EMS) in the Netherlands faces pressures from increasing urbanization, road congestion, and the operational limitations of conventional ground and air transport. Traditional Helicopter EMS (HEMS), while rapid, incurs significant operational costs, noise pollution, and environmental concerns. This Design Synthesis Exercise, undertaken by Group 04, presents **"DoctAir"**, a conceptual design for an electric Vertical Take-Off and Landing (eVTOL) aircraft tailored for EMS operations.

Mission Objective

The primary objective of this project was to develop a faster, quieter, more cost-effective, and sustainable emergency transportation solution, capable of overcoming the challenges of limited landing space and enhancing the critical care delivery within the Dutch operational context.

Market Analysis & Stakeholders

A thorough market analysis confirmed the need for advanced EMS solutions in the Netherlands. Current HEMS operations, primarily performed by ANWB MAA using EC135 helicopters, provide critical service but face limitations in urban accessibility and operational costs. The emerging Urban Air Mobility (UAM) market, with over 200 eVTOL concepts in development, indicates a technological shift, though dedicated EMS applications remain relatively new. Key competitors and benchmarks include existing HEMS and specialized eVTOL designs like the ERC System. This analysis identified critical stakeholders, including EMS operators, medical crew, patients, regulatory bodies (EASA), hospitals, and the general public, whose needs guided the design requirements and trade-off decisions.

Requirements and Mission Profile

The design was driven by a set of requirements derived from stakeholder needs and the operational EMS context. Key performance targets included an operational range sufficient to cover the Netherlands effectively, a minimum cruise speed of 61 [m/s], capability to operate from existing HEMS helipads, significantly lower operational costs than current HEMS, and adherence to EASA SC-VTOL safety standards. A representative mission profile for sizing involved hover take-off, climb to 300m, a 110 km cruise segment, descent, and hover landing, with considerations for a 20-minute rapid turnaround time.

Trade-off Summary

Building on strawman concepts from the Baseline phase, four distinct eVTOL configurations were evaluated: a Tandem Wing with Tilting Propellers, a Delta Flying Wing, a Monowing with V-Tail, and a Monowing with Canard and V-Tail. A trade-off analysis (Table 4.2), based on weighted criteria that consisted of mass, energy consumption, sustainability, control & stability, and risk, identified the **Delta Flying Wing** as the most promising configuration. An initial concept for this design can be visualised in Figure 1.

Table 1: *Summary of design option scores (1=Poor, 5=Excellent) and final weighted scores. column widths for criteria are proportional to their weights.*

Design Option	Mass (20%)	Energy Cons. (25%)	Sust. Scope (15%)	Ctrl. & Stab. Char. (25%)	Risk (15%)	Weighted Score
D1: Delta Wing	5	5	4	3	2	**390**
D2: Tandem	4	3	4	4	4	**375**
D3: Mono Wing 1	3	2	3	4	4	**315**
D4: Mono Wing 2	1	1	2	5	4	**260**

As the design of the selected Delta Wing progressed, a key refinement was made to the propulsion system integration. The initial concept of embedding propulsion units within the wing structure was re-evaluated since the structural analysis indicated that such an embedded design would require significant local reinforcement, leading to a massive increase in structural mass and complexity. Thus the design evolved, using open propellers that would be mounted externally on the wing surface via support structures.

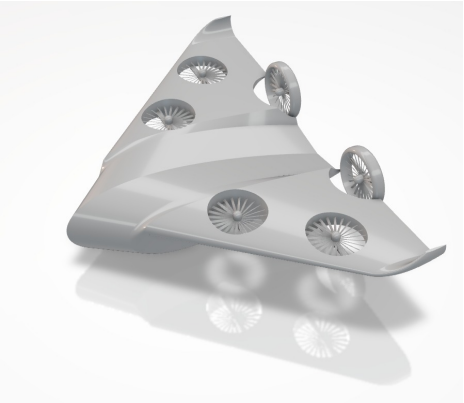

Figure 1: *Selected Delta wing design*

Subsystem Design and Analysis

Following the midterm, a detailed design was initiated, aiming to design each subsystem to meet the mission requirements. Key results from the design include:

- **Aerodynamics** Airfoil selection **(E186 for outboard sections, NACA0025 for centerbody)** was optimized for cruise efficiency and stall characteristics. Full aircraft aerodynamic analysis using OpenVSP (VLM) yielded crucial lift, drag, and moment coefficients (C_L, C_D, C_m) and stability derivatives.
- **Propulsion** A six-propeller distributed electric propulsion system was designed. Three-bladed fixed-pitch propellers (2[m] diameter for front/mid, 1.5[m] for rear) were optimized for hover and cruise efficiency using Blade Element Momentum Theory, achieving target thrust levels within noise constraints of target <80 [dB].
- **Power A Lithium-ion NMC battery system** (Molicel INR-21700-P50B cells) was sized to meet the 212 [kWh] total mission energy requirement, resulting in a battery mass of 727.6 [kg]. Thermal management analysis indicated that no active cooling is required for typical mission profiles.
- **Structures** The wingbox and fuselage structure were designed using **carbon fiber epoxy with Nomex honeycomb core**. Sizing was performed considering critical flight and ground loads, static strength and buckling failure modes, with an emphasis on material efficiency and manufacturability.
- **Control & Stability** Control surfaces were sized to ensure adequate pitch, roll, and yaw authority, particularly for One Engine Inoperative (OEI) conditions. Static and dynamic stability analyses confirmed stable flight characteristics in cruise. Hover control relies on differential thrust from the six propellers.

Mission Simulation & Performance

The integrated DoctAir design was simulated using SUAVE for the critical emergency rescue mission. Results confirmed the vehicle's ability to complete the 110 km (one-way) mission profile, including hover phases, with the designed battery capacity. Key performance metrics such as energy consumption, flight times, and component operating conditions were verified to be within design limits.

Cost Analysis

The economic viability of DoctAir was assessed through a detailed cost analysis that estimated the unit manufacturing cost for a production run of 240 units to be €658,322. The Total Annual Operating Cost (TOC) is projected at €1.07 million. A 20-year cumulative cost of ownership analysis shows DoctAir at €22.1 million, offering a €15.9 million saving compared to an equivalent HEMS helicopter operation over the same period. Sensitivity analysis highlighted annual flight hours and battery cycle life as the most significant drivers of long-term cost.

Final Design: DoctAir

The culmination of this design synthesis exercise is the DoctAir eVTOL EMS vehicle, a Delta Flying Wing configuration. This design balances the demanding requirements of emergency medical transport with the benefits of electric VTOL technology. A render of the final DoctAir concept is presented in Figure 2. Key specifications are summarized in Table 2.

Figure 2: *Side view of the final design.*

Table 2: *Key aircraft parameters after the iteration procedure*

Variable	Value
Maximum take-off mass (MTOW)	1788 [kg]
Battery mass	727.6 [kg]
Fuselage mass	189.4 [kg]
Wing structural mass	271.8 [kg]
Propulsion system mass	96 [kg]
Landing gear mass	103.5 [kg]
Payload mass	400 [kg]
Total mission energy	212.73 [kWh]
Cruise lift coefficient $C_{L_{cruise}}$	0.2137
Cruise drag coefficient $C_{D_{cruise}}$	0.01432
Cruise angle of attack α_{cruise}	5.526 [°]
Wing skin thickness	3 [mm]
Wing spar flange thickness	4 [mm]
Wing stringer thickness	2 [mm]
Wing spar web thickness	3 [mm]
Wing rib spacing	1.25 [m]
Wing total stringers	4

Nomenclature

Abbreviations

AC	Aerodynamic Center
ACAI	Available Control Authority Index
AFP	Automated Fiber Placement
AIT	Assembly, Integration, and Testing
ALS	Advanced Life Support
AoA	Angle of Attack
AOG	Aircraft on Ground
AM	Additive Manufacturing
AWU	All Weight Up
AVIO	Avionics
BEMT	Blade Element Momentum Theory
BMI	Bismaleimide
BMS	Battery Management System
BOL	Beginning of Life
CAD	Computer Aided Design
CFRP	Carbon Fiber Reinforced Polymer
CG	Center of Gravity
COMM	Communications
CPI	Consumer Price Index
CS	Certification Specifications
DEP	Distributed Electric Power
DfD	Design for Disassembly
DLD	Direct Laser Deposition
DoC	Degree of Controllability
DoD	Depth of Discharge
EASA	European Union Aviation Safety Agency
EKF	Extended Kalman Filter
EOL	End of Life
EPNL	Effective Perceived Noise Level
EMS	Emergency Medical Services
ESM	Energy Storage and Management
EV	Electric Vehicle
eVTOL	Electric Vertical Take-Off & Landing
FBP	Functional Breakdown Structure
FC	Flight Computer
FCS	Flight Control System
FFD	Functional Flow Diagram
FOV	Field of View
FY	Financial Year
GFRP	Glass Fiber Reinforced Polymer
GPS	Global Positioning System
HEMS	Helicopter Emergency Medical Services
HUMS	Health and Usage Monitoring System
IMU	Inertial Measurement Unit
ISA	International Standard Atmosphere
LiDAR	Light Detection and Ranging
MAA	Medical Air Assistance
MMT	Mobile Medical Team
MNS	Mission Need Statement
MOB	Main Operating Base
MRO	Maintenance, Repair, and Overhaul
MTOW	Maximum Take-Off Weight
NACA	National Advisory Committee for Aeronautics
NASA	National Aeronautics and Space
NMC	Nickel Manganese Cobalt
NRE	Non-Recurring Engineering
OEI	One Engine Inoperative
OJF	Open Jet Facility
OPS	Operations
PAYL	Payload
PDU	Power Distribution Unit
PEEK	Polyetheretherketone
PID	Proportional-Integral-Derivative
POS	Project Objective Statement
PROP	Propulsion
QMS	Quality Management System
RADAR	Radio Detection and Ranging
RAV	Regional Ambulance Services
RPM	Rotations Per Minute
RMS	Root-Mean-Square
RTM	Resin Transfer Molding
SDG	Sustainable Development Goals
SLAM	Simultaneous Localization and Mapping
SPL	Sound Pressure Level
SWOT	Strengths, Weaknesses, Opportunities, and Threats
TBD	To Be Decided
TLOF	Touchdown and Lift-Off
TOC	Total Operating Cost
UAM	Urban Air Mobility
UAV	Unmanned Aerial Vehicle
UD	Unidirectional
UKF	Unscented Kalman Filter
VEMS	VTOL Emergency Medical Services
VLM	Vortex Lattice Method
WHO	World Health Organization

Symbols

Latin Symbols

A	Area [m^2]
AR	Aspect ratio [–]
B	Number of blades in a propeller [-]
B_2	Spanwise hinge-line factor [–]
b	Wing span [m]
c	Chord length [m]
c_{l_δ}	Airfoil lift-curve slope due to deflection [rad^{-1}]
$c_{l_{\alpha_h}}$	Horizontal-equivalent lift-curve slope [deg^{-1}]
$\bar{c}$	Mean aerodynamic chord [m]
C_D	Drag coefficient [–]
C_L	Lift coefficient [–]
C_{L_α}	Lift curve slope [rad^{-1}]
$C_{L_{\alpha_h}}$	Horizontal-equivalent CL slope [rad^{-1}]
$C_{L_{max}}$	[-]
C_m	Pitch moment coefficient [–]
C_{m_α}	Moment slope [rad^{-1}]
$C_{m_{ac}}$	Moment coefficient about the aerodynamic center [–]
$C_{m_{i_h}}$	Pitch-moment derivative of equivalent tail [rad^{-1}]
$C_{m_{\delta_e}}$	Elevator control power [rad^{-1}]
C_{m_0}	Pitch-moment coefficient at zero lift [–]
C_n	Yaw moment coefficient [–]
C_l	Roll moment coefficient [–]
C_N	Normal-force coefficient [–]
C_{N_α}	Normal-force coefficient slope w.r.t. α [–/deg]
C_P	Power coefficient [-]
C_T	Thrust coefficient [-]
C_Y	Side-force coefficient [–]
C_{h_α}	Hinge-moment coefficient slope w.r.t. α [1/rad]
C_{h_δ}	Hinge-moment coefficient slope w.r.t. δ_e [1/rad]
D	Drag force / Propeller diameter [N, m]
E	Young's Modulus [Pa]
F	Prandtl tip loss factor [-]
g	Graviatational acceleration [m/s^2]
H_e	Elevator hinge moment [Nm]
I_x	Moment of inertia around x-axis [kg·m^2]
I_y	Moment of inertia around y-axis [kg·m^2]
I_z	Moment of inertia around z-axis [kg·m^2]
I_{xz}	Product of inertia [kg·m^2]
J	Advance ratio V/nD
K_b	Spanwise control-power correction factor [–]
K_α	Combined 3D AOA correction factor [–]
K_{α_i}, K_{α_o}	Control-surface dimension correction factors [–]
K_δ	Combined 3D deflection correction factor [–]
K_{δ_i}, K_{δ_o}	Control-surface deflection correction factors [–]
k	Parabolic drag factor [-]
k'	Lift-curve linearity correction [–]
L	Rolling moment [Nm]
M	Pitching moment / Mach number [Nm / –]
M_{tip}	Mach number at blade tip
m	Mass [kg]
n	Rotational speed of propeller [rps]
N	Yawing moment [Nm]
P	Power [W]
q	Pitch rate [rad/s]
Q	Propeller shaft torque [Nm]
R	Strength [Pa]
r	Local radial position in a propeller [m]
Re	Reynolds number [-]
R_{hub}	Propeller hub radius [m]
R_{tip}	Propeller tip radius [m]
S	Wing reference area [m^2]
S_e	Equivalent horizontal tail area [m^2]
T	Thrust [N]
t/c	Thickness-to-chord ratio of elevon [–]
u	Perturbation in forward velocity [m/s]
U_0	Steady flight speed [m/s]
v	Perturbation in lateral velocity [m/s]
v_i	induced propeller velocity [m/s]
v_h	hover induced propeller velocity [m/s]
V	Flight speed [m/s]
V_a	Maneuvering speed [m/s]
V_c	Cruise speed [m/s]
V_d	Dive speed [m/s]
V_s	Stall speed [m/s]
w	Perturbation in vertical velocity [m/s]
W	Aircraft weight / Relative flow velocity at blade section [N, m/s]
x	Longitudinal axis [m]
x_{ac}	Aerodynamic-center longitudinal position [m]
x_{cg}	Center-of-gravity longitudinal position [m]
x_{np}	Neutral-point longitudinal position [m]
x_w	Wing aerodynamic-center longitudinal position [m]
y	Lateral axis [m]
Y_{90}, Y_{99}	Trailing-edge thicknesses as percentage of chord [%]

z	Vertical axis [m]
ΔC_{h_α}	3D hinge-moment AOA increment [rad^{-1}]
ΔC_{h_δ}	3D hinge-moment deflection increment [rad^{-1}]
$(c_{h_\alpha})_{\text{bal}}$	Balance-corrected 2D hinge-moment AOA [rad^{-1}]
$(c_{h_\alpha})_{\text{theory}}$	Theoretical 2D hinge-moment AOA derivative [rad^{-1}]
$(c_{h_\delta})_{\text{bal}}$	Balance-corrected 2D hinge-moment deflection [rad^{-1}]
c'_{h_α}, c''_{h_α}	Intermediate 2D hinge-moment AOA derivatives [rad^{-1}]
c'_{h_δ}, c''_{h_δ}	Intermediate 2D hinge-moment deflection derivatives [rad^{-1}]

Greek Symbols

α	Angle of attack [deg]
α_0	Trim angle of attack [deg]
β	Sideslip angle / Blade pitch angle [deg,deg]
δ_a	Aileron deflection [deg]
δ_e	Elevon (elevator) deflection [deg]
$\delta_{e_{free}}$	Elevon deflection under stick-free condition [deg]
δ_r	Rudder deflection [deg]
ϵ	drag to lift ratio c_d/c_l [-]
η	Control surface station as a fraction of the semi-span / propeller efficiency [-,-]
γ	Specific Weight [kN/m^3]
Γ	Circulation [m^2/s]
λ	Taper ratio [–]
$\Lambda_{c/2_e}$	Elevon mid-chord sweep [rad]
$\Lambda_{c/4}$	Quarter-chord sweep [rad]
Λ_{hl}	Hinge-line sweep [rad]
μ	Dynamics viscosity of air [kg/(ms)]
ν	Poisson's Ratio [-]
Ω	Rotational speed [rad/s]
ϕ	Flow angle at propeller [deg]
ρ	Air density [kg/m^3]
σ	Stress [Pa]
ξ	Nondimensional radial position in a propeller r/R_{tip} [-]
ζ	Displacement velocity ratio [-]

Contents

1

Introduction

The efficacy of Emergency Medical Services (EMS) in the Netherlands, while supported by robust ground ambulance networks and Helicopter Emergency Medical Services (HEMS), faces increasing challenges. Growing urbanization, escalating road congestion, and the centralized nature of specialized healthcare facilities contribute to potential delays and reduced accessibility in various regions.[1] Moreover, conventional HEMS operations, primarily relying on fossil-fueled helicopters, incur substantial operational costs [1], emit significant noise, and contribute to environmental pollution [2], raising concerns regarding urban acceptability and sustainability.

The rapidly emerging market for electric Vertical Take-Off and Landing (eVTOL) aircraft presents a promising opportunity to address these limitations. With characteristics such as zero operational emissions, lower acoustic signatures, reduced maintenance and operational costs, and the potential for compact, urban-compatible designs, eVTOLs offer a compelling alternative for next-generation EMS provision.

This report documents the detailed design phase of a novel eVTOL aircraft tailored for HEMS operations in the Netherlands. The objective is to finalize and substantiate an aircraft concept through system-level integration, performance analysis and interdisciplinary design development. The design builds upon the outcomes of earlier phases and translates them into a coherent engineering solution.

The structure of this report is as follows: Chapter 2, 3 and 4 provide the project objectives, market analysis and the initial configuration established during the preliminary design phase. Chapter 5 to 8 present the detailed subsystem designs, covering aerodynamics, propulsion, power systems, and structural design. Chapter 9 addresses the design iteration process, in which subsystem designs and mass iterations are examined to refine the Maximum Take-Off Weight (MTOW). Chapter 10 evaluates stability and control characteristics, while Chapter 11 provides a mission-level performance analysis using the SUAVE simulation framework [3].

Sustainability considerations integrated throughout the design are described in Chapter 12. Chapter 13 to 16 address key enabling aspects: the production and assembly plan, verification and validation approach, operations and logistics, cost estimation and technical resource budgeting. Finally, Chapter 17 assesses technical risks and Chapter 19 presents overall conclusions and recommendations for future development.

[1] https://www.rtl.nl/nieuws/onderzoek/artikel/5493952/noodhulp-112-hulpdienst-aanrijtijden-wachten-ambulance

2

Project Objectives

This chapter aims to introduce the main reasons for doing the project. Section 2.1 introduces the motivation behind the project and Section 2.2 discusses the stakeholder and mission requirements. Finally, the mission will also be introduced in Section 2.3, where the different stages of each mission are introduced.

2.1. Motivation

The efficacy of Emergency Medical Services (EMS) in the Netherlands, while supported by robust ground ambulance networks and Helicopter Emergency Medical Services (HEMS), faces increasing challenges. Growing urbanization, escalating road congestion [4, 5], and the centralized nature of specialized healthcare facilities contribute to potential delays and impeded access in various regions. Furthermore, conventional HEMS operations, reliant on fossil-fueled helicopters, are associated with significant operational costs [1], substantial noise footprints, and environmental pollution [2], impacting urban acceptability and sustainability goals. The rapidly emerging electric Vertical Take-Off and Landing (eVTOL) aircraft market presents an opportunity to address these limitations. Characterized by zero operational emissions, significantly lower noise signatures, reduced operational costs, and potentially more compact designs, eVTOL technology offers a compelling alternative for future EMS provision.

The project *aims* to develop an Emergency Medical Services (EMS) eVTOL aircraft designed to perform patient rescue and inter-facility patient transfer services in the Netherlands. The vehicle should address the growing challenges in medical transport, such as urban congestion, centralized healthcare, and environmental sustainability, while offering a competitive and operationally viable alternative to current Helicopter EMS (HEMS) systems.

The primary motivation for this project stems from the increasing challenges faced by conventional HEMS and ground ambulance services, including operational costs, noise pollution, and traffic congestion. Based on a comprehensive market and stakeholder analysis, the following Mission Need Statement (MNS) was formulated to address this gap.

Mission Need Statement (MNS)
Ensure a faster, quieter, and more flexible emergency transportation solution to overcome challenges posed by urban congestion, limited landing space, and noise restrictions.

To translate this high-level need into a concrete engineering task for this Design Synthesis Exercise, a specific Project Objective Statement (POS) was defined. The POS establishes the key performance, capacity, and cost targets for the design.

Project Objective Statement (POS)
Design an emergency response eVTOL able to carry at least 1 pilot, 1 crew and 1 patient, operable within the existing EC135 infrastructure and at 50% lower costs in the span of 10 weeks.

2.2. Stakeholder & Mission Requirements

Market analysis revealed that the current EMS landscape in the Netherlands features both ground-based ambulances and HEMS operations. Ground ambulances are increasingly limited by traffic delays [4, 5], while helicopters face high operational costs [4, 1], noise and environmental pollution [2], and limited landing zone access. Market trends and SWOT analysis reveal that there is an emerging gap for a quieter, less polluting, and cost-effective alternative to HEMS helicopters. A purpose-built eVTOL platform for EMS, VTOL emergency medical services (VEMS), can fill this gap by offering faster response times, lower maintenance, lower operational costs [6], and improved public acceptance due to reduced noise and emissions. VEMS can replace existing HEMS operations in a higher volume because of the lower costs, therefore these VTOL's could also respond to the cases in which ambulances cannot reach on time. The market research also highlights the potential for infrastructure reuse, such as existing hospital helipads, further improving integration feasibility.

Key and Driving mission requirements, derived from mission profiles, market insights, and stakeholder analysis

as detailed in the Baseline Report, are summarized in Table 2.1 and Table 2.2. The stakeholder, key and driving requirements are later verified in Chapter 18 to ensure the design meets real world requirements.

Table 2.1: *Driving mission requirements*

Requirement ID	Requirement Text
REQ-OPE-01-MIS-02	The vehicle shall be capable of transporting a patient requiring critical care from an unprepared emergency site to a designated healthcare facility.
REQ-OPE-01-MIS-03	The vehicle shall be capable of transporting a patient requiring critical care between designated healthcare facilities.
REQ-OPE-08-MIS-01	The vehicle shall be capable of operations in weather conditions up to Beaufort 6 wind force.
REQ-USR-05-MIS-01	The overall prototype development cost estimate shall not exceed 3,000,000 EUR (FY2025).

Table 2.2: *Key mission requirements*

Requirement ID	Requirement Text
REQ-OPE-01-MIS-04	The vehicle shall be designed for primary operation within the geographical confines of the Netherlands.
REQ-OPE-03-MIS-01	The vehicle's operational costs shall be significantly lower than current HEMS ($\leq 50\%$ of EC-135).
REQ-MAN-02-MIS-01	The target unit production cost shall enable a viable business case compared to existing HEMS solutions; this can be quantified by $\leq 50\%$ of EC-135.
REQ-USR-04-MIS-01	The final design shall incorporate sustainable principles and address lifecycle considerations.

2.3. Mission

Given the spread of healthcare infrastructure in the Netherlands the following mission profile was derived to be the most critical. The mission comprises the following steps: 1) 30 [second] hover, 2) 1 [min] vertical climb to 300 [m], 3) 30 [min] cruise for 110 [km], 4) 1 [min] vertical descend, 5) 30 [second] hover, 6) Repeat steps 1-5 to go back to the hospital. Cumulatively, for a complete round trip, the eVTOL must therefore achieve a total cruise distance of 220 [km], hover for 2 [min], climb for 2 [min], and descend for 2 [min], all operating on a single battery charge. Furthermore, the energy consumed during the transition phases has been omitted from the sizing calculations. This simplification is justified by existing literature, which indicates that transition typically consumes significantly less energy than the hover or cruise segments [7].

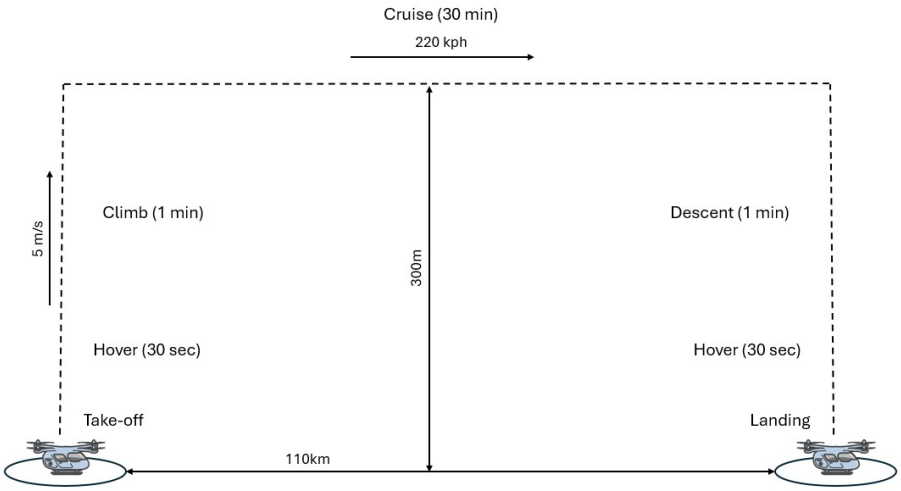

Figure 2.1: *Mission profile for preliminary design concepts*

This mission, in conjunction with all the derived requirements, a concrete project objective is laid out to work toward.

3

Market Analysis

In order for the vehicle to be competitive in the market, current competitors were evaluated. For this, both the current provision of emergency medical services in the Netherlands and the urban air mobility market will be discussed in Section 3.1. A financial (Section 3.2), operational (Section 3.3), and environmental analysis (Section 3.4) was performed on both the current and anticipated markets. Based on these findings, a SWOT analysis was conducted in Section 3.5. The chapter is concluded by identifying the stakeholders (Section 3.6).

3.1. Market Landscape

Emergency Medical Services (EMS) is a system that responds to emergencies requiring highly skilled pre-hospital clinicians. EMS is most recognizable by its vehicles, helicopters, and workforce, which respond to emergency incidents [8]. For the vehicle to remain competitive in the market, both current and projected market conditions must be analyzed. The market will be analyzed from a financial, operational, clinical, and environmental perspective, while considering safety and reliability.

Emergency Medical Services in the Netherlands

The current Emergency Medical Service (EMS) provision in the Netherlands integrates ground-based assets, managed regionally, with national Helicopter Emergency Medical Services (HEMS). Both systems serve as benchmarks for the proposed eVTOL EMS solution.

Ground services are coordinated across 25 Regional Ambulance Services (RAV) [9]. The primary response utilizes Advanced Life Support (ALS) ambulances, typically crewed by two medics, dispatched under urgency codes [10]. The highest urgency (A1) requires arrival within 15 minutes, a target increasingly difficult to achieve consistently in non-urban areas due to increasing traffic constraints [4, 5]. Systematically improving response times solely through ground network expansion faces significant logistical and financial barriers, particularly in personnel recruitment and funding [5]. This operational strain underscores a potential niche where eVTOL technology could provide significant value.

Complementing the ground network, ANWB Medical Air Assistance (MAA) operates 24/7 HEMS from four strategic bases (Amsterdam, Rotterdam, Volkel, Eelde) [11]. Handling over 11,760 calls in 2020 with helicopter deployment in approximately 77% of cases, the service primarily utilizes Airbus EC135 (H135) and H145 helicopters [11, 12]. It is important to note that the core mission of the onboard Mobile Medical Team (MMT), consisting of a pilot, specialist doctor, and medic, is the rapid delivery of advanced medical expertise directly to the scene. Patient transport mode (air or ground) is determined based on overall speed to definitive care [11, 13]. This established HEMS model, its fleet capabilities (particularly the EC135), and team composition provide benchmarks for airborne EMS performance, cost comparison, and operational integration within the Netherlands.

Urban Air Mobility Market

The increasing need for more rapid, cost-effective, and sustainable emergency medical response systems demands innovation beyond traditional transport methods. Road ambulances face limitations due to increasing urban congestion, while conventional helicopters require high operational and maintenance costs. This makes other, cheaper VTOL aircraft a compelling alternative for current EMS vehicles. Additionally, connectivity to the less urban areas in the Netherlands, such as in the southern Europort areas, is less sophisticated, and it could take excessive time to reach these areas [14].

The broader VTOL market, although still developing, is expanding rapidly, as can be seen by over 200 distinct concepts currently under investigation according to a recent EASA study [15]. Significant investment and progress towards certification by leading companies highlight the technical viability and growing maturity of VTOL platforms.

Moreover, developments specifically targeting the unique demands of EMS remain relatively nascent compared to the passenger transport sector. Most of the current industry efforts involve adapting existing airframes rather than exploring purpose-built EMS designs. Notable examples include the collaboration between ADAC Luftrettung and Volocopter, which investigates adapting Volocopter's multicopter for first responder roles [16]. Another example

is the recent consideration by U.S. firms such as Joby Aviation and Beta Technologies to modify their passenger and cargo aircraft for potential medical applications [17, 18]. In contrast, the ERC System represents one of the few initiatives focused on building a dedicated EMS VTOL configuration from the outset [19]. The current market thus showcases the opportunity for developing novel eVTOL concepts specifically optimized for the demanding requirements of EMS operations, as undertaken in this project.

3.2. Financial Analysis

Cost efficiency is one of the most compelling arguments for integrating eVTOLs into Emergency Medical Services (EMS). Current HEMS helicopters (e.g., EC135/H135) typically cost €3 million to over €5 million, setting a standard for comparison [20, 21]. On the contrary, eVTOLs aim for lower costs with passenger models, suggesting potential €1-2 million unit prices [22] without specific EMS features.

Dedicated EMS eVTOL designs, such as the ERC System's Charlie (€3-5 million estimate [19]), are initially comparable to helicopters due to their mission complexity. However, the fundamental design of eVTOLs featuring simpler systems with a potential for lower maintenance costs points towards a significant long-term operational cost advantage over traditional helicopters.

Achieving this requires addressing initial development costs associated with vertiports, charging infrastructure, and operational integration into current EMS systems [6], although these costs are expected to decrease with wider adoption.

Operational Costs

Current Helicopter Emergency Medical Services (HEMS) operations require substantial costs. A study analyzing EC135 operations in rural Germany estimated an annual cost of €1.7 million for 12-hour daily coverage, equating to approximately €763 per primary mission (provision of a patient transfer from the incident site to the hospital with an assumed duration of 20 [min]) [1]. A big portion of these expenses is from fuel consumption and the complex maintenance required for helicopter engines and rotor systems due to high mechanical loads. The average maintenance cost in this scenario is €236.96 per mission, while the rated average fuel consumption per minute considered was €5.83 (traveling speed 254 [km/h] and consumption rate 318 [l/h]). While extending operational hours increases per-mission costs (potentially exceeding €1,100 for 24/7 coverage), higher overall mission volume can lead to improved cost efficiency by distributing fixed costs (staffing, insurance, depreciation) more broadly.

In contrast, eVTOL technology has the potential to significantly reduce operational costs. The transition to electric propulsion systems, characterized by fewer moving parts compared to conventional helicopters, is projected to lower maintenance costs by 30–50% [6]. Furthermore, adopting electricity, which is considerably cheaper than aviation fuel, is anticipated to decrease energy costs per mission by 60–70% [6]. The cumulative effect of lower maintenance and energy expenses suggests substantial long-term savings, particularly advantageous for the high-utilization scenarios typical of effective EMS operations.

3.3. Operational Analysis

Current Emergency Medical Services (EMS) rely primarily on Advanced Life Support (ALS) ambulances, motor ambulances, and Helicopter EMS (HEMS). A comparison of their technical characteristic, shown in Table 3.1 highlights their respective strengths and limitations.

Table 3.1: *Performance analysis of current EMS vehicles*

Description	ALS Ambulance (Mercedes-Benz Sprinter)	Motor Ambulance (BMW R 1200 RT)	HEMS (H135)
Maximum velocity [km/h]	160 [23]	200 [24]	252 [25]
Maximum range (with std. fuel tank) [km]	800 [23]	400 [24]	633 [25]
Maximum endurance (with std. fuel tank)	-	-	3h 36 min [25]
Refuel time [L/min]	40 [26]	40 [26]	Not publicly documented, estimated ±10 min
Fuel type	Diesel [27]	Petrol [24]	Refer to approved RFM [28]
Engine type	4-cylinder turbo engine, 7-speed [27]	Flat twin 4-stroke Boxer engine [24]	SAFRAN ARRIUS 2B2+ or PW206B3 [25]
Number of engines	1	1	2 [29]
Engine power	140 kW [23]	81 kW [24]	2 × 660 SHP [29]
Landing area [m]	-	-	25×25 (day), 50×25 (night) [30]
Length [m]	5.93 [23]	2.23 [24]	12.16 [29]
Width [m]	2.35 [23]	0.91 [24]	- (rotor diameter is limiting)
Height [m]	2.35 [23]	1.43 [24]	3.51 [29]
Rotor diameter [m]	-	-	10.2 [29]
Payload or MTOW [kg]	2998 [23]	236 [24]	2980 [29]
Number of medical staff	2 [31]	1	2 + pilot [29]
Available seat (patient, family)	1, 1 or 2, 0 [31]	0, 0	1, 0 [29]
Average response time [min]	15 [32]	- (assist ambulance)	±15 [33]

Analysis of these conventional transportation modes reveals key operational trade-offs. While HEMS (e.g., H135) offers superior speed and range ($252\,[\mathrm{km/h}]$, $633\,[\mathrm{km}]$ [25]), essential for covering large regions, they require significant landing areas ($25\times25\ [\mathrm{m}]$ minimum [30]) and incurs higher operational costs. ALS ambulances

(e.g., Sprinter [23]), although slower and limited by road networks and congestion (despite regulatory speed allowances [34]), provide substantial payload capacity ($\approx 3000\,[\mathrm{kg}]$) for patient transport and onboard treatment. Motor ambulances prioritize rapid response for initial assessment and care, thereby offering agility in urban settings but lacking patient transport capability [24].

This comparison provides factors for evaluating new VTOL aircraft for EMS. Studies considering the market in U.S., characterized by long-distance air EMS missions often exceeding $200\,[\mathrm{km}]$, suggest that the current battery energy density and recharge times (30-60 minutes minimum, often longer) significantly limit the operational availability and suitability of purely electric eVTOLs compared to helicopters [35].

However, this perspective shifts significantly within the European and specifically in the Dutch landscape, where shorter mission distances (often below $200\,[\mathrm{km}]$) are needed. This leads to a reduction in the criticality of maximum range, making rapid dispatch and turnaround times more important [36]. In such scenarios, the viability of eVTOLs relies more on solving the battery recharge issue. Technological innovations like rapid battery-swapping systems or advancements in fast-charging infrastructure play a greater role in developing the EMS eVTOL concept. Furthermore, research indicates that hybrid VTOLs already present a competitive option. Electric VTOLs equipped for fast turnaround can be viable for shorter trips, offering substantial benefits in lower energy costs, reduced maintenance, and zero direct emissions [37]. This is particularly advantageous in geographically compact regions with dense hospital networks like the Netherlands.

Compatibility with existing infrastructure, such as hospital helipads, is also a critical factor for integration Table 3.2 shows an analysis of Dutch hospital helipads as given in the dutch aeronautical information publication [38] in terms of AUW (all up weight) and TLOF (take-off and landing area).

Table 3.2: *Analysis of Dutch hospital helipads [38]*

Hospital	Max AUW	TLOF dimensions [m]
Amsterdam; AMC	N/A	N/A
Rotterdam; Erasmus MC	N/A	N/A
Tilburg; St. Elisabeth ziekenhuis	N/A	N/A
Utrecht; Universitair Medisch Centrum	MTOW of EC135 [39]	10.2 (max rotor diameter) [39]
Nijmegen; Radboud MC	N/A	N/A
Leiden LUMC	N/A	N/A
Maastricht UMC	N/A (ground helipad) [40]	15 x 15 [40]
Groningen; UMCG	10000 kg [41]	22 x 22 [41]
Zwolle; Isala Klinieken	MTOW of EC135 [42]	18x18 [42]
Enschede; Medisch Spectrum Twente	5000 kg [43]	22 x 22 [43]
Beverwijk; Rode Kruis Ziekenhuis	9000 kg [44]	20 x 20 [44]
Den Haag; Haga Ziekenhuis	N/A	N/A
Den Haag; MC Haaglanden	N/A	N/A
Goes; Adrz	N/A	N/A
Medisch Centrum Leeuwarden	13500 kg [45]	20 x 20 [45]
Sneek; Antonius Ziekenhuis	MTOW of H145 [46]	20 x 20 [46]
Terneuzen; Zienkenhuis Zeeuws-Vlaanderen	N/A	N/A

3.4. Environmental Analysis

Healthcare currently represents a significant carbon-intensive sector and is responsible for approximately 4.4% of global net greenhouse gas emissions [47]. To combat this, international bodies such as the Intergovernmental Panel on Climate Change (IPCC) and the World Health Organisation (WHO) have urged reductions in healthcare's ecological footprint [48, 49]. Medical transport is a contributing factor within this footprint. Although the emissions data presented in Figure 3.1 [50] originates from general transportation studies, it also provides relevant comparisons for Emergency Medical Services (EMS) due to the overlap in vehicle types used, namely helicopters, cars, eVTOLs, etc.

Analysis of specific eVTOL concepts, such as the Lift & Cruise type, revealed that they emit 10.82 [g CO_2/km] per person [50]. This demonstrates notable environmental advantages over traditional transport. As indicated in Figure 3.1, this type of eVTOL achieves considerable CO_2 reductions compared to conventional helicopters (77%), petrol cars (46%), diesel cars (44%), and even hybrid vehicles (9%) [50]. These figures showcase the potential benefits of integrating eVTOLs into EMS fleets. However, it is crucial to note that eVTOLs, based on current energy grids and technology, still exhibit higher emissions than fully electric ground vehicles (approximately 68% more CO_2).

Keeping the environmental analysis in mind, it should be noted that the primary goal of EMS, particularly HEMS, is to save lives. This means that characteristics such as speed and reach outweigh emissions concerns, making performance the key driver in this mission. Moreover, HEMS emissions are minimal compared to the total CO_2 emissions of the healthcare sector in the Netherlands. The healthcare sector is responsible for approximately 7% of national greenhouse gas emissions [51]. In 2021, the Netherlands emitted 146.87 Mton of CO_2 [2], making

healthcare responsible for about 10.28 [Mton] of CO_2 annually. In comparison, with around 10,000 HEMS missions per year in the Netherlands, averaging 50 [km] per flight and approximately 400 [g CO_2/km], total emissions are roughly 200 tonnes CO_2 annually, just 0.002% of the healthcare sector's emissions.

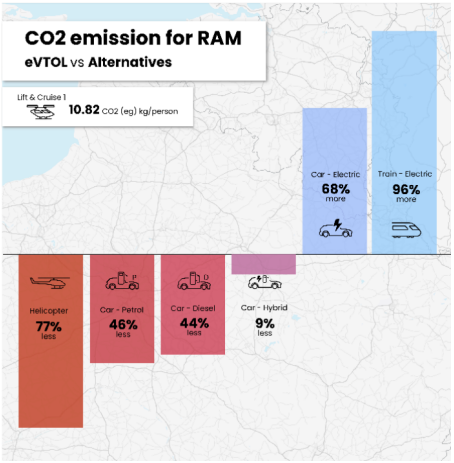

Figure 3.1: *CO2 emissions for RAM: eVTOL vs. alternatives [kg/person] [50]*

3.5. SWOT Analysis

To evaluate the viability of integrating eVTOL technology into Emergency Medical Services (EMS), a SWOT analysis is conducted under the assumption that a purpose-built, fully electric eVTOL is developed specifically for medical missions (3.3). This design would include space for a pilot, paramedic, patient, and medical equipment, with an emphasis on minimizing operating costs, emissions, and noise. While this configuration offers compelling advantages in urban and regional EMS settings, particularly in compact geographies like the Netherlands, key limitations remain, especially regarding battery range and recharge duration. These factors have a direct impact on operational readiness and dispatch time, which are critical for time-sensitive medical missions. In contrast, hybrid-electric VTOL designs, which combine electric lift with fuel-based propulsion for cruise, may offer superior range and endurance and benefit from faster turnaround due to conventional refueling.

Table 3.3: *SWOT analysis of the design and development of an eVTOL vehicle for EMS operations*

	Helpful	Harmful
Internal	Lower operational costs than HEMS, Lower unit costs than HEMS, Purpose-Built EMS Design, Lower carbon footprint, Reduced noise pollution	High initial development costs, Limited range and endurance, Recharge time constraints
External	Urbanization and congestion, Potential of market expansion in other countries, Potential use of current helipads and other infrastructure	Regulatory uncertainty, Some competition (ERC System, ...)

3.6. Stakeholders

Stakeholders encompass all entities that will interact with, benefit from, regulate, enable, or be impacted by the proposed eVTOL EMS system throughout its lifecycle. The identification of these stakeholders is a critical initial step in the design process and was the result of a thorough market analysis, considering the entire lifecycle and operational ecosystem of the proposed service. To manage their diverse interests effectively and ensure all relevant perspectives are considered during the design process, the identified stakeholders have been grouped into logical categories. These categories reflect their primary role or relationship to the project. The categorization is presented in Table 3.4.

The requirements from the various stakeholders presented do not uniformly drive the core design; hence, prioritizing them is essential to ensure that the most critical needs are addressed early in the design process. To facilitate this prioritization, stakeholders were mapped onto an Interest/Influence grid. It is important to note that while the grid defines four nominal quadrants (*Manage Closely, Keep Satisfied, Keep Informed, Monitor*), the placement of stakeholders within this grid should be interpreted as representing a spectrum rather than assignment to four discrete categories. The positioning reflects an assessment of each stakeholder's interest and influence relative to others. For instance, ANWB MAA is positioned with high interest due to its established role

Table 3.4: *Stakeholder Categorization*

Category	Stakeholders Included
Project & Academic	TU Delft (Supervisors, DSE Organization), Design Team
Operational & User Groups	EMS Operators (Customer), Hospitals & Trauma Centers, Medical Crew, Patients, ANWB Medical Air Assistance (MAA), Regional Ambulance Service Providers
Regulatory & Governance	EASA (European Union Aviation Safety Agency), Dutch Government Authorities
Financial	Private Investors
Supply Chain & Manufacturing	Manufacturing Partners, Electronics Suppliers, Materials Suppliers
Societal	General Public
Lifecycle Management	Partner for End-of-Life Disposal / Recycler

in the Dutch HEMS landscape, but its influence on the specific design choices of this project is considered moderate, placing it near the boundary between the 'Keep Satisfied' and 'Manage Closely' areas. This contrasts with entities like EASA, whose high influence via regulatory power places them firmly in the 'Keep Informed' domain. Following this analysis, the requirements stemming from the key stakeholders were determined.

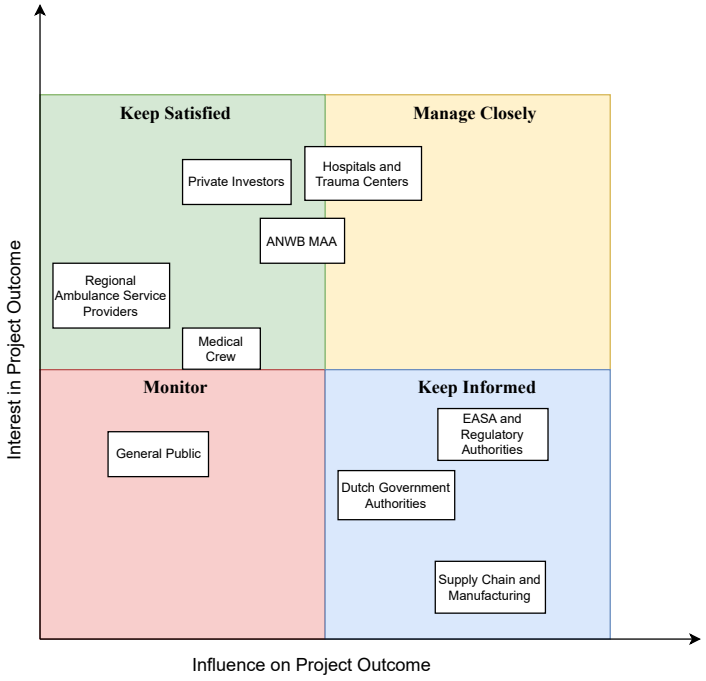

Figure 3.2: *Interest-Influence Map for the Project Stakeholders*

4

Configuration

In this chapter, the conceptual development and selection process of the aircraft configuration are presented. First, Section 4.1 provides an overview of the initial trade-off between several eVTOL concepts, based on mission requirements and key design constraints. Then, Section 4.2 details the refined evaluation of selected concepts using performance, control, and feasibility criteria, ultimately leading to the selection of the final configuration. Lastly, Section 4.3 discusses the internal layout of the aircraft, tailored to meet mission-specific operational needs.

4.1. Initial Configuration Trade-off

In the early stages of the design, six design options were proposed as strawman concepts. The options include a tilt-wing, augmented hover, tilt-prop, thrust-vectoring, gyrodyne, and finally, multicopter. Now, it is important to note that these initial concepts are rough and are merely sketches of initial options obtained from an initial design option tree. Nevertheless, the strawman concepts can be found in Figure 4.1.

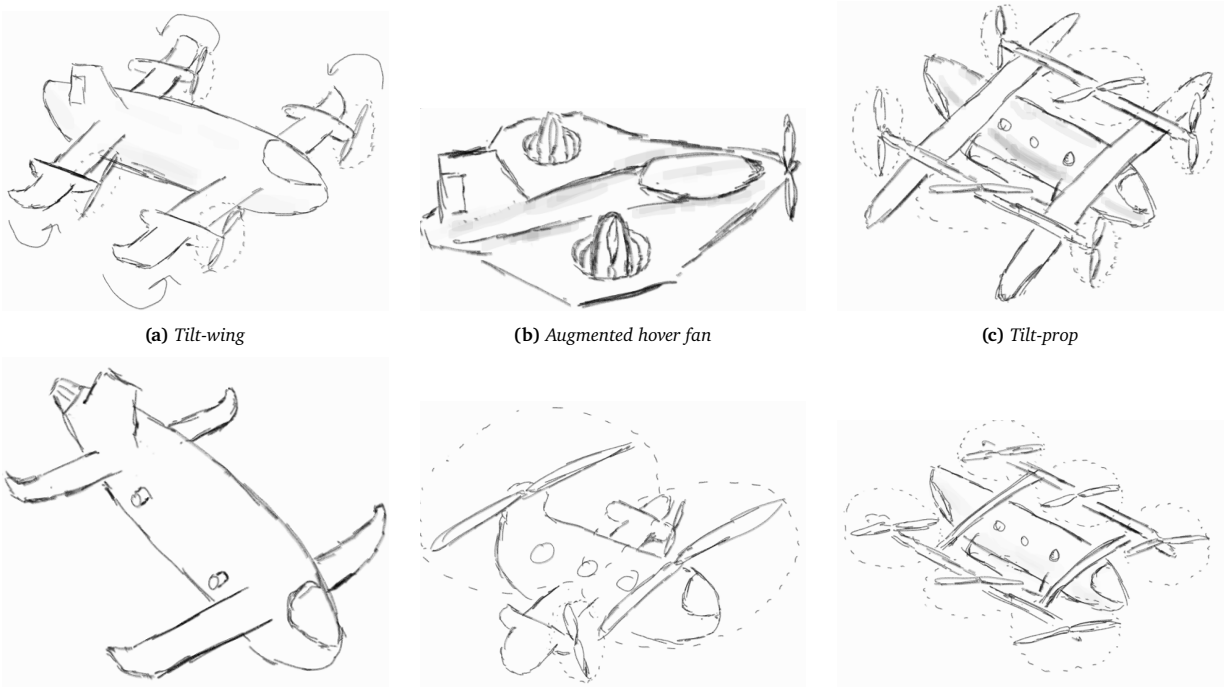

(a) *Tilt-wing* **(b)** *Augmented hover fan* **(c)** *Tilt-prop*

(d) *Thrust-vectoring* **(e)** *Tandem rotor gyrodyne* **(f)** *Multicopter*

Figure 4.1: *Strawman concepts in cruise mode*

These initial strawman concepts are later refined into three design options to be traded off for a final configuration choice. The three chosen options to be carried over to the final configuration trade-off are the tandem-wing similar to the concept shown in Figure 4.1a, the mono-wing configurations, and finally the delta flying wing similar to the aircraft in Figure 4.1b. The reason for discarding options stems from trade-offs conducted on wing types and propulsion systems. Regarding wing types, monoplanes and tandem wings came out on top, mainly due to their relative simplicity and high efficiency. Moreover, reconfiguration must be compact in order to meet REQ-HOS-01 in Table 18.1. Open propellers were chosen because of their low weight, control response, and availability on the market. Nevertheless, the four concepts are shown in Figure 4.2. The concepts are to be regarded as tandem-wing (concept 1), delta flying wing (concept 2), mono-wing with V-tail (concept 3), and finally monowing with canard and V-tail (concept 4).

1. **Concept 1 - Tandem Wing with Tilting Propellers.** The two lifting surfaces allow for a compact design, and the tilting propellers enable a smooth transition to cruise. Numerous existing eVTOL concepts have featured this configuration.

2. **Concept 2 - Delta Flying Wing with Integrated Fans.** A strong candidate due to its high structural and weight efficiency, enabling a greater useful load fraction - a crucial factor in EMS applications. Its low wing loading allows for shorter take-off distances and stable stall characteristics. Its low power consumption helps reduce operational costs without sacrificing transport efficiency.
3. **Concept 3 - Mono Wing with V-Tail.** Advantageous due to its structural simplicity and aerodynamic efficiency. The V-tail combines the roles of horizontal and vertical stabilizers, reducing weight while satisfying control and stability requirements. Mounting two propellers on the V-tail distributes the thrust more evenly across the airframe.
4. **Concept 4 - Mono Wing with Canard and V-Tail.** Similar to the previous concept but with enhanced low-speed stability due to the addition of a canard. The additional control surfaces could also provide outstanding maneuverability, particularly during transitional flight.

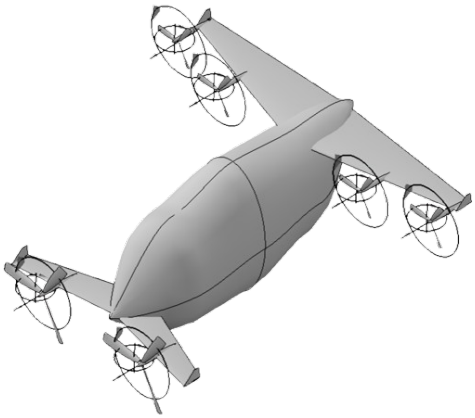

(a) *Tandem-wing (Concept 1).*

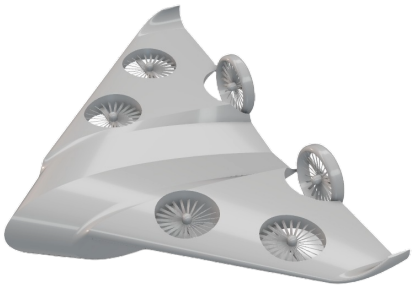

(b) *Delta flying wing (Concept 2).*

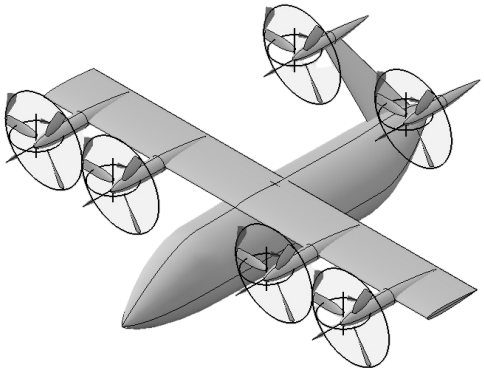

(c) *Mono-wing with V-tail (Concept 3).*

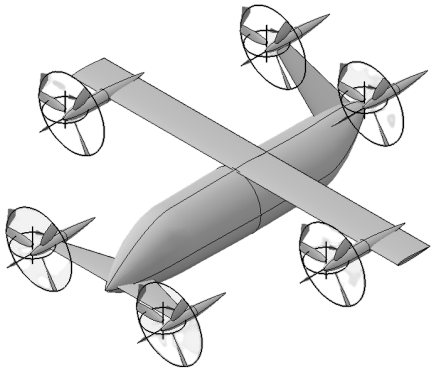

(d) *Mono-wing with canard and V-tail (Concept 4).*

Figure 4.2: *Preliminary design renderings for the four eVTOL concepts: (a) Delta flying wing, (b) Tandem wing, (c) Mono-wing with V-tail, and (d) Mono-wing with canard and V-tail.*

4.2. Final Configuration Trade-Off

The final trade-off of the configuration is done on the basis of an initial weight estimation and the total energy usage of each aircraft. The weight estimation was conducted based on processes proposed by Ugwueze et al. [52].

Table 4.1: *Overview of eVTOL design concepts*

Parameter	Tandem Wing	Delta Flying Wing	Mono + V-Tail	Mono + Canard
MTOW (kg)	1 680	1 228	2 155	3 100
Length (m)	8.3	7.2	8.0	8.0
Width / Wingspan (m)	9.5	9.0	9.5	9.5
Number of Propellers	6	6	6	6
Approx. Total Energy (kWh)	123.5	83.5	153	245

Based on five main criteria: mass, energy consumption, sustainability, control and stability, and risk. The mass is based on the maximum take-off weight (MTOW), the energy consumption is dependent on the energy used throughout the mission, sustainability assessment is done based on the configuration's environmental impact throughout manufacturing, operation, and end-of-life. Control and stability are assessed by how the configuration generally performs, based on similar old aircraft. Finally, risk is assessed by quantifying the potential shortcomings of the design and the contingencies related to these shortcomings.

Table 4.2: *Summary of design option scores (1=Poor, 5=Excellent) and final weighted scores. Column widths for criteria are proportional to their weights.*

Design Option	Mass (20%)	Energy Cons. (25%)	Sust. Scope (15%)	Ctrl. & Stab. Char. (25%)	Risk (15%)	Weighted Score
D1: Delta Wing	5	5	4	3	2	**390**
D2: Tandem	4	3	4	4	4	**375**
D3: Mono Wing 1	3	2	3	4	4	**315**
D4: Mono Wing 2	1	1	2	5	4	**260**

Hence, the delta wing configuration comes out on top and is carried over to the following stages of the design.

4.3. Internal Layout

The internal layout of the aircraft is designed around its primary mission: the rapid and safe transport of injured individuals. As shown in Figure 4.3, the cabin is laid out to ensure that the pilot, patient, and medical crew all have the necessary space and accessibility for safe operation and in-flight treatment.

At the front right-hand side of the aircraft, the pilot is seated in a separate compartment with full forward visibility and access to all flight controls. This position ensures that the pilot can operate the aircraft without interference while also being close to the cabin space if needed.

On the right side of the cabin, a stretcher is mounted longitudinally to allow for quick loading and unloading of the patient. The stretcher is placed in such a way that medical personnel have access from both sides, which is critical during emergency interventions. The stretcher space is also aligned with the main cabin door to allow direct access from the outside.

Two seats are positioned facing inward toward the stretcher; however, they may be swiveled if needed. These are reserved for medical crew and are angled to allow close and continuous monitoring of the patient. The placement also allows for easy communication between the crew and access to any medical equipment stored in the cabin. Medical equipment may also be stored behind the seats, on the right side.

Overall, the layout prioritises function and accessibility, with a clear separation between flight operations and patient care. The internal space is optimised to make use of the available volume while maintaining aircraft balance and keeping all systems accessible for maintenance and inspection.

Figure 4.3: *Top view of the internal layout showing pilot seat, medical crew seats, and stretcher*

5

Aerodynamics

The first step in the design process of DoctAir, is the aerodynamic analysis, with the end goal of obtaining the aircraft's lift, drag and moment curves. This analysis dictates the aerodynamic loads on the aircraft, influencing the required structural strength and battery mass for the aircraft's missions due to drag. This chapter can be split into two subsequent sections; firstly, an airfoil selection is carried out to define the aircraft's geometry since it is a flying wing configuration. Followed by a full aerodynamic analysis to obtain the aircraft's lift, drag, and moment curves, the stall regime will also be estimated through empirical methods. These results are also verified through empirical methods and a validation strategy is also proposed.

5.1. Assumptions

The following assumptions have been used in the subsequent analysis:

- **AS-AERO-1**: The flow is assumed to be inviscid. This is a conventional assumption which is valid for low-speed aerodynamic analysis as the viscous boundary layer can be decoupled from the inviscid flow field around it. This is because the pressure field, which determines the lift and moment of a body, is transferred through the boundary layer in a normal direction onto the surface of the body [53]. To predict the drag and stall regime of the aircraft, empirical estimations from [54] will be employed.
- **AS-AERO-2**: The flow is assumed to be incompressible, irrotational and steady, this is such that potential flow methods can be used for aerodynamic analysis. It is justified since the aircraft operates at a design cruise speed of 61 [m/s] at 300 [m] of height, giving a Mach number of 0.18, which is well in the incompressible regime. Additionally, due to AS-AERO-1, the surface of the body does not introduce rotation either. Finally, steady flow can be assumed as the aerodynamic behavior of the aircraft is analyzed mainly for the cruise condition, which occurs at a steady velocity without large maneuvers.
- **AS-AERO-5**: The angle of attack is assumed to be small, this is such that linear aerodynamic theory is still valid. Below 15 [°] of angle of attack this introduces less than 2% of error considering a Taylor series expansion.
- **AS-AERO-6**: The geometry of the lifting surface is assumed to be thin, this is a consequence of the ultimately chosen Vortex Lattice Method (VLM) model. This means that the camber line of the airfoil is modeled but not the thickness, nevertheless, VLM methods can be sufficiently accurate for delta wing planforms [53].

5.2. Airfoil Selection

Selecting the type of airfoil to be used defines the entire shape of the aircraft due to it being a flying wing; it also determines the main loads, along with control and stability characteristics. Due to this, it is one of the first procedures to be carried out before any of the subsequent chapters' analyses can be performed.

The central part of the aircraft's planform, where the cabin is contained, is given a symmetrical **NACA0025** airfoil. This is to maximize internal space for the passengers, and the section has a width of 1.6 [m], as determined during the midterm report. An additional benefit of the symmetric cross-section is the low or zero generation of a negative pitching moment (pitch-down), which is sought after to guarantee stability of flying wings [55]. Moreover, between these two regions, there is a blending region of 0.9 [m] width, where the two airfoil shapes are transitioned.

For the remaining part of the planform, a preliminary list of airfoils was selected. This selection was based on previous airfoils used for flying wings or tailless aircraft from [56]. These airfoils are usually characterized by a reflexed trailing edge and positive moment coefficient at the aerodynamic center. The final list can be seen on the x-axis of Figure 5.1.

After this, the airfoil geometries are analyzed at the cruise lift coefficient of the aircraft, obtained from equating the lift and weight forces. The analysis is performed in XFOIL, which couples an inviscid panel method with constant source strength and linear vorticity strength per panel, with a viscous formulation based on the compressible momentum and energy equations [57]. Then, either side of the planform is divided into 10 stations at which the Reynolds number is computed based on the local chord length. This allows to compute the lift to drag ratio (L/D) and moment coefficient (c_m) of each airfoil; the one with the highest ratio and positive moment

coefficient is selected. If a large variation of airfoils is chosen at each station, then the difference between their performance can be compared to consider if a reduced number of different airfoils can still give adequate performance while simplifying the geometry. Similarly, if the magnitude of the moment coefficient is seen later on to be too large for stability and control requirements, the analysis can be reevaluated.

The results at a selected spanwise station can be viewed in Figure 5.1. It can be seen that the E186 airfoil performs the best; while the NACA64215 has a higher lift to drag ratio, its moment coefficient is highly negative. The final procedure led to the **E186** airfoil being selected for each spanwise station; the final airfoil distribution is seen in Figure 5.2, where a change in airfoil geometry is shown by the specific airfoil section at that spanwise position.

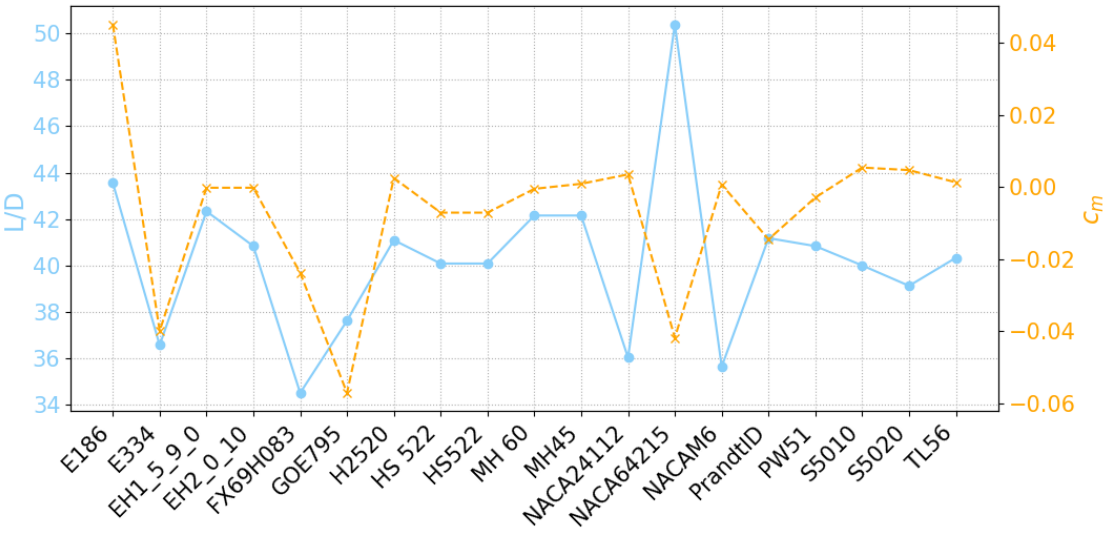

Figure 5.1: *Comparison of selected airfoils' lift to drag (L/D) and moment coefficient c_m at a spanwise station.*

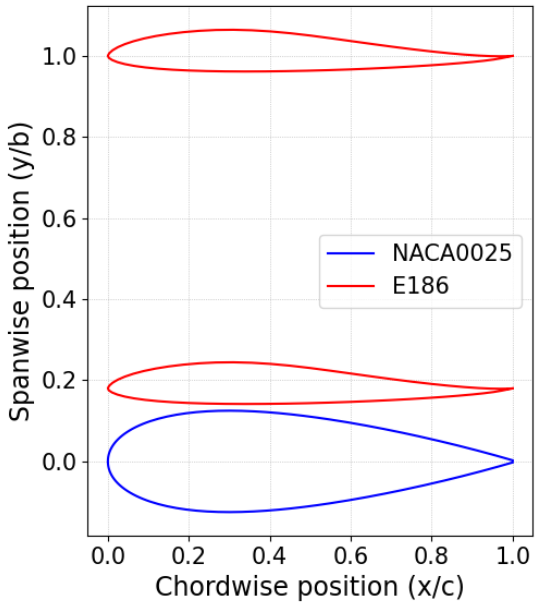

Figure 5.2: *Selected airfoils along the wing span.*

5.3. Full Aircraft Aerodynamic Analysis

Once the airfoil geometry has been chosen, the outer aerodynamic shape of the aircraft is fully defined. This then allows the computation of the lift, drag, and moment curves of the full aircraft, along with the stability derivatives required for controlling the aircraft in Chapter 10.

Selecting the appropriate analysis method is a key step, as the delta wing configuration has complex dynamics not taken into account by traditional aerodynamic methods. As such, lifting line approaches are discarded since their validity applies for high aspect ratio and non-swept wings [53]. The next level consists of vortex lattice methods, which cover the wing planform in a series of horseshoe vortices both in the spanwise and chord-wise direction, as opposed to only the spanwise direction for lifting line methods. These are more applicable to low aspect ratio and swept wings [53]. Another option is panel methods, which discretize the aircraft's 3D geometry into a series of flat panels with specific potential flow functions; these have the advantage of being able to take 3D geometry into account [53]. Lastly, numerical simulation of the Navier-Stokes equations can also be done to take into account the nonlinear behavior of delta wing planforms, such as vortex lift. Nevertheless, this was not performed during the design cycle due to the large number of computing hours required to obtain all the coefficients related to the stability derivatives of the aircraft and the difficulty of accurately calculating them. Moreover, the effects of nonlinearities can be taken into account through validated empirical methods such as [54], which can provide sufficient accuracy for the current design phase and allow for faster iterations. In conclusion, vortex lattice methods (VLM) and panel methods will be used to analyze the aircraft, and a choice will be made between the two based on the obtained data. Instead of creating a proprietary version of these methods, NASA's OpenVSP aircraft analysis platform provides verified and validated implementations of them. While estimation methods from [54] will be used as further validation for the low aspect ratio effects.

Vortex Lattice and Panel Method Comparison

The aircraft's geometry was simulated in OpenVSP with a range of angle of attack from 0 to 10 [°] with 7 data points, both with a VLM and panel method. Overall, the VLM method provided $3\times$ improvements in computation time while requiring significantly fewer iterations to converge. These differences can be seen in Figure 5.3a and Figure 5.3b, wherein the panel method barely achieves any improvement over 5 iterations as compared to VLM.

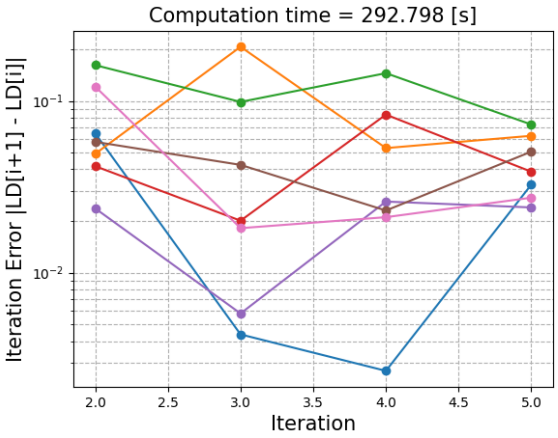

(a) *Lift to drag ratio (L/D) convergence with panel method through 5 iterations for different angles of attack.*

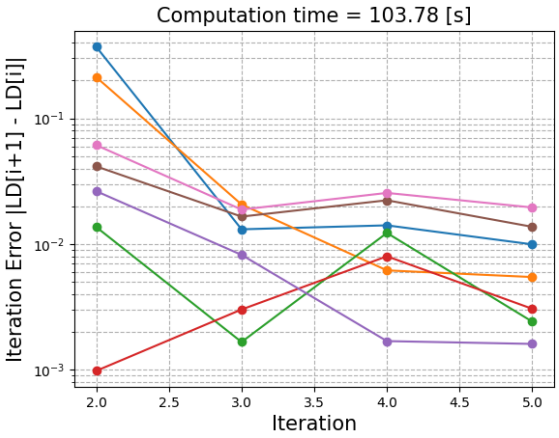

(b) *Lift to drag ratio (L/D) convergence with vortex lattice method (VLM) through 5 iterations for different angles of attack.*

However, these differences are not surprising, since VLM is a 2D method while the panel method requires more elements to cover the 3D geometry. Hence, the results can be analyzed to determine if the additional computational time and iterations are worth the possible increase in precision. Firstly, the spanwise load distribution can be compared. From Figure 5.4b and Figure 5.4a, it can be seen that the panel method suffers from numerical instabilities and non-physical results. Especially near the wing tips and the morphing region between the two airfoils, while another peak is seen at a spanwise position of ± 0.65. On the contrary, VLM provides smooth load distributions even with changing airfoils, while remaining relatively close to the sensible sections of the panel results. The non-physical effects of the panel results were not seen to improve with more iterations nor with an improved panelling; and convergence did not reach the levels of VLM either. It must be noted that the drag distribution cannot be obtained through VLM due to its potential flow foundation. In turn, OPENVSP computes the zero-lift drag from an empirical method such as [54] and the induced drag from the obtained lift distribution of VLM.

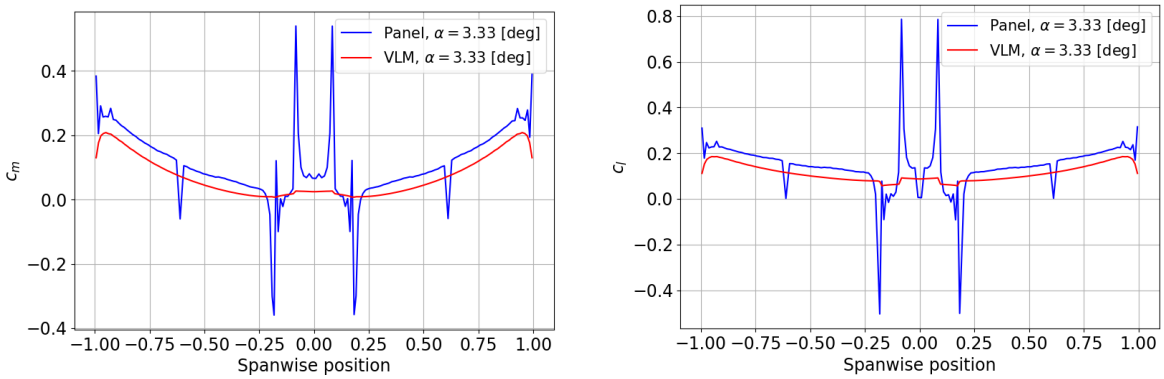

(a) *Moment distribution.*

(b) *Lift distribution*

Figure 5.4: *Aircraft aerodynamic spanwise load distribution comparison between VLM and panel method.*

The lift, drag, and moment curves of the aircraft computed with the two different methods can be seen in Figure 5.5a, Figure 5.5b, and Figure 5.5c, respectively. Both methods have good agreement in the drag curve Figure 5.5b while in the lift and moment, they differ by 6% and 5% in their slopes. The more substantial differences are seen in the intercept of the graphs, which differ by up to 45%.

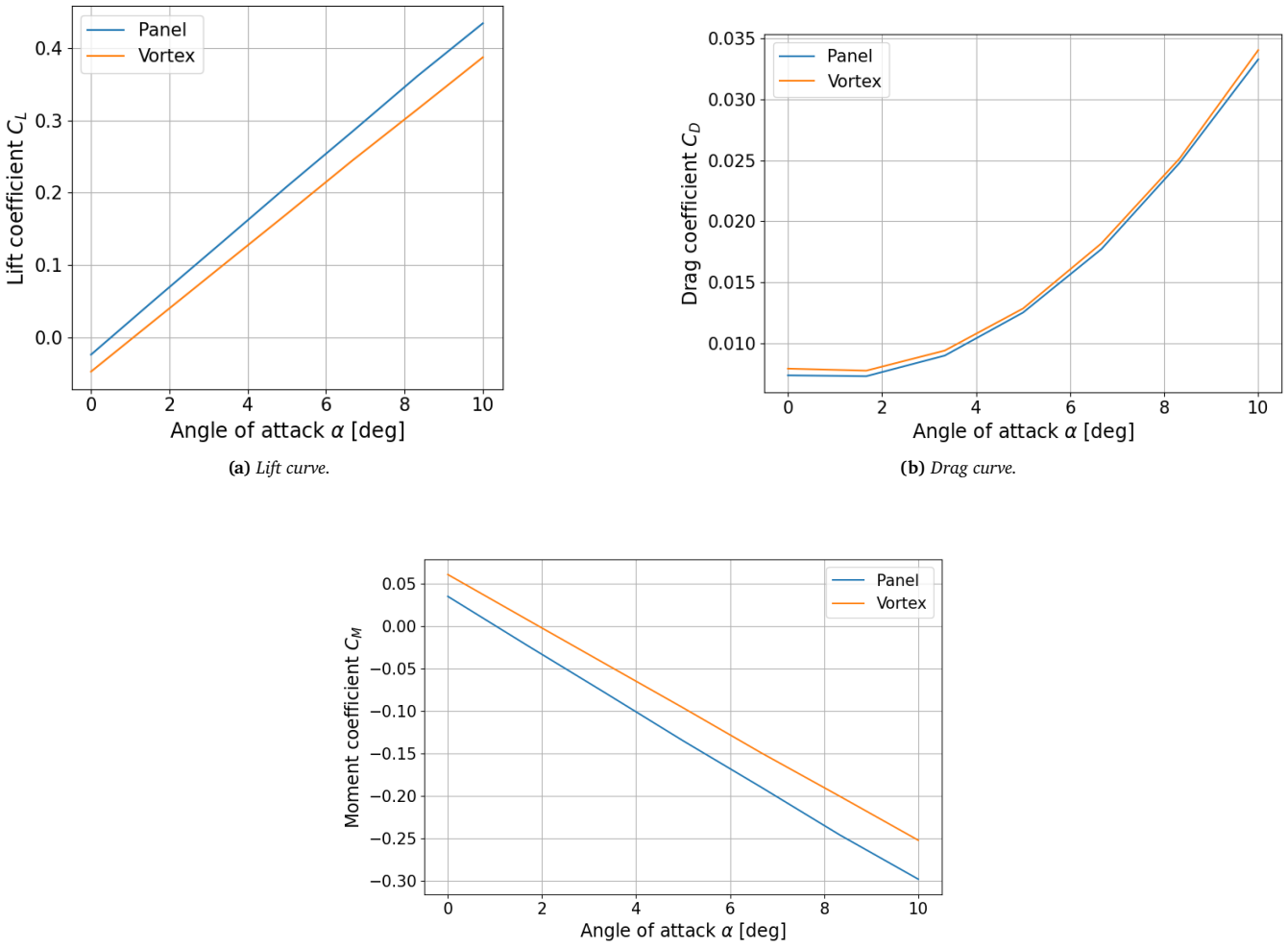

(a) *Lift curve.*

(b) *Drag curve.*

(c) *Moment curve.*

Figure 5.5: *Main aircraft aerodynamic load curves comparison between VLM and panel method.*

Overall, since the spanwise distribution of aerodynamic loads is important for structural calculations, the VLM method offers a more realistic result since, on average, it follows closely the panel method without its numerical

instabilities. The VLM also provides a lower lift result, meaning that if the panel results are considered theoretically more accurate, the VLM underestimates the performance of the aircraft in a conservative way. Hence, with the **chosen VLM method**, the aircraft will not be under-designed, and computation time is also saved.

Final Vortex Lattice Method Results

The aircraft was again simulated in OpenVSP with the VLM method with a range of angle of attack from -5 to 15 [°] with 20 data points. Similarly, for additional stability derivatives of the aircraft, the same was performed for the sideslip angle from 0 to 15 [°]. The final lift, drag and moment curves can be seen in Figure 5.6a, Figure 5.6b and Figure 5.6c, respectively. As desired, the moment curve Figure 5.6c is fully positive for the considered range of angle of attack, while the lift curve Figure 5.6a is shallow but expected for a delta wing planform. The main parameters of these curves can be found in Table 5.1.

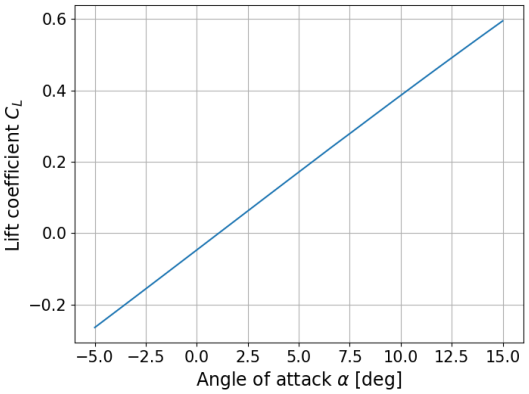

(a) *Lift curve.*

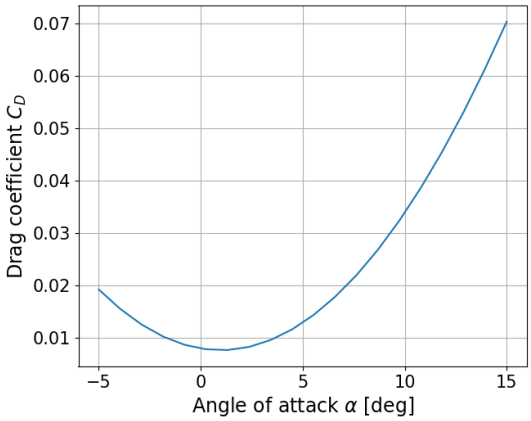

(b) *Drag curve.*

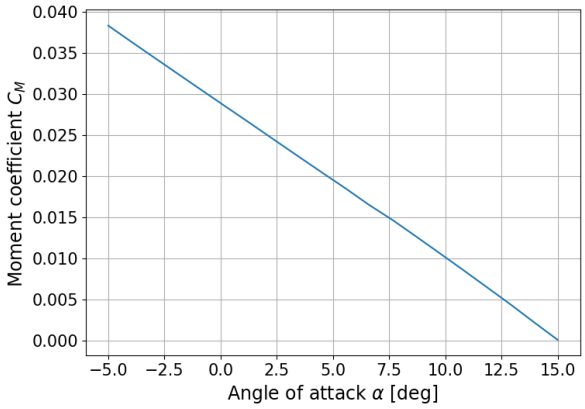

(c) *Moment curve.*

Figure 5.6: *Main aircraft aerodynamic load curves.*

Table 5.1: *VLM aircraft curve parameters.*

Variable	Value
Lift slope C_{L_α}	2.469 $[rad^{-1}]$
Zero-lift angle of attack $\alpha_{L=0}$	1.081 [°]
Moment slope C_{M_α}	-0.1091 $[rad^{-1}]$
Moment coefficient at zero angle of attack $C_{M_{\alpha=0}}$	0.0284
Zero-lfit drag coefficient $C_{D_{L=0}}$	0.00662
Parabolic drag factor k	0.172

Finally, the lift and moment distribution of the aircraft can be visualized in Figure 5.7a and Figure 5.7b, respectively. Overall, the lift distribution Figure 5.7a follows the expected shape of a swept and tapered wings, which

concentrate spanwise flow towards the tip [1]. Additionally, a similar effect is caused by delta wing planforms, which reach higher sectional lift coefficient values near the tips [58]. The abrupt change in the distributions is caused by the change in the airfoil geometry, and downwash from the high-performance E186 airfoil on the wings, which reduces the central sections' effective angle of attack. The moment distribution Figure 5.7b presents both positive and negative sections, the negative part is mostly found at the spanwise stations of the symmetric NACA0025 airfoils, which is expected since it is not reflexed. Most of the remaining sections present the expected and desired positive moment coefficient.

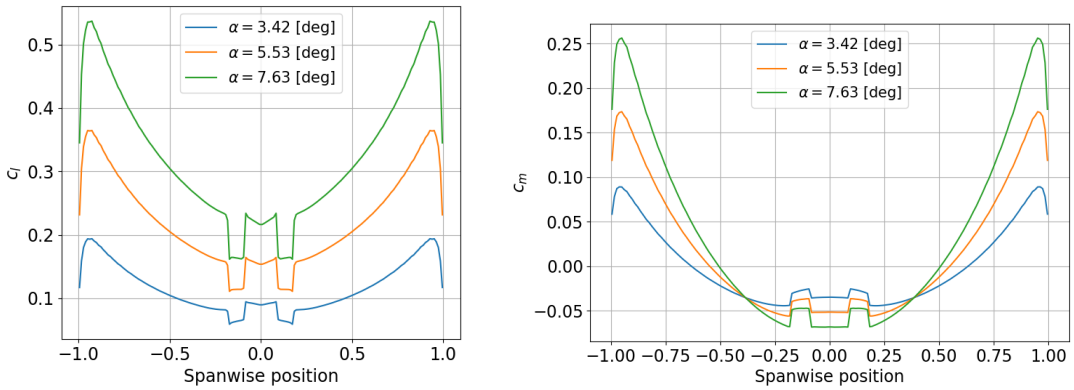

(a) *Lift distribution.* **(b)** *Moment distribution.*

Figure 5.7: *Aircraft spanwise aerodynamic loads at different angles of attack.*

5.4. Stall Estimation

As potential flow methods were considered during the aerodynamic analysis of the aircraft, the conditions near stall must be evaluated through another methodology. Empirical estimations from [54] which are based on experimental data are employed, allowing the calculations of the stall angle of attack α_{stall} and the wing's maximum lift coefficient $C_{L_{max}}$.

5.4.1. Maximum Lift Coefficient

The maximum lift coefficient of the wing can be estimated through the proposed methodology in [54]. The maximum lift coefficient is defined as the total wing lift coefficient at which the spanwise lift distribution of the wing reaches the sectional maximum lift coefficient at any spanwise location.

As seen from the lift distribution in Figure 5.7a, the point at which the sectional maximum lift coefficient will be reached is near the tip. Hence, the lift curve of the E186 airfoil was simulated at the cruise conditions of the aircraft in XFOIL. Resulting in Figure 5.8, with a maximum lift coefficient of 1.6228.

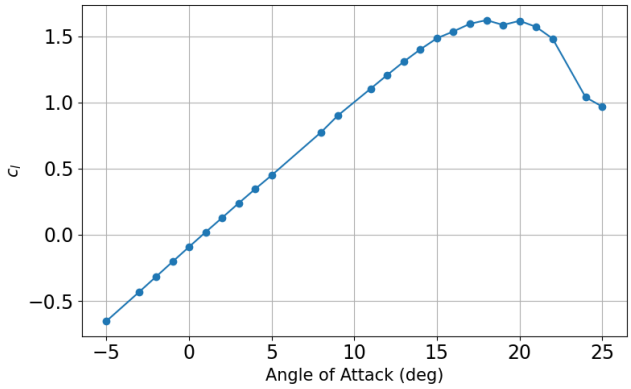

Figure 5.8: *Lift curve of the E186 airfoil simulated in XFOIL at the mean aerodynamic chord and cruise conditions.*

The aircraft was then simulated in OpenVSP at higher values of angle of attack, resulting in Figure 5.9. The first distribution that reaches the previously calculated maximum sectional lift coefficient corresponds to an overall

[1] https://eaglepubs.erau.edu/introductiontoaerospaceflightvehicles/chapter/maximum-lift-stalling-spinning/

maximum lift coefficient of $\mathbf{C_{L_{max}} = 0.7787}$. The spanwise position at which this is predicted to occur is plotted according to the relation $y/(b/2) = 1 - \lambda$ from [54], where λ is the taper ratio of the wing.

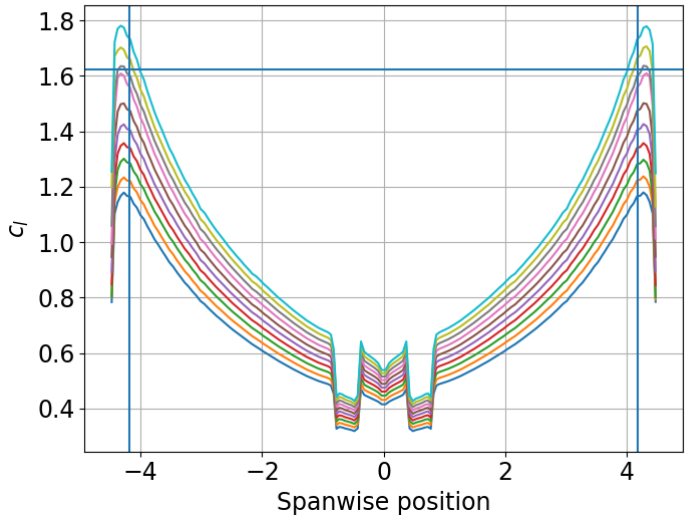

Figure 5.9: *Aircraft lift distribution at various angles of attack.*

5.4.2. Stall Angle of Attack

The stall angle of attack α_{stall} is estimated through the methodology presented in [54]. This method is based on the wing planform parameters, which are used as inputs for the given graphs. The first of these is seen in Figure 5.10a and Figure 5.10b, providing parameters for the next graphs shown in Figure 5.11a and Figure 5.11b. In these graphs, the estimated stall angle of attack values are shown for the final configuration. The final results are shown in Table 5.2, for Equation 5.1.

$$\alpha_{stall} = \alpha_{stall_{base}} + \Delta\alpha_{stall} \tag{5.1}$$

Table 5.2: *Stall angle of attack calculation results*

Variable	Value
α_{stall}	27 [°]
$\alpha_{stall_{base}}$	27 [°]
$\Delta\alpha_{stall}$	0 [°]

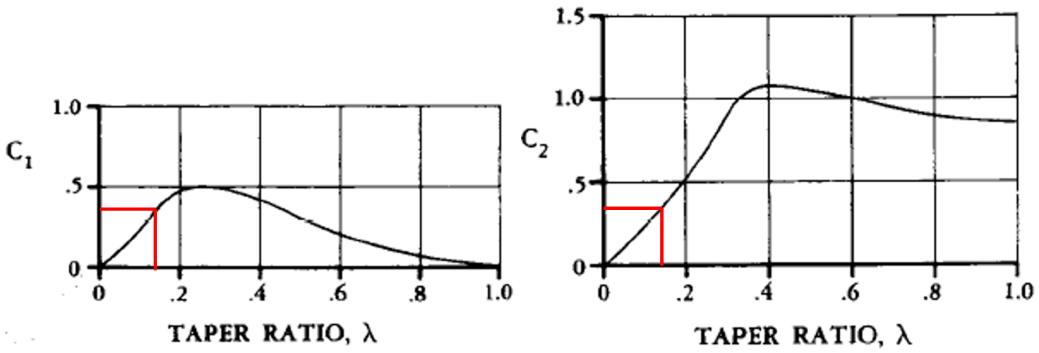

(a) *C1 parameter as a function of wing taper ratio.* **(b)** *C2 parameter as a function of wing taper ratio*

Figure 5.10: *C1 and C2 parameters used in the stall angle of attack estimation from [54].*

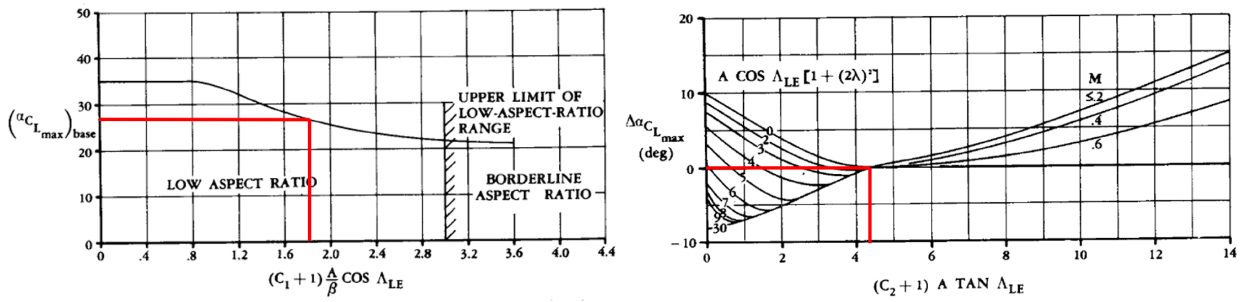

(a) *Base stall angle of attack as a function of wing planform parameters.*

(b) *Stall angle of attack correction factor as a function of wing planform parameters.*

Figure 5.11: *Stall angle of attack estimation graphs from [54].*

5.5. Verification and Validation

The aerodynamic analysis performed does not require a sensitivity analysis nor a formal verification as it makes use of the verified and validated OpenVSP [59] software from NASA. However, verification can be performed as a check for the unsteady effects of vortex lift that are prevalent for delta planforms. The effect of this flow phenomenon is to enhance lift generation at high angles of attack, hence increasing performance. To verify whether the computed lift curve Figure 5.5a should be modified, the methodology presented in [54] is followed to calculate the modified sections of the lift curve for delta wing planforms. This methodology is based on experimental data of delta wing planforms that encompass the planform of DoctAir, hence also serving as a sort of validation.

This method resulted in a linear lift curve graph, meaning that no substantial vortex lift enhancements are present with this planform. Hence, the calculated aerodynamic data can be considered sufficiently accurate and not altered by unsteady effects. Overall, the computed lift curve from [54] and that obtained by OpenVSP differ by 2.15%. The two lift curves can be seen in Figure 5.12, with the main difference being in the zero lift angle of attack. Nevertheless, the method from [54] to estimate this angle is not highly developed and considers it the same as the airfoil's zero lift angle of attack. Under this crude assumption, the obtained results can be considered verified, as the main differences would have been in the vortex lift affected regime instead of the former, but it was shown that their effect was negligible.

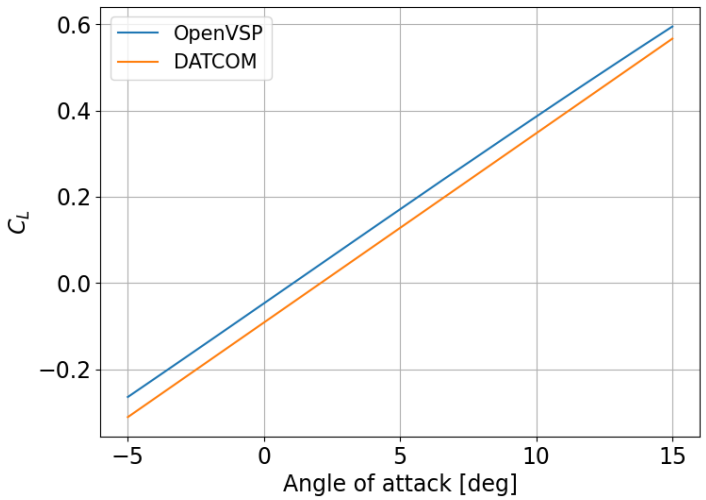

Figure 5.12: *Comparison of the aircraft lift curve obtained from OpenVSP and DATCOM [54].*

In terms of validation, due to the complex behavior of a delta wing platform, experimental validation in a wind tunnel is the most optimal option. The Open Jet Facility (OJF) or W-tunnel, both low-speed wind tunnels, at Delft University of Technology's Aerodynamic Laboratories can be used for this purpose. A force-balance experimental method should be employed to measure the aerodynamic coefficient curves, control, and stability derivatives in terms of angle of attack and sideslip.

6

Propulsion System

The propulsion system is a critical component of the vehicle architecture, particularly due to its influence on thrust generation, aerodynamic integration, and noise emissions. The design process for the propellers follows a semi-analytical method based on blade element and momentum theory, as described by Adkins and Liebeck (1994) [60]. The complete formulation and methodology are detailed in Appendix B. This approach allows for the derivation of optimal blade geometries by minimizing induced energy losses for a given thrust requirement.

The final propeller configuration was established through multiple iterations, considering integration constraints, performance efficiency, and structural feasibility. Once the optimal geometry was obtained, it was assessed under off-design conditions, such as climb, cruise, and descent, as well as during failure scenarios in accordance with the One Engine Inoperative (OEI) requirement. In addition, the acoustic characteristics of the final blade design were evaluated through harmonic SPL (Sound Pressure Level) analysis to assess noise impact in urban environments.

6.1. Assumptions

Before starting and explaining the design procedure, here is an overview of the assumptions made throughout the chapter.

- **AS-PROP-01:** The propulsion system employs six independent electric propellers to satisfy redundancy and the One Engine Inoperative (OEI) requirement.
- **AS-PROP-02:** All propellers have fixed-pitch blades.
- **AS-PROP-03:** Blade geometry (chord and pitch distributions) is optimized for hover thrust and then used without geometric modification in all off-design analyses (climb, cruise, descent, OEI).
- **AS-PROP-04:** Tip Mach number of 0.7 is used for the design RPM, and 0.8 represents the maximum allowable Mach limit for OEI maximum-thrust analysis. This is justified in Section 6.6 and Section 6.5.
- **AS-PROP-05:** A common hub radius of 0.075 [m] is assumed for all six propellers based on typical values of similar propellers [61].
- **AS-PROP-06:** Standard sea-level atmospheric properties ($\rho = 1.225\,\mathrm{kg/m^3}$, $\mu = 1.789 \times 10^{-5}\,\mathrm{kg/(m\,s)}$) are used for all flight phases up to 300 [m] altitude.
- **AS-PROP-07:** Hover and climb inflow velocities are modeled via momentum theory (axial induction, Prandtl tip loss) with induced velocity replacing freestream.
- **AS-PROP-08:** Propeller–wing, propeller–propeller, and fuselage aerodynamic interactions are neglected in the isolated-rotor analyses.
- **AS-PROP-09:** The blade element method uses airfoil data (Cl, Cd) interpolated solely as a function of angle of attack and Reynolds number.
- **AS-PROP-10:** Noise predictions use isolated-propeller harmonic SPL measurements; effects of multi-rotor acoustic interference, ground reflections, and atmospheric absorption are not included.
- **AS-PROP-11:** Only the rear two propellers operate in cruise to minimize power use and drag.
- **AS-PROP-12:** During OEI analysis, two operating propellers are set to maximum thrust to resolve the under determined thrust redistribution problem.

6.2. Propeller Blade Design

The aerodynamic design of the propeller blades in this work follows the optimal blade element momentum theory formulation developed by Adkins and Liebeck [60]. The complete formulation, derivation of key equations, and solution methodology are presented in detail in Appendix B. This section introduces the physical layout and inputs to the procedure, which form the basis for the performance analysis and subsequent design decisions.

The blade is defined as a rotating lifting surface with geometry varying along its span (see Figure 6.1b). The radial coordinate r extends from the hub radius R_{hub} to the tip radius R_{tip}, and the blade is discretized into radial stations of small thickness dr (see Figure 6.1b). At each station, the local chord length $c(r)$ defines the blade

planform, and the objective is to determine the optimal chord and pitch distribution that meets the required performance.

The local aerodynamic angles and velocities are illustrated in Figure 6.1a. At each blade section, the relative flow angle ϕ, angle of attack α, and blade pitch angle β define the orientation of the airfoil with respect to the incoming flow. The relative wind velocity W is composed of the axial component $V(1+a)$ and the tangential component $\Omega r(1-a')$, where a and a' are the axial and rotational interference factors, respectively.

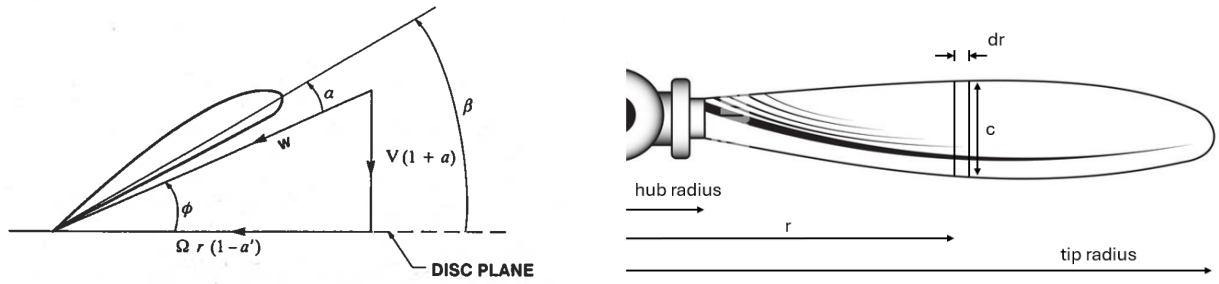

(a) *Blade geometry across the span showing local radius r, hub and tip radius, element thickness dr, and chord c.*

(b) *Cross-sectional view of a blade element showing angle of attack α, flow angle ϕ, pitch angle β, and velocity components [60].*

Figure 6.1: *Propeller blade span-wise and cross-sectional views.*

The required inputs to the design procedure are:

- Desired thrust (T) to be produced by the propeller,
- Freestream velocity (V),
- Rotational speed (Ω) or RPM,
- Number of blades (B),
- Blade span defined by R_{hub} and R_{tip}.

Using these inputs, an iterative optimization procedure determines the spanwise distribution of chord $c(r)$, blade pitch angle $\beta(r)$, power required P, and the efficiency. The resulting blade geometry is then evaluated for structural feasibility and noise compliance, and serves as the baseline for off-design performance assessments in the following sections.

6.3. Structural Considerations

To enable fast initial sizing of the propeller, simplified structural approximations were made for estimating blade stresses. These assumptions, while not capturing full 3D stress effects or manufacturing details, are considered acceptable at this stage for assessing the feasibility of blade geometry under maximum loading conditions.

The normal and shear stresses in the blades must remain below the ultimate tensile strength of carbon fiber composites, which was selected as the blade material due to its widespread use in high-performance propellers. The total normal stress in the blade, σ_{total}, is defined as the sum of the axial centrifugal stress, σ_{axial}, and the bending stress resulting from thrust loading,

$$\sigma_{\text{total}} = \sigma_{\text{axial}} + \sigma_{\text{bending}}.$$

The axial stress is computed by discretizing the blade into radial segments, estimating the mass of each segment based on local chord length and thickness, and summing the centrifugal force contributions. Assuming the total axial load is borne by the root cross-section, the axial stress is given by,

$$\sigma_{\text{axial}} = \frac{\sum_i m_i \omega^2 r_i}{A_{\text{root}}},$$

where ω is maximum angular velocity of the blade in [rads/s] during operation, m_i is the mass of segment i, and A_{root} is the cross-sectional area at the root, estimated as $c_{\text{root}}^2 \cdot (t/c)_{airfoil}$. Note that the $(t/c)_{airfoil}$ is the thickness to chord ratio of the chosen airfoil.

The bending stress is determined by modeling the aerodynamic thrust as a point load concentrated at 50% of the blade span, with the thrust per blade T_{blade} found by dividing total thrust per propeller by the number of blades. This simplification was made since it was deemed sufficiently accurate for a first-order estimation especially given

the time available. Modeling the thrust as acting at mid-span provides a reasonable approximation of the true bending moment without requiring detailed thrust distribution analysis. Following this approach results in a root bending moment of,

$$M_{\text{root}} = T_{blade} \cdot \frac{R_{\text{tip}} - R_{\text{hub}}}{2}.$$

Assuming a rectangular root section, the bending stress is computed using,

$$\sigma_{\text{bending}} = \frac{M_{\text{root}} \cdot y_{\text{max}}}{I},$$

where $y_{\text{max}} = \frac{t_{\text{root}}}{2}$ and the second moment of area is $I = \frac{c_{\text{root}} t_{\text{root}}^3}{12}$. The shear stress is evaluated at the root using a rectangular section approximation. The shear force is taken as the total thrust per blade, and the resulting shear stress is given by,

$$\tau = \frac{VQ}{It},$$

where $V = \frac{T}{N_{\text{blades}}}$, $Q = \frac{c_{\text{root}} t_{\text{root}}^2}{8}$, and t is the local thickness.

The computed values of σ_{total} and τ are multiplied by a 1.5 safety factor and compared to the allowable limits for carbon fiber composites, which are approximately 3 [GPa] in tension and 50 [MPa] in shear [62]. If either limit is exceeded, the blade geometry is rejected as structurally infeasible.

6.4. Design Process and Results

This section presents the results of the propeller design process, beginning with the input parameters used and integrated with key design decisions and constraints that guided the sizing procedure. This process not only aims to design the most efficient blade, but also takes noise and structural aspects into account through iterations. The final propeller geometry is then presented and will be evaluated in the context of performance and system-level requirements in later sections.

The initial design parameters were selected based on the configuration trade study outlined in Chapter 4. This preliminary trade-off analysis established base values for critical quantities such as the maximum take-off weight and propeller radius. Where applicable, these values were refined through iterative estimates and cross-checked against performance benchmarks and empirical references.

Initial Inputs

An important architectural assumption was the use of a **six-propeller configuration**, chosen primarily to meet the One Engine Inoperative (OEI) requirement (`REQ-REG-01-SYS-06`). In the event of a failure of any single propeller during critical flight phases such as hover or climb, the remaining five propellers must be capable of generating sufficient thrust to sustain controlled flight and ensure a safe landing. This configuration shall also enable flexible thrust balancing to maintain stability and avoid uncontrollable pitch or roll moments in the absence of effective aerodynamic control surfaces during low-speed flight. Fewer propellers would require each unit to operate closer to its performance limits, reducing overall robustness and potentially violating redundancy margins.

Additionally, in the initial layout, the front and mid propellers were intended to be embedded within the wing planform. However, due to space constraints and system integration challenges, this configuration was revised. All propellers were ultimately relocated outside the wing structure, preserving the internal wing volume for batteries and other critical subsystems such as wiring and cooling.

The final propeller designs are based on a maximum take-off weight of 1788 [kg]. A common hub radius of 0.075 [m] was assumed for all six propellers.

Thrust

The propeller sizing process is driven by a specified thrust requirement. The maximum thrust demand occurs during hover, where the aircraft must generate enough vertical force to counteract its weight. Accordingly, the propellers are primarily sized to meet this hover condition. On the other hand, thrust requirements during cruise are significantly lower, meaning propellers are sized mainly to overcome aerodynamic drag.

To improve efficiency and reduce energy usage during cruise, only two of the six propellers are active in forward flight. These are designed to be tiltable to allow alignment with the freestream during cruise. Selecting only two propellers for cruise not only minimizes power consumption but also reduces mechanical complexity and drag compared to operating all six throughout the mission.

The two cruise propellers are located at the rear of the aircraft. This placement was intentionally chosen for aerodynamic and stability reasons. Rear-mounted propellers produce less interference with the wing's flow and avoid disturbing the lift distribution during cruise [63].

The total design thrust is calculated using:

$$T_d = MTOW \cdot 1.5 \tag{6.1}$$

where $MTOW$ is the maximum take-off weight of the aircraft, and the factor of 1.5 serves as a design margin to ensure sufficient thrust for control authority, especially in ground effect or gusty conditions, and one engine failure. **The total final design thrust was 26310 [N]**.

To assign thrust targets to individual propellers, their positions relative to the aircraft's center of gravity (CG) must be considered. Preliminary layout studies indicated that the CG is biased toward the forward section of the aircraft. If equal thrust were generated by both the rear and front propellers, the longer moment arm of the aft units would induce a nose-down pitching moment, potentially destabilizing the aircraft, particularly during hover, when aerodynamic control surfaces are less effective due to the lack of freestream airflow.

To achieve moment equilibrium during vertical flight, an asymmetric thrust distribution was implemented. The forward and mid-mounted propellers, located closer to or ahead of the CG, were assigned a larger share of the thrust load. Ultimately, the configuration was tuned such that the front and mid propellers collectively provide 80% of the required hover thrust, while the rear pair accounts for the remaining 20%.

Atmospheric Conditions and Velocities

The propeller design is based on hover operations, which occur near the ground, and cruise at a maximum altitude of 300[m]. As the change in atmospheric conditions over this altitude is minimal, sea level properties are used throughout, with air density ρ and dynamic viscosity μ remaining constant at standard values.

During hover, the freestream velocity is effectively zero since the aircraft is not moving. Nevertheless, there is vertical flow through the propellers due to thrust generation. This induced flow velocity (so the velocity at which the airflow approaches the propeller) can be estimated using the relation [61]:

$$v_i = \sqrt{\frac{T_d}{2\rho\,\pi\,(R_{\text{tip}}^2 - R_{\text{hub}}^2)}} \tag{6.2}$$

where T_d is the design thrust per propeller, R_{tip} and R_{hub} are the tip and hub radii of the propeller.

The design rotational speed Ω was selected based on a target tip Mach number M_t, using the relation:

$$\Omega = \frac{aM_t}{R_{\text{tip}}} \tag{6.3}$$

where a is the speed of sound. **A design tip Mach number of 0.7** was chosen as the design limit, corresponding to hover conditions where a high thrust, and thus a high rotational speed, is required. This value includes a safety margin below the onset of transonic effects (typically around 0.8/0.85), beyond which noise levels rise sharply and efficiency drops due to shock wave formation. Further reducing the tip Mach below 0.7 yields smaller returns in noise reduction, as shown in a study by Neise and Michel [64]. This trend is reflected in the harmonic correction factor discussed in Section 6.6, where, at lower tip Mach numbers, the correction factor for higher harmonics does not change much, indicating that beyond a certain Mach number, further reductions have little effect on the noise of higher harmonics.

Final Propeller Design and Configuration

The front and mid-mounted propellers are designed to operate during the hover and climb phases. During a cruise, these propellers are shut down, which necessitates a mechanism to minimize aerodynamic drag when not in use. Two options were considered: either implementing a folding mechanism or ensuring alignment of the blades with the freestream.

These constraints influenced the selection of blade count. With two blades, the propeller can passively align with the flow axis when not spinning. A three-bladed design requires a folding mechanism, where two blades fold back and align with the third blade. A four-bladed setup would require a coaxial configuration, adding mass and mechanical complexity.

The four-blade coaxial option was discarded due to the added weight penalty from additional blades and supporting hardware, without a significant gain in propulsive efficiency. As shown in Figure 6.2a, the efficiency increase from a 3-blade to a 4-blade configuration was marginal, rising only from 54.2% to 55.0%. Additionally, the loading noise associated with coaxial rotors has been shown to exhibit significantly higher sound pressure levels, particularly in the high-frequency range [65]. In contrast, the two-blade configuration showed a lower efficiency of 52.5%, making it less favorable in terms of performance. Based on this evaluation, **the three-bladed configuration** was selected as the final design **for the front and mid propellers**, offering a strong balance between efficiency, mechanical feasibility, and drag reduction when stowed during cruise.

Additionally, since the number of blades is relatively low, an increase in propeller radius was necessary to avoid having too thick blades and an increase in noise. As a result, **the diameter for the front and mid-mounted propellers was set to 2 [m]**.

The rear-mounted propellers were subject to fewer constraints compared to the front and mid units. These propellers are active during cruise and were designed to provide only 20% of the total hover thrust, as their primary role is to sustain forward flight rather than vertical lift. As a result, smaller propellers could be used while still satisfying thrust requirements.

Unlike the front and mid propellers, the rear propellers did not require folding or alignment mechanisms, even though a tilting mechanism would be needed to switch from hover to cruise mode. This allowed greater flexibility in selecting the number of blades. **A four-blade configuration was chosen for the rear propellers**, offering an efficiency of 55.3%, while increasing to five blades resulted in only a marginal gain to 55.6% (see Figure 6.2). Additionally, **the tip diameter was set to 1.5 [m]** to reduce acoustic emissions and ensure adequate thrust during hover without excessive rotational speed.

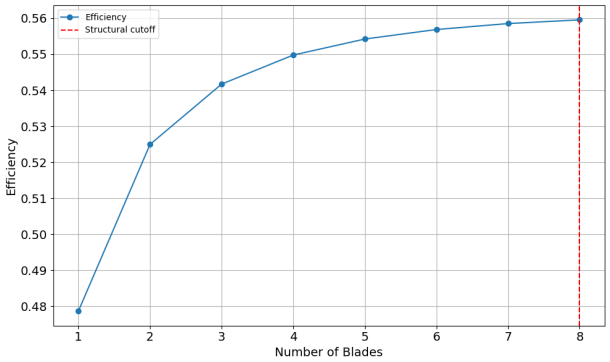

(a) *Efficiencies vs number of blades for front and mid-mounted propellers with a diameter of 2 [m].*

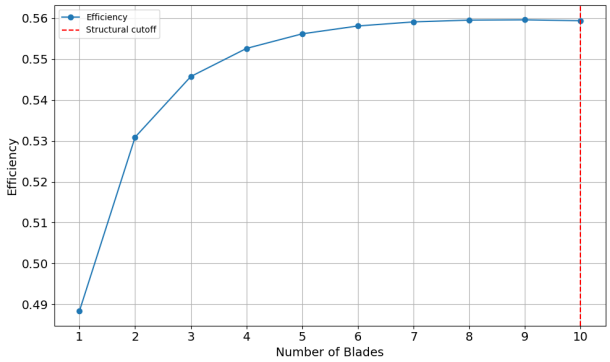

(b) *Efficiencies vs number of blades for rear-mounted propellers with a diameter of 1.5 [m].*

Figure 6.2: *Efficiencies with increasing number of blades. The red dotted line indicates the structural cutoff after which the blade fails.*

As discussed in Section 6.4, the longitudinal placement of the propellers was determined to ensure moment balance about the center of gravity (CG), particularly during hover when aerodynamic control surfaces are ineffective due to the lack of airflow. To achieve equilibrium, the net pitching moment produced by the propeller thrusts must be zero. This condition is expressed by the following moment balance equation:

$$T_{\text{front}} \cdot x_{\text{front}} + T_{\text{mid}} \cdot x_{\text{mid}} + T_{\text{back}} \cdot x_{\text{back}} = 0 \tag{6.4}$$

Here, T_i denotes the design thrust produced by each propeller group and x_i the longitudinal distance from the center of gravity.

The location of the rear propellers was fixed relative to the overall vehicle length, with the back propellers positioned just behind the wing, which measures 7.2 [m] from the nose. The positions of the front and mid propellers were determined through a combination of moment balance calculations and layout constraints. Several configurations were evaluated to ensure that neither propeller overlapped with the wing area, avoiding aerodynamic interference and preserving propeller performance.

The lateral positioning of the propellers was determined based on multiple clearance constraints. These included ensuring sufficient spacing between adjacent propellers to prevent aerodynamic interference, providing adequate clearance around the side-mounted cabin door for safe patient entry and exit, and avoiding overlap with the wing structure.

The performance parameters for all propellers are listed in Table 6.1, while the final propellers designs are illustrated in Figure 6.3.

Table 6.1: *Hover performance and geometric parameters of DoctAir propellers*

Propeller Group	Diameter [m]	No. of Blades	Max Chord [m]	Efficiency [%]	Design RPM	Design Thrust [N]
Front Propellers	2.0	3	0.289	54.2	2272	5262
Mid Propellers	2.0	3	0.289	54.2	2272	5262
Rear Propellers	1.5	4	0.137	55.3	3030	2631

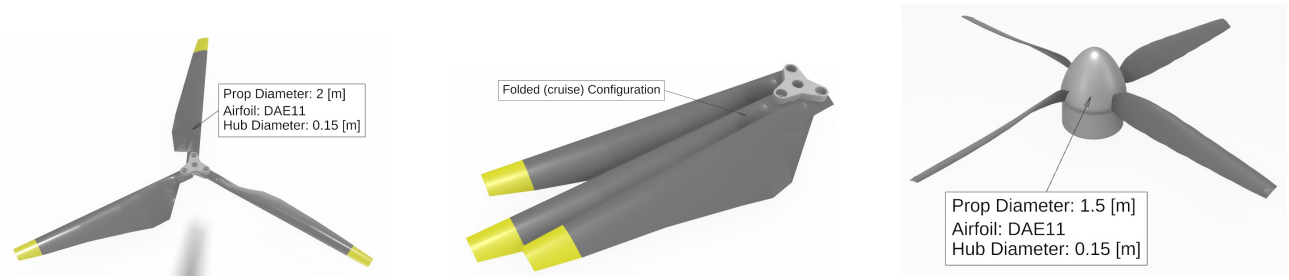

(a) *3-bladed front/mid propeller in deployed configuration.*

(b) *Front/mid propeller in folded (stowed) configuration.*

(c) *4-bladed rear propeller.*

Figure 6.3: *CAD representations of the final propeller configurations: (a) front/mid propeller deployed, (b) front/mid propeller folded for cruise, (c) rear propeller for cruise and hover.*

6.5. Performance Analysis

This section presents the performance evaluation of the designed propellers across various flight conditions, including cruise, climb, hover, descent, and maximum thrust scenarios. The primary objective is to determine the minimum power required to meet the thrust demand in each phase, using the fixed blade geometries obtained from the optimal design.

For cruise, climb, and hover, the method outlined in Section B.6 is used. In this approach, the blade geometry, freestream velocity, and required thrust are specified as inputs, and the procedures used to determine these inputs are discussed in the respective subsections. Many of the inputs are taken from the mission profile outlined in Section 2.3. The analysis iterates over a range of rotational speeds to determine the minimum value at which the generated thrust equals or exceeds the target. This ensures that the power required P, calculated from the torque output Q multiplied by the angular velocity Ω, is minimized.

While the freestream velocity directly represents the inflow condition during cruise, it does not accurately reflect the inflow in hover and climb. In these cases, the inflow velocity is replaced by an induced velocity, which more accurately represents the airspeed through the propeller disc in low-speed or vertical flight.

Descent performance is treated separately using an empirical correction model, as classical momentum theory is invalid in this regime due to the presence of turbulent wake structures and undefined slipstream behavior.

The same off-design analysis method is also used to estimate the maximum thrust capacity of each propeller, which supports the One Engine Inoperative (OEI) evaluation.

A summary of the thrust and power required in each flight condition is provided in Table 6.2, and is used in subsequent sizing of the power subsystem.

Table 6.2: *Propeller performance summary for different flight phases, showing required thrust and power*

Flight Phase	Propeller Group	Thrust [N]	Power [kW]
Cruise	Rear Propellers	2×278	2×43.0
Hover	Rear Propellers	2×1754	2×80.6
	Front/Mid Propellers	4×3508	4×167.4
Climb	Rear Propellers	2×1754	2×75.4
	Front/Mid Propellers	4×3508	4×164.1
Descent	Rear Propellers	–	2×69.1
	Front/Mid Propellers	–	4×156.0

Hover Performance

The hover condition is already central to the blade design procedure, as it represents the most demanding thrust requirement. However, for performance assessment, a key distinction is made: the thrust required in this phase is now computed using the actual Maximum Take-Off Weight (MTOW), without applying the 1.5 safety factor used during the sizing process. The induced velocity in hover is recalculated accordingly using Equation 6.2. This ensures that the correct power required is known, crucial for other subsystem designs.

Cruise Performance

During cruise, only the two rear propellers are active, as explained in Section 6.4. These propellers are responsible for generating the thrust required to overcome aerodynamic drag. The required thrust T_{cruise} is computed from the drag equation:

$$T_{\text{cruise}} = D = \frac{1}{2}\rho S_W C_{D,\text{cruise}} V^2 \tag{6.5}$$

where $S_W = 36.9$ [m^2] is the wing reference area, $C_{D,\text{cruise}}$ is the cruise drag coefficient (taken from aerodynamic analysis), $V = 61.11$ [m/s] is the cruise velocity.

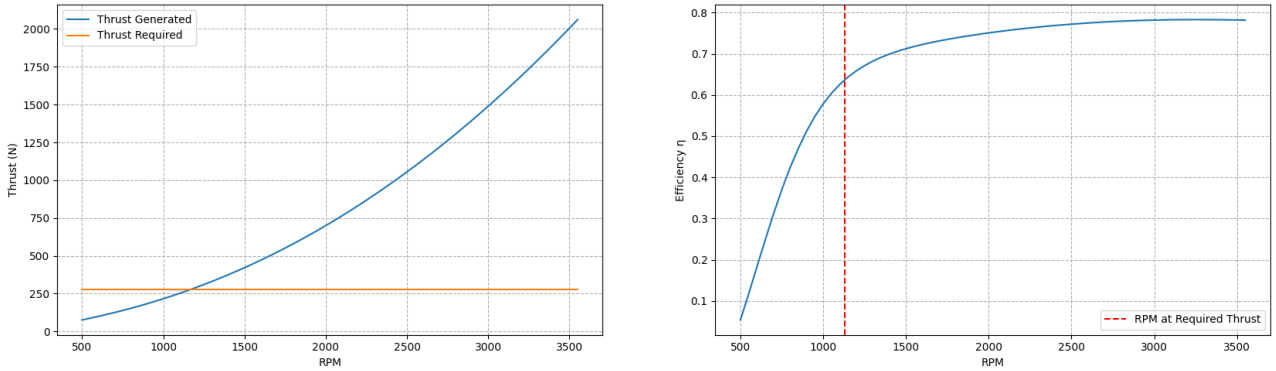

(a) *Thrust vs RPM.*

(b) *Efficiencies vs RPM with the red vertical line indicating the minimum RPM needed to satisfy the thrust requirement.*

Figure 6.4: *Cruise performance of rear-mounted propellers.*

Climb Performance

In the climb phase, all six propellers are active, and the thrust distribution remains consistent with that used during hover, 80% of the total thrust is produced by the front and mid propellers, and 20% by the rear propellers. The objective during climb is to overcome the aircraft's weight while maintaining a steady upward velocity, which implies that the total required thrust is approximately equal to the Maximum Take-Off Weight (MTOW) of the aircraft:

$$T_{climb} = MTOW \tag{6.6}$$

The induced velocity during climb is different from that in hover and is estimated using the following expression [61]:

$$v_i = -\frac{V_c}{2} + \sqrt{\left(\frac{V_c}{2}\right)^2 + v_h^2} \tag{6.7}$$

where V_c is the vertical climb speed (5 [m/s]) and v_h is the induced velocity in hover from Equation 6.2.

Descent Performance

Unlike hover, climb, and cruise, the descent phase presents conditions where classical momentum theory becomes invalid. Specifically, when the descent speed falls within the range $-2V_h < V < 0$, where V_h is the induced velocity in hover, no valid wake model exists [66]. In this so-called vortex ring state, the flow becomes highly unsteady and turbulent, with an upward motion through the rotor disc conflicting with a downward wake in the far field. As a result, no steady-state slipstream can be defined, and the traditional actuator disk assumptions break down.

In this analysis, the descent speed V_d is 5 [m/s], which places it within this invalid region. Therefore, the induced velocity cannot be computed using standard momentum theory. Instead, it is estimated using an empirical correction based on velocity curves derived from experimental data. The ratio between induced velocity during descent v_i and hover-induced velocity V_h is calculated using the polynomial expression:

$$\frac{v_i}{v_h} = k + k_1\mu + k_2\mu^2 + k_3\mu^3 + k_4\mu^4 \tag{6.8}$$

where $\mu = V_d/v_h$ is the ratio of descent velocity V_d to hover-induced velocity. The constants are set as: $k = 1$, $k_1 = -1.125$, $k_2 = -1.372$, $k_3 = -1.718$, and $k_4 = -0.655$.

Once the corrected induced velocity is known, the required power in descent is estimated using:

$$P_{\text{descent}} = P_{\text{hover}} \left(\frac{V_d}{v_h} + \frac{v_i}{v_h} \right) \tag{6.9}$$

Maximum Thrust and OEI Analysis

To evaluate the maximum thrust capability of the designed propellers in hover conditions, an off-design performance analysis is performed using the method described in Section B.6. The analysis is based on the maximum allowable tip Mach number, which is set to 0.8. This value represents the operational upper limit, beyond which transonic effects such as shock-induced drag and high-frequency noise become significant. Additionally, exceeding this limit can lead to complex unsteady phenomena, including flow separation and dynamic stall, which degrade thrust generation and can introduce structural and control instabilities.

The corresponding rotational speed is computed from the tip Mach number using the standard relation shown in Equation 6.3. The same induced velocity used during the design procedure (see Section 6.4) is applied here to remain consistent with the original design assumptions. The resulting maximum thrust values serve as an upper bound for the performance capability of each propeller during hover and are used to verify compliance with the One Engine Inoperative (OEI) requirement.

OEI Condition and Thrust Redistribution

The OEI condition mandates that the aircraft must remain controllable and capable of stable flight following the failure of one propulsion unit. In hover or low-speed regimes, this condition becomes particularly critical because aerodynamic control surfaces are ineffective due to the absence of freestream airflow. As such, the remaining five propellers must not only generate sufficient total thrust to support the aircraft's maximum take-off weight (MTOW), but must also do so without inducing uncontrolled pitching or rolling moments about the center of gravity (CG).

To ensure static equilibrium during OEI, the following three conditions must be satisfied:

$$\sum T_i = W \quad \text{(Force balance)} \tag{6.10}$$

$$\sum T_i \cdot x_i = 0 \quad \text{(Pitch moment balance)} \tag{6.11}$$

$$\sum T_i \cdot y_i = 0 \quad \text{(Roll moment balance)} \tag{6.12}$$

Here, T_i is the thrust of the i-th propeller, and x_i and y_i represent the longitudinal and lateral distances from the CG, respectively.

However, with five unknown thrusts and only three balance equations, the problem is underdetermined. To resolve this, the thrust of the two propellers is fixed at their maximum value based on the earlier analysis. By iterating through all combinations of two operating propellers at maximum capability, each pair is tested to see whether the remaining three thrusts can satisfy the equilibrium equations while remaining below their respective maximum thrust limits.

The results of this analysis are shown in Figure 6.5, which illustrates all the cases. Due to the symmetry of the vehicle configuration, only three cases are shown. All analyzed scenarios successfully satisfy the OEI condition, demonstrating that the current propeller configuration can maintain stability and lift even in the event of a single engine failure.

Although the feasibility is confirmed, further optimization is recommended to minimize the total power consumption in the OEI condition. This can be achieved by adjusting the thrust and rpm levels for the remaining working propellers.

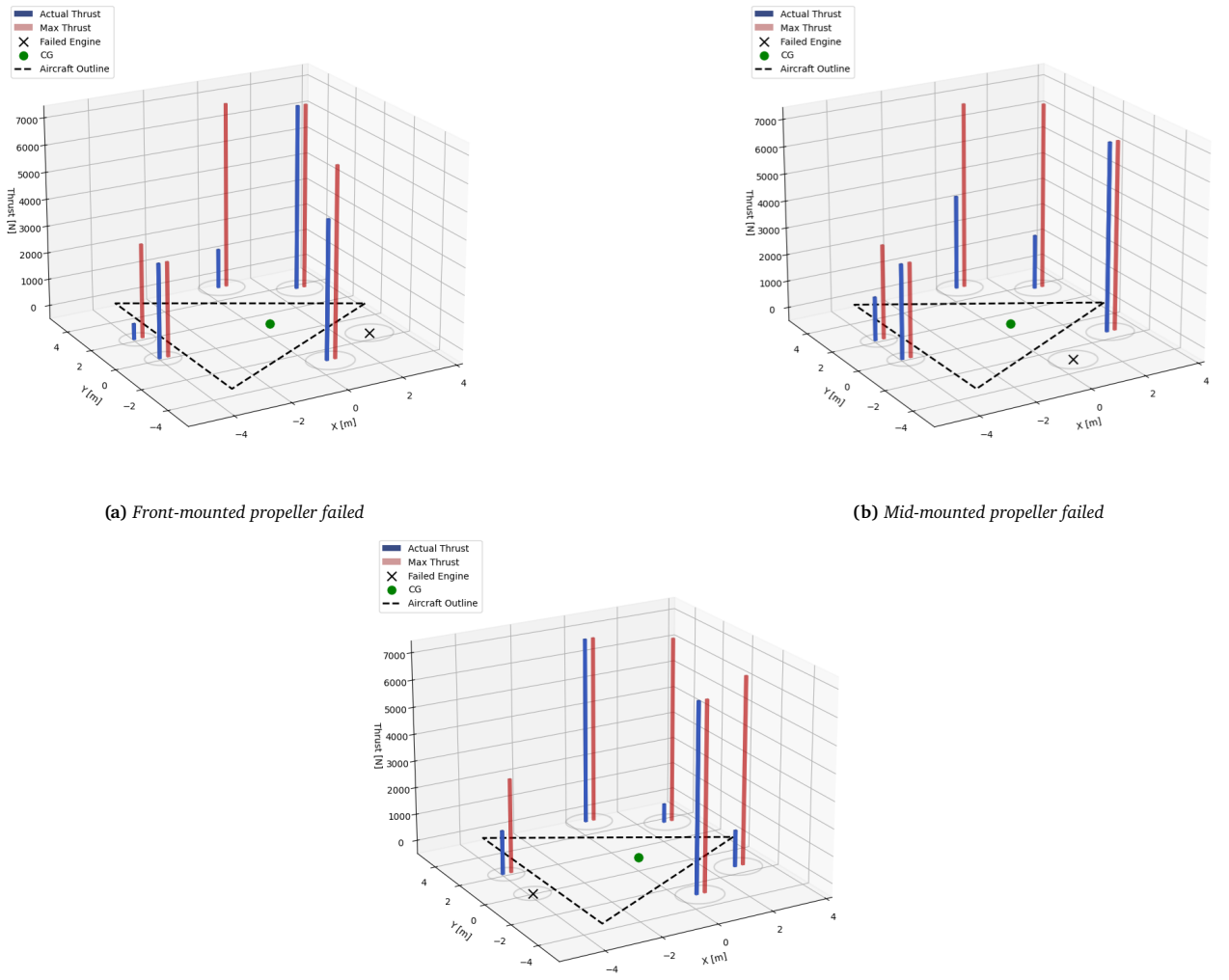

(a) *Front-mounted propeller failed*

(b) *Mid-mounted propeller failed*

(c) *Rear-mounted propeller failed*

Figure 6.5: *One engine inoperative performance for different cases. The blue line shows the actual propeller thrust to ensure a stable and flying vehicle. The red line indicates the maximum thrust that the propeller can generate.*

6.6. Noise Analysis

Acoustic performance is a critical design consideration for DoctAir, designed for medical transport, where operations will occur in populated areas. Among the primary contributors to overall noise are the propellers, especially during hover and low-speed flight phases.

A general framework for estimating the far-field noise produced by isolated propellers is provided in a NASA study by Marte and Kurtz [67]. Although this model applies to isolated rotors and does not account for complex interactions in multi-rotor configurations, it serves as a valuable first-order approximation. The formulation is empirical and based on a reference noise level modified by a series of correction factors that account for key geometric and operational parameters.

The far-field sound pressure level (SPL), measured in decibels [dB] at a distance greater than one propeller diameter, is estimated using the following expression:

$$SPL = L_1 + 20\log_{10}\left(\frac{4}{B}\right) + 40\log_{10}\left(\frac{15.5}{D}\right) + C_{mach} + C_\theta - 20\log_{10}(r-1) \tag{6.13}$$

In this equation, L_1 represents the reference noise level, obtained from Figure B.2 in [67]. This value depends on the power delivered to the propeller, which is available from the propeller design procedure. The next two terms apply correction factors based on the number of blades B and the propeller diameter D. As the equation suggests, increasing the number of blades or using a larger diameter tends to reduce noise emissions.

The term C_{mach} corrects for the rotational speed of the propeller and depends on the tip Mach number M_t and the radial distance from a standard reference point to the propeller disc, typically taken as 1 ft according to Marte and Kurtz. The value of C_{mach} is obtained from Figure B.3 in [67].

The factor C_θ accounts for the observer angle relative to the propeller plane. It is angle dependent and obtained from Figure B.8 in [67]. In this analysis, the worst-case correction of $+4$ [dB], which indicates the maximum values in the graph, is used to provide a conservative estimate. The final term in the equation accounts for spherical spreading of the acoustic wave with distance, where r is the distance from the center of the propeller to the observation point.

Summing all contributions yields the overall sound pressure level in [dB]. However, SPL alone does not fully characterize perceived noise. Human perception is more sensitive to tonal content and frequency distribution, with high-frequency tones often perceived as more annoying even at lower intensity. To address this, the harmonic distribution of the total SPL is considered.

This distribution is derived from empirical relations shown in Figure B.6 of [67], which provides correction factors for each harmonic based on the tip Mach number. By applying these corrections, the contribution of each harmonic to the overall SPL can be determined, offering a more perceptually relevant assessment of noise.

Once the noise characteristics at various frequencies are known for a given propeller design, the results can be evaluated against regulatory or mission-specific acoustic requirements. If the noise levels exceed acceptable limits, design modifications can be introduced. Potential adjustments include altering the number of blades, increasing propeller diameter, or reducing tip speed to lower the tip Mach number.

Noise Results

Figure 6.6 shows the harmonic sound pressure level (SPL) distribution for both front and rear propellers. The front propellers exhibit higher SPL values, particularly in the lower-frequency range. This is attributed to their lower blade-passage frequency, which is defined as:

$$f_{\text{BPF}} = B \cdot n$$

where B is the number of blades and n is the rotational speed in revolutions per second. In contrast, the rear propellers operate at higher rotational speeds and smaller diameters, which shifts their noise signature toward higher frequencies with slightly lower overall SPL levels.

Although the data are presented as harmonic SPL values in decibels (dB), a more accurate representation of perceived loudness would require conversion to Effective Perceived Noise Level (EPNL dB). This process involves frequency weighting, tonal corrections, and duration adjustments.

Nevertheless, these SPL distributions are useful for assessing potential human exposure. Studies suggest that prolonged exposure, such as 8 hours per day, to SPL levels above the range 80–100 [dB] [1] (depending on frequency) may cause discomfort and adverse health effects. These results helped in determining an **upper limit for the noise levels, which was set to 80[dB]**.

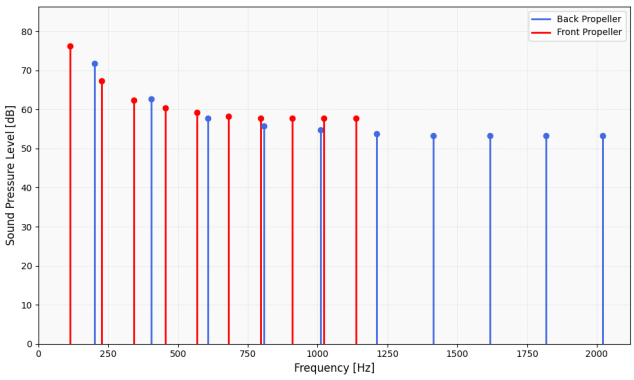

Figure 6.6: *Harmonic sound pressure level distribution of front (red) and rear (blue) propellers.*

6.7. Verification and Validation

To ensure the reliability of the propulsion analysis, both verification and validation efforts were carried out at multiple levels of the development process.

[1] Table VI-1 in https://pmc.ncbi.nlm.nih.gov/articles/PMC11841800/

Code Verification Throughout the codebase, small unit tests were implemented to confirm that individual functions performed as expected. Each function was manually reviewed and checked to ensure it returned physically consistent values. During the blade design process, outputs were regularly cross-checked against values from literature to identify unphysical results, such as efficiencies exceeding 100% or unrealistic thrust levels.

Additionally, diagnostic plots were generated to visualize the blade geometry. These included three-dimensional reconstructions of the blade along with spanwise plots of chord and pitch angle distributions. Such visual checks helped identify irregularities such as discontinuities, unexpected peaks, or non-smooth transitions in blade geometry that would indicate numerical issues.

Calculation Verification To verify the correctness of the blade performance analysis, a critical test was conducted by re-inserting the exact design conditions (thrust, freestream velocity, rotational speed) into the off-design performance model. The expectation was that the analysis would reproduce the original thrust, power, and efficiency values obtained during the optimal design phase. Successful recovery of these design outputs provided strong evidence of internal model consistency.

Furthermore, the power estimates obtained during off-design performance analysis (e.g., in cruise and climb) were cross-validated against results from a higher-level mission simulation performed using the SUAVE framework, which is discussed in Chapter 11. This system-level comparison served as an additional verification of both the physics and energy requirements derived from the propeller models.

Model Validation Although experimental validation is beyond the scope of this study, the adopted design methodology, based on Blade Element Momentum Theory (BEMT), has been widely validated in literature and is considered reliable for preliminary design. For future work, the results obtained here could be further validated through higher-fidelity simulations such as Computational Fluid Dynamics (CFD) blade analysis, which would provide detailed flow predictions and capture three-dimensional effects such as tip vortices, unsteady loads, and interaction with the fuselage or wing, thereby offering more accurate thrust and noise predictions.

6.8. Sensitivity Analysis

To evaluate the robustness of the blade design and assess how efficiency is influenced by varying input parameters, a sensitivity analysis was conducted. Among all design inputs, only two were identified as free variables with significant impact on performance: the propeller tip radius and the rotational speed, the latter expressed through the nondimensional tip Mach number M_{tip}. Other design inputs, such as required thrust and freestream velocity, are constrained by mission performance requirements. On the other hand, the number of blades was the variable that the propeller is optimized for to achieve the best efficiency.

The sensitivity analysis was carried out for both front and rear propellers (see Figure 6.7). Results show that increasing the propeller radius or reducing the tip Mach number generally leads to improved aerodynamic efficiency across both configurations. However, the practical benefits of these variations are limited by integration constraints: in particular, the aircraft's maximum projected footprint was restricted to a $10\,[\text{m}] \times 10\,[\text{m}]$ space, which placed an upper bound on allowable propeller diameter.

Furthermore, the observed gains in efficiency with increasing radius or decreasing tip speed were modest, typically less than 5%, and had to be weighed against added mass. As such, the final values for tip radius and Mach number represent a balanced choice between performance, structural feasibility, and dimensional constraints.

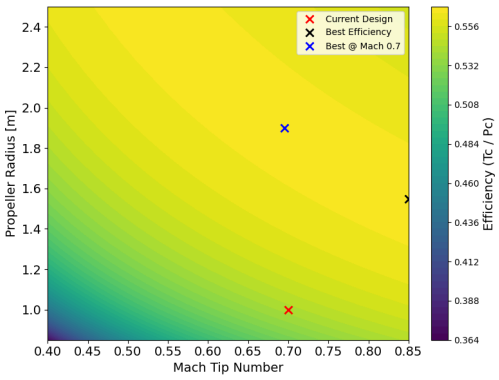

(a) *Variation of propulsive efficiency for front propellers as a function of tip radius and tip Mach number.*

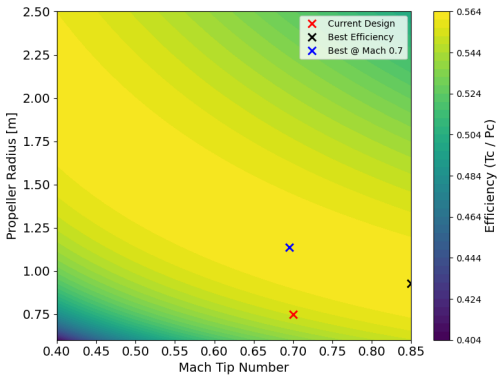

(b) *Variation of propulsive efficiency for rear propellers as a function of tip radius and tip Mach number.*

Figure 6.7: *Sensitivity of propulsive efficiency to tip radius and tip Mach number for front/mid and rear propellers.*

7

Power

In order to determine key battery parameters such as mass, dimensions, and charging time, the power consumed by the vehicle during each mission phase must be integrated over time to calculate the total energy requirement. Using both the total energy requirement and the peak power demand, the battery system can be sized appropriately. This chapter begins by examining the power consumption during each mission phase, followed by battery sizing, and concludes with the electric block diagram of the vehicle. Finally, the sensors used for semi-autonomous operations are discussed and distributed around the aircraft.

7.1. Assumptions

A list of assumptions made in the power and energy estimation, battery design and thermal management and the electric systems on board is presented below,

- **AS-ELEC-1:** The block diagram in Figure 7.6 represents a simplified version of the system, omitting detailed circuit-level elements and signal paths.
- **AS-ELEC-2:** It is assumed that the flight computers have sufficient computational capacity and interface compatibility to handle all signal processing and control routing.
- **AS-ELEC-3:** Battery output voltage is assumed to be consistently 400 [V], with minimal variation under load or during discharge.
- **AS-ELEC-4:** The power draw of all auxiliary systems is assumed to negligible compared to the propulsion system. This assumption is justified since the power draw of typical ambulance auxiliary systems is around 1.5 [kW][1] which is around 1% of the propulsion systems hover power meaning it can be safely neglected.
- **AS-ELEC-5:** The PDU is assumed to respond instantly to Battery Management System (BMS) signals and can safely relay power to all downstream components without delay or interference.
- **AS-ELEC-6:** The power inversion process from DC to 400 [V] RMS AC is assumed to be lossless and stable.
- **AS-ELEC-7:** ESCs are assumed to perform accurate and instantaneous motor control in response to flight computer commands.
- **AS-ELEC-8:** All four batteries are assumed to be symmetrically integrated and share load evenly under nominal conditions.
- **AS-ELEC-9:** Power losses due to resistance in cables or connectors are neglected in the system diagram.
- **AS-ELEC-10:** The 24 [V] DC supply for low-power systems is assumed to be regulated and isolated from the high-voltage system without failure.
- **AS-SENS-1:** Sensor fusion algorithms (EKF/UKF) are assumed to provide accurate estimates of the aircraft's state and surroundings under nominal noise and drift conditions.
- **AS-SENS-2:** All sensors are assumed to be properly calibrated and synchronized in time to allow effective data fusion.
- **AS-SENS-3:** Redundant sensors (e.g., dual GPS, IMUs) are assumed to function independently without interference and to take over seamlessly in case of primary sensor failure.
- **AS-SENS-4:** The obstacle avoidance system is assumed to detect and process static and dynamic hazards in real-time without latency.
- **AS-SENS-5:** LiDAR sensors are assumed to maintain full 360° coverage as shown in Figure 7.8, with negligible obstruction.
- **AS-SENS-6:** Sensor performance in adverse conditions (rain, fog, dust) is assumed to remain within operational limits, especially for RADAR.
- **AS-SENS-7:** SLAM-based localization is assumed to be applicable only in GPS-degraded environments and not as the primary navigation method.

[1] https://www.victronenergy.com/markets/professional-vehicles/ambulance

- **AS-SENS-8:** LiDAR range limits (70–100 m) are assumed to be sufficient for timely obstacle detection during low-speed hover or lower-altitude hover operations.
- **AS-SENS-9:** Sensor data is assumed to be free from systemic biases caused by structural vibrations or thermal drift due to isolation measures.
- **AS-SENS-10:** All sensor fields of view are assumed to be free from physical obstructions caused by the airframe or rotating components.

7.2. Total Energy Required

The maximum total energy required during the mission, E_{total}, can be found by multiplying the power required, P_i, during the i^{th} mission phase by the duration, t_i, of that phase, and summing the results. Some efficiency factors are also taken into account; the expression for total energy in Watt-hours is therefore,

$$E_{total,Wh} = \frac{P_{hover} \cdot t_{hover} + P_{climb} \cdot t_{climb} + P_{cruise} \cdot t_{cruise} + P_{descend} \cdot t_{descend}}{3600 \cdot DoD \cdot e_{battery} \cdot e_{motor}}, \tag{7.1}$$

where $e_{battery}$ is the battery discharge efficiency given by the manufacturer typically 0.9 for lithium-ion, e_{motor} is the motor's mechanical efficiency given by the manufacturer typically 0.9 and DoD is the depth of discharge of the battery set to 85% in order to preserve battery health. Power for hover, cruise, climb, and descent was determined in Section 6.5 and has been restated below for the reader's convenience,

Table 7.1: *Mission Power Required Summary*

Mission phase	$P_{required}$ front four [kW]	$P_{required}$ back two [kW]	Total power [kW]	Time [min]
Hover	4×167.4	2×80.6	830.8	4×0.5
Cruise	-	2×43.0	86.0	2×30
Climb	4×164.1	2×75.4	807.4	2×1
Descent	4×156.0	2×69.1	722.1	2×1

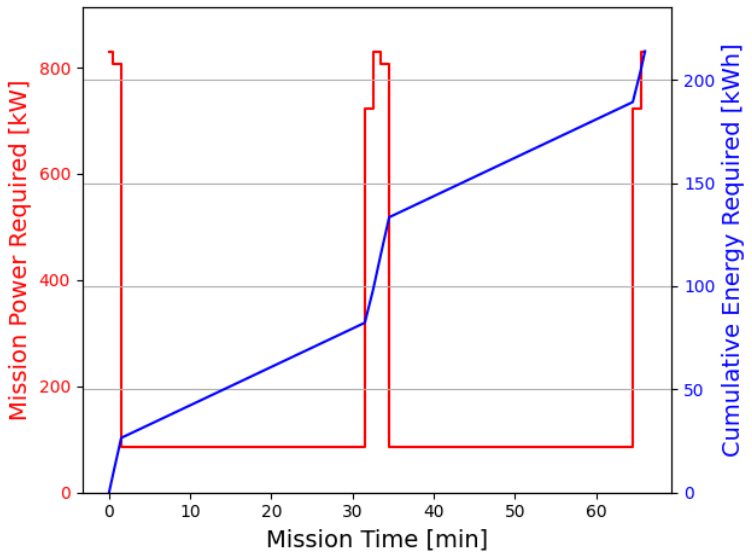

Figure 7.1: *Power Required [kW] and Energy Consumed [kWh] during Patient Rescue Mission*

Based on Table 7.1, Figure 7.1 above shows variation of power required and energy consumed throughout the patient rescue mission can be made. The peak in power in the middle of the mission is during the patient rescue part since the vehicle has to do vertical descend, hover and take-off from the patient recovery site. Evidently, the **peak power required is 830.8 [kW]** and the **total energy required is 212 [kWh]**

7.3. Battery Design

In the preliminary design phase, a simple estimate of battery mass was obtained by dividing the total energy required for the mission by 220 [Wh/kg], which is the typical energy density of lithium-ion batteries. If this method is used, based on the total energy required of 212 [kWh] from the previous section, the battery mass

needed becomes 909 [kg]. This, however, is not enough detail since the sizing is purely based on energy density neglects the battery power and voltage requirements. Therefore, in this section, the exact number of cells in series, parallel, and the type and make of the cells shall be found.

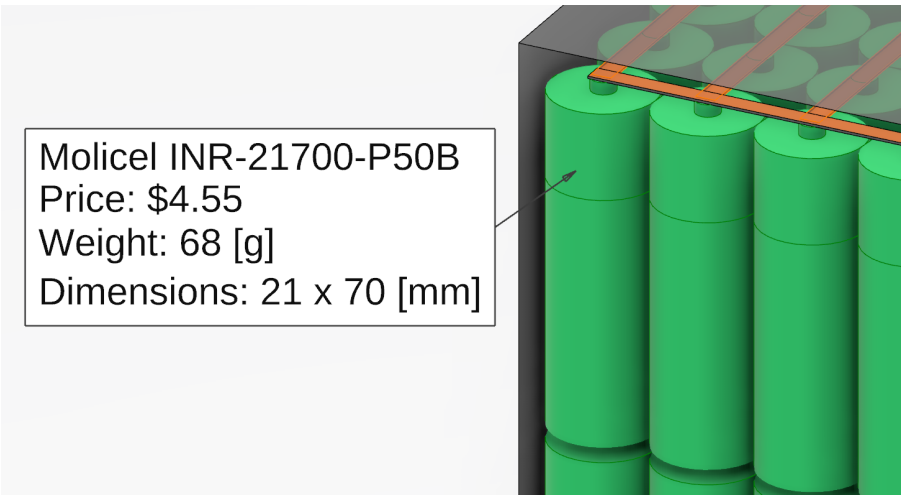

Figure 7.2: *Battery Internal Cells*

Lithium-ion chemistry was chosen based on a trade-off study conducted in the midterm report. Several commercially available lithium-ion cells used in eVTOL applications were evaluated by applying the sizing method described below to each candidate to minimize the total battery mass. The best-performing cell was the *Molicel™ INR-21700-P50B*, a lithium-ion NMC cell priced at approximately $4.55 per cell (estimated $4 in bulk). Each cell has a nominal voltage of 4 [V], a capacity of 5 [Ah], a maximum discharge current of 60 [A], an operating temperature limit of 80 [°C], and a mass of 68 [g][2].

The number of cells in series, N_s, is determined based on the aircraft's maximum voltage requirement. Since electric motors are typically the highest-voltage components in eVTOL systems, the required maximum battery voltage, V_{max}, is set equal to the motor's operating voltage. Based on typical motors used for large eVTOL applications, such as the *FreeRCHobby™ 240150*, a maximum operating voltage of 400 [V] is deemed sufficient. With each cell having a nominal voltage of 4 [V], the required number of series cells is:

$$N_s = \frac{400}{4} = \textbf{100 cells in series}.$$

The number of cells in parallel has to be determined by considering two key battery requirements: the total energy needed to be stored, and the maximum power that must be delivered. To meet peak power requirements the number of cells in parallel is given by,

$$N_p = \left\lceil \frac{P_{required,max}}{V_{max} \cdot I_{max,cell}} \right\rceil = \left\lceil \frac{830800}{400 \cdot 60} \right\rceil = 35, \tag{7.2}$$

whilst the number of parallel cells needed to store enough energy on board is given by,

$$N_p = \left\lceil \frac{E_{total,Wh}}{V_{max} \cdot C_{nominal,cell}} \right\rceil = \left\lceil \frac{212000}{400 \cdot 5} \right\rceil = 107. \tag{7.3}$$

Since the energy storage requirement leads to a higher parallel count, it is the most limiting constraint. Therefore, the final configuration requires **107 cells in parallel**. Consequently, the total number of cells needed in the battery pack is 100 × 107 = 10,700 cells, which combined gives,

$$m_{battery} = N_s \cdot N_p \cdot m_{cell} = \textbf{727.6 [kg] of battery mass.}$$

Since the dimensions of such a battery pack would be too large to fit all in one place, the battery **pack is split into 4 smaller, equal-sized *battery modules*** wired in parallel, where each module has 100 × 27 = 2700 cells. The overall dimensions of one of the four modules can be seen in the figure below,

[2] https://www.nkon.nl/novat/amfile/file/download/file/232/product/5518/

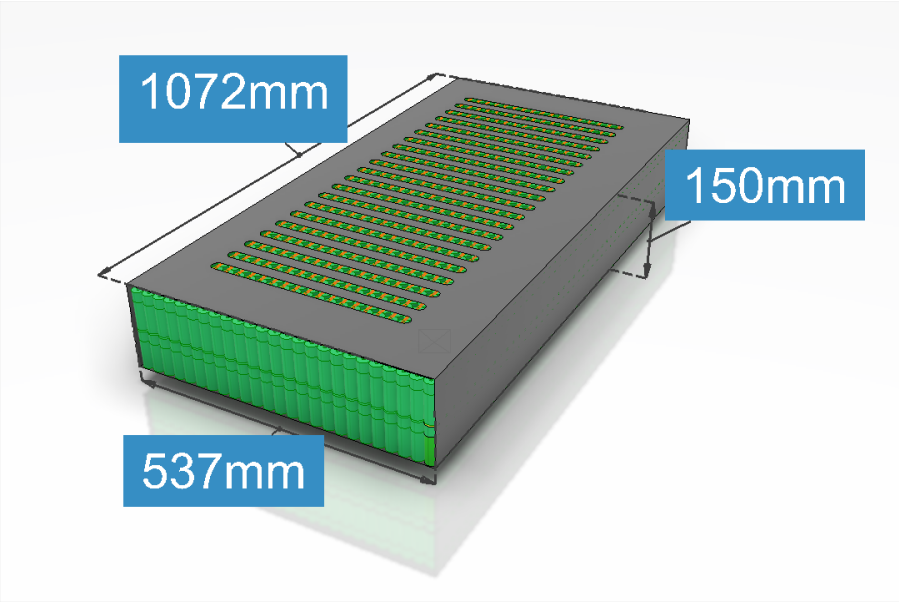

Figure 7.3: *Battery Module Dimensions*

To evaluate the charging time of the battery pack, two common high-power electric vehicle (EV) chargers available on the market were considered:

- **Tesla™ V4 Supercharger** [3]: Delivers up to 325 [kW] at 1000 [V] DC and 325 [A].
- **BYD™ Super e-Platform Charger** [4]: Supports up to 1000 [V] DC and 1000 [A].

The charge time is found via the following equation,

$$t_{charge} = \frac{C_{cell} \cdot N_{p,module}}{I_{charger}}, \tag{7.4}$$

where $C_{cell} \cdot N_{p,module}$ is the total capacity of the battery module in [Ah] and $I_{charger}$ is the current outputted by the charger in [A] and $t_{charger}$ is the time in [hours] to charge the battery module. It is important to ensure, however, that during charge that the current flowing in each cell does not exceed the cell's max rated charging current of 25 [A]. The current in each cell during charge $I_{cell,charging}$ is simply the charger's voltage divided by the number of cells in parallel in the module $I_{charger}/N_{p,module}$. Note that to achieve the charge times written summarized in Table 7.2 below, each battery *module* is assumed to be connected to a super charger, i.e, there are four super chargers connected to the vehicle.

Table 7.2: *Charging time estimates for different charger configurations.*

Charger Configuration	Current (A)	Charge Time	Notes
Tesla™ V4 (325 kW @ 1000 V)	325	24.7 min	Within cell current limit
BYD™ Charger (@ 500 A)	500	16.0 min	Within cell current limit
BYD™ Charger (@ 1000 A)	1000	(n.a.)	**Not allowed** - exceeds 25 A/cell limit
Tesla™ V4 (1C current, 133.75 A)	133.75	1 hr	For optimal battery health

7.4. Battery Thermal Management

The maximum allowable charging and discharging temperatures for the cells chosen in Section 7.3 are 70 [°C] and 80 [°C], respectively. Exceeding these temperatures negatively affects battery performance and significantly reduces its life cycle and hence must be avoided. This section evaluates whether active cooling is necessary for the battery pack and sizes the cooling system if required.

[3] https://www.tesla.com/support/charging/supercharger
[4] https://www.byd.com/mea/news-list/byd-unveils-super-e-platform-with-megawatt-flash-charging

Charging

The heat generated per cell during charging, due to the internal resistance R_{cell} of 8 $[m\Omega]$[5], is given by:

$$P_{lost,heat} = I^2_{cell,charging} \cdot R_{cell}. \tag{7.5}$$

Since each battery module is charged with its own charger, the cell current during charging is the charger current divided by the number of cells in parallel per module $N_{p,module}$. Then the heat loss per cell can be rewritten as:

$$P_{lost,heat} = \left(\frac{I_{charger}}{N_{p,module}} \right)^2 \cdot R_{cell}.$$

Assuming a typical lithium-ion NMC cell specific heat capacity $c_{p,battery} = 1040$ [J/kg/K] [68] and using the battery mass $m_{battery}$ from Section 7.3, the temperature increase of the battery pack during charging over a time period t_{charge} is calculated by:

$$\Delta T = \frac{P_{lost,heat} \cdot N_s \cdot N_p \cdot t_{charge}}{m_{battery} \cdot c_{p,battery}}, \tag{7.6}$$

The temperature rise during charging under the various charging schemes shown in Table 7.2 is depicted in Figure 7.4 below.

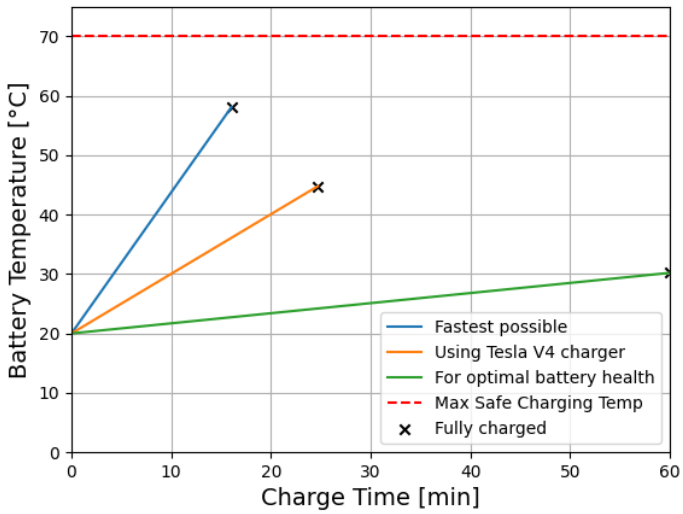

Figure 7.4: *Battery Temperature during Charging*

It is evident that charging with either the Tesla™ V4 Supercharger at 325 [A] or the BYD™ Super e-platform charger at 500 [A] does *not* cause the battery temperature to exceed safe limits.

Discharging

The temperature rise during battery discharge is estimated using a similar approach. However, instead of using charger current $I_{charger}$, the cell current I_{cell} is derived from the power demand P_i in the i^{th} mission phase, as shown in Figure 7.1, using the relation,

$$I_{cell_i} = \frac{P_i}{N_p}.$$

Figure 7.5 shows the battery temperature throughout the mission profile. The temperature remains more than 40 [°C] below the maximum safe discharge temperature.

[5] https://www.nkon.nl/novat/amfile/file/download/file/232/product/5518/

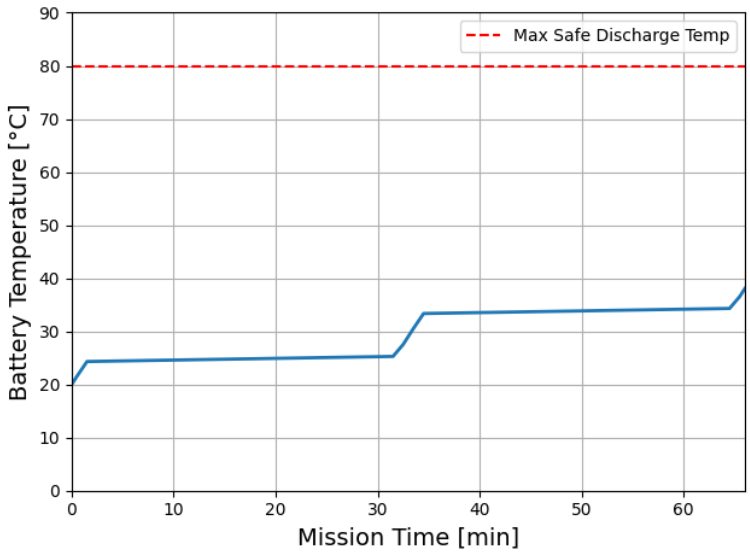

Figure 7.5: *Battery Temperature during Mission Discharge*

Based on these analyses, the **battery pack does not require an active cooling system** while charging or while discharging during the mission.

7.5. Electrical Architecture

The electrical architecture can be described using block diagrams. The flow is indicated by the arrows' directions, where each arrow represents a flow of signals or power. In Figure 7.6, the flight computer takes data from sensors, the pilot inputs, battery charge levels, as well as power distribution to optimize the performance and energy efficiency of the aircraft.

Now, when it comes to the battery, initially, the flight computer relays signals to the battery management system (BMS), which will, in turn, regulate the battery levels to ensure safe and efficient operation. If the BMS approves the request from the flight controller, then the power distribution unit (PDU) will relay electrical power at the output voltage of the battery, 400 [V], to the inverters and transformers. It is important to note that there are four batteries, which will be fitted inside the wing. Nevertheless, the power will be transferred to the inverters, where the electricity is inverted to a three-phase alternating current (AC), in the form of 400 [V] RMS current. The electronic speed controllers (ESCs) then regulate the speed of the motors by changing the power. The power is then fed to the electric motors, where the power is turned into mechanical power. The lower power systems, like the hydraulic pumps, sensors, cabin, and auxiliary systems, are operated at lower voltage, specifically 24 [V] direct current. This is viable, as in the real electrical architecture, there will be circuits parallel to ensure that the required capacity is reached.

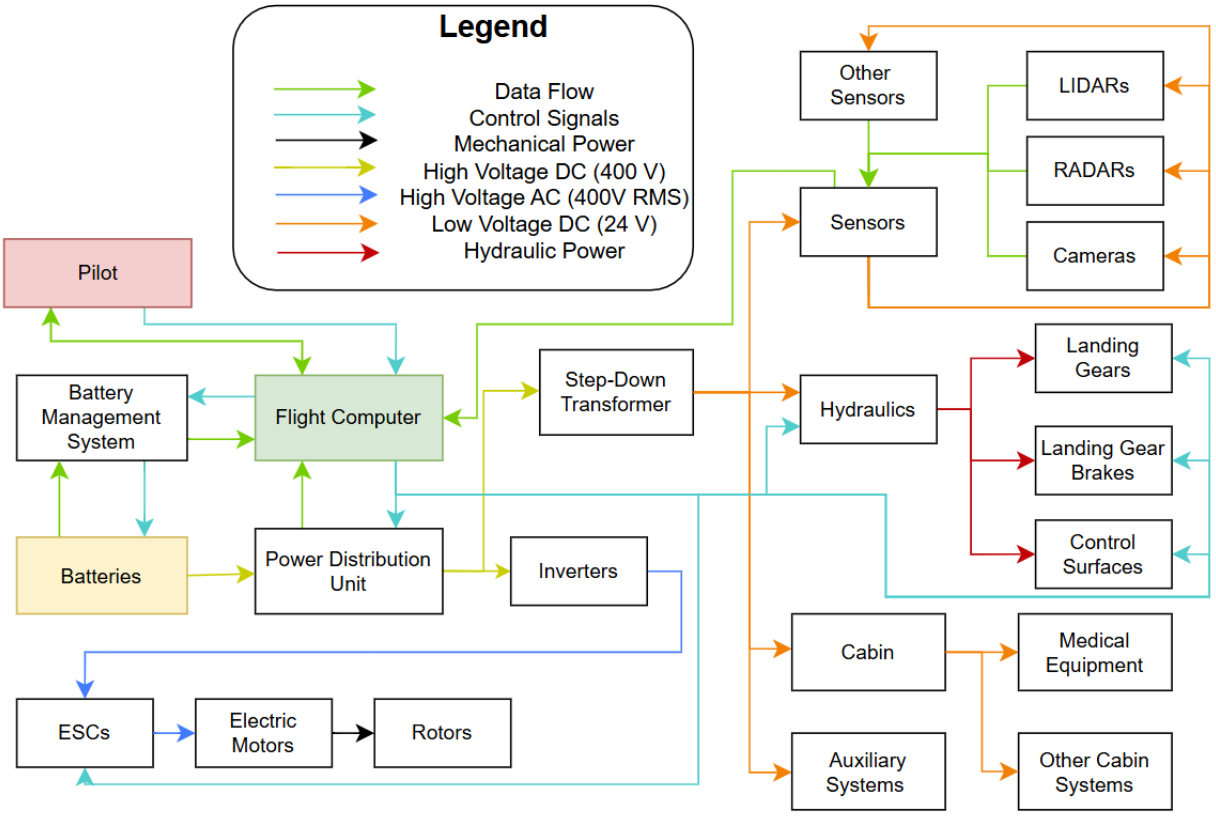

Figure 7.6: *Block diagram of electrical architecture*

Redundancy

It is important to note that Figure 7.6 is oversimplified when it comes to redundancy. In the real system, there will be a backup flight computer in case of failure in the first one. In essence, there are two flight computers (FC1 and FC2), both receiving information from sensors and the pilot. They should both be capable of sending control inputs to the ESCs, control surfaces, and hydraulics. Additionally, both flight controllers should have the ability to take over the tasks of the other flight computer in case of failure.

The use of multiple battery packs allows for redundancy in the power supply. Additionally, there will be a backup PDU in case of failure. Moreover, there will be dual ESCs for each of the six motors, also to maintain a satisfactory level of redundancy. This is as per the EASA requirements set as regulation for safe operations of eVTOLs [69].

7.6. Sensors

In aircraft design, sensors can be used to provide the pilot with additional aid, but more importantly, they serve as the core input sources for autonomous or semi-autonomous control. As shown in Figure 7.7, the sensors are divided into several categories depending on their function and operating principle. These include LiDARs, RADARs, and cameras, all of which provide complementary data to the flight computer. LiDARs generate high-resolution point clouds useful for obstacle detection and mapping. Conversely, RADARs are a great option against adverse weather conditions and provide reliable range and velocity measurements of surrounding objects. Making use of the Doppler effect, they can track the relative velocity between objects and the aircraft. Cameras offer additional views of the surroundings and are critical for visual perception tasks such as object recognition or landing pad detection. Moreover, Figure 7.6 shows the use of LiDARs, RADARs, and cameras. The unspecified sensors under ”Other Sensors” are GPS, IMUs, Pitot Static Tubes, and barometers.

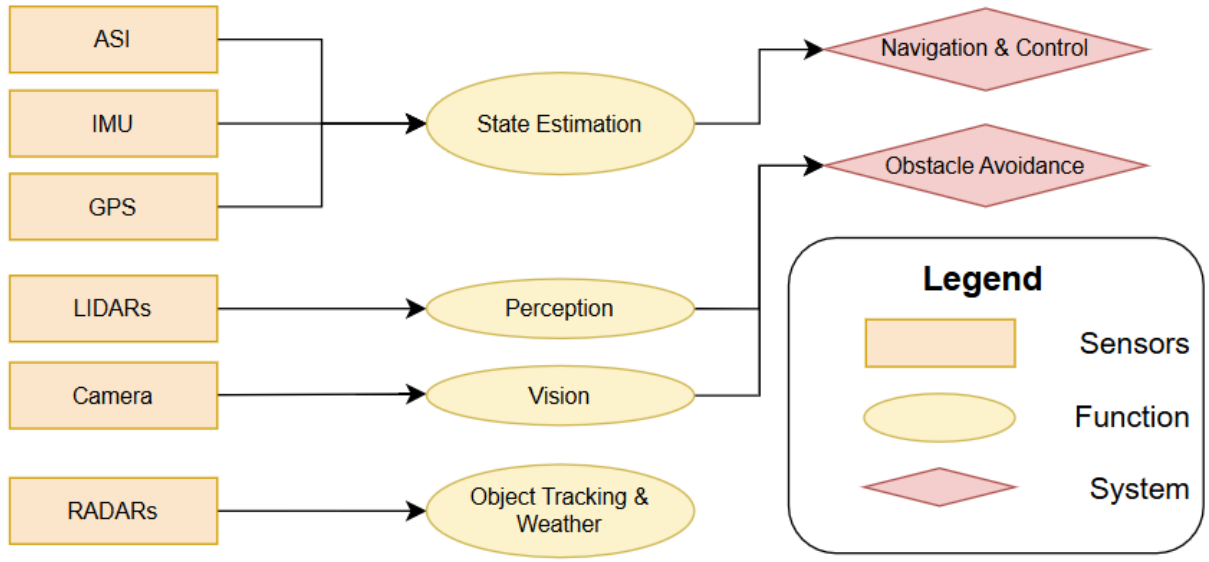

Figure 7.7: *Functional block diagram of sensors*

The raw data from these sensors is processed by a central fusion module within the flight computer. This module makes use of sensor fusion to combine the inputs to create an estimate of the aircraft's state and its surroundings. Sensor fusion typically relies on filtering techniques such as the Extended Kalman Filter (EKF) or Unscented Kalman Filter (UKF), which enable accurate estimation of position, velocity, and orientation by integrating data from inertial sensors, GPS, barometers, and vision-based systems. Simultaneous Localization and Mapping (SLAM) algorithms will also be used to support autonomous navigation and obstacle avoidance in unknown environments.

Additionally, the system architecture supports redundancy in sensor data paths as well. Multiple independent sensor units (e.g., dual IMUs, dual GPS receivers) can be used to ensure that sensor failure does not compromise situational awareness. The fusion module is designed to assess the consistency of sensor inputs and switch to secondary sources when discrepancies or faults are detected. For example, in case of failure of the LiDARs, RADARs may be used to aid the systems reliant on LiDARs. This all ensures compliance with aviation safety standards and maintains operational reliability.

Sensor Systems in Operation

Once the data has been fused into a reliable picture of the environment and the aircraft's state, the flight computer uses it to assist with both obstacle avoidance and navigation. These functions are critical to ensuring safe and stable flight during all phases of the mission, especially when operating at low altitudes or in cluttered environments.

Obstacle Avoidance

The obstacle avoidance system makes real-time use of the fused sensor data to detect potential hazards in the flight path. If an obstacle is identified—whether static, like a building, or dynamic, like another aircraft or drone- the system can react by adjusting the trajectory or alerting the pilot, depending on the situation. In a semi-autonomous setup like this, the goal is not to be fully autonomous, but rather to give the pilot enough time and information to respond effectively while also allowing the system to take quick corrective actions if needed.

This feature is particularly useful during takeoff, landing, and low-speed maneuvers where terrain or infrastructure may be close. It adds an extra layer of safety, especially in urban or confined environments where reaction time is limited. Judging by the operation of this aircraft, close encounters with obstacles will be inevitable, and the obstacle avoidance system will surely aid in this.

Navigation and Control

In terms of navigation and flight control, the processed sensor data is used to track the aircraft's location and attitude relative to its intended flight path. On this basis, the flight computer can assist in keeping the aircraft stable and following predefined routes or waypoints. This includes tasks like maintaining altitude, heading, and speed—even in the presence of wind or turbulence. Similar systems have been applied to drones and other UAVs for decades, and their reliability has become satisfactory.

Nevertheless, the pilot still has full authority but is supported by these systems, which reduce workload and help maintain smooth, efficient flight. The navigation assistance also plays a role in semi-autonomous mission phases, such as automatically transitioning between hover and forward flight or aligning with landing markers.

Sensor Positioning

The placement of sensors around the aircraft is essential to achieving full situational awareness and enabling the obstacle avoidance and navigation systems to function effectively. As shown in Figure 7.8, the LiDAR sensors are distributed radially around the aircraft to ensure continuous 360-degree coverage. This configuration was chosen to maximize the field of view (FOV) and eliminate blind spots, particularly during low-altitude flight or close-proximity maneuvers where environmental awareness is critical. Note that each LiDAR has an FOV of 100 [°], and has a range up to 70 [m], with lower reliability up to 100 [m].

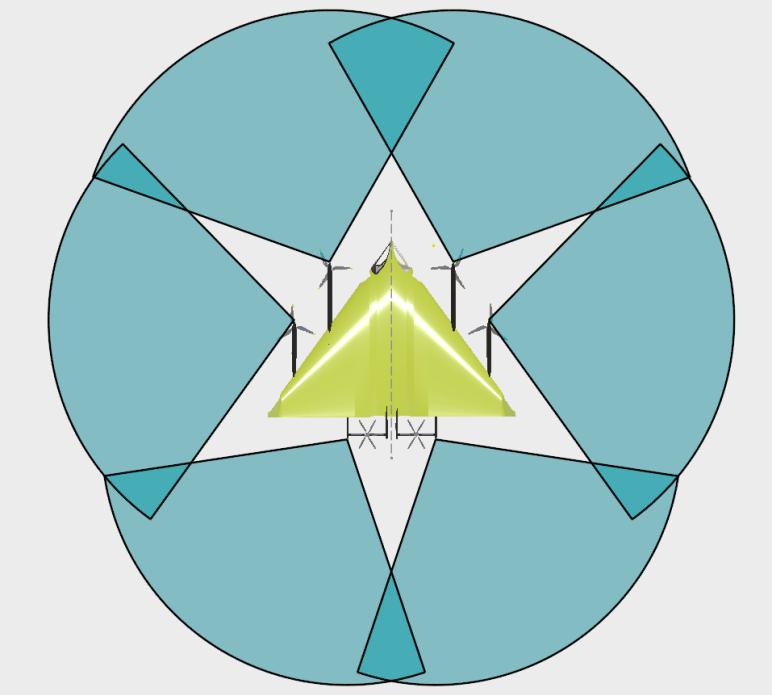

Figure 7.8: *Positioning of LiDAR sensors and their field of view*

A total of six LiDAR units are mounted externally, each angled to provide overlapping conical fields of view that extend both horizontally and vertically. These are oriented in such a way that their combined coverage forms a dome around the aircraft. The frontal sensors are angled with a slightly narrower vertical aperture but increased forward reach to prioritize obstacle detection in the direction of flight. The lateral sensors, mounted near the wing roots, cover wide arcs to both sides and downward, which is particularly useful during descent or when flying through narrow corridors. Meanwhile, the rear sensor pair maintains full coverage behind the aircraft, where visibility is often limited due to the airframe geometry.

To prevent signal interference and ensure a clear optical path, each LiDAR unit is placed away from the propeller arc and isolated from the vibrational disturbances generated by the motors. This is achieved through damped mounting points located on structurally stable sections of the wing and central fuselage. Importantly, all sensors are positioned with sufficient redundancy in mind: in case of failure of any one unit, the remaining LiDARs can collectively compensate for the blind zone, although at a reduced resolution.

In addition to LiDARs, RADAR and visual cameras are positioned in complementary locations to support multi-spectral sensing. RADAR units are installed beneath the fuselage, providing downward and forward-looking capability even in low-visibility conditions. Cameras are embedded at strategic points along the leading edge and near the nose of the aircraft, where they benefit from unobstructed views and minimal airflow distortion. These visual sensors play a supporting role in recognition tasks and offer redundancy during conditions where LiDAR or RADAR performance might degrade. Moreover, cameras will be mounted at the rear end of the airframe to ensure visibility of the back of the aircraft.

Altogether, the arrangement of sensors has been designed with full operational envelopes in mind, from hover to transition and forward flight, ensuring that the aircraft maintains a robust and redundant perception of its surroundings at all times.

8

Structures

DoctAir should be designed to carry all loads. In this chapter, the design of the structure is explained. Section 8.1 specifies the assumptions used in the design process. Then, Section 8.2 discusses the material selection of DoctAir. Before proceeding with the full design, the loads must first be identified, as covered in Section 8.3. Section 8.4 explores the structural design of the wingbox. Then, Section 8.5 focuses on the design of the landing gear. Furthermore, Section 8.6 verifies and validates the code used, and lastly, Section 8.7 provides the sensitivity analysis.

8.1. Assumptions

- **AS-STRU-1:** Atmospheric conditions are assumed constant with air density of 1.225 [kg/m^3] and cruise speed of 61 [m/s].
- **AS-STRU-2:** Material properties remain constant across all environmental operating conditions.
- **AS-STRU-3:** Wing box cross-section geometry is simplified to a closed-cell structure with straight spars and constant thickness panels.
- **AS-STRU-4:** Stringer spacing and arrangement remain constant throughout the wing span.
- **AS-STRU-5:** Wing root is assumed to be fully fixed (cantilevered boundary condition).
- **AS-STRU-6:** A safety factor of 1.5 is applied to all yield strength calculations for conservative design.
- **AS-STRU-7:** The landing gear can be modeled as a cantilever beam with the aircraft being the fixed end
- **AS-STRU-8:** The landing gear and aircraft system can be modeled as an equivalent spring-dampener system

8.2. Material Selection

Material selection is crucial in the structural design of the eVTOL Delta-wing. NASA research shows that a 10% reduction in engine weight leads to a 1% decrease in jet fuel use [70], highlighting the significant impact of weight on efficiency. For eVTOLs, structural efficiency is even more critical due to the lower energy density of batteries compared to fuel-powered VTOLs. Reducing weight offers key benefits [71] such as extended range, higher payload, and improved acceleration. The eVTOL is composed of multiple materials, each selected based on performance, cost, sustainability, and manufacturability. This section evaluates material options for the wingbox, stringers, skin, ribs, and fasteners using these criteria.

CS-23 Requirements

All structural materials in the eVTOL Delta-wing must comply with EASA CS-23.2260 [72]. This regulation requires that:

- Proven suitability and durability of materials, especially for load-critical, safety-related parts.
- Reliable, consistent manufacturing methods; tightly controlled processes must follow approved specifications.
- Statistically validated material strength values, reflecting structural criticality and material variability.
- Consideration of thermal and environmental effects in design.
- Component testing, when necessary, to verify design values.

These requirements ensure safety, reliability, and compliance, guiding material selection, testing, and validation.

Composites

The primary limiting factor is weight; exceeding the structural mass budget would prevent meeting the efficiency and range targets defined in `REQ-OPE-01-SYS-02` and `REQ-OPE-04-SYS-01`. Therefore, the eVTOL will mainly use lightweight composite materials.

Composites are widely used in aerospace due to their high strength-to-weight ratio, reduced carbon emissions, good thermal and radiation resistance, fatigue and damage durability, and overall mechanical performance [73]. However, they are more expensive than metals and sometimes less sustainable, with drawbacks including higher

breakage rates and difficult repair [74]. Other disadvantages include cold cracking, moisture absorption, limited temperature resistance, and cost [73].

As shown in Figure 8.1, composites can provide equal or greater strength than metals at significantly lower weight. A full metal design is therefore unsuitable, and composites must be used for the main structure. Smaller parts may still use metals if needed.

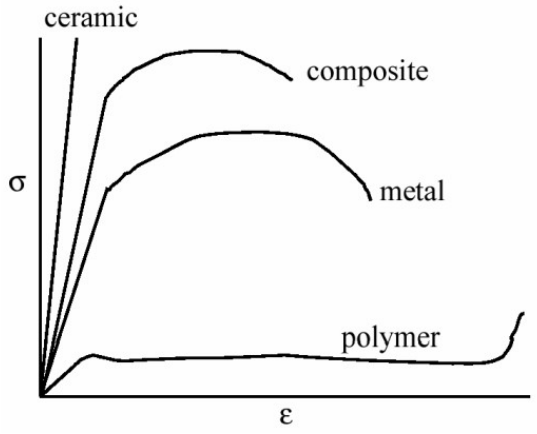

Figure 8.1: *Stress-strain curve for composites and metals [75]*

Before addressing potential challenges and solutions, an overview of available composites is given. The table below presents commonly used fiber types, resin systems, and core materials. Not all fibers are compatible with all resins—for example, carbon fiber is typically combined with epoxy for its strong adhesion, while fiberglass is often paired with polyester or epoxy resins [76].

Table 8.1: *Composite material options*

Category	Option	Note
Fiber Type [77]	Carbon Fiber (CFRP)	High stiffness/strength, low weight
	Glass Fiber (GFRP)	Low cost, good impact resistance
	Aramid Fiber (Kevlar)	High toughness, ballistic protection
	Hybrid (Carbon + Aramid)	Tailored strength/toughness
	Basalt Fiber	Mid-cost, temperature resistance
Matrix / Resin [78]	Epoxy	Most common, structural-grade
	Bismaleimide (BMI)	High-temp resistance (200–250°C)
	Polyimide	Very high temp (>300°C)
	Vinyl Ester	Corrosion resistance
	Thermoplastics (PEEK, PEKK, PPS)	Recyclable, weldable
Core Materials [79]	Nomex Honeycomb	Lightweight, fire-resistant
	Aluminum Honeycomb	Stiffer, high-temp resistant
	PVC/PMI/PET Foam	Low density, low cost

Wingbox

The wingbox (including spars, stringers, and ribs) is the most load-carrying structure and works together to carry load and maintain structural integrity [80]. The wingbox will be made of composite material due to weight constraints. A metal wingbox design will not be feasible and is thus not taken into account when deciding on the material of the wingbox and stringers. However, there are many types of composite materials, and only a small selection is given in Table 8.1. A fiber type, resin, and core material need to be specified. First, the type of fiber is assessed, and afterward, the resin and core material for the wingbox are considered.

For the wingbox design, both glass fibers and carbon fibers need to be evaluated. Both offer strength and are preferred over Aramid, Hybrid, and Basalt fibers, as these are more difficult to manufacture or have fewer proven aerospace applications [81]. To compare glass fibers to carbon fibers, it is necessary to look at the relevant properties (Table 8.2).

The property on which the design is based is stiffness, as the wings are not allowed to bend under load [83]. From Table 8.2, it can be seen that carbon fibers have better stiffness characteristics than glass in all configurations.

Table 8.2: *Fiber properties with respect to aluminum [82]*

Material	γ [kN/m^3]	E [GPa]	E/γ [km]	σ_t [MPa]	σ_t/γ [km]
Carbon dry tow	18	250	**13330**	4500	**250**
Carbon/Epoxy UD [0/0] $v_f = 66\%$	16	147	**9187**	2280	**142.5**
Carbon/Epoxy fabric [0/90] $v_f = 62\%$	16	77	**4812**	963	**60.2**
Dural 7075 (Aluminum alloy)	27	70	**2590**	500	**18.5**
E-glass dry tow	25	75	**3000**	3450	**138**
E-glass/epoxy UD $v_f = 55\%$	20	41	**2050**	1140	**57**
E-glass/epoxy fabric [0/90] $v_f = 35\%$	20	27.5	**1375**	435	**21.75**

To compare carbon with glass, the ratio of specific stiffness can be used. To meet the same stiffness requirement, the carbon design will be lighter [83]:

$$\frac{(\frac{E}{\gamma})Carbon}{(\frac{E}{\gamma})Glass} = \frac{4812}{1375} \approx 3.50. \tag{8.1}$$

Furthermore, carbon fibers will be more cost-efficient, even though the initial costs are higher than those of glass fibers. However, due to carbon fibers being lighter, cost savings will be made on the power system, meaning carbon fibers will ultimately be more efficient [83]. Figure 8.2 shows how the price of high-modulus carbon fiber decreases as more distance is flown. This figure is based on a fuel-propelled aircraft; however, the same principle applies to an eVTOL, as weight efficiency is considered even more important.

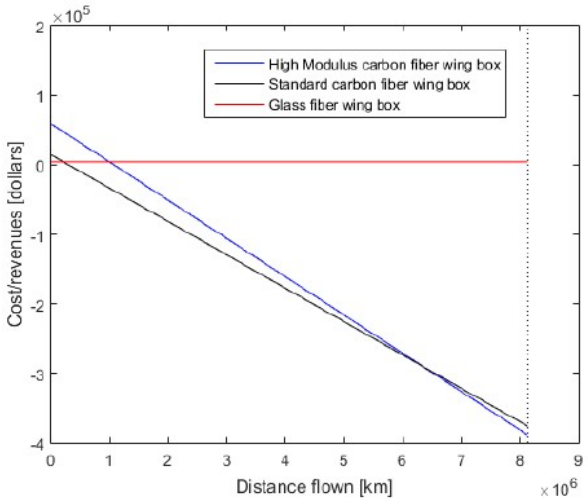

Figure 8.2: *Break-even diagram for carbon and glass fiber [83]*

There are many carbon fibers available on the market. An overview can be found in Table 8.3. **Tenax IMS 65** will be chosen as it has the highest tensile strength, a high tensile modulus (but is not excessively brittle), good strain at break for dynamic loads and vibrations, and a low density compared to other competitors. The prices of the high-strength fiber types are similar and are thus excluded from the trade-off.

Table 8.3: *Mechanical Properties of Feasible Carbon Fibers [84]*

Fiber Type	**Tensile Strength** (MPa)	**Tensile Modulus** (GPa)	**Strain at Break (%)**	**Density** (g/cm^3)
Torayca T 700 SC	4900	230	2.1	1.80
Tenax IMS 65	6000	290	1.9	1.79
Torayca M 30 S	5490	294	1.9	1.79
Tenax HTS 40	4300	240	1.8	1.80
HexTow AS4	4433	231	1.8	1.80
Pyrofil TR 50 S	4900	240	1.8	1.80

Now that the fiber type and the specific fiber have been selected, a resin must be chosen. Two resin types from Table 8.1 are unfeasible: vinyl ester does not bond well with carbon fiber, and thermoplastics have weak thermal

performance [85]. Furthermore, bismaleimide is less impact resistant [86] . Polyimide composites have higher operating temperatures than epoxy systems due to their higher glass transition temperature; however, polyimides suffer from lower toughness and reduced interlaminar properties [87]. Thus, **epoxy** will be used as the resin for our wingbox design.

Now that the type of fiber and resin has been decided, the core material can be selected. The core is used to make the structure stiffer by increasing the distance of the stiff skins from the neutral line [83]. The core material is usually about ten times less dense than the outer layer (the skin). Because of this, the entire structure becomes much stiffer while adding only a little extra weight [83]. There is a wide variety of core materials available, such as those specified in Table 8.1. To choose the best core material, a comparison must be made in terms of shear and compressive strength, as well as relative performance with respect to cost.

Figure 8.3 offers a comparison of shear strength and compressive strength. From Figure 8.3a, it can be seen that Nomex honeycomb offers the highest strength-to-weight ratio. Furthermore, high compressive strength is desired to prevent the skins from wrinkling. In both shear and compressive strength, honeycomb outperforms other materials. Furthermore, a study showed that adding a 20mm honeycomb core to a beam only increased the mass by about 20%, but reduced bending deflection by a factor of about 22 [88].

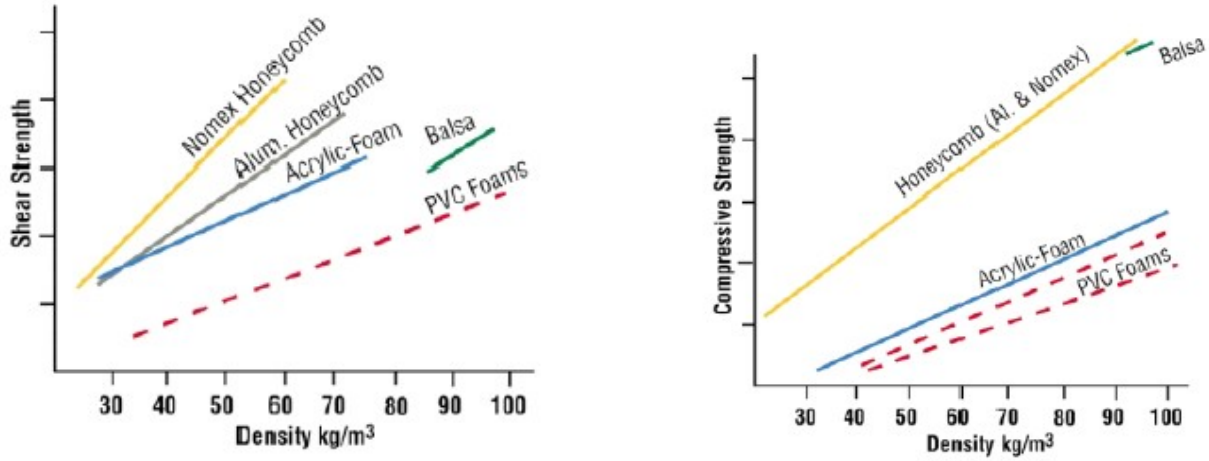

(a) *Comparison of shear strength*

(b) *Comparison of compressive strength*

Figure 8.3: *Comparing shear and compressive strength of various core materials [83]*

Nomex honeycomb is the best in terms of strength and will be chosen as the core material. However, when looking at Figure 8.4, aluminum is much better in terms of cost and performance. Therefore, aluminum honeycomb will be used if Nomex honeycomb does not fit the budget.

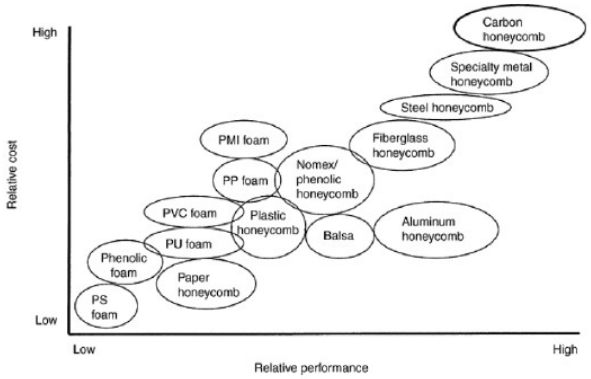

Figure 8.4: *Relative cost vs performance of various core materials [89]*

Using all this information, it has been decided to use ***Carbon Fiber Tenax IMS 65 Epoxy Nomex Honeycomb*** as the material for the design of the wingbox. Table 8.4 shows the mechanical properties of this carbon fiber/epoxy composite. The density of Tenax IMS 65 carbon fibers is approximately 1.79 [g/cm^3] (Table 8.3), while the densities of epoxy and Nomex honeycomb are about 1.2 [g/cm^3] and 0.048 [g/cm^3], respectively [90] [91]. The overall density depends on the volume fractions of the fibers, resin, and core, and is estimated to be 1.14 [g/cm^3] [92].

Table 8.4: *Material properties Tenax IMS65 E23 24K 830 tex / Epoxy 50% FVG [93]*

Property	Value	Property	Value
E_x	167000 [MPa]	$R_1(+)$	2774 [MPa]
E_y	9500 [MPa	$R_1(-)$	-1507 [MPa]
E_z	9500 [MPa]	$R_2(+)$	77 [MPa]
G_{xy}	4500 [MPa]	$R_2(-)$	-190 [MPa]
G_{yz}	3653.8 [MPa]	$R_3(+)$	77 [MPa]
G_{xz}	4500 [MPa]	$R_3(-)$	-190 [MPa]
ν_{xy}	0.3	R_{12}	55 [MPa]
ν_{yz}	0.3	R_{23}	48 [MPa]
ν_{xz}	0.3	R_{21}	55 [MPa]

Table 8.4 presents the ultimate strengths. E depicts the Young's Modulus (E_x is in the fiber direction). G depicts the shear modulus and v the Poisson's ratio, which is calculated using the elasticity law. R depicts the strength in both tension (+) and compression (-). To determine the material parameters, tensile and shear tests were performed on composite plates with various fiber orientations using a Zwick Z100 testing machine, following DIN EN ISO 527-5 and DIN EN ISO 14129 standards. Additional plates with specific fiber angles were tested to validate and adjust the shear-related properties of the unidirectional layers. [93]

Skin and other components

The wingbox is constructed from carbon fiber (Tenax IMS65) with epoxy resin and a Nomex honeycomb core. To maintain structural efficiency and manufacturability, the skin is best made from the same material [94].

For the skin, however, it is useful to bond fine metal mesh to the skin surfaces. This improves the electrical conductivity of the carbon fiber in the event of a lightning strike. Typically, copper mesh is applied together with the carbon fiber [95].

Many parts of the eVTOL will thus be made of composite materials. However, some components are not suitable for composites, such as engine parts, wheels and landing gear, electrical components, and certain interior elements. Since these do not interfere with the composite manufacturing process, their materials are considered beyond the scope of this detailed design phase.

Composite Layup

As shown in Table 8.4, composite materials exhibit anisotropic behavior, meaning their mechanical properties vary with direction. Therefore, the fiber orientation, or layup, significantly influences the overall stiffness and strength of the structure.

A layup with a high proportion of fibers oriented at 0°, aligned with the primary loading direction, offers superior axial stiffness and strength [82]. This configuration, referred to as a *dominant layup*, is suitable for wing skin structures subjected to spanwise bending [82].

The proposed fiber orientation for the wing skin is either:

$$[0/\pm 45/90/0]_s \quad \text{or} \quad [0/\pm 45/0/90]_s.$$

For the honeycomb structure, increasing the core thickness increases the overall bending stiffness of the panel [79]. For high bending loads such as experienced by the wing panels, a core thickness of 5–15 mm will be used [82]. Thinner cores (approximately 3 mm) will be used for lightly loaded or space-constrained components [82].

Fasteners

Advanced composite materials have different properties compared to the metals they are replacing. Therefore, fasteners used in composite-material joints must be specifically designed to account for these differences. First of all, most metallic fasteners are unfeasible, as carbon fiber is highly cathodic, which can lead to galvanic corrosion [96]. As a result, alloy steel and aluminum fasteners should be avoided.

Current density is a good indicator of material compatibility. As shown in Figure 8.5, the 6Al-4V titanium alloy exhibits a very low current density—close to zero—indicating the formation of a tightly adhering protective oxide film that resists further corrosion [96]. 6Al-4V titanium would thus be a good option. This behavior contrasts with that of other materials.

Titanium and its alloys, as well as multiphase alloys such as MP159, MP35N, and Inconel alloys 600 and 718, are

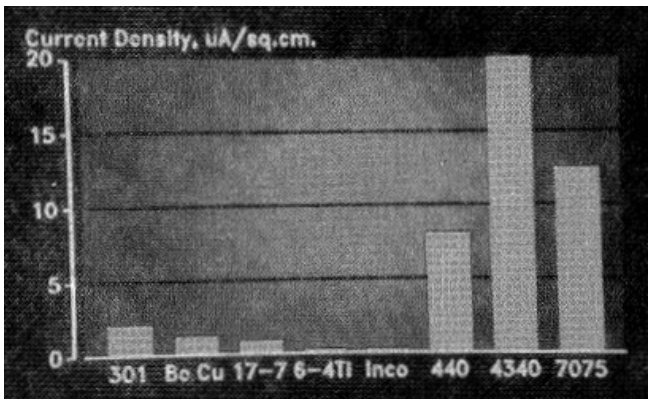

Figure 8.5: *Galvanic Corrosion - Current Density [96]*

compatible with graphite-fiber composites because they are corrosion resistant [96]. Table 8.5 presents the trade-off of the different fasteners based on density, strength, and cost. **Titanium (AI-4V)** is chosen as the fastener to be used, as it does not corrode with carbon composite, has the lowest density and estimated cost, while having enough ultimate strength.

Table 8.5: *Comparison of Fastener Materials for Composite eVTOL Structures*

Material	Density (g/cm^3)	Ultimate Strength (MPa)	Estimated Cost*
Titanium (6Al-4V) [97]	4.43	950	Low
MP159 [98]	8.33	848	High
MP35N [99]	8.55	896	High
Inconel 600 [100]	8.47	655	Medium

*Estimated cost is relative (Low–Medium–High) and difficult to quantify precisely due to variations by supplier, country, and form of material.

8.3. Load identification

Critical load cases need to be considered when designing a safe and reliable aircraft. Gust and manoeuvre loading diagrams are used to determine these critical load cases and create the aircraft's flight envelope. This flight envelope is then used in the structural design of the wing box, cabin, and landing gear, ensuring the aircraft can withstand all expected loads.

Parameter overview

Before defining the flight envelope, the parameters used in the aircraft design must be clearly defined. Table 8.6 provides an overview of the parameters used for the structural design. Most of these parameters are derived from design elements discussed in previous chapters or that will be discussed later in this report. Others originate from CS-23 requirements, such as the minimum and maximum load factors and gust velocities.

Flight Envelope

The flight envelope consists of two key components: the gust loading diagram and the manoeuvre load diagram. First, the gust loading diagram was computed based on certification specifications. Subsequently, the manoeuvre diagram was computed. Finally, both diagrams were combined into a single figure to determine the most critical load factors.

Gust Loading Diagram

The gust loading diagram was constructed in accordance with CS-23 (Certification Specifications for Normal, Utility, Aerobatic, and Commuter Category Aeroplanes) [72]. According to these specifications, the maximum gust velocities are defined as follows:

- $U_{de} = 15.24\,\mathrm{m\,s^{-1}}$ at cruise speed V_C
- $U_{de} = 7.62\,\mathrm{m\,s^{-1}}$ at dive speed V_D

To compute the gust load factors n_{gust}, the following standard equation was used [72]:

Table 8.6: *Aircraft parameters and constants*

Parameter	Abbreviation	Value	Unit
Maximum Take-Off Weight	MTOW	1745	kg
Wingspan	b	9	m
Wing Area	S	36.9	m^2
Aspect Ratio	AR	2.195	–
Air Density (Sea Level)	ρ	1.225	kg/m^3
Gravitational Acceleration	g	9.80665	m/s^2
Cruise Speed	V_c	61	m/s
Stall Speed	V_s	33*	m/s
Dive Speed	V_d	76.25	m/s
Maneuvering Speed	V_a	60.73	m/s
Lift Curve Slope	$C_{L,\alpha}$	2.46912451071	rad^-1
Maximum Lift Coefficient	$C_{L,\max}$	0.78	–
Maximum Load Factor	$n_{\max}$	3.8 [72]	–
Minimum Load Factor	$n_{\min}$	-1.52 [72]	–
Gust Velocity (Cruise)	$U_{de,1}$	15.24 [72]	m/s
Gust Velocity (Dive)	$U_{de,2}$	7.62 [72]	m/s

*Value derived based on reference aircraft.

$$n_{\text{gust}} = 1 \pm \frac{K_g \cdot \rho \cdot V \cdot U_{de} \cdot C_{L_\alpha}}{2 \cdot W/S} \tag{8.2}$$

where ρ is the air density, V the flight speed, U_{de} the design gust velocity, $C_{L\alpha}$ the lift curve slope in radians, and W/S the wing loading. The gust alleviation factor, K_g, accounts for the aircraft's dynamic response and is derived from the following relation [72]:

$$\mu = \frac{2W}{\rho \cdot C_{L_\alpha} \cdot c \cdot g} \Rightarrow K_g = \frac{0.88 \cdot \mu}{5.3 + \mu} \tag{8.3}$$

Here, c is the mean aerodynamic chord.

Manoeuvre Diagram

Next to the gust diagram, a manoeuvre diagram must be constructed to determine the critical flight loads. For normal category aircraft, the regulatory limits are:

- Maximum positive load factor: $n_{\max} = +3.8$ [72]
- Maximum negative load factor: $n_{\min} = -1.52$ [72]

The dive speed (V_D), defined as the maximum allowable aircraft speed, must satisfy $V_D \geq 1.25 \times V_C$ as per CS 23.335. The stall condition further constrains the maneuver envelope. The load factor at stall speed is derived from:

$$n = \pm \frac{0.5 \rho V^2 C_{L_{\max}}}{(W/S)} \tag{8.4}$$

with ρ as air density, V as velocity, $C_{L_{\max}}$ the maximum lift coefficient, and W/S the wing loading.

Critical Load Cases & Failure Modes

To design the structure to withstand critical flight conditions, the most severe load cases at different velocities must be identified. At this stage of the design process, specific eVTOL delta-wing characteristics can be neglected; the vehicle parameters alone, together with CS-23 requirements, are sufficient to calculate the critical loads. This approach was confirmed in discussions with Dr. ir. Roelof Vos. The resulting flight envelope is shown in Figure 8.6. The gust load factors are depicted in blue, the different velocities (stall, maneuver, cruise, and dive) are indicated by green dashed lines, and the maneuver envelope is shown in yellow. Furthermore, the maneuver speed is defined as the maximum speed at which an aircraft can be fully controlled [72], and can be read to be 60.73 [m/s]. The dive speed is considered to be exactly $1.25 \cdot V_c$; however, as this does not influence the minimum or maximum load factor, it is not further detailed. The most critical load cases occur at points n_{max} and F, corresponding to maximum load factors of $n_{max} = 3.800$ and $n_{min} = -1.609$.

In order for the aircraft to withstand all expected loads, CS-23 defines an ultimate load factor [72]. This ultimate load factor means that the maximum loads need to be multiplied by 1.5 before performing structural calculations. In this way, the aircraft has a margin to unexpectedly handle additional loads.

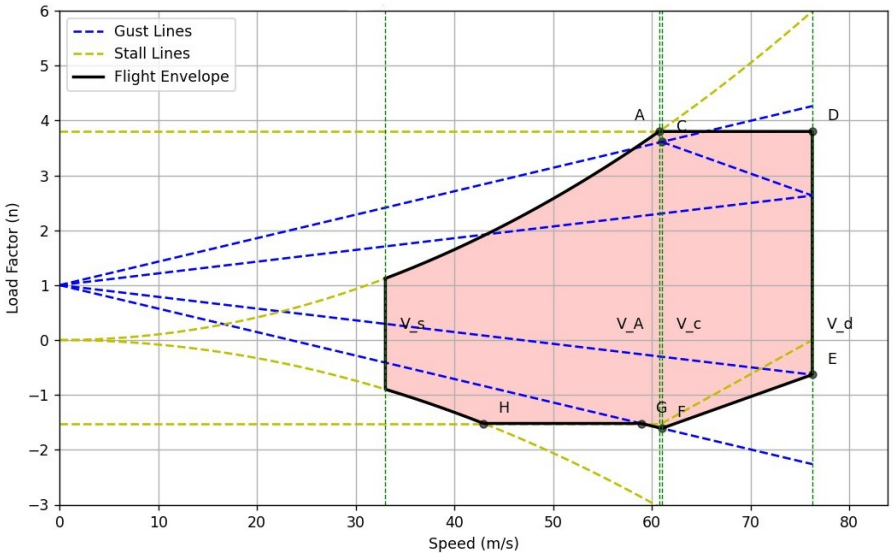

Figure 8.6: *Flight envelope for low-altitude eVTOL: DoctAir*

In addition to load analysis, principal failure modes must be considered. According to an article published in *Materials Today* [101], the most common failure modes in aircraft (in order of prevalence) are fatigue, overload, and corrosion. Overload failures further break down into buckling and yielding. Each of these failure modes is addressed in the structural design process.

8.4. Wingbox Design

Internal Loading Diagrams for Wing Structural Sizing

The determination of internal loads within the wing structure is a critical precursor to detailed sizing. This was achieved by applying the previously established load factors to the relevant mass and aerodynamic distributions, and subsequently constructing internal shear force, bending moment, and torsional moment diagrams along the wing span.

The primary loads considered for the wing's structural analysis included:

- Aerodynamic Lift Distribution
- Aerodynamic Pitching Moment Distribution
- Distributed Wing Self-Weight
- Concentrated Mass of Propulsion Units and their Mounting Structures
- Distributed or Concentrated Mass of Batteries Housed within the Wing
- Concentrated Mass of the Main Landing Gear (if wing-mounted)

Aerodynamic drag was not explicitly included in these sizing load diagrams since its magnitude was significantly smaller than the primary aerodynamic lift and moment forces, thus having a comparatively minor impact on the dominant internal bending and shear loads.

For the purpose of this analysis, the wing was modeled as a cantilever beam, with reaction forces and moments developed at the wing root, where it attaches to the fuselage. A conceptual free body diagram illustrating this idealization and the applied loads is presented in Figure 8.7.

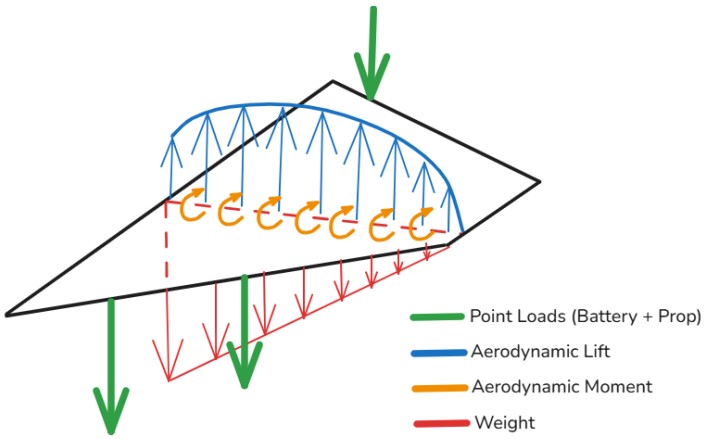

Figure 8.7: *Representation of applied loads on the wing*

To derive the internal load diagrams, discrete sections were analyzed along the wing span. An initial estimate for the wing weight was obtained using Class II weight estimation methods as detailed by Roskam [102]. The spanwise distribution of this wing weight was then modeled according to the following relationship, where $c(y)$ is the local chord length at spanwise location y, and K is a scaling constant [103]:

$$m(y) = K \cdot c(y)^{\frac{1}{2}} \tag{8.5}$$

The constant K was determined by integrating the right-hand side of Equation 8.5 over the wing span and equating the result to the total wing mass estimated via the Class II method.

Once the mass distributions were established, the aerodynamic force and moment distributions as detailed in Chapter 5 were applied. For each critical load case, these aerodynamic loads were scaled by the appropriate load factor. By systematically sectioning the wing and applying equilibrium equations, the internal shear force, bending moment, and torsional moment diagrams were constructed. These diagrams were developed with respect to the right-handed vehicle carried body axis, with x pointing outwards from the nose, y along the wingspan, and z pointing down.

The internal load diagrams corresponding to the critical load cases are presented in Figure 8.8a and Figure 8.8b, respectively. These diagrams provide the basis for the subsequent stress analysis.

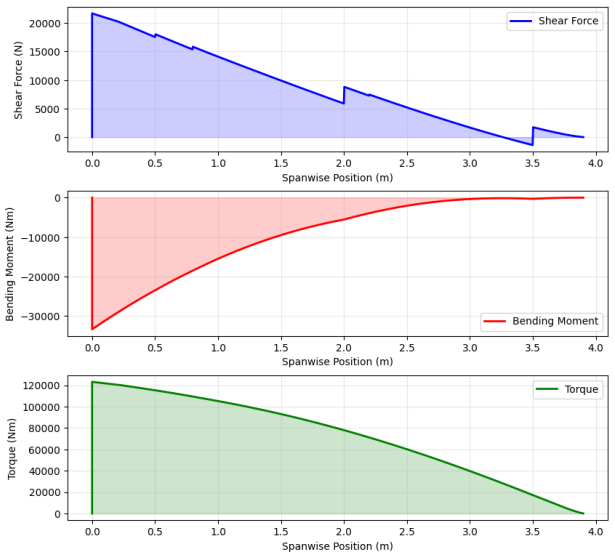

(a) *Internal force diagram corresponding to max load factor = 3.8*

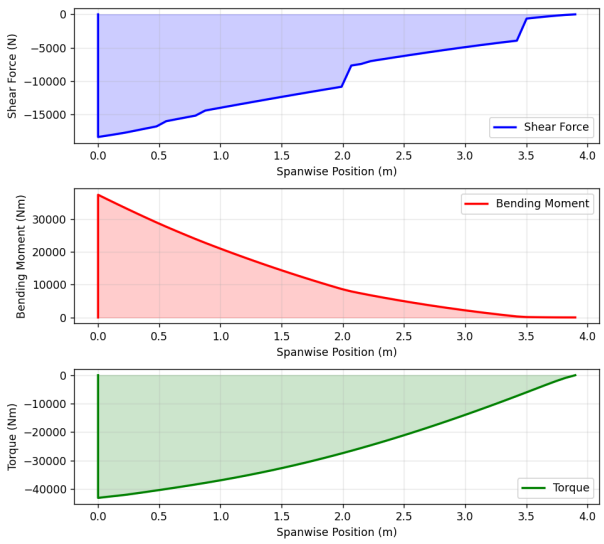

(b) *Internal force diagram corresponding to min load factor = -1.58*

Figure 8.8: *Internal force diagrams.*

Geometry setup

To facilitate the stress analysis of the structure, a defined internal geometry for the wing was established. The primary load-carrying structure, the wingbox, was designed with two main spars, with the front spar positioned

at 25% of the local chord length from the leading edge, and the rear spar at 75% of the chord. The overall wing planform parameters, carried forward from the Midterm Report, are summarized in Table 8.7.

Table 8.7: *Key Wing Planform Parameters*

Parameter	Value
Root Chord	7.2 [m]
Semi-Span	4.5 [m]
Reference Surface Area	36.9 [m^2]
Aspect Ratio	2.195
Taper Ratio (λ)	0.1329
Leading Edge Sweep Angle (Λ_{LE})	54.03 [deg]

For the internal structural elements, specific cross-sectional profiles were selected. The spars are designed with an I-beam profile, chosen for its favorable strength and stiffness-to-weight characteristics, particularly in bending [104]. To enhance the buckling resistance of the upper and lower skin panels, stringers are incorporated, with two stringers placed on both the upper and lower surfaces of each wing bay, positioned equidistantly from each other and from the spars. These stringers have a T-shaped cross-section, offering good axial stiffness[105].

Furthermore, wing ribs are oriented parallel to the aircraft's longitudinal axis and are aligned with the free-stream velocity. This orientation was selected primarily to facilitate the integration of the retracting main landing gear within the wing structure. The placement of batteries within the wing volume is also considered, which can provide a degree of structural relief by favorably distributing mass along the span. Similarly, the propulsion units are mounted to the lower surface of the wing. Their mass contributes to the overall wing loading, and their placement can influence local bending relief, as reflected in the internal shear and bending moment diagrams in Figure 8.8 .

Structural analysis

The structural analysis and subsequent sizing were performed using the Python package `sectionproperties`. The wing's external profile was defined by the airfoil geometry determined in Chapter 5. The internal structural elements such as spars, skin, and stringers were parameterized to allow for design optimization. For this analysis and ease of manufacturing, a constant thickness was assumed for the skin, spar , and the stringer across the span. By defining these parameters, a unique wing cross-section could be generated at any desired spanwise station, an example of which is illustrated in Figure 8.9.

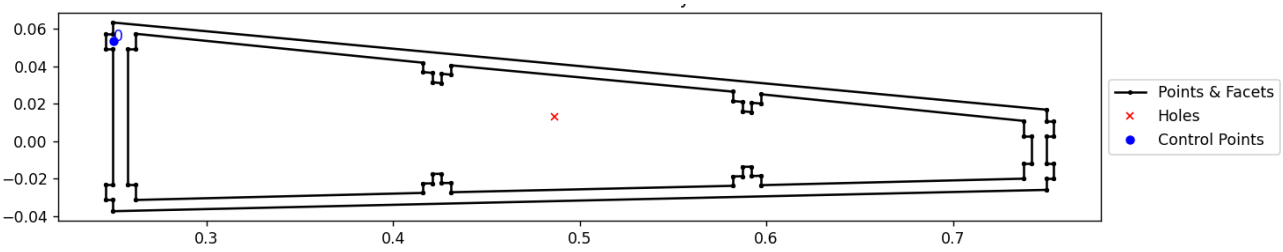

Figure 8.9: *Cross section geometry for chord length 1[m]*

Using `sectionproperties`, a Finite Element Analysis approach is employed by the library to determine the stress distributions across each defined cross-section. This analysis depicted how stresses varied throughout the section components under the applied internal loads, after applying a suitable mesh for the cross-section. An example of such a stress distribution plot, highlighting variations across the spars, skin, and stringers for a given set of loads, is shown in Figure 8.10. After applying the material properties of the selected composite, it was ensured that the maximum tensile, compressive, and shear stresses at all points within each analyzed cross-section remained below the material's allowable strength when subjected to a safety factor of 1.5.

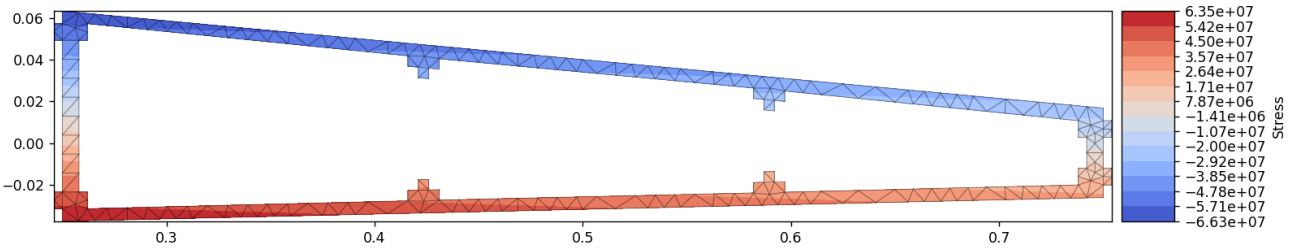

Figure 8.10: *Result from python library showing variation of stress in the cross-section*

In addition to direct stress limitations, several critical buckling failure modes were considered for the stiffening elements and skin panels to ensure structural integrity under compressive and shear loads. These are detailed below:

Shear Buckling of Spar Webs

The spar webs can be modeled as flat plates subjected to significant shear loading from both shear forces and torsion and are susceptible to shear buckling. The critical shear stress, τ_{crit}, at which buckling starts, was computed using the following equation:

$$\tau_{crit} = \frac{\pi^2 k_s E}{12(1-\nu^2)} \left(\frac{t_w}{h_w}\right)^2 \tag{8.6}$$

Here, E is the material's Young's modulus, ν is Poisson's ratio, t_w is the web thickness, and h_w is the web height. The buckling coefficient k_s is dependent on the aspect ratio of the web panel and the boundary conditions imposed. The determination of k_s was based on standard relations for plate buckling, an example of which is shown in Figure 8.11. The calculated τ_{crit} was then compared against the maximum shear stress experienced by the spar web under the design load cases to ensure an adequate margin of safety.

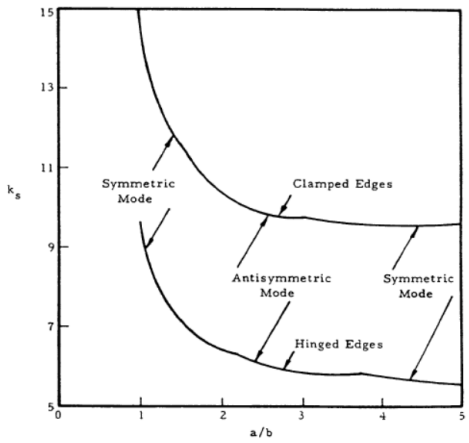

Figure 8.11: *Shear buckling stress coefficient of plates as a function of aspect ratio for clamped and hinged edges[***buckling***]*

Buckling of Wing Skin Panels

Similarly, the wing skin panels, particularly those on the upper surface experiencing compressive are prone to buckling. The critical buckling stress for these skin panels was evaluated using an equation analogous to Equation 8.6 when considering compressive buckling. For compressive buckling, the equation takes the form:

$$\sigma_{crit} = \frac{\pi^2 k_c E}{12(1-\nu^2)} \left(\frac{t_s}{b_s}\right)^2 \tag{8.7}$$

where t_s is the skin thickness, b_s typically represents the stringer spacing (width of the skin panel bay), and k_c is the compressive buckling coefficient, dependent on panel aspect ratio and edge support conditions provided by spars and stringers. The calculated critical stress was compared against the actual compressive and shear stresses in the skin to prevent premature failure.

Column Buckling of Stringers

Longitudinal stringers, designed to carry significant axial loads, can fail due to column buckling between the supporting wing ribs. This failure mode occurs when these slender compressive members deflect laterally. The

critical buckling stress, σ_{crit}, for the stringers was estimated using Euler's column buckling formula:

$$\sigma_{crit} = \frac{K\pi^2 E I_{str}}{L_{eff}^2 A_{str}} \tag{8.8}$$

In Equation 8.8, K is the column effective length factor, dependent on the boundary conditions of the stringer where it attaches to the ribs and thus a value of $K = 4$ was assumed, representing clamped-clamped conditions between ribs. E is the Young's modulus, A_{str} is the cross-sectional area of the stringer, L_{eff} is the rib spacing, and I_{str} is the area moment of inertia of the stringer's cross-section about the bending axis. The `sectionproperties` library outputs these geometric properties (A_{str}, I_{str}) for the defined T-shaped stringer profile. This σ_{crit} was then compared to the maximum compressive stress developed in the stringers, primarily due to wing bending, to ensure strength of the component.

Following the establishment of the stress calculation, a design optimization procedure was implemented with the primary objective of minimizing the wing's structural mass. This iterative process involved varying the thickness of the wing skin, the thickness of the spar web, the dimensions of the spar flange, and the dimensions of the stringer.

The optimization loop was initiated with a minimal initial thickness of 0 [mm] for all components. In each iteration, the `sectionproperties` analysis was performed for all cross-sections under the loading. The dimensions of components exceeding stress were incrementally increased until all failure criteria were satisfied. This iteration was performed to find the combination of component dimensions that met all strength requirements while resulting in the minimum overall structural mass. This optimization was then integrated into a broader iterative loop with other subsystem designs to achieve an overall converged aircraft design.

The final results about weight and geometry of the wingbox can be found in Chapter 9.

8.5. Landing Gear

The landing gear plays a crucial role in the crashworthiness of eVTOL aircraft, as their vertical takeoff and landing capabilities demand design considerations for vertical crash scenarios where the impact during emergency landings is much higher than those experienced by traditional fixed-wing aircraft. This section deals with the design, sizing, and performance of a landing gear, taking into account the g-limit and safety of an average passenger. Additionally, landing gears are generally fabricated in two types - skids or wheels. Skids are simple, relatively lightweight, and cost-effective. On the other hand, wheels offer the advantage of taxi capabilities and ground maneuverability, which can be important during certain rescue operations, maintenance phases, and even conventional landings. The latter is particularly emphasised - consider the eVTOL cruising but with not enough power to continue the mission because of, for example, multiple engine failures. In this case, it is still possible to land horizontally as a conventional fixed-wing aircraft if wheels are used as landing gear. With skids, however, this would be difficult and dangerous. Overall, although skids decrease the structural mass of the vehicle, the taxiing capability of wheels adds another degree of safety to the eVTOL, which is prioritized. Lastly, in order to reduce drag during cruise, the landing gears will be retractable.

Landing Gear Positioning

The design process begins with determining the location of the main and nose landing gears. This is governed by four requirements to ensure safety during ground maneuvering, which are displayed on Figure 8.12 and listed after.

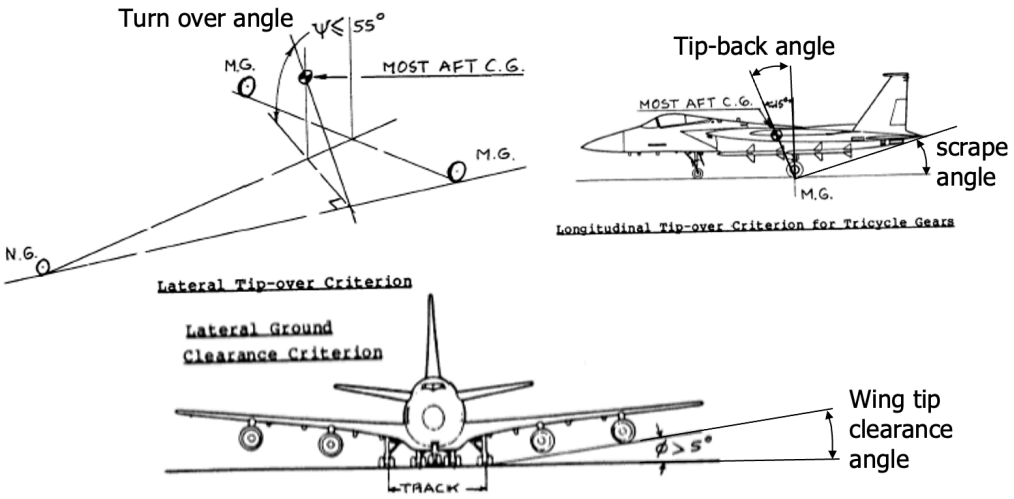

Figure 8.12: *Angle requirements for stability and ground clearance [106]*

1. Scrape angle, $\theta_{scrape} > 15°$: Typically, this scrape angle is to ensure the undercarriage of the empennage avoids scraping the ground during takeoff of fixed-wing aircraft. However, in the case of eVTOLs, this requirement simply stems from clearance considerations.
2. Tip-back angle, $\theta_{tip-back} > 18°$: This is to ensure the center of gravity of the vehicle stays in front of the main landing gears during ground maneuvering.
3. Wing tip clearance angle, $\phi > 5°$: This is a clearance criterion between the main landing gears and the wing tips
4. Turn over angle, $\Psi < 55°$: During sharp taxiing turns, the vehicle should not tip over. These requirements ensure the track is wide and adequate enough to ensure stability.

As implied by the requirements above, the location of the center of gravity plays an important role in determining ground stability. Furthermore, the center of gravity can move significantly along the body axis of the aircraft depending on how it is loaded. In order to design for the worst-case scenario, it is important to make sure that the angle requirements in Figure 8.12 are satisfied for all possible CG locations. Hence, as the aft center of gravity CG_{aft} is the most limiting for the turn over, tip-back, and scrape angles (see Figure 8.12), it will be used for the remainder of the analysis, apart from the calculation of the nose landing gear location which will use the forward center of gravity $CG_{forward}$.

Now, using Figure 8.12 and trigonometry, one can find the required height of the main landing gear such that the scrape and tip-back angle criteria are fulfilled. These expressions are shown below.

$$h_{scrape} = (l_{AC} - x_{mg}) \cdot tan(\theta_{scrape}) \tag{8.9}$$

$$h_{tip-back} = \frac{x_{mg} - CG_{aft}}{tan(\theta_{tip-back})} - CG_z \tag{8.10}$$

where in addition to previously mention parameters, h_{scrape} and $h_{tip-back}$ are landing gear heights needed to satisfy angle requirements, l_{AC} is the length of the aircraft, CG_z is the vertical height of the center of gravity from the ground, and x_{mg} is the position of the main landing gear. Note that all distances are measured from the nose of the aircraft. The values of h_{scrape} and h_{tip_back} are compared, and the maximum value results in the height of the main landing gear (and nose landing gear, to avoid pitch on level ground).

The position of the nose landing gear x_{ng} is directly related to the amount of static load it carries, and for adequate steering capacity, this should be at least 8% of the maximum take-off weight [107]. From simple moment equilibrium analysis, the position of the nose gear becomes,

$$x_{ng} = \left(\frac{1}{w_n} - 1\right) \cdot (x_{mg} - CG_{forward}) \tag{8.11}$$

where w_n is the amount of static load carried by the nose landing gear as a fraction of the total load. Next, the main landing gear width (track) is determined based on two angles as well, namely the wing tip clearance angle

ϕ and the turn over angle Ψ. Trigonometry is used again to derive two expressions for the required width to satisfy the criteria, which are given below.

$$w_{tip} = \frac{b}{2} - \frac{z_t}{tan(\phi)} \tag{8.12}$$

$$w_{turn} = \frac{x_{ng} - x_{mg}}{\sqrt{\frac{x_{ng}^2 \cdot tan^2(\Psi)}{CG_z^2}} - 1} \tag{8.13}$$

where w_{tip} and w_{turn} are the required wheel track widths to meet angle requirements, b is the wing span, and z_t is the wing tip height from the ground. The minimum of w_{tip} and w_{turn} is the most driving and is therefore chosen as the track width. Finally, a nose tip clearance of 15° from the bottom of the nose landing gear is added as a constraint to account for ground stability during braking and general clearance.

Equations 8.9 - 8.13 are implemented in a Python script for iteration. The solving process begins with an initial guess of where the main and nose landing gears are, and with w_n initially set to 0.08. Then, the solver iterates through different values of x_{mg}, x_{ng}, and w_n until all angle requirements in Figure 8.12 are satisfied. It is worth mentioning that there are, of course, many arrangements of the landing gears that satisfy the angle requirements. The goal of the iteration is to find one of such arrangements. Figure 8.13 shows the final configuration result after iteration, satisfying all requirements.

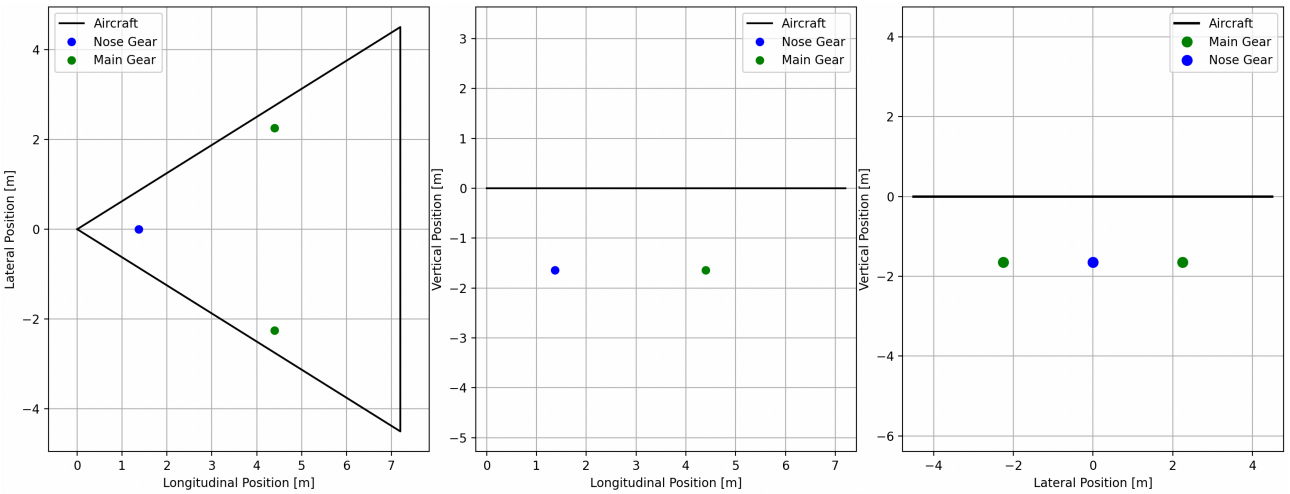

Figure 8.13: *Position of main and nose landing gears from top view [LEFT], side view [CENTER], front view [RIGHT]. Note: the black lines indicate the middle of the wing*

The configuration of landing gears as shown on Figure 8.13 corresponds to a nose wheel loading of 41%. This is important to know as it will be used to determine the wheel dimensions in the following subsection. Additionally, the computed gear height is 1.621 [m].

Tire Sizing

The known locations of the gears give the static load on the nose and main landing gears, using which, the wheels can be sized. The number of wheels on a single gear is decided based on the criteria that an aircraft with a maximum take-off weight not exceeding 5700 [kg] needs two wheels per strut, which applies for both the main and nose landing gears. Furthermore, the landing surface of the emergency rescue locations may be unprepared, for which a lower tire pressure is desired because it helps the tire to smooth out in bumps and uneven ground. Table 8.8 shows what the maximum allowable tire pressure is for various unprepared surfaces.

Table 8.8: *Maximum allowable tire pressure in [kPa] for different unprepared surfaces [106]*

Description of Surface	Maximum Allowable p (kPa)
Soft, loose desert sand	170–240
Wet and boggy grass	210–310
Hard desert sand	280–410
Hard grass	310–410

Using the guidelines on Table 8.8, a tire pressure of 410 [kPa] is selected (for all landing gears). This value is appropriate not only for unprepared surfaces but also offers sufficient performance on slightly harder terrain such as asphalt, giving a balance between unprepared and prepared surfaces. Next, the wheel dimensions can be estimated based on tire pressure and static load per wheel. In order to do this, the following figure is to be used for existing wheels.

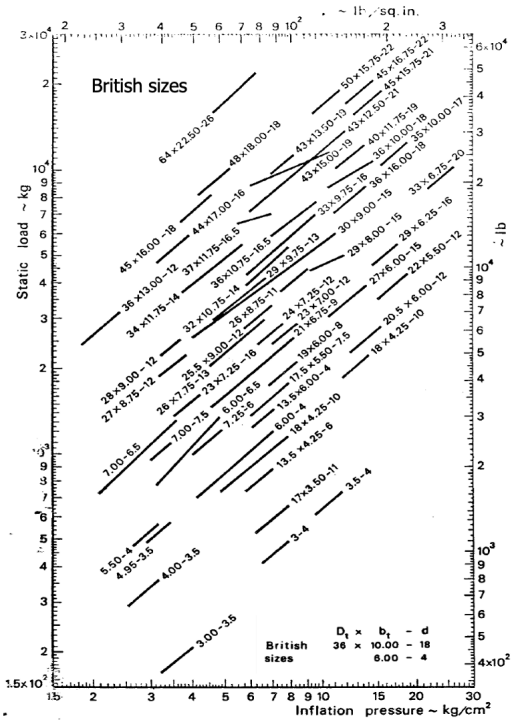

Figure 8.14: *Tire inflation pressure vs static load for existing British tires. Note 1: The conversion between [kg/cm^3] and [kPa] is roughly 100. Note 2: the static load is in [kg] [106]*

The landing gear static loading found in the previous subsection gives a static load of 349 [kg] and 256 [kg] on each nose and main wheel, respectively. Moreover, the tire inflation pressure for each wheel converted to appropriate units is 4.1 [kg/cm^3]. Inspecting Figure 8.14 and applying contingencies gives a tire dimension for both nose and main wheels of: D_w, w_w, D_{w_r} = [18.0, 4.25, 6.0], where D_w, w_w, D_{w_r} are the wheel diameter, wheel width, and wheel inner rim diameter respectively.

Strut Sizing

The strut is the main vertical part of the landing gear and is responsible for carrying the loads experienced during ground maneuvering and landings. The latter is driving since the vehicle experiences the greatest loads during vertical and sideways impacts. There are a few requirements and assumptions to consider first, which are listed below.

- LG-1: Landing gears struts are typically made of high strength aluminum alloys such as aluminum 7075 [108, 109], with a Young's Modulus of $E_{alu} = 71.7$ [GPa], a tensile yield strength of $\sigma_{y_t} = 476$ [MPa], and a compressive yield strength of $\sigma_{y_c} = 530$ [MPa] [110].
- LG-2: The landing gear strut will utilize a hollow, thin-walled tube. This has several benefits, including weight saving and free volume which can be used for impact energy absorbing honeycomb structure, a second level of safety in the case that the landing gear fails during impact [111]. The thickness of the hollow strut's thin wall can be pre-determined based on the upper limits of the manufacturability of aluminum 7075 tubes, which is 50 [mm] [112].
- LG-3: According to the Code of Federal Regulations, requirements stipulate that structures should be able to withstand accelerations of up to 12 [G] vertically and 6 [G] sideways (G = 9.81 $[m/s^2]$) during emergency landings [113]. In the design of the landing gear strut, the impact forces are simply the product of the maximum take-off weight and the accelerations, and they are applied at the lower end of the strut.

From LG-3, undoubtedly the largest load is the compressive force from the 12 [G] of acceleration (causing axial compression), followed by the horizontal (sideways) force (causing bending). Furthermore, due to the thin-walled structure of the beam (see LG-2), it is important to introduce buckling as a failure mode to consider as

well. Because emergency landings are often difficult to control and predict, the vehicle often lands on a single landing gear rather than two or all three at the same time. This is also exacerbated by possibly uneven landing surfaces or strong gusts during landing, which can alter the attitude of the vehicle. Hence, all landing gears will be designed to withstand the 12 [G] of vertical and 6 [G] of sideways acceleration alone.

The analysis begins with calculating the minimum required strut diameter D_{min} for maintaining and supporting the axial load. From the simple mechanics of materials of thin-walled tubes, this is,

$$D_{min} = \frac{MTOW \cdot 12g \cdot SF}{\sigma_{y_c} \cdot \pi \cdot t} \tag{8.14}$$

where $g = 9.81$ [m/s/s], $SF = 1.5$ is the safety factor, $t = 50$ [mm] is the wall thickness of the hollow strut. Note that $12g$ comes from the vertical acceleration requirement in `LG-3`. Next is determining the minimum required diameter to avoid failure by buckling. Euler's buckling formula is given by,

$$F_{euler} = \frac{n \cdot \pi^2 \cdot E_{alu} \cdot I}{L^2} \tag{8.15}$$

where F_{euler} is the amount of force needed to buckle the column, n depends on loading condition and in this case $n = 0.25$ since the bottom end of the landing gear is free to move both vertically and horizontally, $I = \frac{\pi}{64} \cdot (D^4 - (D - 2t)^4)$ is the area moment of inertia of the thin-walled hollow cross-section of the strut, and $t = 0.050$ [m] is the wall thickness of the tube. This formula is translated into a Python code, and the diameter D is iterated in ascending order until Euler's buckling force F_{euler} becomes more than the applied compressive axial force of $MTOW \cdot 12g \cdot SF$. The last failure mode to consider is bending. The landing gear can be modeled as a cantilever beam with the horizontal force of $MTOW \cdot 6g \cdot SF$ acting perpendicularly on the free end. With these simplifications, the maximum bending moment is $M_{max} = MTOW \cdot 6g \cdot SF \cdot L$ and it occurs at the fixed end where the normal stress σ induced at that point is given by,

$$\sigma = \frac{MTOW \cdot 6g \cdot SF \cdot L \cdot c}{I} \tag{8.16}$$

where, in addition to previously mentioned parameters, $c = 0.5 \cdot D$ is where the maximum normal force occurs from the neutral axis of the cross section. Similar to the buckling analysis, Equation 8.16 is translated into Python where the diameter D is varied until the normal stress becomes smaller than σ_{y_c}. Formulas 8.14-8.16 are solved, and the required diameter for the strut becomes the maximum of the three computed. This was found to be $D = 0.3141$ [m].

Landing Gear Performance

The final step in landing gear design deals with crashworthiness and is important for verifying the safety of the passengers. This subsection simulates an emergency landing and concludes if passengers are able to survive the landing based on the acceleration of the vehicle at impact, which in turn, is influenced by the dampening and stiffness of the landing gear struts designed previously. According to the Code of Federal Regulations for emergency landing conditions, crashworthiness is regulated by the requirement that the vertical acceleration should not exceed 20 [G] at a vertical impact speed of 9.144 [m/s] [113]. In order to simulate this, the procedure described in 'Preliminary design and analysis of crashworthy structures for a long-range eVTOL aircraft' [111] is used. The aircraft and landing gear systems are modelled as shown on Figure 8.15.

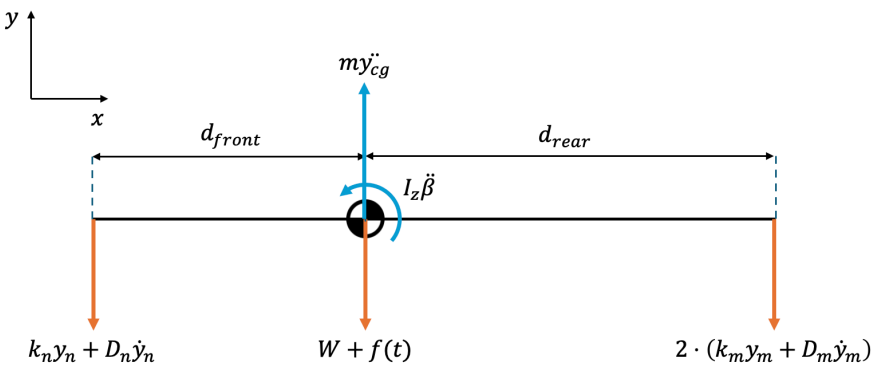

Figure 8.15: *Aircraft and landing gear system free body and kinetic diagram*

where k_n, D_n, d_{front}, and k_m, D_m, d_{rear}, are the spring constant, damping coefficient, and distance from the center of gravity of the nose and main landing gears, respectively. Furthermore, m is the maximum take-off mass of the aircraft with W as the corresponding weight, I_z is the mass moment of inertia of the aircraft about the z-axis, $f(t)$ is the impact forcing function approximated as a dirac delta function, β is the angular displacement, and y_n, y_m, y_{cg} are the vertical displacements (compressions and extensions) of the landing gear struts and the center of gravity. Based on the previously determined landing gear positions, the distances are $d_{front} = 2.23$ [m] and $d_{rear} = 0.8$. Additionally, note that the point at which the impact force $f(t)$ acts can be toggled between the front gear, center of gravity, and rear gear by simply adding $f(t)$ at a different location.

The stiffness and damping parameters k_n, D_n, k_m, D_m must be found first. For a beam with cross-sectional area A, Young's Modulus E, and initial length l, the spring constant k is given by $\frac{A \cdot E}{l}$. Applying values calculated previously and considering that the nose and main landing gears have identical struts yields $k_n = k_m = 2.18$ [GN/m]. Similarly, the damping coefficient of a beam with spring constant k and damping ratio ζ pushing a mass m is $D = 2\zeta \cdot \sqrt{c \cdot m}$. For continuous metal structures like the landing gear strut, the damping ratio is roughly $\zeta = 0.03$ [114]. Substituting values gives $D_n = D_m = 115$ [kNs/m].

Now, the system in Figure 8.15 is converted into a state-space model in Python. It was found that for an initial impact speed of 9.144 [m/s], as set by the Code of Federal Regulations, the acceleration post-impact drastically exceeds the limit of 20 [G]. That is, the landing gear alone poorly controls the impact. However, this is expected because the spring constants and damping ratios for the struts are exceedingly large. Such large values will cause the system to return to its natural state very quickly, causing an extremely large acceleration, which is fatal. Therefore, an additional energy-absorbing structure with a relatively low spring constant and damping coefficient is added on top of each landing gear in series to greatly reduce the effective stiffness. A similar approach was done in 'Preliminary design and analysis of crashworthy structures for a long-range eVTOL aircraft' [111], where it was found that aramid composite honeycomb structures are suitable for such applications. FIBERMAX produces these structures with Young's Modulus of 127.553 [MPa] [115]. Assuming the honeycomb structures have a shape of 1.0x0.1x0.1 [m], the spring constant and damping ratios become 64 [MPa] and 1500 [Ns/m] respectively. With these aramid honeycomb composite structures placed in series above each landing gear, the response of the aircraft's center of gravity to a 9.144 [m/s] vertical impact is shown in the following figure.

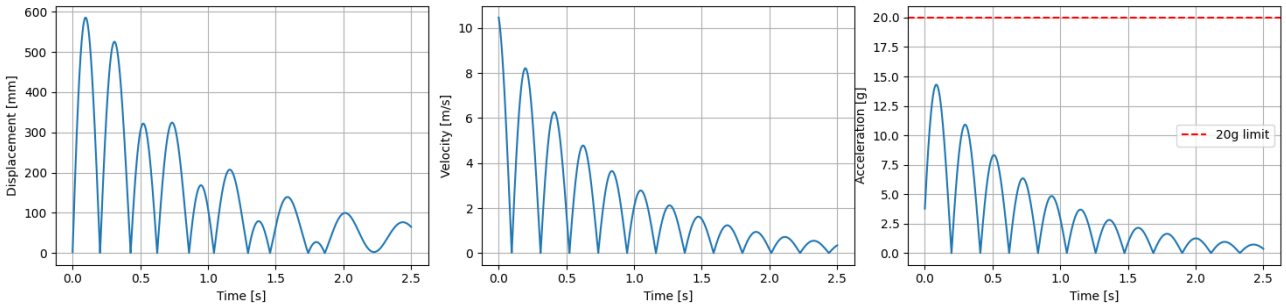

Figure 8.16: *Vertical response magnitudes of aircraft landing gear system at CG with applied impulse at CG*

Clearly, from Figure 8.16 it can be seen that at a vertical impact speed of 9.144 [m/s], the passengers would endure a maximum acceleration slightly below 15 [G]. Because this is under the 20 [G] limit, these analyses confirm the validity of the proposed landing gear design as a crash-worthy structure. Finally, the landing gear mass is estimated based on empirical relations and the following formula [116],

$$m_{LG} = k_{LG} \cdot (A_{LG} + B_{LG} \cdot m_{MTOW}^{\frac{3}{4}} + C_{LG} \cdot m_{MTOW} + D_{LG} \cdot m_{MTOW}^{\frac{3}{2}}) \tag{8.17}$$

where m_{LG} is the mass of the nose or main landing gear (both), k_{LG} is 1.08 for high wing aircraft, A_{LG} is 18.1 and 9.1, B_{LG} is 0.131 and 0.0, C_{LG} is 0.0190 and 0.0031, D_{LG} is $2.23 \cdot 10^{-5}$ and 0.0, for retractable main and landing gears respectively, and MTOW is the maximum take-off weight of the aircraft [116]. Substituting in all the numbers gives a total landing gear system mass of 103.5 [kg].

8.6. Verification and Validation

This section outlines the verification and validation processes applied to the structural analysis methods.

Verification

The Python code developed for the structural assessment of the design was verified through unit testing. The tests aimed to confirm the correct implementation of geometric property calculations, internal load determination, stress analysis using the `sectionproperties` library, and analytical buckling calculations for critical failure modes. A comprehensive list of these unit tests and their outcomes is provided in Appendix E.

Key aspects of the verification included the following:

- **Comparison with Reference Aircraft Data:** The flight envelope calculated was compared with published V-n diagrams for aircraft of similar size and mission profile. This included assessing the general shape of the envelope and the magnitude of limit load factors.
- **Geometric Calculations:** Individual functions for determining local chord lengths, spanwise weight distributions, and cross-sectional properties were tested against hand calculations for simplified geometries and known inputs.
- **Internal Load Determination:** The calculation of spanwise shear force and bending moment diagrams was verified by checking static equilibrium at the wing root and comparing results with analytical solutions for cantilever beams under simplified load distributions.
- **Stress Analysis:** Stress calculations performed by the `sectionproperties` library were implicitly verified by ensuring the library itself is well-tested.
- **Buckling Calculations:** Analytical formulas for critical shear buckling of spar webs (Equation 8.6), compressive/shear buckling of wing skin panels (Equation 8.7), and column buckling of stringers (Equation 8.8) were verified by performing hand calculations.
- **Robustness and Edge Cases:** The code was tested with edge case inputs, such as zero loads, extreme geometric parameters, and evaluations at wing root/tip, to ensure numerical stability and correct handling of boundary conditions.

The overall test coverage for the structural analysis modules achieved a coverage of 98%, indicating a high degree of confidence in the numerical correctness of the implemented code.

Validation

The primary validation for the structural sizing methodology was performed by comparing the obtained stress levels with those expected for similar aerospace structures and loading conditions. Furthermore, the overall structural layout, such as the placement of spars, profile of stringers and their thickness, aligns with standard designs for load-carrying wing structures[102].

8.7. Sensitivity Analysis

To evaluate the sensitivity of the wingbox structural design to initial assumptions, the design load factor and Class I component weight estimates were varied by $\pm$ 5%. Figure 8.17 depicts the change in calculated wing mass due to these variations, with the x-axis representing load factor changes and the y-axis representing changes from initial mass estimates. The results demonstrate that the final wing mass varies by less than approximately 3% from the original value, indicating a low susceptibility of the design outcome to minor changes in these input parameters.

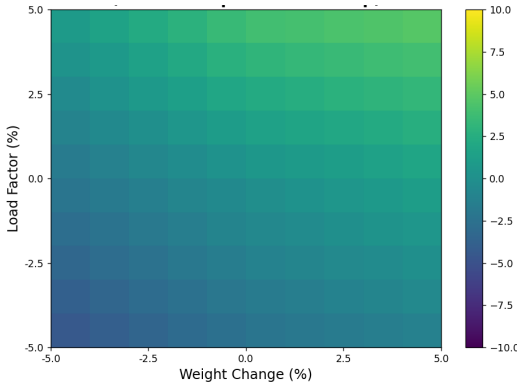

Figure 8.17: *Variation in wing mass with input parameters*

9

Design Iteration

This chapter is a key step in the design procedure, it merges the theory and methods developed in Chapter 5, Chapter 6 and Chapter 8 to achieve a final design configuration. Its results, are then used as input in subsequent design procedures such as in Chapter 10. Firstly, the outline of the iteration loop will be presented, followed by presenting the obtained results along with the main aircraft parameters.

9.1. Iteration Structure

The iteration procedure was applied for the M1 mission or patient rescue mission as this is the most energy critical mission. A part of the design which was not deeply explored in prior chapters is the structural design of the fuselage. This procedure is more elaborate, with complex loading cases, the absence of an equally developed methodology such as for the wing's structural design in Chapter 8 and the limited time frame of the project, meant the mass of the fuselage was instead estimated through an empirical method from [117] given in Equation 9.1. Wherein, l_{fus} is the fuselage length, P_{max} is the maximum perimeter of the fuselage and N_{pas} is the number of passengers. In the final configuration, these values corresponds to 7.2 [m], 5.26 [m] and 3 [passengers].

$$m_{fus} = 14.86 m_{MTOW}^{0.1448} \frac{l_{fus}}{P_{max}} l_{fus}^{0.383} N_{pas}^{0.455} \tag{9.1}$$

The iteration procedure is outlined in a block diagram format as shown in Figure 9.1. It begins with a specified aircraft geometry for which the aerodynamic properties and loads are calculated. It is followed by a mass estimation of the various components, these are then summed and convergence is checked. If the mass is found to be converged, the design is analyzed from a control and stability perspective, if the design is deemed controllable and stable, then the design iteration is finished. If otherwise, design changes are implemented to solve the instability issues, which can affect the geometry of the aircraft and hence required a recalculation of the aerodynamic properties.

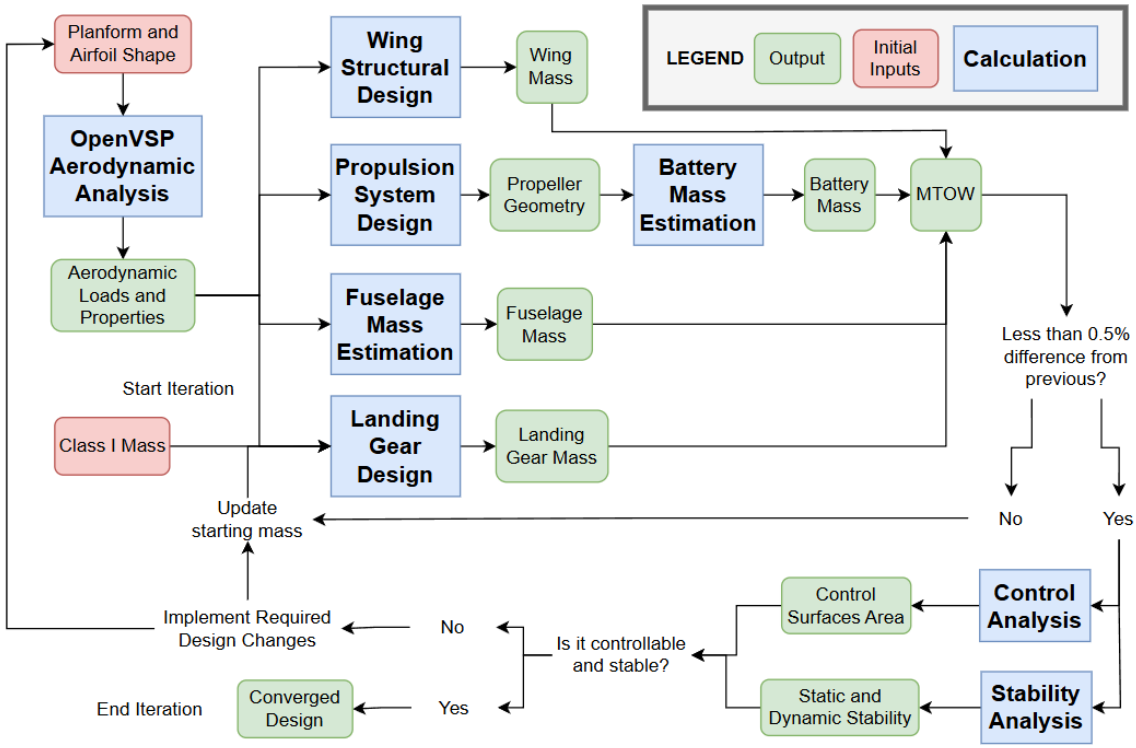

Figure 9.1: *Iteration procedure block diagram.*

9.2. Iteration Results

The iterative process' mass evolution can be viewed in Figure 9.2, showing a quickly converging procedure with just four iterations required for a mass difference threshold of 0.5% between subsequent iterations.

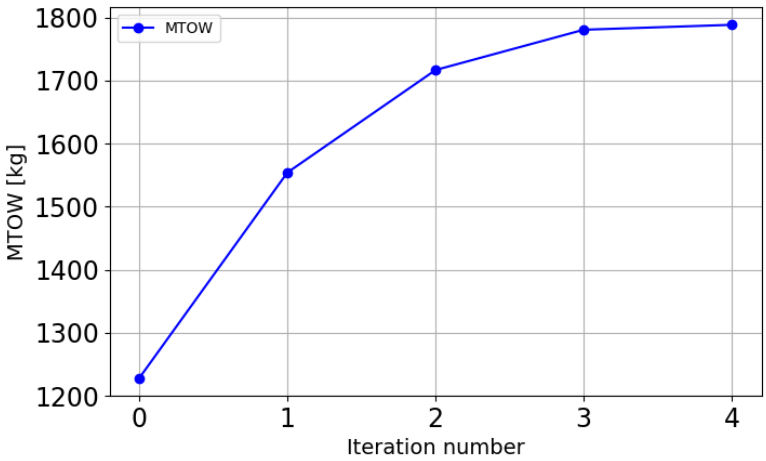

Figure 9.2: *Maximum take-off mass evolution throughout the iteration procedure.*

Selected key aircraft parameters which resulted from this procedure are given in Table 9.1. A more detailed mass breakdown is given in Chapter 16. Finally, a verification of the results for this M1 mission is performed in Chapter 11.

Table 9.1: *Key aircraft parameters after the iteration procedure.*

Variable	Value
Maximum take-off mass (MTOW)	1788 [kg]
Battery mass	727.6 [kg]
Fuselage mass	189.4 [kg]
Wing structural mass	271.8 [kg]
Propulsion system mass	96 [kg]
Landing gear mass	103.5 [kg]
Payload mass	400 [kg]
Total mission energy	212.73 [kWh]
Cruise lift coefficient $C_{L_{cruise}}$	0.2137
Cruise drag coefficient $C_{D_{cruise}}$	0.01432
Cruise angle of attack α_{cruise}	5.526 [°]
Wing skin thickness	3 [mm]
Wing spar flange thickness	4 [mm]
Wing stringer thickness	2 [mm]
Wing spar web thickness	3 [mm]
Wing rib spacing	1.25 [m]
Wing total stringers	4

10

Control and Stability

This chapter covers the control and stability of the aircraft in both hover and cruise. First, the basic assumptions used in the analysis are introduced. Then, the hover control logic is explained, including how the aircraft balances and responds to inputs using distributed thrust. After that, the focus shifts to cruise, where control is handled by aerodynamic surfaces. The surfaces are sized based on the required control authority in both the longitudinal and lateral-directional axes. A static longitudinal analysis is then carried out to ensure that a stable equilibrium in cruise exists and the aircraft can be trimmed properly. To assess dynamic behavior, a state-space model is created using aerodynamic derivatives obtained from OpenVSP and DATCOM. Using this model, the different motion modes of the aircraft are studied, like phugoid, short-period, roll, Dutch roll, and spiral. These are found by looking at the eigenvalues and simulating how the aircraft responds to control inputs. Finally, the results are compared with expected behavior to check if the aircraft reacts in a stable and predictable way, especially in cruise. This forms the basis for verifying that the control surfaces and flight dynamics are acceptable for a safe mission.

10.1. Assumptions

The following assumptions were made to support the aircraft's design, control, and stability analyses.

- **AS-CTRL-1:** The aircraft's aerodynamic effects are considered to be negligible during hover and disturbance analysis.
- **AS-CTRL-2:** Propeller thrust and torque responses are modeled as instantaneous, neglecting motor and actuator dynamics for initial control allocation.
- **AS-CTRL-3:** The aerodynamic lift curve slope of the rudder and elevon control surfaces is assumed to be linear up to the maximum deflection angle of 25 degrees.
- **AS-CTRL-4:** A lift slope of 2π is considered for the rudder.
- **AS-CTRL-5:** During the One-Engine-Inoperative (OEI) analysis, the failed propeller is assumed to create no residual drag or torque.
- **AS-CTRL-6:** For the purposes of the analysis, it is assumed the rudder only produces a yawing moment.
- **AS-CTRL-7:** For the purposes of the analysis, it is assumed the elevons only produce a pitching and rolling moment.
- **AS-STAB-1:** Stability at CG extremes (3.45 m and 3.76 m) is assumed to validate the robustness of the design across the CG envelope.
- **AS-STAB-2:** Due to the unconventional configuration of the aircraft, CFD simulations are assumed to be more suitable than empirical methods.
- **AS-STAB-3:** OpenVSP is assumed to provide sufficiently accurate aerodynamic derivatives for the purpose of dynamic modeling, despite using a simplified panel method.
- **AS-STAB-4:** The aerodynamic center of the aircraft is assumed to coincide with the neutral point, as is the case for flying wings.
- **AS-STAB-5:** The aerodynamic center is located by assuming $C_{m\alpha} = 0$, which implies neutral stability.
- **AS-STAB-6:** A static stability margin of 5% of the aircraft length is assumed to be sufficient to account for CG variation.
- **AS-STAB-7:** The center of gravity for the dynamic analysis is assumed to lie at $x_{CG} = 3.6$ m.
- **AS-STAB-8:** DATCOM-based stability derivatives are assumed to be reliable when OpenVSP data is not available.
- **AS-STAB-9:** Eigenvalues of the $\mathbf{A}$ matrix are assumed to be representative of the real aircraft's dynamic modes.
- **AS-STAB-10:** Step control inputs of 10 [deg] applied for 1 or 2 seconds are assumed to sufficiently excite the dynamic modes for simulation and assessment.

- **AS-STAB-11:** The observed eigenmodes from the simulation are assumed to represent actual aircraft behavior in cruise conditions.
- **AS-STAB-12:** The neutral spiral mode is assumed to be acceptable and consistent with conventional aircraft behavior.
- **AS-STAB-13:** A high $C_{n\beta}$ from the wing design is assumed to be the main contributor to the strong Dutch roll damping observed.
- **AS-STAB-14:** The roll mode not returning to zero is assumed to be acceptable since aircraft typically require pilot intervention to return to wings level.
- **AS-STAB-15:** Combined symmetric and asymmetric control inputs (elevon and rudder) are assumed to give a realistic full dynamic response.
- **AS-STAB-16:** The linearization of aerodynamic coefficients around cruise conditions is assumed valid for small perturbations.
- **AS-STAB-17:** Environmental effects such as wind gusts and turbulence are neglected in the current dynamic stability analysis.
- **AS-STAB-18:** The estimations of hinge moment derivatives for conventional aircraft are assumed to be valid approximations for DoctAir.

10.2. Hover Control

In the vertical flight phase, the DoctAir operates as a hexacopter, with lift and control moments generated exclusively by its six electric propellers. The wings produce negligible aerodynamic forces at low speeds, making a robust attitude and position control system essential. The control objective is to achieve stable hover and precise tracking of position and altitude setpoints, enabling operations in confined spaces. Since the aircraft is designed to be naturally stable in cruise, as demonstrated in Section D.1, active control is most critical during this propulsor-borne flight phase.

Propeller Spin Directions

To determine the propeller spin directions which give the most controllability during hover, the analysis will be based on the available control authority index (ACAI), a figure that describes the degree of controllability (DoC) of a vertical takeoff configuration [118] based on the relative positions of propellers and other inputs such as vehicle mass. A Python code developed by Quan Quan [118] was adapted and used to evaluate the controllability for each propeller spin direction. Furthermore, as given by requirement `REQ-REG-01-SYS-06` and `REQ-REG-01-SYS-07`, the vehicle must retain controllability for all possible cases of engine failure, guaranteeing that it is still possible to reach the intended destination. Hence, this analysis assumes OEI. Because the design has 6 propellers, 3 on either side of the longitudinal body axis, the propeller spin directions analysed are PPPNNN, NPPNNP, PNPNPN, and PPNPNN, where P means positive/clockwise and N means negative/counter-clockwise rotation. The following table indicates the ACAI-based DoC averaged over all six one-engine inoperative failures as a percentage of the max DoC with all engines operational. Moreover, the coefficient of variation is introduced as a metric to measure the configuration's uniformity in controllability [118], for which low values are preferred.

Table 10.1: *The ACAI-based DoC values for different propeller spin directions*

Propeller Spin Directions	Operational all-engine-operative DoC	Average OEI DoC	Variance of DoC	Coefficient of variation of DoC
PPPNNN	10965.1	5972.6 (54.47%)	3590616.8	0.32
NPPNNP	24623.1	8959.0 (36.38%)	20078086.5	0.5
PNPNPN	26524.4	12199.7 (45.99%)	6703689.0	0.21
PPNPNN	23495.2	6177.0 (26.29%)	11591060.3	0.55

It was found that the propeller spin directions corresponding to PNPNPN had the greatest controllability in all OEI and all-engine-operative cases. Furthermore, its low coefficient of variation indicates more consistent controllability under propeller failure scenarios. Overall, using this configuration will maximize passenger safety in the event of propeller failure by retaining sufficient control.

Control Architecture

A cascaded Proportional-Integral-Derivative (PID) control architecture is implemented to manage the aircraft's dynamics. This architecture decouples the control problem into nested loops, allowing for systematic tuning and

robust performance. The structure consists of fast inner loops for attitude rate stabilization and slower outer loops for attitude and position tracking.

Inner Loops: Attitude Rate Control. The fastest loops control the aircraft's angular rates (p, q, r). Their primary function is to provide active damping and rapid response to attitude commands. The controllers take the error between the desired angular rates (p_d, q_d, r_d) and the measured rates (p, q, r) to compute the required control moments (M_x, M_y, M_z). A generic PID rate controller is of the form:

$$M_x(t) = K_{p,p}(p_d - p) + K_{i,p}\int (p_d - p)dt + K_{d,p}\frac{d(p_d - p)}{dt} \tag{10.1}$$

Equivalent controllers are implemented for pitch rate (q) and yaw rate (r).

Outer Loops: Attitude and Position Control. The outer loops provide higher-level command tracking. The attitude controller calculates desired angular rates based on the error between desired attitude $(\phi_d, \theta_d, \psi_d)$ and measured attitude. Similarly, the position controller calculates desired pitch and roll angles based on position error in the horizontal plane (x_e, y_e). The altitude controller generates a collective thrust command $(F_{z,\text{total}})$ based on altitude and vertical velocity error $(z_e, \dot{z}_e)$. For example, the desired roll angle is computed from the lateral position error:

$$\phi_d(t) = K_{p,y}(y_d - y) + K_{i,y}\int (y_d - y)dt + K_{d,y}\frac{d(y_d - y)}{dt} \tag{10.2}$$

Control Allocation Mixer

The control mixer is a critical component that translates the high-level commands from the PID controllers (total thrust $F_{z,\text{total}}$ and control moments M_x, M_y, M_z) into individual thrust commands, T_i, for each of the six propellers. The required thrust for each propeller is then converted to a specific RPM command. The relationship is defined by the geometry of the aircraft and the thrust/torque characteristics of each propeller. The allocation can be represented in matrix form:

$$\begin{bmatrix} F_{z,\text{total}} \\ M_x \\ M_y \\ M_z \end{bmatrix} = \begin{bmatrix} 1 & 1 & 1 & 1 & 1 & 1 \\ l_{y,1} & -l_{y,2} & l_{y,3} & -l_{y,4} & l_{y,5} & -l_{y,6} \\ l_{x,1} & l_{x,2} & l_{x,3} & l_{x,4} & -l_{x,5} & -l_{x,6} \\ k_{T,1} & -k_{T,2} & -k_{T,3} & k_{T,4} & k_{T,5} & -k_{T,6} \end{bmatrix} \begin{bmatrix} T_1 \\ T_2 \\ T_3 \\ T_4 \\ T_5 \\ T_6 \end{bmatrix} \tag{10.3}$$

where l_x and l_y are the lever arms of each propeller from the center of gravity, and k_T is the thrust-to-torque coefficient, with its sign determined by the propeller's direction of rotation. The individual thrust commands T_i are found by taking the pseudo-inverse of the allocation matrix.

Hover Performance and Disturbance Rejection

The effectiveness of the hover control system is demonstrated through simulation. Figure 10.1 shows the aircraft's response to an initial condition error. The aircraft is initialized at an altitude 10 [m] below the desired setpoint. The altitude controller commands a descent, while the attitude controllers maintain stable roll, pitch, and yaw angles. The plot clearly shows a well-damped response where the aircraft smoothly rejects the initial disturbance and settles at the target altitude without significant overshoot or oscillation, proving the stability and effectiveness of the designed hover control system.

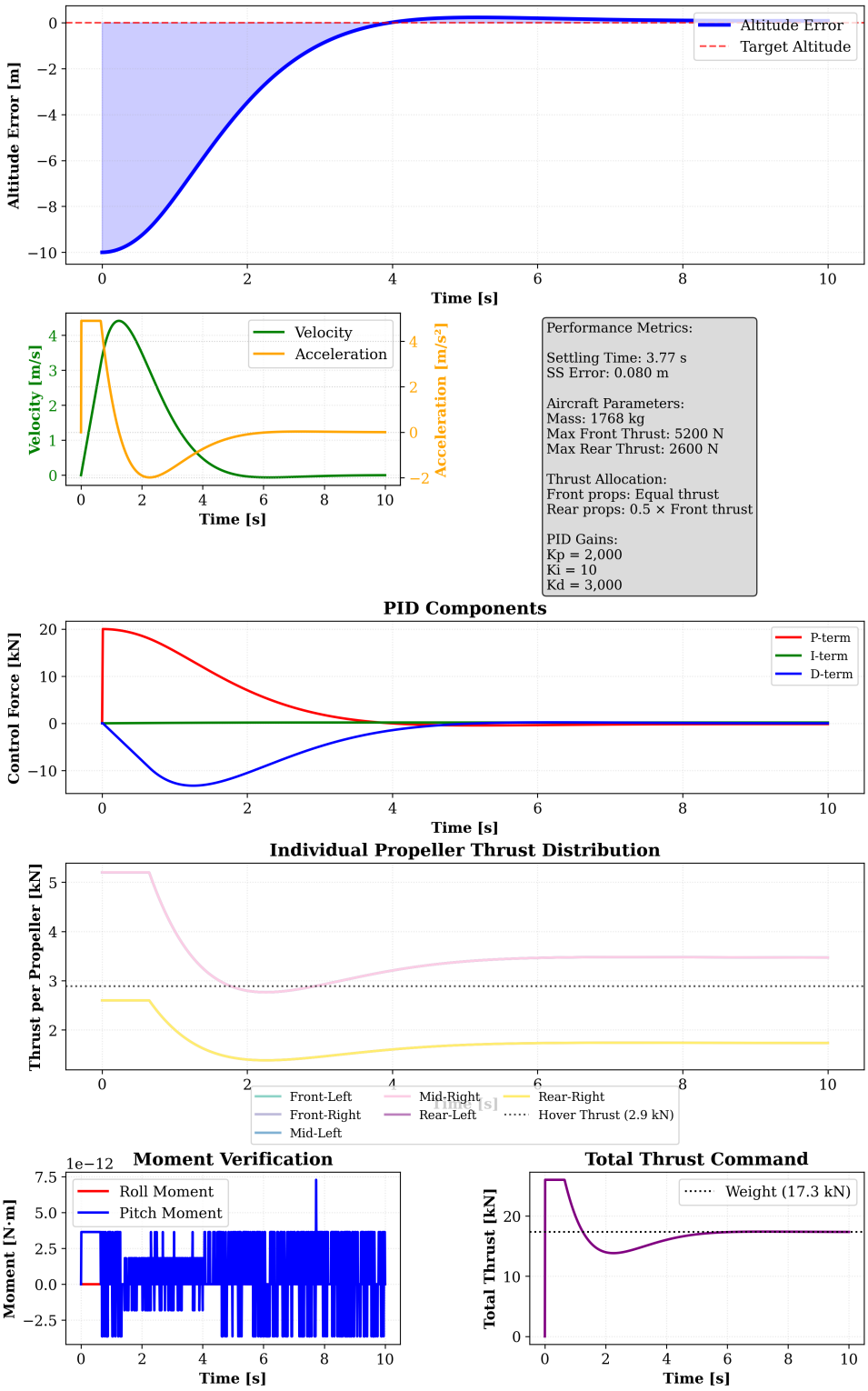

Figure 10.1: *Altitude and attitude response to an initial 10m altitude disturbance, demonstrating controller stability in hover.*

The lack of a dedicated control system design for the transition and cruise phases is a deliberate engineering decision for this design stage. As demonstrated in Section D.1, the DoctAir is designed with inherent static and dynamic stability in its cruise configuration. This natural stability significantly reduces the reliance on complex active control systems for safe flight, simplifying the overall architecture. While a production aircraft would feature autopilot and stability augmentation systems for workload reduction and handling quality enhancement, the fundamental safety and controllability in cruise are ensured by the aerodynamic design itself. Hover, being an inherently unstable flight regime, necessitates the active control system detailed here.

10.3. Control Surface Sizing for Cruise Flight

With the DoctAir designed for controllability in hover, the next critical task is the sizing of its aerodynamic control surfaces before conducting a stability analysis for the other phases. This process ensures the aircraft possesses sufficient control authority to perform required maneuvers and, most importantly, to maintain controlled flight during critical failure scenarios. The primary control surfaces for the cruise phase are the two elevons for pitch and roll, and the twin wingtip rudders (analyzed as a single equivalent surface) for yaw. The sizing methodology is based on meeting a set of defined performance and safety requirements, with the One Engine Inoperative (OEI) condition being the principal design driver for the rudder.

Sizing Requirements and Methodology

The sizing process is driven by ensuring that the moments generated by the control surfaces are sufficient to overcome the moments required for maneuvers or induced by failures, with an adequate safety margin. The core requirements for sizing are:

- **Pitch Authority:** The elevons must generate enough pitching moment to execute a specified pitch maneuver, such as achieving a 10° angle of attack change within one second at minimum cruise speed. This ensures agility for obstacle avoidance and flight path correction.
- **Roll Authority:** The elevons, deflected differentially, must provide sufficient rolling moment to achieve a 30° bank angle within three seconds, enabling standard rate turns and lateral maneuvering.
- **Yaw Authority (OEI):** This is the most critical requirement for the rudder. In the event of a single cruise engine failure, the rudder must generate enough yawing moment to counteract the asymmetric thrust and maintain straight, controlled flight. The sizing is based on using no more than 80% of the maximum rudder deflection to provide a margin for the pilot or autopilot.

A grid-search optimization was performed, iterating through a range of possible surface sizes to find the minimal dimensions that satisfy all defined requirements across the flight envelope. A hefty safety margin of 2 was applied for this sizing. This is to account for various aspects that cannot be taken into account in a simplistic analysis. For example, the wingtip vortices are not taken into account, which could heavily affect the effectiveness of the rudders.

Elevon Sizing for Pitch and Roll Control

The elevons are sized to meet both longitudinal and lateral maneuverability requirements. The primary sizing condition is typically pitch authority at low cruise speeds, where dynamic pressure is lowest. The analysis confirmed that elevons with a span-wise length of **1.50 [m]** each, representing 33.3% of the semi-span and an affected area of **3.05 [m^2]** each, provide the necessary control power.

Figure 10.2 illustrates the sizing trade-off, plotting available pitch and roll moments against the elevon's span-wise length. The selected length clearly exceeds the required moment for both pitch and roll maneuvers, providing a robust safety margin. The maximum deflection is set to **±25.0°**, with an actuator time constant of **0.1 [s]** to simulate real-life behavior. The plot demonstrates that while pitch authority is the driving constraint, the sized elevons also possess ample roll authority.

Rudder Sizing for OEI and Yaw Control

The rudder's primary function is to provide directional control, with its size being dictated by the most demanding yaw control scenario: a one-engine-inoperative event at low speed and high power. The OEI condition produces a significant yawing moment ($M_{z,OEI}$) due to the asymmetric thrust from the remaining cruise propeller. The rudder must be large enough to generate an equal and opposite moment to maintain aircraft control.

The analysis determined a required total rudder area of **1.20 [m²]** (0.60 [m²] per wingtip rudder). Similarly to the elevons, Figure 10.3 illustrates the sizing trade-off. Figure 10.4 presents the core of this analysis. It plots the yawing moment induced by OEI against the counteracting moment available from the rudder at various airspeeds. The plot confirms that the selected rudder area provides sufficient authority to overcome the OEI moment at the critical minimum control speed (V_{mc}) and across the entire cruise envelope. The rudder's maximum deflection is set to **±25.0°**, with a time constant of **0.15 [s]**.

Verification of Control Authority Envelope

With the control surfaces sized, a final verification confirms that sufficient control margins exist across all critical flight conditions. Figure 10.5 provides a summary of the safety margins for key scenarios, defined as the percentage by which available control authority exceeds the required authority. The results show that all critical design requirements are met with margins that exceed the minimum design target. This sizing ensures that the DoctAir is fully controllable during both nominal and emergency flight conditions in the cruise phase. However,

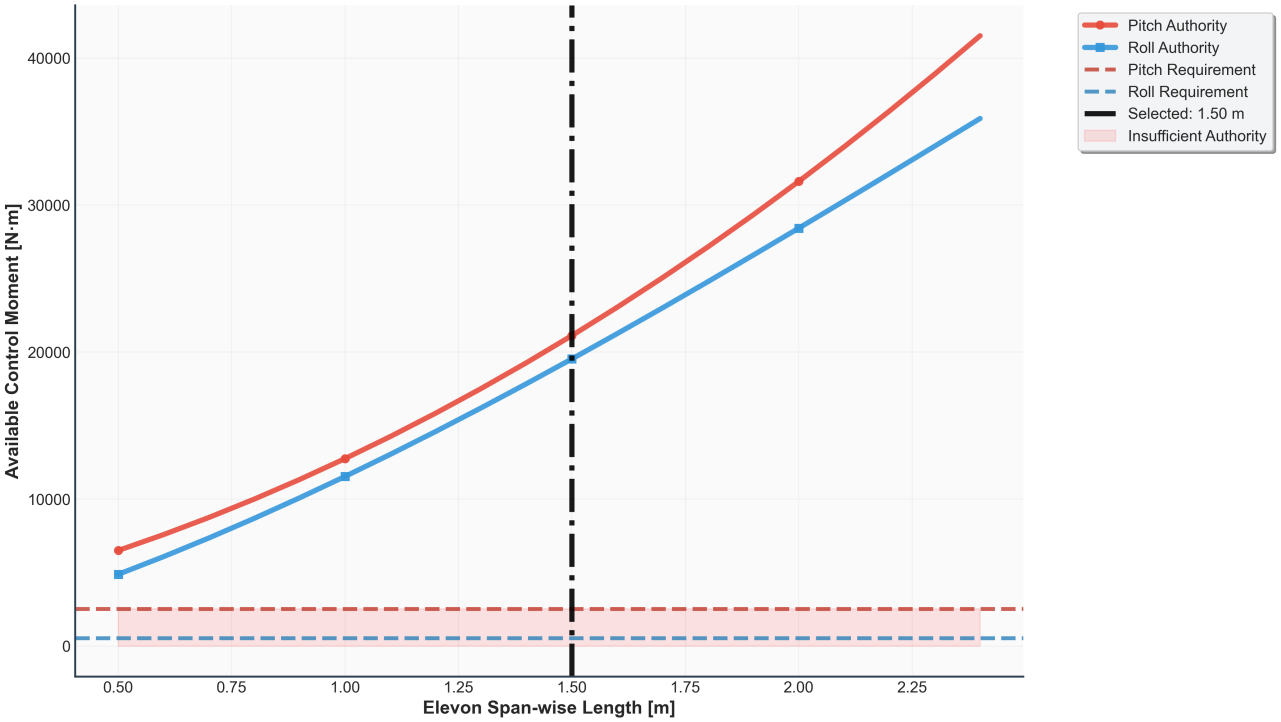

Figure 10.2: *Elevon sizing sweep, showing available pitch and roll authority versus elevon span-wise length. The selected size (vertical line) meets all maneuverability requirements with a significant margin. (Gust Margin not included in plot)*

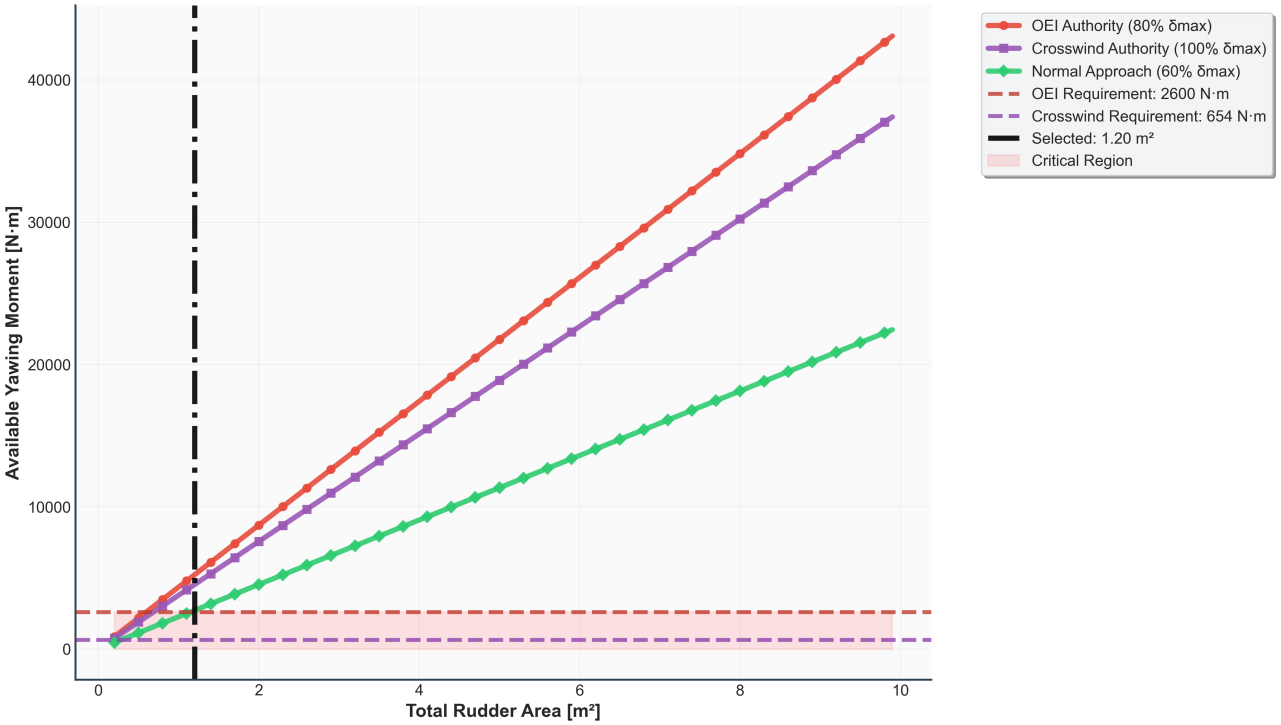

Figure 10.3: *Rudder sizing sweep, showing available control authority versus rudder area. The selected size (vertical line) meets all maneuverability requirements with a significant margin.*

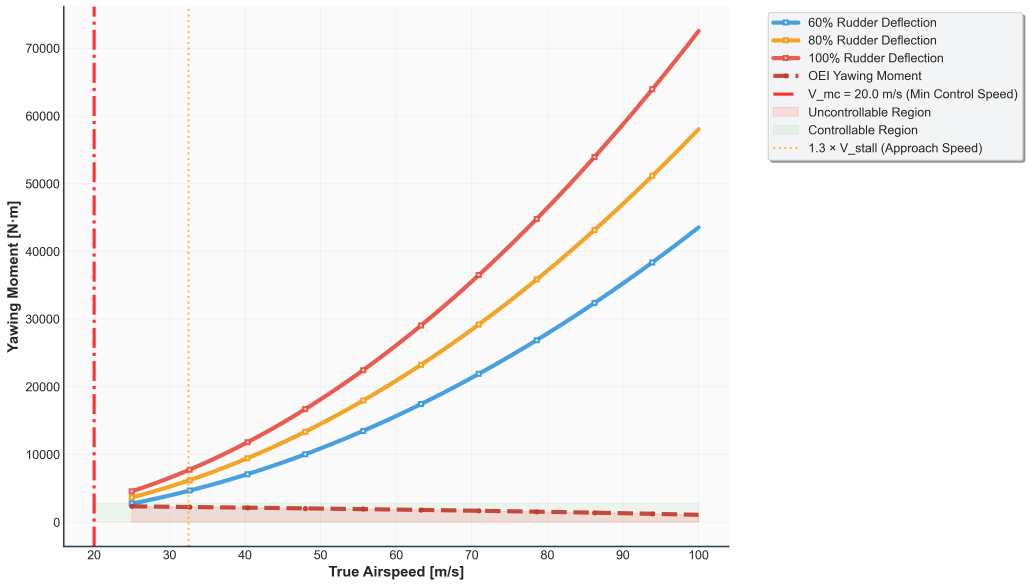

Figure 10.4: *One Engine Inoperative (OEI) analysis. The plot shows the required yawing moment to counteract asymmetric thrust versus the available authority from the sized rudder at different deflection levels. The intersection determines the minimum control speed (V_{mc}).*

it does not guarantee natural stability, which will be further analyzed in the coming sections.

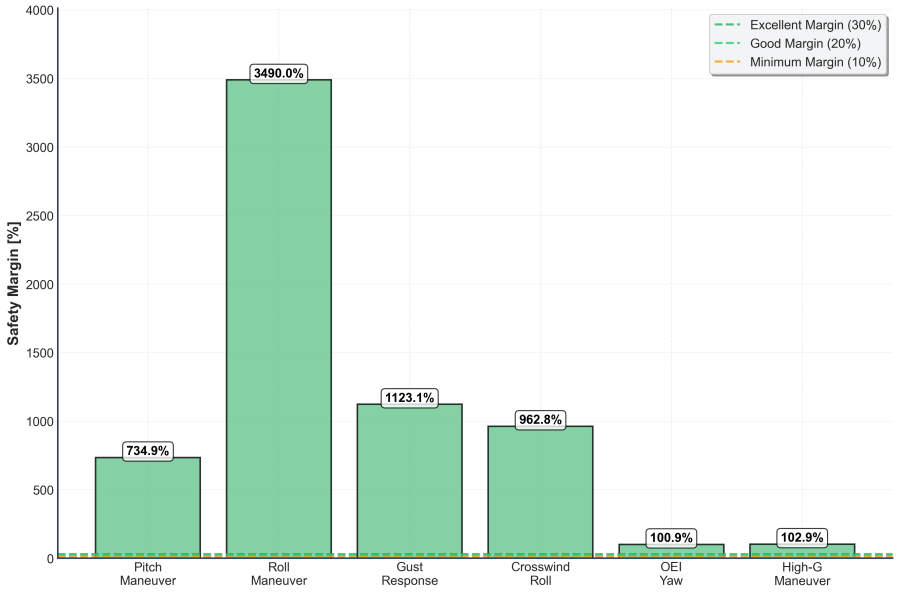

Figure 10.5: *Summary of control surface safety margins for critical flight scenarios, verifying that available control authority exceeds requirements by at least a factor of 2.*

10.4. Assessment of Longitudinal Static Stability in Cruise

In this section, the static longitudinal stability of the aircraft is analyzed. First, the conditions for stick-fixed and stick-free stability are presented. The estimation of the hinge moments and control power necessary for stability evaluation is described in Appendix C. The results of the analysis and the design implications are then discussed.

Stick Fixed Static Longitudinal Stability Conditions

Suppose the aircraft in steady flight with no moment around the center of gravity, $C_m = 0$, experiences a disturbance that causes its angle of attack to increase. A stable aircraft would respond to this disturbance with a restoring negative C_m, which would cause the angle of attack to decrease back to equilibrium. Hence, the change in the moment coefficient with respect to the angle of attack, C_{m_α}, has to be negative. Considering Equation 10.4, which gives the moment coefficient for a tailless aircraft, the static longitudinal stability condition becomes Equation 10.5.

$$C_m = C_{m_{ac}} + C_N \frac{x_{cg} - x_{ac}}{\bar{c}} \tag{10.4}$$

$$C_{m_\alpha} = C_{N_\alpha} \frac{x_{cg} - x_{ac}}{\bar{c}} < 0 \tag{10.5}$$

Here, C_{m_α} is the pitching moment slope and C_N is the normal force coefficient. Since the normal force increases for increasing angles of attack before stall, i.e., $C_{N_\alpha} > 0$, the stability implies that the center of gravity has to lie ahead of the aerodynamic center of the wing, that is,

$$x_{cg} < x_{ac}. \tag{10.6}$$

Furthermore, looking at Equation 10.4, a stable equilibrium, i.e. $C_m = 0$, for positive values of C_N can only exist if $C_{m_{ac}}$, the pitching moment about the aerodynamic center, is positive, so the second condition states,

$$C_{m_{ac}} > 0. \tag{10.7}$$

Another aspect of static longitudinal stability is the elevon trim curve, which represents the required elevon deflection angle to maintain a specific angle of attack or velocity and dictates the stick position stability of the aircraft. Elevon deflection required for equilibrium as a function of the angle of attack is given by Equation 10.8.

$$\delta_e = -\frac{1}{C_{m_{\delta_e}}}[C_{m_0} + C_{m_\alpha}(\alpha - \alpha_0)] \tag{10.8}$$

Here, C_{m_0} is the pitching moment at zero lift, $C_{m_{\delta_e}}$ is the elevon control power, α is the actual angle of attack, and α_0 is the zero-lift angle of attack. This can be rewritten using vertical equilibrium, $C_N \approx C_{N_\alpha}(\alpha - \alpha_0) \approx \frac{W}{\frac{1}{2}\rho V^2 S}$, to obtain the elevon deflection for equilibrium as a function of velocity as shown by Equation 10.9.

$$\delta_e = -\frac{1}{C_{m_{\delta_e}}} \left(C_{m_0} + \frac{C_{m_\alpha}}{C_{N_\alpha}} \frac{W}{\frac{1}{2}\rho V^2 S} \right) \tag{10.9}$$

Firstly, the slope of the $\delta_e - \alpha$ curve has to be negative. This ensures that a downward elevon deflection decreases the angle of attack and pitches the aircraft down. Secondly, the slope of the $\delta_e - V$ curve has to be positive, which prevents a complex sequence of control inputs needed to alter the trim speed. Using the previously stated trim curve equations, the conditions for elevon stick position stability become,

$$\frac{d\delta_e}{d\alpha} = -\frac{C_{m_\alpha}}{C_{m_{\delta_e}}} < 0 \tag{10.10}$$

and,

$$\frac{d\delta_e}{dV} = \frac{4W}{\rho V^3 S} \frac{1}{C_{m_{\delta_e}}} \frac{C_{m_\alpha}}{C_{N_\alpha}} > 0. \tag{10.11}$$

Satisfying these conditions leads to an aircraft that is controlled easily and intuitively by the pilot.

Stick Free Static Longitudinal Stability Conditions

In the previous section, the static stability under the assumption that the pilot is holding the control stick fixed was discussed. To ensure safe operation and elevon stick force stability, it is also necessary to consider the stick-free condition. Assuming that the hinge moment of the elevon is free, $H_e = 0$, and considering that DoctAir does not have a separate trim tab gives Equation 10.12.

$$C_{h_{e_{free}}} = C_{h_\alpha}\alpha + C_{h_\delta}\delta_{e_{free}} = 0 \tag{10.12}$$

The elevon deflection is then given by Equation 10.13.

$$\delta_{e_{free}} = -\frac{C_{h_\alpha}}{C_{h_\delta}}\alpha \tag{10.13}$$

The sign of the hinge moment derivative due to angle of attack, C_{h_α}, can be positive or negative, however the hinge moment derivative due to control surface deflection, C_{h_δ}, has to be negative to ensure that the control surface returns to its equilibrium position following a disturbance.

The stick-free stability criterion for tailless aircraft as derived by H.V. de Castro [119] is given by Equation 10.14.

$$(C_{m_\alpha})_{free} = C_{m_\alpha} + C_{m_{\delta_e}} \left(\frac{d\delta_e}{d\alpha} \right)_{free} = C_{m_\alpha} - C_{m_{\delta_e}} \frac{C_{h_\alpha}}{C_{h_\delta}} < 0 \tag{10.14}$$

Results From Static Analysis and Design Implications

With the stability criteria defined, the three-dimensional hinge moments and the control power are estimated using Roskam as described in Appendix C. The stability criteria that are not satisfied are then identified and the design parameters are adjusted accordingly. The design parameters that can be altered at this stage of the design are the elevon dimensions (keeping in mind the pitch authority requirements as mentioned in Section 10.3), airfoil, and positioning, as well as the hinge line sweep. This process is iterated to converge to a design that is longitudinally stable and controllable.

The key stability parameters of the converged design are highlighted in Table 10.2. DoctAir is stick fixed longitudinally stable as long as the center of gravity is not aft of **3.752 [m]**, with a 5% margin implemented. The trim curves are shown in Figure 10.6, following the convention of plotting negative elevon deflections up, and possess the correct signs of the gradients for stick position stability. In cruise, the trimmed angle of attack is approximately 6 [deg] with an elevon deflection of 2 [deg]. Stick free stability criteria are also satisfied, as seen by the correct signs of the hinge moment derivatives and the negative C_{m_α}.

To achieve these stability characteristics, the elevons have been assigned the **NACA 0009 airfoil** and up-sized to **2.75 [m]** width each. The hinge line is at the quarter-chord of the elevon, has a **16 [deg]** sweep, and lies approximately parallel to the rear spar which facilitates practical implementation. It is important to note that since empirical estimations were used in the process of the stability analysis, there is a degree of uncertainty to the calculated values. It is imperative that a sub-scale model is developed and wind tunnel tests carried out to calculate better approximations of the stability characteristics.

Table 10.2: *Longitudinal stability parameters of the converged design*

Property	Description	Value	Unit
$x_{cg_{max}}$	Aftmost limit for the center of gravity	3.752	m
$C_{m_{ac}}$	Moment coefficient about the aerodynamic center	0.020	-
$\frac{d\delta_e}{d\alpha}$	Slope of the $\delta_e - \alpha$	-0.399	-
$\frac{d\delta_e}{dV}$	Slope of the $\delta_e - V$	8.940×10^{-4}	rad/m^2
C_{h_α}	Hinge moment derivative due to angle of attack	1.210	rad^{-1}
C_{h_δ}	Hinge moment derivative due to elevon deflection	-0.1012	rad^{-1}
$C_{m_{\delta_e}}$	Elevon control power	-0.2731	rad^{-1}
$(C_{m_\alpha})_{free}$	Pitch moment derivative due to angle of attack with stick free	-3.376	rad^{-1}

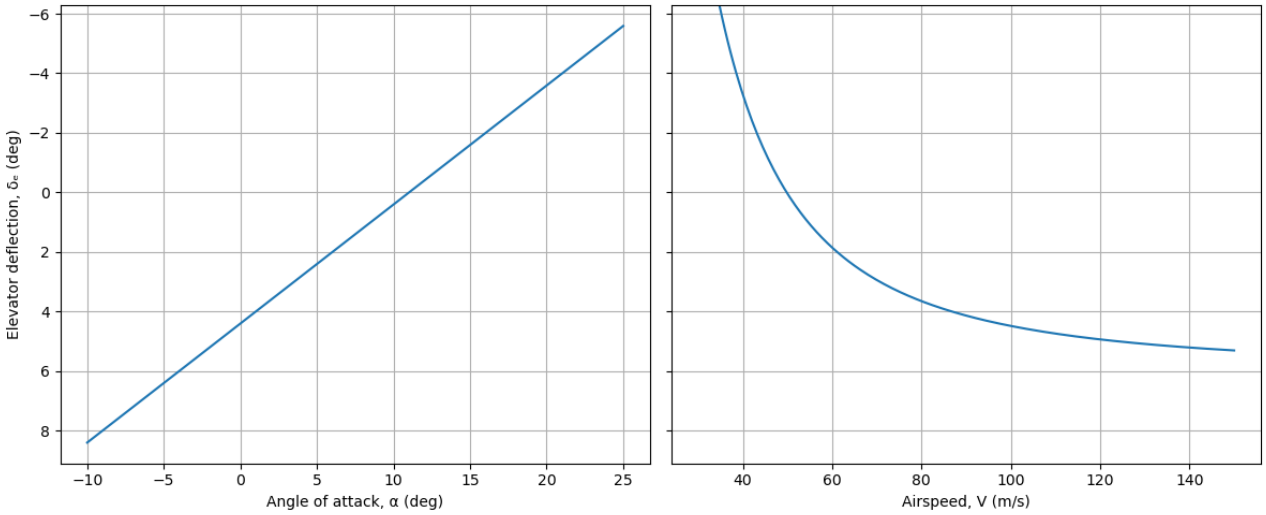

Figure 10.6: *Trim curves of the converged design.*

10.5. Assessment of Dynamic Stability in Cruise

The assessment of dynamic stability is conducted by proposing a method for modeling the aircraft dynamics, which involves the use of a state-space system, as shown in Appendix D. The state space is then modeled using

the MATLAB control module on Python [120]. The behavior of the aircraft can then be assessed by analyzing the eigenvalues, as well as the response to inputs on the control surfaces.

Acquisition of Stability and Control Derivatives

The process of obtaining the aircraft's stability and control derivatives involves using computational fluid dynamics (CFD) simulations and empirical formulae. However, due to the unconventional configuration of the aircraft, CFD was opted for as opposed to empirical formulae. Many software programs are available; however, OpenVSP [59] was chosen due to its ability to run quick simulations using the panel method. The parameters are found through using a linearization of the aerodynamic coefficients with respect to various flight parameters. Additionally, the stability and control derivatives that were not attainable using OpenVSP are found using DATCOM [121] methods. The parameters found in the state space are summarized below, in Table 10.3[1]. It is important to note that the position of the neutral point, which coincides with the aerodynamic center for flying wings, is located using OpenVSP. The process involved trial and error, where the position for which the pitching moment derivative with respect to angle of attack, $C_{m\alpha}$, is null. The position of the aerodynamic center from the front datum set at the tip of the nose is hence

$$x_{ac} = 3.95[m], \tag{10.15}$$

which serves as the point at which the center of gravity would lie for neutral stability of the aircraft. Now, to stabilize the aircraft, the aerodynamic center needs to lie to the rear of the center of gravity. An additional stability margin should also be added to ensure that discrepancies in center of gravity calculations can be accounted for. With a stability margin of two percent of the total length of the aircraft, the CG excursion goes from 3.45 [m] to 3.8 [m]. For the purposes of the dynamic stability analysis, a center of gravity position is assumed to be at 3.6 [m].

Table 10.3: *State-space model parameters for aircraft dynamics*

Parameter	Abbreviation	Value	Obtained From
Flight Condition Parameters			
Cruise Speed	V	61.111	Mission
Mean Aerodynamic Chord	c	3.9655	Aircraft Parameter
Wingspan	b	9.0	Aircraft Parameter
Mass / Inertia Parameters			
Non-Dimensional Mass	μ	8.5774	Aircraft Parameter
Non-Dimensional Pitch Inertia	K_Y^2	0.30724	Aircraft Parameter
Non-Dimensional Roll Inertia	K_X^2	0.03825	Aircraft Parameter
Non-Dimensional Yaw Inertia	K_Z^2	0.08881	Aircraft Parameter
Non-Dimensional Inertia Cross Term	K_{XZ}	-0.003565	Aircraft Parameter
Longitudinal Stability Derivative Coefficients			
Thrust Derivative (forward speed)	C_{TXu}	-0.012	OpenVSP
X-Force Derivative (angle of attack)	$C_{X\alpha}$	-0.1157	OpenVSP
X-Force Offset	C_{X0}	-0.012	OpenVSP
Z-Force Offset	C_{Z0}	-0.05	OpenVSP
Z-Force Derivative (forward speed)	C_{Zu}	0.0	OpenVSP
Z-Force Derivative (angle of attack)	$C_{Z\alpha}$	-1.23	OpenVSP
Z-Force Derivative (pitch rate)	C_{Zq}	-3.5655e-05	DATCOM
Z-Force Derivative (angle of attack rate)	$C_{Z\dot{\alpha}}$	0.0	OpenVSP
Pitch Moment Derivative (forward speed)	C_{Mu}	0.025	OpenVSP
Pitch Moment Derivative (angle of attack)	$C_{M\alpha}$	-0.1091	OpenVSP
Pitch Moment Derivative (pitch rate)	C_{Mq}	-5.3482e-06	DATCOM

Continued on next page

[1]Note that the derivatives shown in Table 10.3 are normalized versions of the aerodynamic coefficients.

Parameter	Abbreviation	Value	Obtained From
Pitch Moment Derivative (angle of attack rate)	$C_{M\dot{\alpha}}$	0.0	OpenVSP
X-Force Derivative (elevon deflection)	$C_{X\delta_e}$	-6.6667e-08	DATCOM
Z-Force Derivative (elevon deflection)	$C_{Z\delta_e}$	-0.05495	DATCOM
Pitch Moment Derivative (elevon deflection)	$C_{M\delta_e}$	-0.04157	DATCOM
Lateral-Directional Stability Derivative Coefficients			
Side Force Derivative (sideslip)	$C_{Y\beta}$	-0.03106	OpenVSP
Side Force Derivative (roll rate)	C_{Yp}	0.59560	DATCOM
Side Force Derivative (yaw rate)	C_{Yr}	-0.15003	DATCOM
Side Force Derivative (rudder deflection)	$C_{Y\delta_r}$	0.18316	DATCOM
Rolling Moment Offset	C_{l0}	0.0	OpenVSP
Rolling Moment Derivative (sideslip)	$C_{l\beta}$	0.01561	OpenVSP
Rolling Moment Derivative (roll rate)	C_{lp}	-0.4991	DATCOM
Rolling Moment Derivative (yaw rate)	C_{lr}	0.15327	DATCOM
Rolling Moment Derivative (aileron deflection)	$C_{l\delta_a}$	0.45683	DATCOM
Rolling Moment Derivative (rudder deflection)	$C_{l\delta_r}$	0.00356	DATCOM
Yawing Moment Derivative (sideslip)	$C_{n\beta}$	0.00803	OpenVSP
Yawing Moment Derivative (roll rate)	C_{np}	0.04020	DATCOM
Yawing Moment Derivative (yaw rate)	C_{nr}	-0.08366	DATCOM
Yawing Moment Derivative (aileron deflection)	$C_{n\delta_a}$	0.02383	DATCOM
Yawing Moment Derivative (rudder deflection)	$C_{n\delta_r}$	0.08140	DATCOM

The parameters in Table 10.3 are input to the state space system, as described in Subsection D.1.1 and Subsection D.1.2, which yields the results found in the subsequent section.

Results From Dynamic Analysis

The dynamics of the aircraft are assessed by simulating the movement, observing several states defined in the output vectors of the state space system, shown in Appendix D. The inputs to the simulation stem from the control inputs; hence, the analysis will be conducted at various control inputs. Nevertheless, the main eigenmodes, namely phugoid, short period, Dutch roll, spiral, and roll modes, can be analyzed by finding the eigenvalues of the **A** in Equation D.1. The eigenmodes are tabulated in Table 10.4,

Table 10.4: *Eigenmodes of the aircraft at $V = 61.11$ m/s*

Mode Type	Mode Name	Eigenvalue(s)	Description
Symmetric Modes			
Symmetric	Short Period	$-0.5551 \pm 2.1453j$	Rapid pitch oscillation; high damping and frequency
Symmetric	Phugoid	$-0.0028 \pm 0.1060j$	Long-period motion; $\zeta = 0.46$, $T = 27.69$ s, $\omega_n = 0.227$ rad/s
Asymmetric Modes			
Asymmetric	Aperiodic Roll	-25.9710	Very fast damping in roll (non-oscillatory)
Asymmetric	Spiral	0.0	Marginally stable spiral divergence (no damping)
Asymmetric	Dutch Roll	$-0.0966 \pm 0.4900j$	Lateral oscillation; moderately damped

Now, these eigenmodes will be clearly visible in the plots from the simulations. The short-period mode is heavily damped, which is consistent with recent research [122]. Moreover, the Phugoid mode is lightly damped, which is desirable [123]. Likewise, with the asymmetric eigenmodes, the eigenvalues seem to make sense. The aperiodic roll mode is heavily damped, which is a desired quality of the aircraft. Curiously, the spiral mode is neutrally stable. Finally, the Dutch roll is quite heavily damped. Now, when applying an elevon step input of 10 [deg] for two seconds, Figure 10.7a is found. Additionally, an aileron input of 10 [deg] for two seconds is simulated, and the plots are shown in Figure 10.7b.

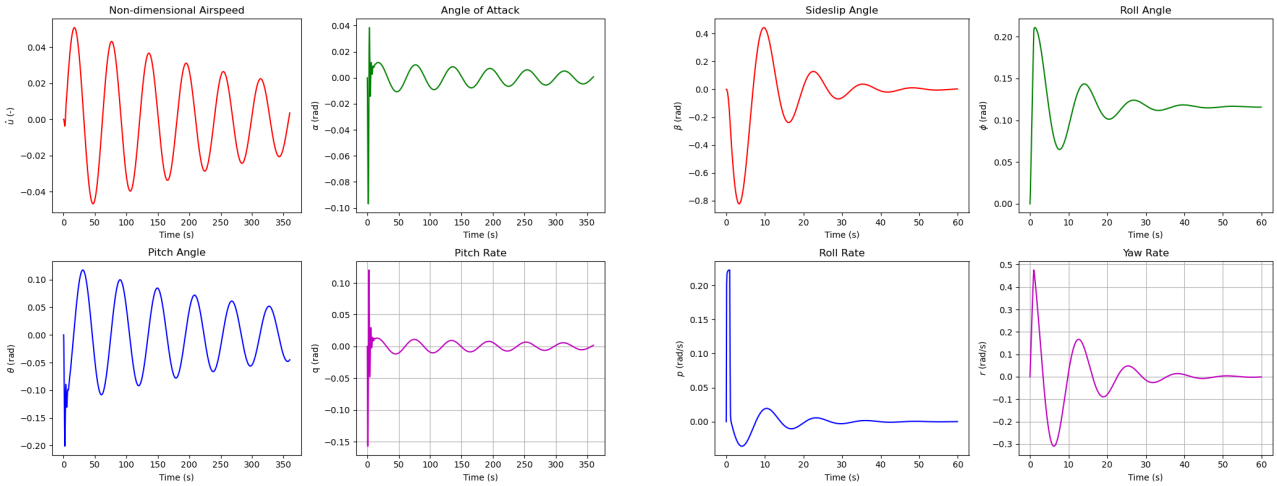

(a) *Symmetric simulation with δ_e of 10 [deg] for 1 [s]*

(b) *Asymmetric simulation with δ_a of 10 [deg] for 1 [s]*

Figure 10.7: *Simulation of state space model.*

Looking at Figure 10.7, it is clear that the aircraft shows stable qualities, both longitudinally and laterally. Now, when the elevon is deflected 10 [deg], as shown in Figure 10.7a, the response is mainly seen in the airspeed and pitch angle. The angle of attack remains nearly constant, as is commonly seen in phugoid motions. Moreover, the period of the phugoid mode is high, which is desirable. Nevertheless, the aircraft is quite clearly stable in the phugoid mode. There is also a clear influence of the short-period eigenmode; however, it is damped out quickly.

When observing Figure 10.7b, the sideslip angle seems to stabilize fast, however, with some oscillation. This is rather normal for aircraft, although the sideslip angle does reach rather extreme values. The high damping can be attributed to the high $C_{n\beta}$, stemming from the large wings providing an adverse yaw. Now, the roll angle does not settle back to 0 [deg] after the control inputs. It does recover to some extent; however, this is quite common for aircraft, as it requires a deliberate control input from the pilot.

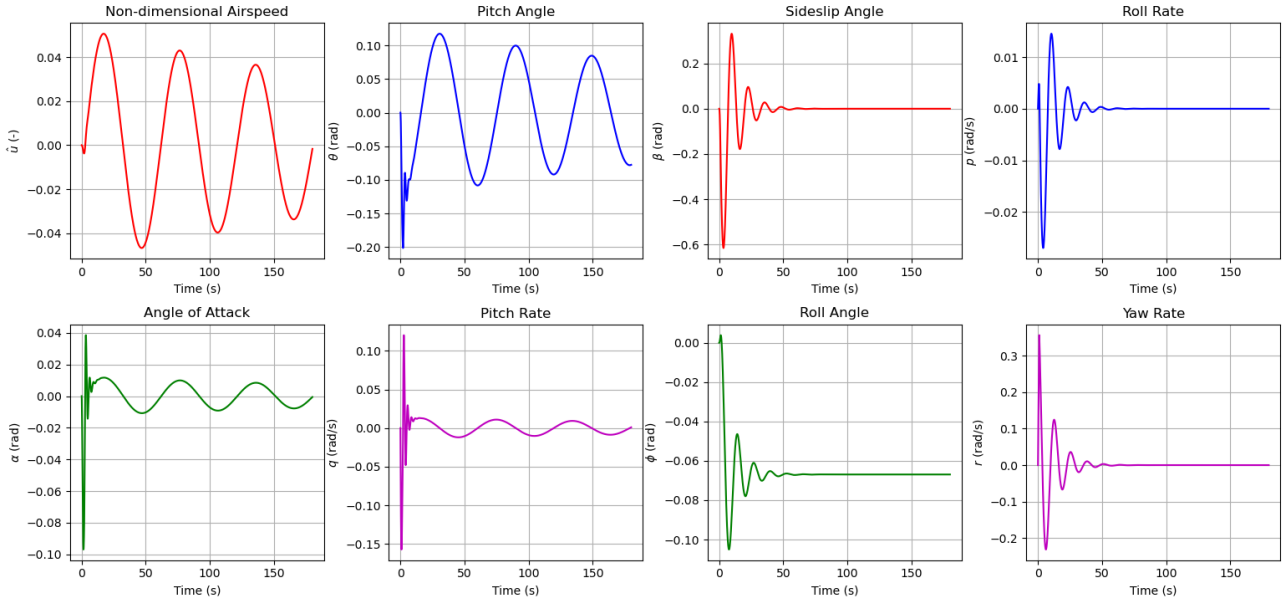

Figure 10.8: *Symmetric and asymmetric simulation with δ_e of 10 [deg] and δ_r of 10 [deg] for 1 [s].*

Figure 10.8 shows the dynamics of the aircraft, both longitudinally and laterally. Combining inputs from the elevons and rudders gives a more concrete picture of the aircraft dynamics. There is a recovery in all modes, other than the roll. Additionally, the extrema of the center of gravity excursion, namely 3.45 [m] and 3.8 [m] from the front datum, were also assessed, and both configurations proved stable.

10.6. Verification and Validation

Verification

The verification of codes used in the assessment of control and stability was conducted using unit tests. The Python code assessing stability takes the stability and control derivatives from OpenVSP [59], as discussed in Section 10.5, and returns the eigenvalues and simulation plots. Now, when it comes to verifying the process, using shifts in the center of gravity (CG) can prove useful. To ensure dynamic stability of the aircraft in question, the CG needs to remain ahead of the aerodynamic center (AC) [121].

Center of Gravity Shift

Essentially, to test the code, the CG will be shifted to the rear of the aerodynamic center, and the new output of the code will be observed. Shifting the CG changed various stability and control derivatives, including $C_{X\alpha}$, $C_{m\alpha}$, $C_{n\beta}$, and $C_{n\delta_r}$, among others. CFD was conducted with this newly shifted CG position, and the results were observed to give an unstable aircraft. The test was hence passed, as the results are proven to be physical and satisfactory.

Validation

Validation of the method for assessing the dynamic stability, as shown in Section D.1, is conducted through making use of reference aircraft to ensure the validity of the model. For this purpose, the parameters, including stability and control derivatives from the Flying V [124], were attained. A simulation was run to compare the recorded data from model flight tests with the simulation output. The experimental and simulated data matched closely, and hence, the model is deemed satisfactory. In addition to this, the use of the Flying V aircraft highlights that the model is indeed compatible with flying wing aircraft, and that the original model from Mulder [125] can be adapted to other aircraft configurations.

Validation Plan

Further validation can be conducted once a scaled model or prototype is constructed. Experimental flight data can be compared to simulated data, which could aid in further tuning stability and control derivatives to match the aircraft dynamics better [125]. Wind tunnels would be the best option to start with, as for now, everything is derived from semi-empirical formulae and CFD analysis.

11

Mission Simulation

Unlike conventional aircraft such as airliners or multi-copters for which well-established design methodologies and sizing techniques exist, the proposed eVTOL configuration is relatively unconventional. This means that although each subsystem, such as the wing, propulsion system, and energy management system, was developed to comply with set mission requirements using consistent parameters, the integrated behavior of the complete vehicle cannot be assumed from these isolated designs alone. Unconventional configurations, such as the design of DoctAir, involve interactions that may not be completely captured by traditional design tools and empirical relations. As a result, the complete vehicle mission simulation becomes a crucial step in validating whether these subsystems work cohesively when operating together. It also provides insights into whether performance targets and requirements are met, and if any over-designs need to be attributed to further iteration. For example, if the remaining energy stored in the battery post-mission is relatively large (contingencies considered), it means that the battery mass could be reduced to achieve a lighter aircraft. This procedure is beneficial from a sustainability point of view as it reduces and optimizes the design's energy consumption and materials. Lastly, a simulation of this fidelity will be useful in verifying a lot of the calculations, values, and properties of the subsystems designed in previous chapters. There are various Python-based open-source mission simulators for eVTOL aircraft. In this case, SUAVE [126], developed by Stanford University, is used.

11.1. SUAVE Setup

Using the subsystems defined from the previous chapters as inputs, an open-source multi-fidelity conceptual design environment and solver developed by Stanford University, SUAVE (Stanford University Aerospace Vehicle Environment), was adapted and used to simulate the performance of DoctAir in the emergency rescue and inter-facility patient transport missions. SUAVE provides versatile tools for analyzing and optimizing both conventional and unconventional aircraft configurations, including eVTOLs, airliners, multicopters, UAVs, and blended wing body aircraft. It functions by dividing a given mission into several control points, each having unknown values for the vehicle's state. Then, using an iterative solver, SUAVE guesses, adjusts, and recalculates the residuals and unknowns until they converge to near zero, combining physical models with empirical relations and numerical methods to achieve accurate results. For the purposes of this design phase, SUAVE was used to simulate complete mission profiles, assess battery conditions and propulsion systems, and identify any opportunities for mass reduction and optimization. It also allows for verifying calculations and values made previously for most of the subsystems. To do this, a simulation code was developed using SUAVE packages, of which the inner workings are shown on Figure 11.1.

It is worth elaborating that SUAVE provides multiple aerodynamic solvers/methods. The team chose to use 'Fidelity Zero' because it has a good balance between computational efficiency and accuracy, making it ideal for use in iteration and conceptual design. The only inaccuracies introduced by this model arise when simulating missions in the transonic regime due to its inability to predict shockwaves, which can be ignored for the mission profile under consideration for DoctAir [3]. Furthermore, Fidelity Zero is a vortex lattice method (VLM) with Mach and drag corrections, and its accuracy has been confirmed by comparing it with experimental data [3], unlike most of the other aerodynamic solvers that SUAVE contains. Fidelity Zero will calculate aerodynamic parameters such as lift and drag coefficients throughout the mission profile, and the results can be used to verify aerodynamic values calculated for the eVTOL in previous chapters. In order to do this, the method requires the vehicle's geometry and mesh settings as input. To save computational time, three chord-wise vortices are used (at least two are needed to capture the flow behavior around the leading and trailing edges of the wing), and six span-wise vortices are used. Increasing the fineness any more would sacrifice computational efficiency. However, the selected mesh fineness was indeed examined for convergence, and it was found that increasing the number of vortices in either direction changes results by no more than $\approx 3\%$, which is reasonable when the computational time is considered, thus justifying the mesh used.

In order to test the limits of the design, the simulation is done under the worst-case operating conditions. Firstly, the most demanding mission in terms of energy consumption and range is the emergency rescue mission, with a maximum cruise range of 110 [km] (one way). In this mission, the vehicle spends a significant amount of time in hover mode, which requires a lot of power. Consequently, the inter-facility patient transfer mission poses a significantly lower challenge and can be considered a trivial case. This is because if the proposed eVTOL

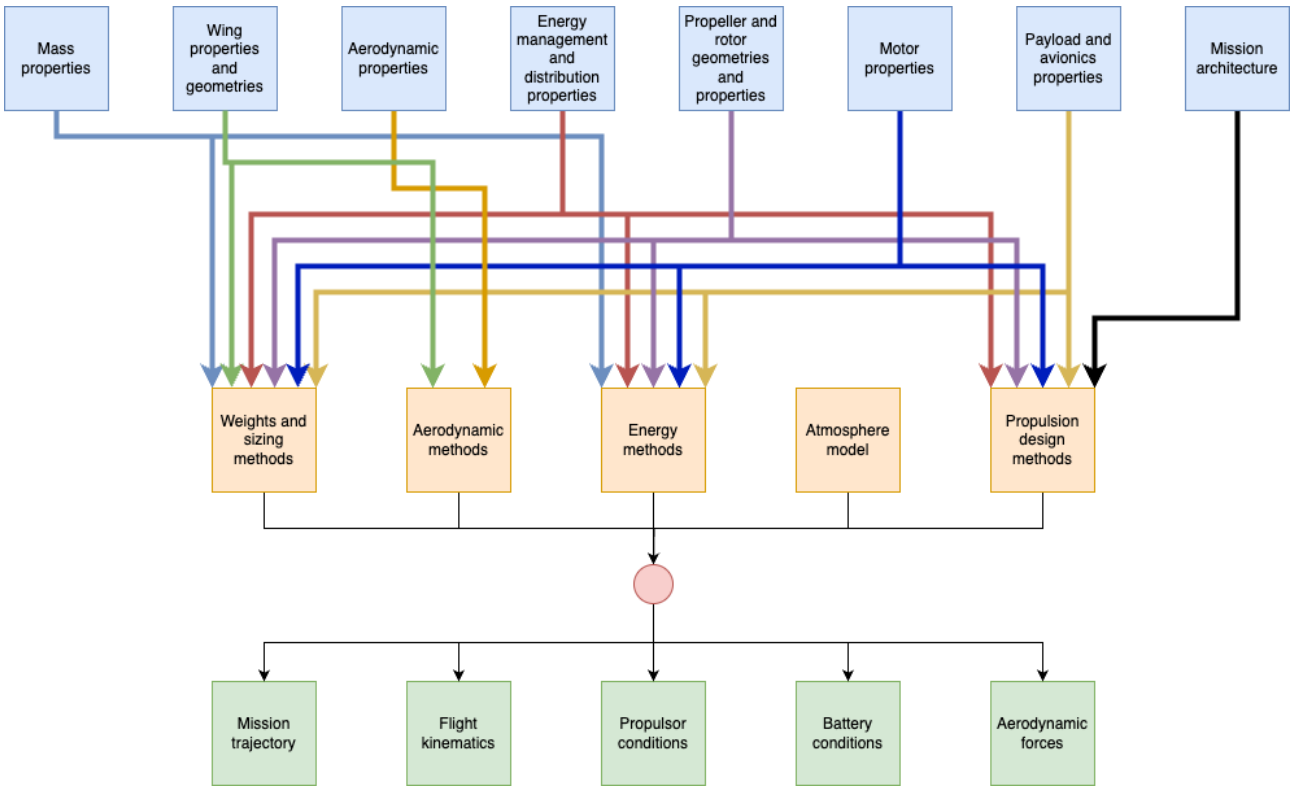

Figure 11.1: *Inputs (blue), analysis methods (orange), outputs (green) of implemented SUAVE simulation.*

design can successfully complete the emergency rescue mission, it will have no difficulty handling the inter-facility patient transfer scenario. Secondly, the mission profiles will be simulated at maximum take-off weight to evaluate energy and propulsion capabilities. Furthermore, in order to simulate as close to real-world operating conditions as possible, the initial battery state of charge will be set to 95% of its full capacity instead of 100%. During the operational life of the vehicle, batteries will not be fully charged before each mission, as frequently charging to full capacity can degrade the battery's health over time. Lastly, the cruise range will be set to 125 [km] (one way) to account for unplanned maneuvers and loiters which often happen in real-world operation.

An important part of the mission is the transition phase between vertical ascent and cruise. In order to begin cruising, the vehicle needs to be able to generate lift from its wings and use the rear two propellers as propulsion. This requires a minimum amount of horizontal velocity. During the transition phase, the vehicle leaves the vertical ascent attitude and starts to pitch down to produce some horizontal velocity. The vehicle now acts as a conventional multi-copter, but of course, attaining the required cruise speed of 61.1 [m/s] would require a large pitch down angle, causing the propellers to drain lots of energy to maintain lift. This is extremely power-consuming and may not even be possible. Instead, the vehicle simply accelerates from 0 [m/s]. Eventually, enough speed is attained for the wings and rear propellers to generate sufficient lift and thrust (potentially, in combination with a slow descent to pick up some more speed and lift). Now, it is worth mentioning that the transition phase can not be explicitly simulated in SUAVE due to the unsteady aerodynamics involved and the change in propulsion from the lift rotors to the rear propellers. This phase involves complex dynamics in thrust distribution and control mechanisms, which are difficult to model accurately within the scope of SUAVE's current release. However, it is still possible to determine what the minimum horizontal velocity required is to initiate the cruising phase, i.e., the velocity at the end of transition. This is the lowest speed at which the wings can generate sufficient lift and the rear propellers can produce sufficient forward thrust to sustain flight. At speeds below this threshold, a higher angle of attack is needed to generate lift, which in turn demands significantly more power from the rear propellers to maintain both lift and acceleration. Due to these propulsion limitations, a minimum viable transition speed naturally emerges and can be found by simply iterating through different initial cruise speeds. The results will be shown in subsequent sections.

11.2. Simulation Results

This section shows and discusses the results from the SUAVE simulation. Several plots are produced but only the relevant ones are shown. Beginning with the mission profile,

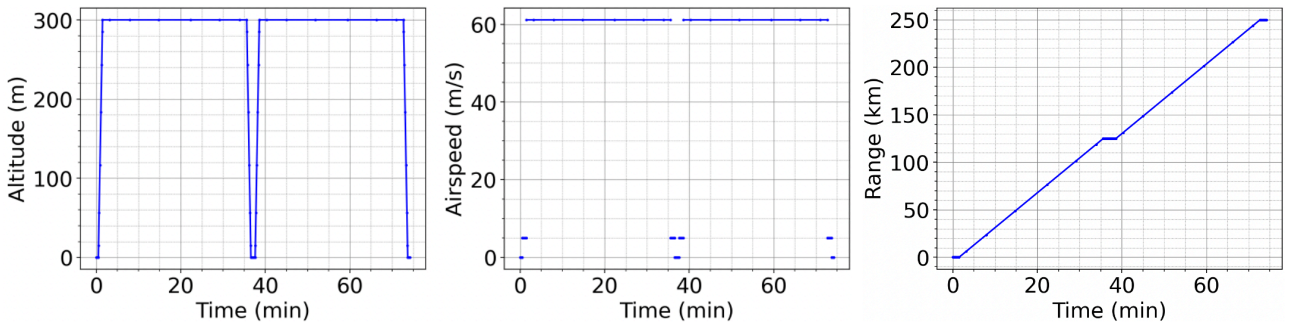

Figure 11.2: *Mission profile inputted into SUAVE*

As indicated by Figure 11.2, the total cruise length is set to 250 [km] (increased by 30 [km] to account for unexpected maneuvers and loiter which often occur in real-world scenarios, testing the limits of the design). Cruise altitude and airspeed is set to 300 [m] and 61.1 [m/s] respectively with a 5 [m/s] climb and descent rate. Next, is a plot of the vehicle. Figure 11.3 shows an isometric view of the vehicle's resulting geometry and mesh inputted to SUAVE. Again, to avoid computational costs yet maintain aerodynamic accuracy, the eVTOL vehicle is inputted as a simplified wing with appropriate wing geometry and NACA0025 and E186 distributions.

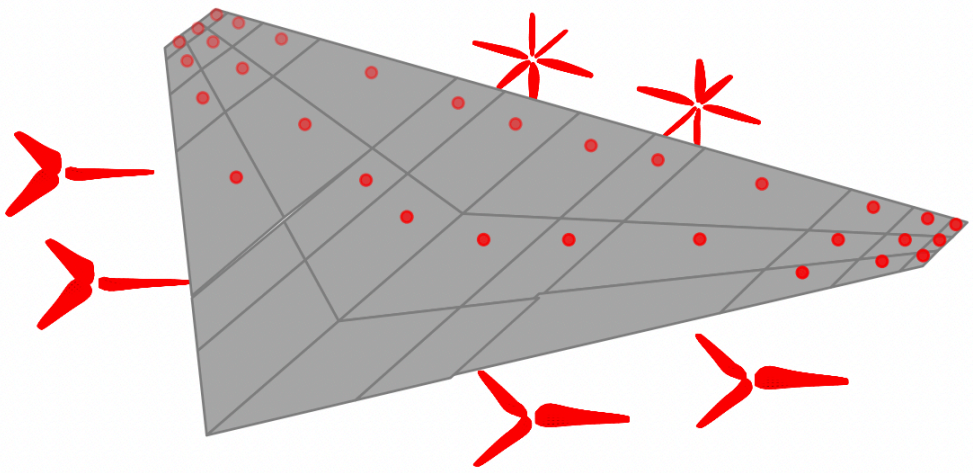

Figure 11.3: *Isometric view of vehicle built in SUAVE*

The reader might question the six blades on the rear propellers, as it should be 4. However, the image represents a combination of how they appear in both cruise and hover configurations, shown together for illustrative purposes. Figure 11.3 above also shows the geometry's mesh, with 3 chord-wise vortices and 6 span-wise vortices on either side. The following figures are aerodynamic plots computed from SUAVE.

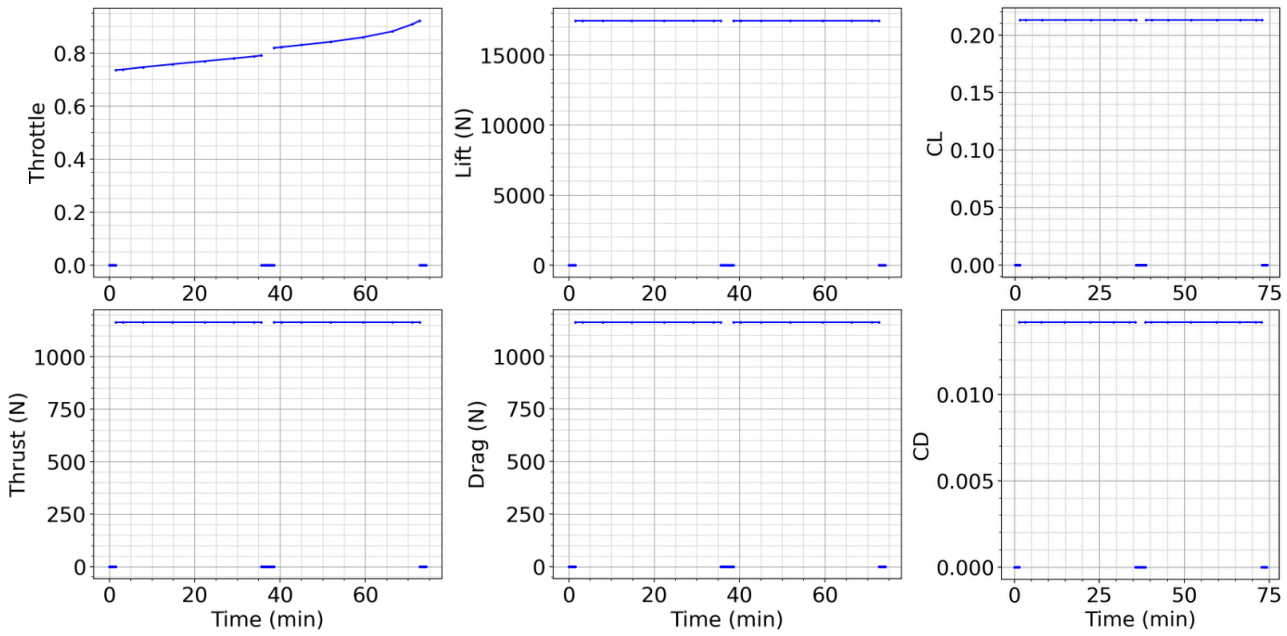

Figure 11.4: *Aerodynamic results from SUAVE as a function of mission time*

Firstly, it is important to check when designing a vehicle that the throttle setting is not larger than 1 at any point, otherwise it means the vehicle is using more power than it has available. From Figure 11.4, it is clear that this is not the case. Moreover, the reason for the throttle increasing throughout the mission is that as the battery drains, the amount of power available to the vehicle reduces as the battery has less voltage (this will be shown later with mission plots for battery pack conditions). As a result, the throttle setting needs to increase to account for the reduced provided power. The parameters in the other plots, namely lift, thrust, drag, C_L, and C_D remain constant throughout the mission, which makes sense because the mass and surface properties of the vehicle are invariant. Lastly, the following table compares aerodynamic coefficients computed through SUAVE's Fidelity Zero with those calculated with OpenVSP in Chapter 5, during cruise flight.

Table 11.1: *Comparison of aerodynamic parameters during cruise flight calculated from SUAVE's Fidelity Zero with OpenVSP's VLM*

Aerodynamic Coefficient	OpenVSP VLM	SUAVE Fidelity Zero
CL	0.2137	0.2130
CD	0.01432	0.01418
L/D	14.9232	15.0284

The accuracy of the results supports the choice of the geometry's mesh, and also validates the aerodynamics properties of the vehicle found in Chapter 5 through OpenVSP's vortex lattice method (VLM). The battery pack conditions are also simulated in SUAVE. Figure 11.5 indicates how relevant parameters vary throughout the mission.

Immediately, it is clear from Figure 11.5 that the hover segments of the mission are the most energy demanding, which is expected. For example, the power consumed during hover is 4-5 times that of cruise. Additionally, even with the state of charge (SOC) initially set at 95%, some battery energy still remains after the mission is complete, showing the capability of the designed battery in Chapter 7. Figure 11.5 also indicates the current supplied by the battery. It is important when simulating this vehicle to ensure the peak current does not exceed the rated current. The peak current can be seen as approximately 1800 [A], and with 107 cells in parallel (see Chapter Chapter 7), the result per cell is 16.82 [A], well below the maximum continuous rated value. Lastly, SUAVE also simulates the temperature of the battery pack through the mission. From Figure 11.5 the cells reach a maximum temperature of 311 [K] = 37.85 [°C] which verifies the result of approximately 37.5 [°C] in Figure 7.5 in Chapter 7. Next, the propeller conditions and propulsion system state is simulated using SUAVE, the results of which are shown on Figure 11.6.

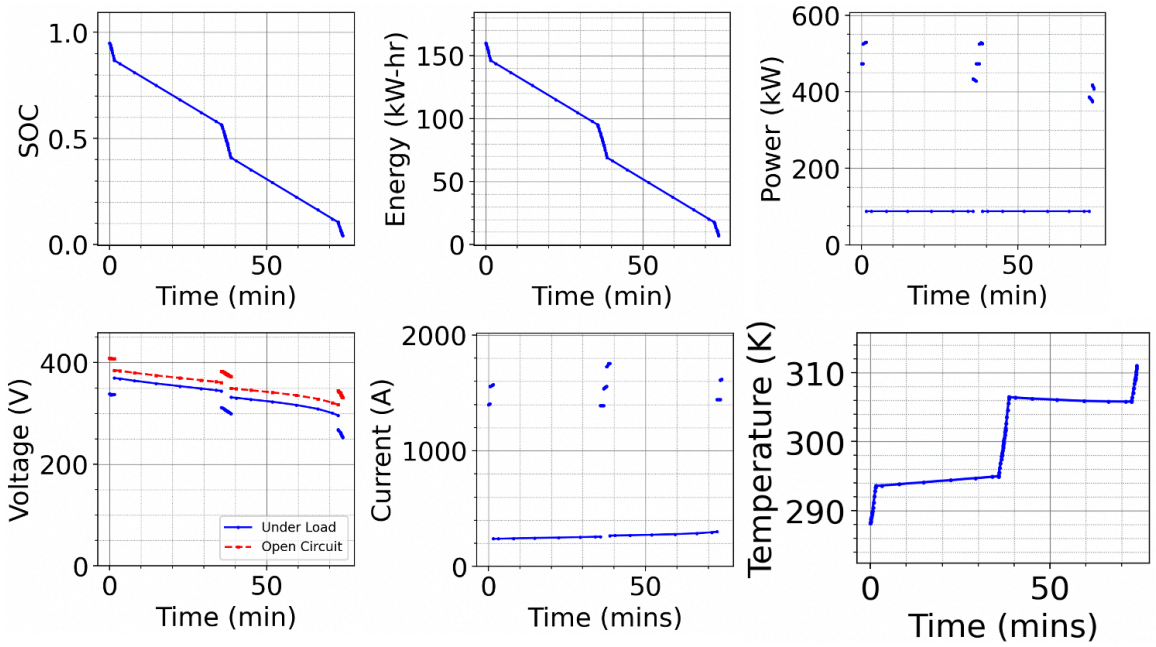

Figure 11.5: *Battery pack condition results from SUAVE as a function of mission time*

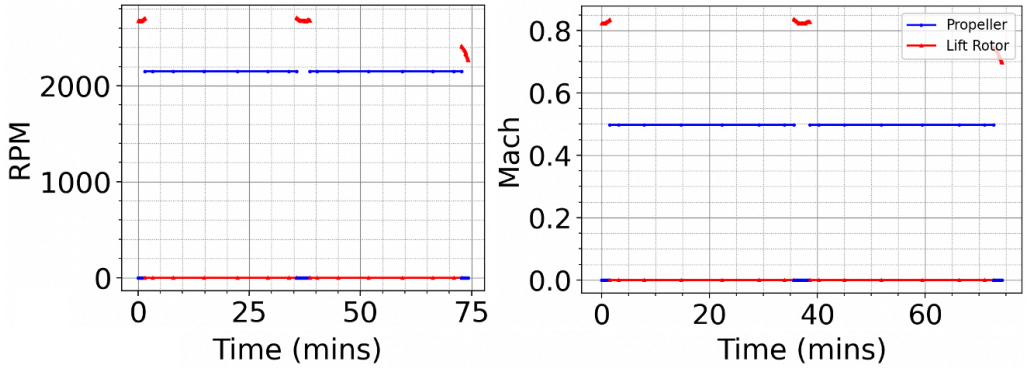

Figure 11.6: *Propeller condition results from SUAVE as a function of mission time. Note: the red and blue lines indicates the performance of the front 4 and rear 2 propellers respectively*

Firstly, from Chapter 6, the design RPM (rotations per minute) for the front four and rear two propellers are 2272 and 3030 respectively. From Figure 11.6 it is clear that the simulated RPMs do not exceed these design specifications. On top of this, generally propellers are able to handle RPMs greater than their design value for short bursts, showing the propulsion system design's capability to handle adverse conditions when necessary. Furthermore, the propellers were designed for a tip mach number of 0.7. From Figure 11.6, the cruise tip mach number never surpasses 0.7 however, SUAVE over-estimates it for the hover phase of the mission. This can be explained by these phases being particularly demanding in terms of thrust.

Finally, an accelerated cruise segment was added before the first cruise phase for the purpose of finding the minimum post-transition speed to avoid stall and remain in the air. By iterating through different speeds, this minimum speed was found to be 36 [m/s] and is attained at a lift coefficient of $C_L = 0.6$ and angle of attack $\alpha = 11°$, still below the maximum (stall). To clarify, this is the speed which the eVTOL needs to achieve in the end of transition by accelerating conventionally in multicopter configuration and/or performing a shallow dive.

12

Sustainability Approach

Integrating sustainable development principles is a core commitment in the design of the vehicle. This chapter details the strategic approach adopted in response to environmental responsibility, operational efficiencies, and specific stakeholder requirements, including achieving zero operational greenhouse gas emissions (REQ-USR-04-SYS-01-PPS-01), incorporating sustainable design principles (REQ-USR-04-MIS-01), and planning for responsible end-of-life management (REQ-EOL-01-SYS-01). The following sections describe how sustainability is considered at different phases of the vehicle's life cycle from design and manufacturing, to operation and end-of-life (EoL).

Design and Manufacturing Phase

The design phase offered the greatest leverage for sustainability. Firstly, lower-impact, durable, and recyclable materials that are suitable for the environment are selected, minimizing hazardous substances and complying with REQ-USR-04-SYS-02. Furthermore, critical items like batteries and composites were planned for recyclability. Secondly, in terms of energy efficiency, aerodynamics analysis and structure design have been optimized for lightweighting. Furthermore, DoctAir has been designed for modularity (battery packs), ease of disassembly (see Section 13.2), and material identification for easy EoL sorting, complying with requirements REQ-MAI-01-SYS-01-STR-01, REQ-EOL-01-SYS-01, REQ-USR-05-MIS-01, and REQ-REG-01-SYS-03.

Several examples of these strategies have been employed throughout the design phase. For example, in the design of the aircraft's structure, the structural mass was optimized to use as little material as possible while still satisfying requirements. In the propulsion chapter, propeller RPMs for the cruise phase was selected based on which one minimizes the power required. In designing the power system, lithium ion batteries were selected which can generally be recycled to extract for lithium, cobalt, manganese. Also, in the aerodynamic analysis, airfoils with the greatest L/D were selected to maximize cruise performance and reduce the required energy. Last but not least, one of the trade-off criteria used in selecting the delta flying wing out of the four other options in Chapter 4 was a sustainability score. This evaluated quantitatively how sustainable a design is, incorporating aspects such as material selection, repairability, modularity, energy efficiency, noise emissions, and circularity. The delta flying wing had the greatest sustainability score out of all four designs. Ultimately, the electric nature of the designed eVTOL completely eliminates greenhouse gas emissions.

As for manufacturing, future considerations include prioritizing partners using renewable energy, selecting processes that minimize waste and energy (REQ-USR-04-SYS-03), and evaluating supply chain logistics for reduced impact, favoring local sourcing where feasible (REQ-USR-04-SYS-03).

Operational and End-of-Life (EoL) Phase

The electric powertrain inherently reduces operational environmental impact. For example, zero direct emissions meets requirement REQ-USR-04-SYS-01-PPS-01. Also, charging is recommended with renewable electricity to operators to maximize overall environmental benefit complying with REQ-USR-04-SYS-04. Furthermore, compliance with REQ-REG-02-SYS-01 and REQ-REG-02-SYS-03 is achieved through quiet propulsion design and optimized mission procedures (first segment of the mission profile consists of a 300 [m] ascent to minimize noise when cruising above populated areas), supporting public acceptance (REQ-PUB-02). Lastly, REQ-MAI-01-SYS-03-CCC-01 is complied with by monitoring the health of subsystems for condition-based maintenance, reducing recourse consumption and favoring repair over replacement.

Responsible EoL management involves identifying components (avionics, motors) with potential for secondary life, plan pathways for major material streams (batteries, composites, metals, e-waste) according to regulations (REQ-EOL-01-SYS-01), and define safe procedures for non-recyclable materials (REQ-EOL-01-SYS-01). Additionally, after 500 cycles, battery degradation prevents full-range missions. However, degraded batteries can be repurposed for short-range missions at dense-area MOBs, extending battery life and reducing e-waste and costs.

All in all, the project contributes positively to sustainable development goals. Improved emergency care access via faster response times targets SDG 3, quieter urban environments comapred to helicopters targets SDG 11, demonstrating advanced air mobility technology for societal benifit targets SDG 9, and zero operational emissions contributions targets SDG 13. A summary of our approach can be found in Table 12.1.

Table 12.1: *Subsystem-level and lifecycle sustainability considerations for DoctAir.*

Department	Key design decisions	Sustainability impact
Aerodynamics	Delta flying wing configuration with high L/D airfoils (E186, NACA0025).	Reduced power requirement during cruise phase, lowering overall mission energy consumption.
Propulsion	Distributed electric propulsion (DEP); optimized three- and four-blade propellers; use of only two rear propellers for cruise.	Zero operational emissions; increased redundancy and safety (OEI); lower noise signature than helicopters; minimized energy use in cruise.
Power	Lithium-ion NMC battery pack sized for mission without need for active cooling; modular battery design.	Reduced system mass and complexity by avoiding cooling hardware; enables battery second-life applications and simpler maintenance, reducing e-waste.
Structures & Materials	Lightweight carbon-fiber composite structure; wingtip rudders double as winglets.	Lower aircraft mass reduces energy consumption; dual-function rudders improve aerodynamic efficiency without additional mass or parts.
Control & Stability	Inherent aerodynamic stability in cruise; OEI control authority via differential thrust and rudder.	Reduced reliance on complex, energy-intensive stability augmentation systems; enhanced operational safety in case of engine failure.
Operations & Logistics	Mission profile optimized for rapid ascent from helipads; use of existing HEMS infrastructure and charging networks.	Minimized noise footprint over populated areas; reduced need for new, dedicated infrastructure, lowering initial investment and environmental disruption.

Phase	Environmental	Social	Financial
Design	Electric powertrain for zero operational emissions; lightweight materials and high L/D configuration to minimize energy use.	Designed for One-Engine-Inoperative (OEI) safety; low-noise propellers for urban acceptance; cabin layout optimized for patient care.	Configuration selected for low operational energy cost; modular battery design lowers long-term replacement cost.
Manufacturing	Use of efficient composite materials to reduce structural weight and material consumption compared to metal airframes.	Design based on established manufacturing processes for composites and standard fasteners, ensuring process reliability.	Lower aircraft weight reduces material costs; high production volumes amortize non-recurring engineering costs.
Assembly, Integration & Testing	Modular design (e.g., battery packs) reduces potential for waste during assembly and allows for easier part replacement.	Use of standard components and linear assembly flow ensures a repeatable and safe integration process.	Simplified powertrain (fewer parts than a turbine) and modularity reduce assembly time and cost.
Operations	Zero in-flight greenhouse gas emissions; energy replenishment from renewable grid sources is possible.	Lower noise footprint than HEMS helicopters; faster response times in congested areas; improved safety via redundancy.	Significantly lower total annual operating cost compared to an EC135; higher potential for 24/7 availability increases asset utilization.
Maintenance & Repair (MRO)	Fewer moving parts in electric powertrain leads to less material waste from routine component replacements.	Simpler systems reduce maintenance complexity and associated risks for ground personnel.	Lower maintenance costs are a primary driver of reduced total cost of ownership; modular parts allow for rapid replacement.
End-of-Life (EoL)	Recyclable battery materials (lithium, cobalt); DfD principles facilitate component separation. Degraded batteries repurposed for short-range missions.	Clear end-of-life plan ensures safe decommissioning and disposal, preventing environmental and public nuisance.	Second-life use of batteries creates residual value from a depreciated asset and defers recycling costs.

13

Production Plan

In this chapter, the production of the DoctAir is elaborated. Section 13.1 demonstrates the manufacturing techniques, and Section 13.2 dives into the assembly of the DoctAir.

13.1. Manufacturing Methods

Section 8.2 discusses the materials used for the wingbox, skin, and fasteners. Furthermore, most of the interior will be made from thermoplastics, and the landing gear will most likely be made from titanium alloys [127]. Each manufacturing technique has a different cost due to the facilities and machinery required. The manufacturing processes for each material are briefly explained below.

To start, the wingbox and skin will be made out of carbon epoxy fibers (see Table 8.2). The process to create carbon epoxy composites involves several critical steps: first, the carbon fibers need to be produced. During this process, the epoxy must be prepared to be used as a resin. Lastly, the fibers and resin are combined using one of the various available techniques. These include, for example, hand lay-up, filament winding, pultrusion, and resin transfer molding (RTM) [128].

Parts that have a constant cross-sectional shape, such as some stiffeners, can be manufactured using pultrusion [128]. This continuous manufacturing process can produce both simple and moderately complex cross-sections, as shown in Figure 13.1a.

For more complex parts, prepreg (pre-impregnated composite fibers) can be used to fabricate high-performance composite structures. In this process, the fiber is passed through a resin solution and calendared to achieve the desired resin content. Afterwards, it is heated to remove the solvent. This method is illustrated in Figure 13.1b. [129]

If even greater precision is needed, resin transfer molding (RTM) can be employed. This method offers tight control over resin content and fiber orientation. It involves injecting resin under pressure into a mold cavity containing dry reinforcements [128]. The process is schematically shown in Figure 13.1c.

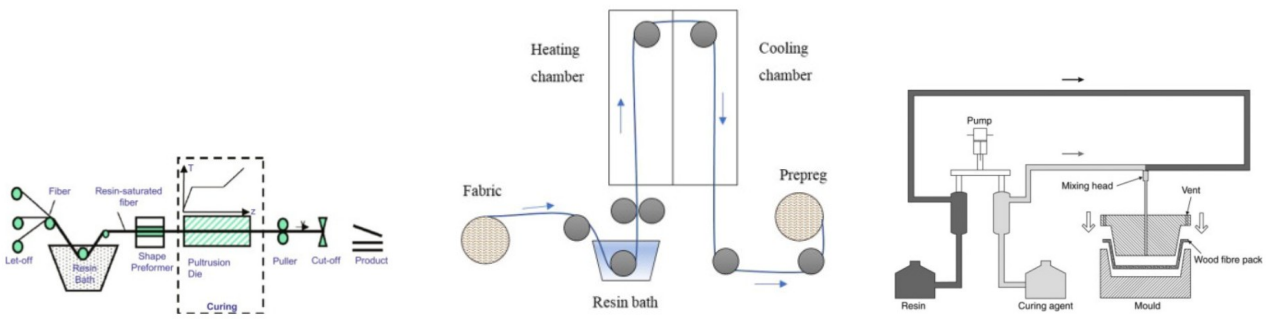

(a) *Pultrusion process [128]*

(b) *Prepreg production [129]*

(c) *Resin Transfer Molding (RTM) [128]*

Figure 13.1: *Composite manufacturing methods: (a) Pultrusion, (b) Prepreg production, (c) Resin Transfer Molding (RTM)*

Furthermore, the fasteners will be made out of titanium (Al-4V) and the landing gear will most likely be made from aluminium alloys. High-performance metal alloy components are generally fabricated by the conventional forging process [130]. However, additive manufacturing (AM) can provide an alternative process to achieve a resource-efficient production [130]. Direct Laser Deposition (DLD) is a good method that can be used to fabricate fasteners directly from metal powders [130]. However, at this stage, DLD is still limited by its productivity, and thus, DLD first needs to be developed further to improve the building rate and reduce cost. Meaning that at this stage, metal forging is used to manufacture the fasteners. The landing gear is manufactured using many closed die forgings. Heat treatment of parts is performed after rough machining to create a higher precision [108].

Lastly, thermoplastics can be extensively used inside the cabin for the furnishing and other parts of the interior. Injection molding is used for producing plastic parts for seats, panels, and other interior components. This

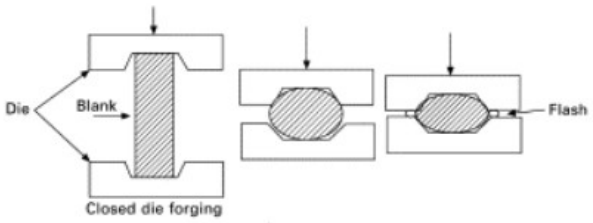

Figure 13.2: *Closed Die Forging [131]*

technology enables low-cost mass production, meaning this is mainly feasible if production of this part is high [132]. However, since production costs decrease with higher volumes, third-party manufacturers can efficiently supply these interior components without significantly increasing overall costs.

13.2. Assembly

Prior to entering the final assembly line, all major components and subsystems of the DoctAir are manufactured—either using methods described in Section 13.1 or through certified suppliers. After quality control of the sub-assemblies is completed, the eVTOL can be fully assembled. In-process inspections are performed at key integration points. The assembly is visualized as a linear flow system.

Assembly line

The design of efficient assembly systems can significantly contribute to the profitability of the products [133]. When a subsystem needs to be fastened, the following sequence must be used [133]: Loading, Drilling, Riveting, Inspecting, and then Unloading. To calculate the minimum number of stations required for each process (loading, drilling, riveting, inspecting) to reach the production of 250 eVTOLs in 5 years, the following equation is used [133]:

$$\text{number of workstations} = \frac{\text{process cycle time}}{\text{takt time}}, \tag{13.1}$$

where takt time is defined as follows:

$$\text{takt time} = \frac{\text{total time available/year}}{\text{number of units required/year}} \tag{13.2}$$

Figure 13.3 presents the assembly flow diagram of the DoctAir drone manufacturing process. First, the primary structure needs to be installed. The wing structures are built, and spars, stringers, and wingbox are integrated. With the airframe joined, primary electrical harnesses and fiber-optic data lines are installed throughout the fuselage and wings. Simultaneously, thermal management is laid out to support battery and motor cooling requirements. Then, the battery packs are installed. These are located in the wings. The batteries are checked before and after assembly to verify voltage.

Subsequently, electric propulsion units are installed—four propulsion systems are located in front of the wing and two at the back. Each propeller includes an electric motor, propeller, and speed controller. Afterwards, the landing gear is assembled. The landing gear is stored in the wing. Retraction tests and emergency deployment simulations are performed as part of the installation validation.

In Stage 6, the avionics and flight control are integrated—for example, the GPS module, data link transceiver, and flight displays. Once every subsystem is installed, all systems—electrical, thermal, propulsion, avionics, and flight control—are integrated and subjected to end-to-end testing.

After successful integration, the vehicle undergoes finishing: exterior surfaces are wrapped and interior components (cockpit interfaces, medical equipment) are fitted. Lastly, the eVTOL is tested, pre-flight checklists are completed, and ground operations checks are performed.

Design for Disassembly (DfD)

Design for Disassembly (DfD) refers to incorporating ease of disassembly into the design process [134]. When a vehicle is designed for disassembly, its sustainability improves, as components can be reused or recycled, reducing overall waste at the end of life. In most cases, disassembling products consumes less energy than grinding and melting materials for recycling [135]. Therefore, DfD must be considered to enable effective recycling at

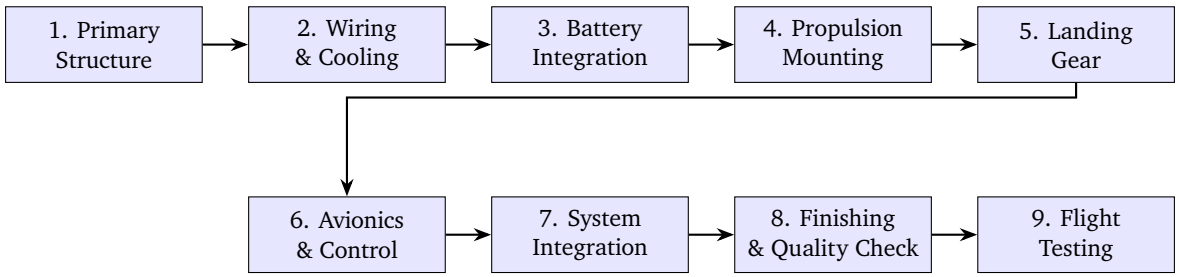

Figure 13.3: *Assembly flow diagram of the DoctAir eVTOL manufacturing process*

the end of a product's lifecycle.

By designing for disassembly, the complexity of the disassembly process is reduced, which saves resources, lowers costs, and promotes circularity [136]. There are five essential steps to follow when designing for disassembly [135]:

- **Use standardized, reversible fasteners:** Fasteners should be easy to remove and compatible with common tools [136].
- **Select materials that can be easily separated and recycled:** Currently, carbon fiber composite is the primary material used in aircraft. When carbon fiber breaks, it is difficult to repair. Also, when the material is disassembled it cannot be easily re-used without recycling, meaning it is not well designed for disassembly. However, it can be recycled using processes such as thermal recycling (e.g., pyrolysis), which uses heat to break down the resin, allowing the carbon fibers to be recovered [137].
- **Enable easy access:** Products should be designed to allow straightforward disassembly using common tools.
- **Incorporate modularity:** Components should be modular, allowing individual parts to be replaced or upgraded. Materials should be easily accessible so that, during the aircraft's life, components can be replaced by those recovered from end-of-life aircraft, without completely disassembling the entire structure.
- **Simulate disassembly:** Disassembly processes should be modeled and optimized during product development. Therefore, disassembly considerations should be fully integrated into the further design phase.

14

Operations & Logistics

14.1. Operational Profile

The operational phase encompasses all activities from mission dispatch to patient delivery. The DoctAir EMS is designed to execute two primary mission profiles: emergency scene response and inter-facility patient transport. While specific timelines differ, the core operational sequence remains consistent, as depicted in Figure 14.1. The mission involves multiple subsystems, including Propulsion (PROP), Crew (CREW), Payload (PAYL), Communications (COMM), Flight Control System (FCS), Ground Operations (GOPS), Energy Storage and Management (ESM), and Avionics (AVIO), each with defined responsibilities throughout the sequence.

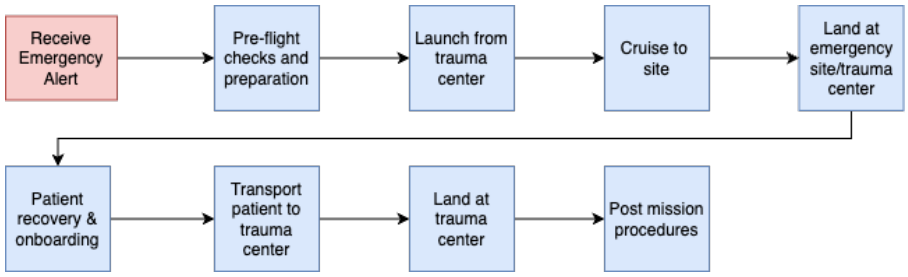

Figure 14.1: *General operational sequence for emergency missions.*

The aircraft is designed for a one-way operational range of $R = 110$ [km]. To estimate the average mission distance, a uniform distribution is assumed for emergency incidents across the circular coverage area. The number of incidents dN in an infinitesimally thin ring (refer to Figure 14.2[1]) at a distance r from the Main Operating Base (MOB) is proportional to the area of that ring, $dA = 2\pi r\, dr$. The average distance, $\bar{r}$, can therefore be found by calculating the centroid of this distribution, which is equivalent to finding the expected value of r:

$$\bar{r} = \frac{\int_0^R r \cdot dN}{\int_0^R dN} = \frac{\int_0^R r \cdot (2\pi r\, dr)}{\int_0^R 2\pi r\, dr} \tag{14.1}$$

Solving the integrals yields:

$$\bar{r} = \frac{2\pi \int_0^R r^2\, dr}{2\pi \int_0^R r\, dr} = \frac{[\frac{1}{3}r^3]_0^R}{[\frac{1}{2}r^2]_0^R} = \frac{\frac{1}{3}R^3}{\frac{1}{2}R^2} = \frac{2}{3}R \tag{14.2}$$

For a maximum range of $R = 110$ [km], the average one-way mission distance is statistically $\frac{2}{3} \times 110 \approx$ **75 [km]**. The flight time for an average one-way mission segment is calculated based on the flight profile: 30[s] hover take-off, 60[s] climb, cruise at 61.1 [m/s] (220 [km/h]), 60[s] descent, and 30[s] hover landing. This results in a one-way flight time of approximately 23.5 [min] for a 75 [km] mission, and a round-trip mission time of approximately 47 [min].

It is critical to note that the average mission distance of 75 [km] represents a deliberately conservative estimate. The calculation's foundational assumption of a single, isolated base with a uniform incident distribution does not reflect the operational reality. Firstly, the VEMS fleet will operate as a network from multiple MOBs, creating overlapping coverage zones (refer to Figure 14.3). The closest available aircraft will always be dispatched, inherently reducing the effective response distance for any given incident. Secondly, the assumption of uniform population density is pessimistic. MOBs will be co-located with major hospitals situated in urban population centers, where a significant majority of emergency calls originate. This heavily skews the statistical distribution of mission distances towards much shorter flights. Consequently, the actual average mission distance is expected to be substantially lower, ensuring the designed operational scenario provides a robust margin for the vast majority of real-world operational scenarios.

[1] Calculate moment of inertia of ring and sphere.: https://vedantu.com

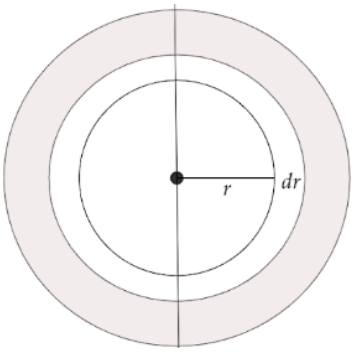

Figure 14.2: *Visualization of an infinitesimally thin ring in a circle.*

Based on UK HEMS operational data, a utilization rate of 10 missions per 24-hour period per aircraft is a reasonable target[2]. For an average round-trip mission time of 47 [min], this equates to approximately **8 flight hours per day**. Given a 20-minute rapid charging turnaround time between missions (`REQ-OPE-01-SYS-07`), the aircraft would spend 3 hours charging, resulting in a total daily operational time of 11 hours. This indicates high asset availability, with sufficient buffer for unscheduled maintenance or contingency.

14.2. Logistics Framework

The logistics framework supports the entire lifecycle of the DoctAir EMS fleet, from manufacturing to deployment and end-of-life management.

Manufacturing and Assembly

The manufacturing strategy balances in-house production with specialized supplier sourcing. A make-versus-buy analysis will determine the most efficient approach for key components like the airframe, propulsion units, and avionics. The blended wing body structure will likely require specialist contractors with experience in composite materials and advanced manufacturing techniques like automated fiber placement (AFP). Assembly, Integration, and Testing (AIT) will be conducted at a central facility, following a phased process: structural assembly, powertrain installation, avionics integration, and finally payload system fit-out, with interface and functional checks at each stage. A Quality Management System (QMS) compliant with aerospace standards will ensure full traceability of components and processes.

Deployment and MRO

Effective deployment hinges on strategic basing, energy replenishment infrastructure, and comprehensive Maintenance, Repair, and Overhaul (MRO) support. Figure 14.3 illustrates the conceptual operational network for the Netherlands.

Basing Strategy. MOBs will be established at locations with existing infrastructure (e.g., HEMS hangars) and proximity to major trauma networks. This minimizes initial investment and leverages existing HEMS airspace corridors. Compatibility with hospital helipads is a core design feature (`REQ-HOS-01-SYS-03`), allowing direct patient transfer at destination facilities. Additionally, since DoctAir is an electric vehicle, it can be refueled anywhere with a charging station. Hence, as the framework becomes more established, the basis shall be expanded to hospitals that have equipped themselves with the appropriate energy replenishment infrastructure.

Energy Replenishment. MOBs will be equipped with rapid charging systems capable of replenishing the aircraft's energy stores within the 20-minute turnaround target.

Ground Support and Personnel. Standardized Ground Support Equipment (GSE), including battery chargers, diagnostic tools, and towing equipment,t will be deployed at each MOB. Personnel training will follow EASA-compliant curricula for pilots (type rating, emergency procedures) and maintenance technicians. Medical crews will receive specialized training on in-flight systems and patient handling specific to the eVTOL platform. Given the aircraft's stark difference from a conventional helicopter, extensive and appropriate training of personnel is essential to the vehicle's success, both in the short and long term.

[2]The Air Ambulance Service UK: https://theairambulanceservice.org.uk/our-work/

Maintenance, Repair, and Overhaul. A two-level maintenance strategy will be employed. Line maintenance (daily checks, minor servicing) will be performed at MOBs. Heavy maintenance and major overhauls will occur at a central MRO facility; this can be at the HEMS MRO facility to minimize overhead costs. The maintenance program will be driven by data from the onboard Health and Usage Monitoring System (HUMS), enabling a shift towards condition-based and predictive maintenance to maximize availability and reduce costs. A logistics plan for critical spare parts will be established to minimize Aircraft on Ground (AOG) time.

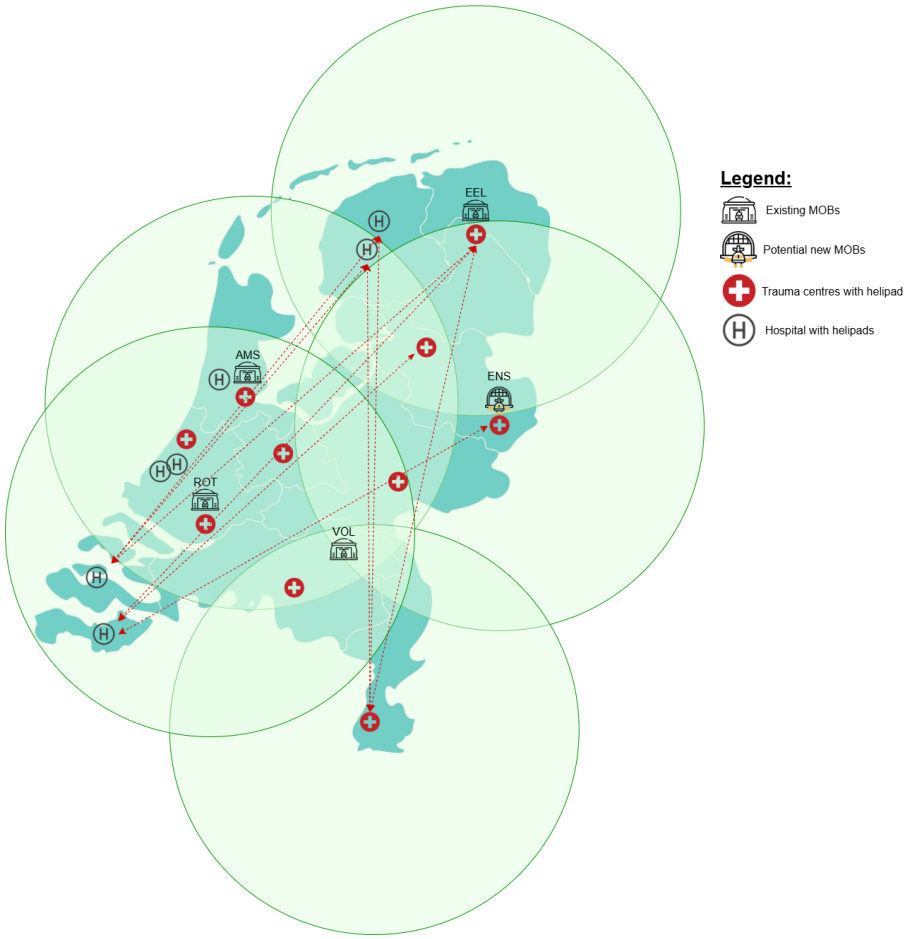

Figure 14.3: *Conceptual operational network for the DoctAir EMS system in the Netherlands.*

End-of-Life (EoL) Management

A responsible EoL strategy is integral to the system's sustainability. The design incorporates Design for Disassembly (DfD) principles, using reversible fasteners and clear material labeling (`REQ-EOL-01-SYS-01`). At the end of the aircraft's service life, a standardized decommissioning process will be followed. High-value components such as avionics and motors will be evaluated for refurbishment and recertification. Materials like composites and battery cells will be segregated and sent to specialized partners for recycling, maximizing material recovery rates (`REQ-USR-04-MIS-01`). Additionally, the number of battery cycles before noticeable degradation is given by the manufacturer to be 500 [cycles]. This implies that the eVTOL cannot perform a full-range mission with the same battery anymore. However, this issue can be planned around by identifying MOBs that regularly perform short-range missions—think about MOBs located in dense areas—and allocating them the degraded batteries. This allows a significant extension in battery lifetime, and in the long run, heavily reduces e-waste and operational costs.

14.3. RAMS Analysis

This section analyzes the Reliability, Availability, Maintainability, and Safety (RAMS) characteristics of the DoctAir to ensure it meets the demanding requirements of EMS.

14.3.1. Reliability

Reliability is the probability that the vehicle and its subsystems will perform their required functions under specified conditions for a given period. It is quantified using the relation:

$$R(t) = e^{-t/\text{MTBF}} \tag{14.3}$$

where t is the operational time interval and MTBF is the Mean Time Between Failure. The time interval t is set to 100 flight hours, a common period for scheduled maintenance inspections.

The reliability of critical subsystems is calculated and presented in Table 14.1. The overall system reliability is the product of these individual values.

Table 14.1: *Reliability of key subsystems for a 100-hour operational period.*

Subsystem	MTBF [hour]	Reliability
GNSS [2x]	60464[3]	0.99835
Barometer [2x]	50000[4]	0.99800
IMU [3x]	10500[5]	0.99052
Vision Camera	40000[6]	0.99750
LiDAR Sensor [6x]	751296[7]	0.99987
Radar	1000[8]	0.90484
Airspeed Sensor [2x]	55400[9]	0.99820
Flight Computer [2x]	N/A	–
Electric Motor [6x]	N/A	–

The overall system reliability cannot be fully quantified without MTBF data for the flight computers and electric motors. However, the high reliability of the listed avionic components provides a strong baseline.

14.3.2. Availability

Availability is the probability that the vehicle is ready to perform its function when required. It is expressed as the ratio of operational time to total time:

$$A = \frac{\text{Uptime}}{\text{Uptime} + \text{Downtime}} \tag{14.4}$$

High availability is critical for EMS operations. DoctAir's design promotes high availability through a 20-minute rapid charging capability, which minimizes downtime between missions. This allows the vehicle to maintain a high state of readiness, a significant advantage over systems requiring longer refueling or maintenance cycles.

14.3.3. Maintainability

Maintainability is the measure of ease and speed with which a system can be restored to operational status after a failure. It is quantified by:

$$M(t) = 1 - e^{-t/\text{MTTR}} \tag{14.5}$$

where MTTR is the Mean Time To Repair. The maintenance strategy for DoctAir employs a two-level approach, with line maintenance at the MOB and heavy maintenance at a central facility. The onboard HUMS enables a shift to predictive, condition-based maintenance, reducing unscheduled downtime. Furthermore, the principles of Design for Disassembly discussed previously are intended to simplify component access and replacement, thus minimizing the MTTR and ensuring high maintainability.

14.3.4. Safety

Safety is the system's ability to operate without causing unacceptable risk to people, property, or the environment. The design of DoctAir prioritizes safety through redundancy and fail-safe principles.

- **Redundancy:** Key systems feature redundancy to mitigate the risk of single-point failures. This includes a One-Engine-Inoperative (OEI) tolerant propulsion system (Chapter 6), dual flight computers, multiple independent battery modules (Chapter 7), and redundant sensor suites (Chapter 7).

[3] https://www.uavnavigation.com/sites/default/files/docs/2024-02/UAV_Navigation-GrupoOesia_GNSS_Denied_Navigation_Kit_Brochure.pdf
[4] https://www.shipmotion.eu/barometric-pressure-sensor-smc-630.html
[5] https://docs.novatel.com/OEM7/Content/Technical_Specs_IMU/CPT_Electrical_Environmental.htm
[6] https://www.mech-mind.com/news/Mech-MindReachesMTBFMarkof40,000Hours.html
[7] https://cdn.sick.com/media/pdf/7/57/657/dataSheet_LD-LRS3601_1060832_en.pdf
[8] https://ui.adsabs.harvard.edu/abs/1983rad..symp..532D/abstract
[9] https://www.aerocontact.com/public/img/aviaexpo/produits/catalogues/312/MD21-Datasheet.pdf

- **Safety-Critical Components:** Despite built-in redundancy, some components remain safety-critical, where a failure could have catastrophic consequences. These include:
  - The primary airframe (wingbox and fuselage structure)
  - The landing gear system
  - The overall battery and power distribution system

To mitigate the risk associated with these critical components, the design incorporates high safety factors in the structural analysis (Chapter 8) and a crashworthy landing gear design intended to absorb impact energy during emergency landings (Section 8.5).

15

Cost Analysis

The cost analysis of the vehicle is broken down into two major parts, the unit production cost and the annual total operating cost (TOC). This chapter starts with statistical estimates based on the Eastlake model [138]for the unit cost. The operational cost is then estimated using the method described by Stoll [139]. At the end a sensitivity analysis and the final cost results of the vehicle are presented.

15.1. Assumptions

The cost analysis is conducted based on the assumptions presented below.

- **AS-COST-1:** A 10% profit margin is applied to the total manufacturing cost to determine the final aircraft purchase price.
- **AS-COST-2:** The operational model assumes a consistent utilization rate of 3,000 flight hours per year over the aircraft's lifespan.
- **AS-COST-3:** Labor rates for engineering, tooling, and manufacturing are based on current industry averages for aerospace production.
- **AS-COST-4:** Landing fees are assumed to be waived for all medical transport operations conducted at hospital helipads.
- **AS-COST-5:** The battery pack requires complete replacement after 1,000 full charge-discharge cycles. This takes into account the 500 cycles and reallocation of batteries.

15.2. Unit Cost Methodology

The unit cost estimates the total cost to produce a single aircraft. Based on the Eastlake and Blackwell model [138], the unit cost is composed of the following main components:

- Engineering Cost
- Development Cost
- Flight Test Cost
- Tooling Cost
- Manufacturing Cost
- Quality Control Cost
- Materials Cost
- Propulsion System Cost
- Avionics Cost

Statistical, multivariable least squares regression relations for these components are presented below, along with the various assumptions and constants used in the unit cost estimation.

Unit Cost Components

The total unit cost of the aircraft is composed of certification-related costs, manufacturing costs, quality control costs, materials costs, propulsion system costs, and avionics costs. The certification, manufacturing, quality control, and materials costs are summed and then divided by the total number of aircraft produced over five years, N. The propulsion and avionics costs are treated as fixed per-unit expenses and added separately. The overall unit cost formula is:

$$\text{Unit Cost} = \frac{C_{\text{cert}} + C_{\text{mfg}} + C_{\text{qc}} + C_{\text{mat}}}{N} + C_{\text{prop}} + C_{\text{avionics}}$$

where the total certification cost, C_{cert}, is the sum of engineering, development, flight test, and tooling costs.

Engineering Cost: This cost represents the labor hours required for the engineering design, analysis, and development of the aircraft. It is calculated based on a regression formula involving the airframe weight W_{airframe} in pounds, the cruise speed V_H in knots true airspeed, the total production quantity N, and certification and design complexity factors. These complexity factors include the certification factor F_{cert}, the flap configuration factor F_{cf}, the composite material factor F_{comp}, and the cabin pressurization factor F_{press}. The engineering labor hours H_{eng} are computed as:

$$H_{\text{eng}} = 0.0396 \cdot W_{\text{airframe}}^{0.791} \cdot V_H^{1.526} \cdot N^{0.183} \cdot F_{\text{cert}} \cdot F_{\text{cf}} \cdot F_{\text{comp}} \cdot F_{\text{press}}$$

The resulting labor hours are then multiplied by the engineering labor rate R_{eng} (in dollars per hour) and adjusted by the consumer price index relative to 2012, CPI_{2012}, to yield the engineering cost:

$$C_{\text{eng}} = 2.0969 \times H_{\text{eng}} \times R_{\text{eng}} \times \text{CPI}_{2012}$$

Development Cost: This cost accounts for expenses related to the development and production of prototypes. It depends on the airframe weight W_{airframe}, cruise speed V_H, number of prototypes N_p, and the same certification and design complexity factors used in the engineering cost. The development cost is given by:

$$C_{\text{dev}} = 0.06458 \cdot W_{\text{airframe}}^{0.873} \cdot V_H^{1.89} \cdot N_p^{0.346} \cdot \text{CPI}_{2012} \cdot F_{\text{cert}} \cdot F_{\text{cf}} \cdot F_{\text{comp}} \cdot F_{\text{press}}$$

Flight Test Cost: This cost represents the expenses related to flight testing and certification flight hours. It is influenced by the airframe weight W_{airframe}, cruise speed V_H, number of prototypes N_p, and certification factor F_{cert}. The formula is:

$$C_{\text{ft}} = 0.009646 \cdot W_{\text{airframe}}^{1.16} \cdot V_H^{1.3718} \cdot N_p^{1.281} \cdot \text{CPI}_{2012} \cdot F_{\text{cert}}$$

Tooling Cost: This cost covers the labor hours and expenses related to manufacturing tooling development. Tooling labor hours H_{tool} depend on airframe weight W_{airframe}, cruise speed V_H, total production quantity N, monthly production rate Q_m (in aircraft per month), wing taper factor F_{taper}, flap configuration F_{cf}, composite factor F_{comp}, and cabin pressurization F_{press}. Tooling labor hours are calculated as:

$$H_{\text{tool}} = 1.0032 \cdot W_{\text{airframe}}^{0.764} \cdot V_H^{0.899} \cdot N^{0.178} \cdot Q_m^{0.066} \cdot F_{\text{taper}} \cdot F_{\text{cf}} \cdot F_{\text{comp}} \cdot F_{\text{press}}$$

The tooling cost is then obtained by multiplying H_{tool} by the tooling labor rate R_{tool} and adjusting with CPI_{2012}:

$$C_{\text{tool}} = 2.0969 \times H_{\text{tool}} \times R_{\text{tool}} \times \text{CPI}_{2012}$$

Manufacturing Cost: This cost includes labor hours and overhead for the manufacturing process. Manufacturing labor hours H_{mfg} depend on airframe weight W_{airframe}, cruise speed V_H, production quantity N, certification factor F_{cert}, flap configuration F_{cf}, and composite factor F_{comp}:

$$H_{\text{mfg}} = 9.6613 \cdot W_{\text{airframe}}^{0.74} \cdot V_H^{0.543} \cdot N^{0.524} \cdot F_{\text{cert}} \cdot F_{\text{cf}} \cdot F_{\text{comp}}$$

Manufacturing cost is calculated by multiplying H_{mfg} by the manufacturing labor rate R_{mfg} and adjusting for inflation:

$$C_{\text{mfg}} = 2.0969 \times H_{\text{mfg}} \times R_{\text{mfg}} \times \text{CPI}_{2012}$$

Quality Control Cost: Quality control costs are estimated as a percentage (13%) of the manufacturing cost, scaled by certification and composite factors:

$$C_{\text{qc}} = 0.13 \times C_{\text{mfg}} \times F_{\text{cert}} \times F_{\text{comp}}$$

Materials Cost: Materials costs cover the expenses of raw materials required for the airframe construction. This cost depends on the airframe weight W_{airframe}, cruise speed V_H, production quantity N, certification factor F_{cert}, flap configuration factor F_{cf}, and cabin pressurization factor F_{press}:

$$C_{\text{mat}} = 24.896 \cdot W_{\text{airframe}}^{0.689} \cdot V_H^{0.624} \cdot N^{0.792} \cdot \text{CPI}_{2012} \cdot F_{\text{cert}} \cdot F_{\text{cf}} \cdot F_{\text{press}}$$

Propulsion System Cost: This is a fixed per-unit cost representing the electric motors and propeller costs. The electric motor cost is given by Stoll et al. [139] (2016 USD, to be appropriately converted) whilst the propeller cost by [138],

$$C_{\text{prop}} = P_{max} \times 50 + n_{engines} \times 3145$$

Avionics Cost: The avionics cost is estimated as a fixed cost of $60,000 (2016 USD, to be appropriately converted) per aircraft according to Stoll et al. [139].

Unit Cost Input Parameters

The unit cost estimation methodology presented above uses the following input parameters to estimate the unit cost of the *DoctAir* eVTOL,

Table 15.1: *Unit-Cost Model Input Parameters and Assumptions [138].*

Parameter	Value	Notes / Source
Labor Rates		
CPI, rel. to 2012 (CPI_{2012})	1.4	U.S. BLS (June 2025)[1]
Engineering Labor Rate (R_{ENG})	\$92 /hr	Industry average
Tooling Labor Rate (R_{TOOL})	\$61 /hr	Industry average
Manufacturing Labor Rate (R_{MFG})	\$53 /hr	Industry average
Vehicle & Production Parameters		
Airframe Weight (W_{airframe})	1 014 lb	460 kg design mass
Cruise Speed (V_H)	116.6 kt	60 m s^{-1} design target
Total A/C Produced in 5 yr (N)	240	10 + 10 + 20 + 80 + 120 build schedule
Monthly Production Rate (Q_m)	4 a/c /mo	$N/60$ months
Number of Prototypes (N_p)	1	Development plan
Design-Complexity Factors[138]		
Certification Factor (F_{cert})	1.0	CFR Part 23 baseline
Flap Configuration Factor (F_{cf})	1.0	Simple flap system
Composite Usage Fraction (f_{comp})	0.70	Structural concept
Composite Cost Factor (F_{comp})	1.35	$1 + 0.5 f_{\text{comp}}$
Wing-Taper Factor (F_{taper})	1.0	Moderate taper
Pressurization Factor (F_{press})	1.0	Un-pressurised cabin
Fixed Per-Unit System Costs		
Propulsion System Cost (C_{prop})	\$68 870	[139], 2016 USD
Avionics Cost (C_{avionics})	\$60 000	[139], 2016 USD

15.3. Operational Cost Methodology

The total operating cost (TOC) is a critical metric for assessing the economic feasibility of an aircraft. This analysis employs a methodology adapted from the framework presented by Stoll et al. [139] to estimate the annual operating costs. The TOC is disaggregated into several key components to provide a detailed cost profile. These components are:

[1] CPI Inflation Calculator: `https://www.in2013dollars.com/us/inflation/2012?amount=1`

- Battery Amortization
- Electricity Cost
- Engine Overhaul
- Depreciation (for both the aircraft and ground infrastructure)
- Interest
- Pilot and Maintenance Costs
- Insurance
- Landing Fees

Each component is calculated based on a set of assumptions and input parameters, which are detailed in the subsequent subsections. All monetary values are calculated in U.S. Dollars (USD).

Cost Component Calculation

The annual cost for each component is determined as follows.

Battery Amortization

The battery pack has a finite lifespan, specified in charge-discharge cycles, and its replacement cost is amortized over this period. The total battery cost is a function of the number of cells, the cost per cell, and a combining factor for packaging and integration. The annual amortization cost, C_{batt_amort}, is calculated as:

$$C_{batt\_amort} = \frac{N_{cells} \cdot P_{cell} \cdot f_{comb} \cdot N_{flights/yr}}{L_{batt\_cycles}} \tag{15.1}$$

where N_{cells} is the number of cells, P_{cell} is the price per cell, f_{comb} is the combining factor, $N_{flights/yr}$ is the annual number of flights, and L_{batt_cycles} is the battery life in cycles.

Electricity Cost

This component represents the annual cost of electricity required for battery charging. It is a function of the energy consumed per flight, the overall charging and powertrain efficiency, and the cost of electricity.

$$C_{elec} = \frac{E_{flight}}{\eta_{charge} \cdot \eta_{powertrain}} \cdot P_{kWh} \cdot N_{flights/yr} \tag{15.2}$$

Here, E_{flight} is the energy consumption per flight, η_{charge} is the charging efficiency, $\eta_{powertrain}$ is the combined efficiency of the battery, motor, and depth of discharge, and P_{kWh} is the industrial electricity rate.

Engine Overhaul

The electric motors require periodic overhauls based on their operational hours. The annual overhaul cost is prorated from the total overhaul cost and the period. It is assumed that different motor groups have different utilization factors.

$$C_{overhaul} = \sum_{i \in \text{groups}} N_{motors,i} \cdot \frac{P_{motor\_overhaul} \cdot H_{flight/yr} \cdot U_i}{T_{overhaul}} \tag{15.3}$$

where $N_{motors,i}$ is the number of motors in group i, $P_{motor\_overhaul}$ is the cost per motor overhaul, $H_{flight/yr}$ is the total annual flight hours, U_i is the utilization factor for group i, and $T_{overhaul}$ is the time between overhauls.

Depreciation

Depreciation accounts for the loss in value of capital assets: the aircraft and the mandatory ground-based charging infrastructure. The annual depreciation cost is calculated as:

$$C_{depr} = \left(\frac{P_{ac\_purchase}}{T_{depr\_ac}} + \frac{P_{station}}{T_{depr\_station}} \right) \cdot H_{flight/yr} \tag{15.4}$$

where $P_{ac\_purchase}$ is the aircraft purchase price, T_{depr_ac} is the aircraft depreciation period, $P_{station}$ is the charging station cost, and $T_{depr\_station}$ is its depreciation period.

Direct Annual and Per-Flight Costs

Several operating costs are calculated based on annual utilization or on a per-flight basis, following the model in [139].

Interest The annual cost of capital is the product of the aircraft purchase price and the annual interest rate, i.

$$C_{interest} = P_{ac\_purchase} \cdot i \tag{15.5}$$

Pilot and Maintenance Costs The mission requires 24/7 pilot availability. Assuming a standard 8-hour flight day, a pilot's on-site time is three times the average daily flight time. A base rate of $40 per hour for on-site presence thus translates to an effective rate of $120 per flight hour. The annual pilot cost is therefore:

$$C_{pilot} = R_{pilot\_eff} \cdot H_{flight/yr} \tag{15.6}$$

where R_{pilot_eff} is the effective pilot rate per flight hour. Similarly, the annual cost for routine maintenance (excluding engine overhauls) is calculated based on an hourly rate applied to the total annual flight hours.

Insurance The annual insurance premium is composed of a component proportional to the aircraft's value and a fixed cost per flight.

$$C_{insurance} = (R_{ins\_value} \cdot P_{ac\_purchase}) + (P_{ins\_flight} \cdot N_{flights/yr}) \tag{15.7}$$

where R_{ins_value} is the value-based insurance rate and P_{ins_flight} is the fixed price per flight.

Landing Fees Calculated based on the Maximum Takeoff Weight (MTOW). It is assumed that for the intended medical transport mission, these fees may be waived by operating hospitals and are therefore analyzed but not necessarily included in the final TOC summation.

Assumptions and Input Parameters

The operational cost calculations are based on the input parameters and assumptions summarized in Table 15.2. These values are derived from the reference study [139], industry standards, or specific project requirements, where cited.

Table 15.2: *Operational Cost Model Input Parameters and Assumptions.*

Parameter	Value	Notes / Source
Note: Costs from 2016 sources are adjusted to 2025 USD in the calculations using a CPI factor of 1.34[2]*.*		
General Operations		
Annual Flight Hours ($H_{flight/yr}$)	3000 hr	Based on Chapter 14
Average Flight Time	47 min	Mission profile
Aircraft MTOW	1788 kg	Design specification
Aircraft Purchase Price ($P_{ac\_purchase}$)	—	Input from unit cost model
Battery & Powertrain		
Battery Replacement Period (L_{batt_cycles})	1000 cycles	Manufacturer data [3]
Price per Cell (P_{cell})	$4.00	Supplier quote
Number of Cells (N_{cells})	10700	Battery design
Cell Combining Factor (f_{comb})	1.1	Engineering estimate
Energy per Flight (E_{flight})	133 kWh	Mission simulation
Electricity Price (P_{kWh})	$0.1725 / kWh	Netherlands rate, conv. to USD [4]
Charging Efficiency (η_{charge})	95%	[139]
Powertrain Efficiency ($\eta_{powertrain}$)	72.9%	Product of component efficiencies (0.9^3)
Maintenance & Depreciation		
Engine Overhaul Price ($P_{motor\_overhaul}$)	$10,000 / motor	Industry estimate
Time Between Overhaul ($T_{overhaul}$)	10,000 hr	Manufacturer data

[2] CPI Inflation Calculator: `https://www.in2013dollars.com/us/inflation/2016?amount=1`
[3] `https://www.nkon.nl/novat/amfile/file/download/file/232/product/5518/`
[4] `https://www.overstappen.nl/energie/compare-energy/energy-prices-netherlands/`

Table 15.2 continued from previous page

Parameter	Value	Notes / Source
Engine Utilization (Forward/Aft)	10% / 100%	Operational profile assumption
Aircraft Depreciation Time (T_{depr_ac})	30,000 hr	[139]
Charging Station Price ($P_{station}$)	$300,000	[139], 2016 USD
Station Depreciation Time ($T_{depr\_station}$)	100,000 hr	[139]
Direct & Financial Costs		
Interest Rate (i)	6% / year	[139]
Pilot Rate, Effective (R_{pilot_eff})	$120 / flight hr	Based on $40/hr for 24/7 on-site presence[5]
Maintenance Rate	$100 / flight hr	[139], 2016 USD
Insurance Rate, Value (R_{ins_value})	$1.60 / $1M / yr	[139], 2016 USD
Insurance Price, Flight (P_{ins_flight})	$4.70 / flight	[139], 2016 USD
Landing Fee Rate	$4.00 / 1000 lb	[139], 2016 USD

15.4. Analysis

The cost models detailed in the previous sections are applied to the DoctAir eVTOL to determine its economic viability. The analysis is presented in three parts: the aircraft's unit and operating cost breakdowns, a learning curve analysis showing the effect of production volume on unit cost, and a long-term cost of ownership comparison against the incumbent HEMS helicopter, the Airbus EC135. All costs are presented in 2025 Euros unless otherwise specified. A rate of 1.15 has been considered to convert from 2025 USD to EUR[6].

15.4.1. Cost Breakdown

For a production run of 240 units, the estimated **unit (purchase) price of the DoctAir is €658,322.** Figure 15.1 (left) shows the manufacturing cost breakdown. Manufacturing labor constitutes the largest share at €288,758 per unit, followed by the propulsion system (€80,249) and avionics (€69,913). The amortized non-recurring costs for development, testing, and tooling contribute a smaller fraction to the per-unit cost at this production volume.

The total **annual operating cost (TOC) is estimated at €1.07 million.** The breakdown is shown in Figure 15.1 (right). The primary drivers of the TOC are personnel and direct maintenance, with maintenance costs at €349,565 and pilot costs at €313,043 per year. Battery amortization is the next largest contributor at €156,788. Aircraft depreciation and electricity costs are secondary drivers. It is important to note that landing fees are excluded from this total, as they are assumed to be waived for medical operations at hospitals.

15.4.2. Production Volume and Learning Curve

The unit cost of the aircraft is highly dependent on the total production volume due to the amortization of non-recurring engineering (NRE) costs and the effects of the manufacturing learning curve. Figure 15.2 illustrates this relationship. The cost for the first prototype unit is estimated at €12.5 million. This cost decreases sharply as production scales; at a volume of 500 units, the manufacturing cost per aircraft reduces to approximately €0.5 million. This highlights the importance of achieving a significant production run to ensure the aircraft is economically competitive. From an operational point of view, this encourages the sale of this aircraft beyond domestic bounds. International adoption would also facilitate greater streamlining of the production chain while making the infrastructure more accessible. The baseline analysis assumes a production of 240 units.

15.4.3. Long-Term Cost of Ownership

A 20-year cumulative cost of ownership analysis was performed to compare the DoctAir against the EC135. As shown in Figure 15.3, the total 20-year cost for the DoctAir is €22.1 million. In contrast, the cost for the EC135 over the same period is €38.0 million. This results in a total savings of €15.9 million over two decades per aircraft.

This financial advantage is compounded by a significant operational improvement. The DoctAir, with its lower maintenance requirements and electric powertrain, is designed for 24/7 availability. The figure used for the operational cost of the EC135 is typically for 12 hours per day [1]. The ability to provide continuous service while simultaneously reducing long-term costs presents a substantial value proposition for HEMS operators.

[5]This effective rate accounts for three 8-hour pilot shifts required for one 8-hour flight operations day, ensuring continuous availability.
[6]Currency Converter: `https://www.xe.com/currencyconverter/convert/?Amount=1&From=EUR&To=USD`

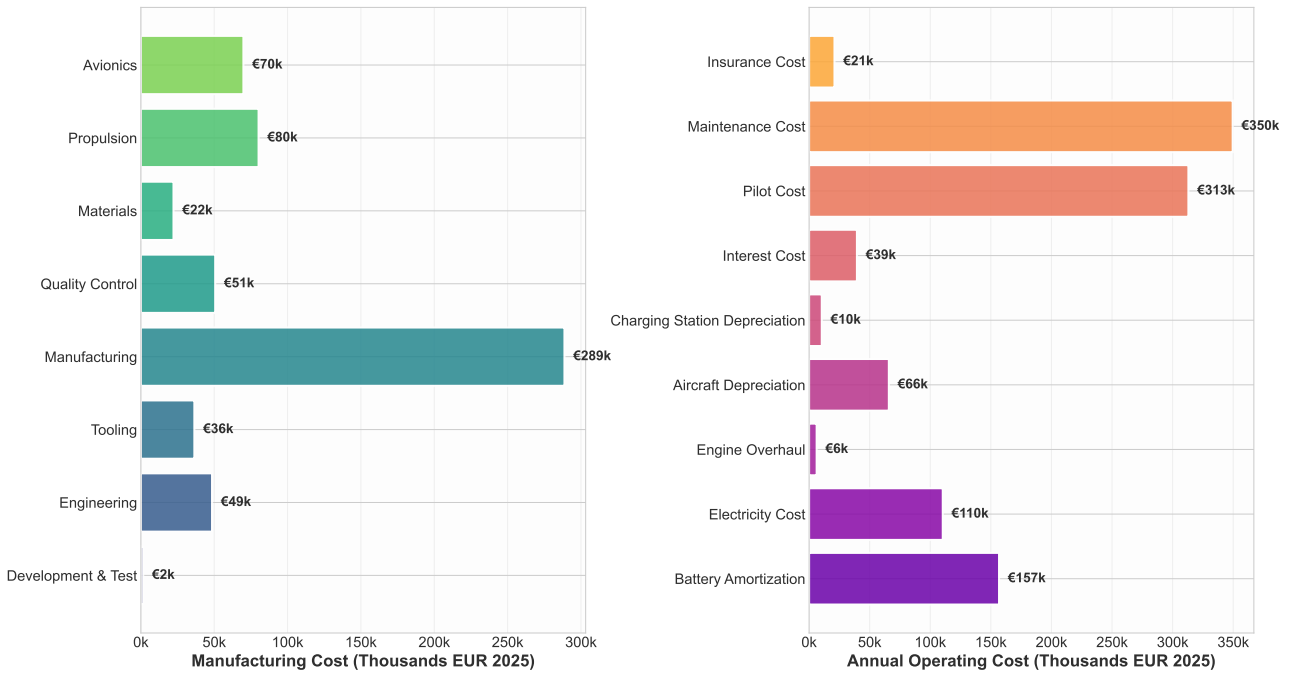

Figure 15.1: *Breakdown of the manufacturing cost (left) and annual operating cost (right) for the DoctAir eVTOL, presented in 2025 Euros.*

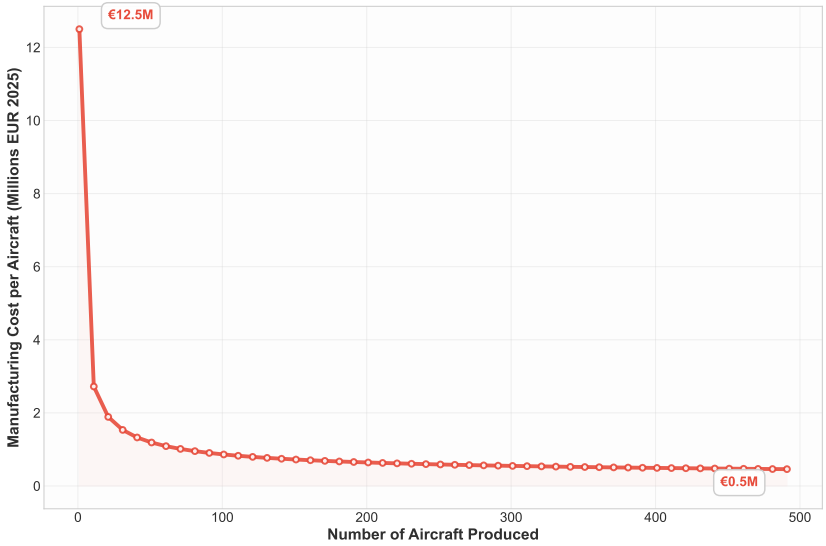

Figure 15.2: *Effect of production volume on the manufacturing cost per aircraft.*

15.5. Sensitivity Analysis

To assess the robustness of the cost projections, a sensitivity analysis was performed on four key parameters influencing the 20-year total cost of ownership: production volume, annual flight hours, battery cycle life, and interest rate. The results, visualized in Figure 15.4, indicate the relative impact of each variable on the overall economic case.

- **Annual Flight Hours:** This is the most sensitive parameter. Varying the annual utilization from 1,000 to 6,000 hours changes the 20-year total cost from €8.3 million to €42.8 million. This strong linear relationship is driven by the direct and proportional influence of flight hours on major operating costs like maintenance, pilot salaries, and battery amortization. High utilization is essential for the business model but directly scales the majority of operational expenses.
- **Battery Cycle Life:** The lifespan of the battery pack has a significant impact on the TOC. Extending the battery's replacement period from 500 to 2,000 cycles reduces the 20-year cost from €25.2 million to €20.5 million. This underscores the importance of battery technology development and achieving the specified cycle life targets to control long-term replacement costs. This is also a strong positive indicator since it implies a substantial reduction in TOC as new battery technologies can be retrofitted into the aircraft in

Figure 15.3: *Cumulative 20-year cost of ownership comparison between the DoctAir eVTOL and the EC135 helicopter.*

the future.

- **Production Volume:** Increasing the production volume from 50 to 500 units reduces the 20-year cost from €24.9 million to €21.5 million. While the unit manufacturing cost is highly sensitive to volume (as seen in Figure 15.2), its effect on the 20-year total cost is moderated because the purchase price is only one component of the long-term expenditure.
- **Interest Rate:** The model shows low sensitivity to the interest rate. A change in the rate from 2% to 12% results in a modest increase in the 20-year total cost, from €21.6 million to €22.9 million. This indicates that financing costs, while a factor, are not a primary driver of the long-term economic outlook compared to operational and technological variables.

In summary, the economic viability of the DoctAir is most dependent on achieving high operational utilization and meeting the specified battery cycle life. The purchase price, while important, is less influential on the total long-term cost.

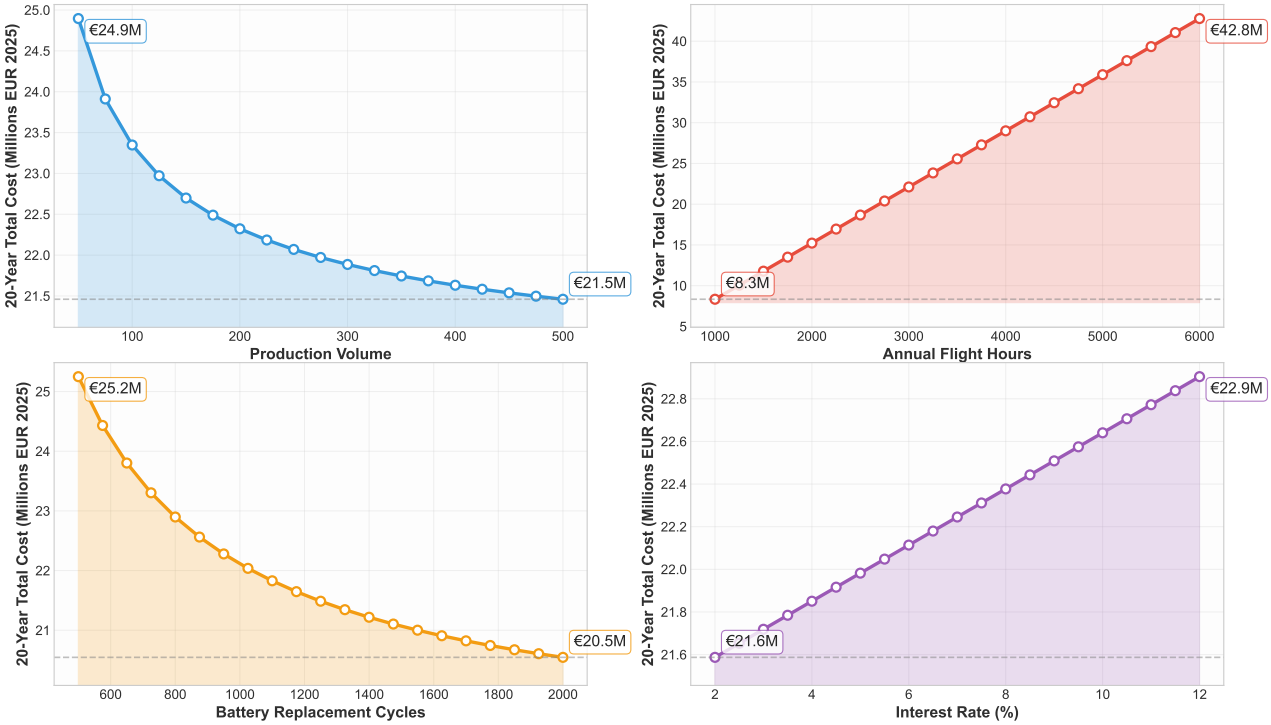

Figure 15.4: *Sensitivity of the 20-year total cost of ownership to primary input parameters.*

16

Technical Resource Budget Breakdown

With the mission definition, configuration selection, and performance analysis completed, this final chapter consolidates the technical resource estimation for the DoctAir vehicle in terms of mass and cost. These two aspects represent of the final steps of the detailed design phase, translating abstract requirements and design iterations into tangible figures. The final Maximum Take-Off Weight (MTOW), obtained through multiple refinement loops detailed in Chapter 9, anchors the mass breakdown by subsystem, while cost estimations reflect post-design considerations critical to industrial viability. Together, they offer a snapshot of DoctAir's readiness for advancement into more detailed phases, where both technical and financial feasibility must be demonstrated.

16.1. Mass Breakdown Structure

The final Maximum Take-Off Weight (MTOW) of $1788.3\,\mathrm{kg}$ was obtained through an iterative process as described in Chapter 9. Each subsystem's mass was calculated using estimation methods detailed in their respective chapters (e.g., fuselage, propulsion, power, payload). Certain minor subsystems, such as control surfaces, are included in major subsystems like wing.

The mass breakdown presented here represents the final consolidated distribution based on the current state of the design. While further design refinement may lead to adjustments in the absolute MTOW value, the relative mass fractions of the subsystems are expected to remain largely stable. This makes the current breakdown a useful reference point for future advanced design iterations, trade studies, or optimizations, particularly in conceptual or preliminary design phases.

A visual representation of the mass distribution is shown in Figure 16.1, and the numerical values are detailed in Table 16.1.

Table 16.1: *Mass breakdown by subsystem.*

Subsystem	Mass	
	Fraction [%]	Value [kg]
Fuselage	10.59	189.4
Wing	15.20	271.8
Propulsion	5.37	96
Power	40.68	727.6
Payload	22.37	400
Landing Gear	5.79	103.5
Total MTOW	**-**	**1788.3**

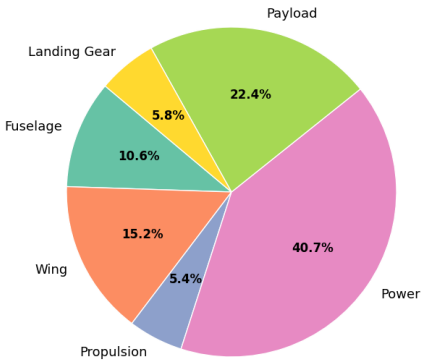

Figure 16.1: *Pie chart of subsystem mass distribution.*

16.2. Unit Manufacturing Cost Breakdown

Unlike the mass breakdown, the unit manufacturing cost was not calculated per subsystem. Instead, the analysis focused on post-design phase cost categories such as engineering, tooling, manufacturing. A detailed explanation on how this is estimated is given in Section 15.2.

The breakdown shown in Table 16.2 is based on established cost estimation practices and reflects the total manufacturing cost and final sales price (with a 10% profit margin) for a single aircraft unit.

Table 16.2: *Unit manufacturing cost breakdown in euros.*

Cost Element	Cost [€]
Development & Test	1,603.79
Engineering	48,537.68
Tooling	36,481.14
Manufacturing	288,757.93
Quality Control	50,677.02
Materials	22,255.50
Propulsion	80,248.52
Avionics	69,913.04
Total Manufacturing Cost	**598,474.63**
Purchase Price (10% margin)	**658,322.09**

16.3. Annual Operating Cost Breakdown

The annual operating cost includes all recurring expenses associated with using the aircraft over a typical year of operation. These include both direct costs (e.g., electricity, maintenance, battery amortization) and indirect costs (e.g., depreciation, insurance, interest). For further details on the estimation process, refer back to Section 15.3.

This cost breakdown, presented in Table 16.3, serves as a baseline for economic viability assessments and can be adapted based on different mission profiles or utilization rates.

Table 16.3: *Annual operating cost breakdown in euros.*

Cost Element	Cost [€]
Battery Amortization	156,788.16
Electricity Cost	110,323.09
Engine Overhaul	6,260.87
Aircraft Depreciation	65,832.21
Charging Station Depreciation	10,486.96
Interest Cost	39,499.33
Pilot Cost	313,043.48
Maintenance Cost	349,565.22
Insurance Cost	20,975.32
Total Annual Operating Cost	**1,072,774.63**

17

Technical Risk Assessment

This chapter presents the technical risk assessment for the final design. This process is crucial for identifying potential operational hazards, analyzing their severity, and establishing strategies to ensure the safety and success of the EMS mission. The overall risk score (R) is a product of its Likelihood (L) and Consequence (C).

Table 17.1: *Definitions for Risk Assessment Scales*

Score	Likelihood (L) Definition	Consequence (C) Definition
1	**Very Unlikely (<1%):** Not expected to occur during the aircraft's operational life.	**Negligible:** Minor operational inconvenience; no impact on safety or mission.
2	**Unlikely (1-10%):** Could occur a few times in the fleet's operational life.	**Moderate:** Reduced performance, mission abort is possible. Minor system damage.
3	**Likely (10-40%):** Will occur several times in the fleet's operational life.	**Critical:** Major system damage, significant reduction in safety margins, potential for serious injury.
4	**Very Likely (>40%):** Expected to occur frequently.	**Catastrophic:** Loss of the aircraft, multiple fatalities, complete mission failure.

17.1. Risk Identification

The following risks have been identified through a systematic analysis of the aircraft's flight phases and system interactions.

Table 17.2: *Operational Risk Identification for DoctAir*

Tab. ID	Risk ID	Name / Description	L	C	Risk
DA-01	RSK-DA-SAF-01	**Unstable Lift Transition**	3	4	12
		Reasoning L3: The transition from fully propulsive lift (hexacopter mode) to fully aerodynamic lift (fixed-wing mode) is an aerodynamically complex phase with potential for control challenges. C4: A loss of control during this critical, low-altitude phase is catastrophic.			
DA-02	RSK-DA-PPS-01	**Fore-Propeller Freewheeling/Alignment Failure**	3	4	12
		Reasoning L3: The mechanism of independently spinning blades for self-alignment is mechanically complex and has a higher likelihood of failure (e.g., seizure, flutter, misalignment) compared to standard systems. C4: Failure to align correctly would create significant asymmetric drag, leading to a loss of control.			
DA-03	RSK-DA-AER-01	**Low-Speed Stall / High AoA Instability**	3	4	12
		Reasoning L3: The delta wing requires a high angle of attack (AoA) for lift at low speeds, particularly during the final stages of transition or a slow approach. C4: A stall at low altitude is catastrophic and could be unrecoverable.			
DA-04	RSK-DA-SAF-02	**Engine-Out Control Asymmetry in VTOL**	2	4	8
		Reasoning L2: While individual motor reliability is high, failure is a possible event. A failure of one of the six propellers during hover or vertical flight will create a significant thrust asymmetry that the flight control system (FCS) must counteract instantly. C4: Failure to manage the asymmetry leads to catastrophic loss of control.			
DA-05	RSK-DA-PPS-02	**Aft Tilt-Propeller Mechanism Failure**	2	4	8

Continued on next page

Table 17.2 continued from previous page

Tab. ID	Risk ID	Name / Description	L	C	Risk
		Reasoning L2: Tilt mechanisms are a known point of failure in VTOL aircraft. A failure where a propeller becomes stuck in a vertical or intermediate position during cruise would be critical. C4: An asymmetric stuck propeller would induce severe yaw and roll, likely leading to a loss of control.			
DA-06	RSK-DA-ENV-01	**Vulnerability to Urban Wind Gusts/Turbulence**	3	3	9
		Reasoning L3: Operating in confined urban environments or near hospital structures exposes the aircraft to unpredictable wind gusts and turbulence. The large surface area of the delta wing makes it susceptible to these effects during low-speed VTOL phases. C3: Strong gusts could lead to a hard landing, collision with obstacles, or exceed the control authority of the FCS.			
DA-07	RSK-DA-AER-02	**Adverse Propeller Wash Interaction**	2	3	6
		Reasoning L2: The downwash from the four large fore-propellers will interact with the wing surface and aft tilt-propellers/control surfaces, especially during transition. This can cause unpredictable aerodynamic effects. C3: The interaction could lead to control difficulties or reduced performance, impacting mission execution and safety margins.			
DA-08	RSK-DA-STR-01	**Fore-Propeller Support Beam Failure**	1	4	4
		Reasoning L1: With proper design and materials, structural failure is very unlikely. However, the beam is a single, flight-critical component subject to high loads and vibrations from four propellers. C4: A fatigue failure of this beam would be catastrophic.			
DA-09	RSK-DA-PAY-01	**High Cabin Vibration During Patient Transport**	3	2	6
		Reasoning L3: The proximity of six large propellers to the fuselage makes it likely that vibrations will be transmitted to the cabin, despite the electric nature of the motors. C2: Excessive vibration can cause patient discomfort, interfere with delicate medical procedures, and degrade medical equipment performance, compromising the primary mission.			
DA-10	RSK-DA-ENV-02	**Unacceptable Operational Noise Footprint**	2	2	4
		Reasoning L2: While quieter than helicopters, six open propellers operating in close proximity to hospitals and residential areas may still exceed noise limits for routine EMS operations. C2: Noise complaints could lead to operational restrictions, limiting the aircraft's utility and public acceptance.			

17.2. Risk Maps

The identified risks are visualized in the following tables, which map each risk according to its likelihood and consequence. Table 17.3 shows the initial risk assessment, while Table 17.4 shows the anticipated risk levels after the implementation of the mitigation strategies outlined in the next section.

Table 17.3: *Pre-Mitigation Operational Risk Map*

	1 - Very Unlikely <1%	2 - Unlikely 1-10%	3 - Likely 10-40%	4 - Very Likely >40%
4 - Catastrophic	DA-08	DA-04 DA-05	DA-01 DA-02 DA-03	
3 - Critical		DA-07	DA-06	
2 - Moderate		DA-10	DA-09	
1 - Negligible				

Table 17.4: *Post-Mitigation Operational Risk Map*

	1 - Very Unlikely <1%	2 - Unlikely 1-10%	3 - Likely 10-40%	4 - Very Likely >40%
4 - Catastrophic	DA-05 DA-08	DA-01 DA-02 DA-03 DA-04		
3 - Critical	DA-07	DA-06		
2 - Moderate	DA-09	DA-10		
1 - Negligible				

17.3. Mitigation Strategies

For each identified risk, specific mitigation strategies are proposed to reduce the likelihood, consequence, or both. These strategies focus on a combination of operational procedures, pilot training, and detailed design refinements.

Table 17.5: *Operational Risk Mitigation Strategies for DoctAir*

Tab. ID	Risk ID	Mitigation Strategy	Responsible Role(s)	PML	PMC	PMR
DA-01	RSK-DA-SAF-01	Develop a highly automated transition corridor managed by the FCS. Implement rigorous simulator training for pilots focusing on manual reversion and recovery techniques during transition anomalies.	Flight Controls, Training Dept.	2	4	8
DA-02	RSK-DA-PPS-01	Incorporate a robust, fail-safe mechanical lock for both the feathered and operational positions. Implement extensive fatigue life testing on the mechanism. Operational: Pre-flight automated check and continuous health monitoring of the alignment mechanism.	Mechanical Design, Propulsion Team, Flight Ops	2	4	8
DA-03	RSK-DA-AER-01	Implement hard flight envelope protection in the FCS to prevent exceeding critical AoA. Operational: Mandate stabilized approach criteria for all landings; automated go-around if parameters are exceeded.	Flight Controls, Training Dept.	2	4	8
DA-04	RSK-DA-SAF-02	FCS to provide instantaneous control reallocation and thrust compensation in OEI. Operational: Pilots must undergo extensive simulator training for all OEI scenarios in VTOL, including landings in high-wind conditions.	Flight Controls, Systems Engineer	2	4	8
DA-05	RSK-DA-PPS-02	Utilize triple-redundant, dissimilar actuators and sensors for the tilt mechanism. Design a fail-safe mode that defaults the propeller to a low-drag cruise position upon failure. Operational: Regular, detailed inspection and lubrication schedule for the tilt mechanism.	Mechanical Design, Maintenance Team	1	4	4

Continued on next page

Table 17.5 continued from previous page

Tab. ID	Risk ID	Mitigation Strategy	Responsible Role(s)	PML	PMC	PMR
DA-06	RSK-DA-ENV-01	Integrate real-time urban weather data and on-board Lidar for turbulence detection. Operational: Establish conservative wind-gust limits for takeoff/landing at specific sites. Prohibit operations in known wind-shear prone areas if conditions are marginal.	Flight Ops, Systems Engineer	2	3	6
DA-07	RSK-DA-AER-02	Use high-fidelity CFD to model prop-wash effects and tune the FCS to actively dampen resulting instabilities. Conduct flight tests to validate the models and control laws.	Aerodynamics, Flight Controls	1	3	3
DA-08	RSK-DA-STR-01	Design the beam with a high safety factor (e.g., >2.0 on ultimate load). Implement a structural health monitoring system with embedded fiber-optic sensors to detect crack initiation. Operational: Mandatory NDT inspection of the beam at specified flight-hour intervals.	Structures Team, Maintenance Team	1	4	4
DA-09	RSK-DA-PAY-01	Integrate an active vibration-damping system into the fuselage structure and cabin mounts. Operational: Provide medical crew with noise-canceling headsets with integrated communication. Assess critical medical equipment for vibration tolerance.	Structures Team, Interior Design	1	2	2
DA-10	RSK-DA-ENV-02	Design and test propeller blade shapes for minimum acoustic signature. Operational: Develop and implement noise abatement flight procedures (e.g., steeper approach angles, optimized RPM settings) for use near sensitive locations.	Propulsion Team, Flight Ops	2	2	4

17.4. Contingency Plans

For significant residual risks or in the event that a mitigation strategy fails, clear and actionable contingency plans are required for the safety of the crew, patient, and public.

Table 17.6: *Operational Contingency Plans for DoctAir*

Tab. ID	Contingency Plan
DA-01	If uncommanded pitch/roll/yaw occurs during transition: Immediately abort transition and revert to full hexacopter mode.
DA-02	If a fore-propeller fails to align: The FCS will declare an emergency, limit airspeed, and command a landing at the nearest suitable location using a pre-programmed, high-drag approach profile. Mission is aborted.
DA-03	If a stall warning is activated despite envelope protection: Pilot executes the trained stall recovery procedure, which prioritizes reducing AoA over maintaining altitude. If at low altitude, attempt to transition to vertical flight.
DA-04	If OEI occurs in VTOL and the FCS cannot maintain stability (e.g., due to extreme wind): Pilot will command an immediate, controlled descent to the ground from the current position, accepting a hard landing over a total loss of control.
DA-06	If the aircraft encounters unexpected severe turbulence/gusts exceeding control limits: The FCS will maximize control authority and alert the pilot. The pilot's immediate action is to increase altitude to gain a safety margin, if possible, or execute a go-around and divert to an alternate, safer landing site.

18

Compliance Matrix

The requirements laid out during the Baseline Report are presented again below. This chapter focuses on a requirements compliance analysis, specifically evaluating how closely the team adhered to the requirements and whether each of them was fully met.

18.1. Requirement Compliance

The driving and key requirements represent the most critical objectives for the vehicle design. The table below summarizes whether each requirement has been complied with, using four categories: yes, no, partial, or N/A if further analysis is needed. This provides a clear overview of how well the design meets the primary goals.

Table 18.1: *Compliance matrix for Driving and Key requirements.*

Required IB	Requirement	Compliance Status	Remark
REQ-OPE-01-MIS-02	The vehicle shall be capable of transporting a patient requiring critical care from an unprepared emergency site to a designated healthcare facility.	Yes	Rescue mission profile with the desired 400 [kg] payload is achievable (see Section 7.3).
REQ-OPE-01-MIS-03	The vehicle shall be capable of transporting a patient requiring critical care between designated healthcare facilities.	Yes	Inter-facility transfer mission with desired 450 [kg] payload is achievable (see Section 7.3).
REQ-OPE-01-MIS-04	The vehicle shall be designed for primary operation within the geographical confines of the Netherlands.	Yes	110 [km] cruise range ensures furthest trauma centers can be reached.
REQ-OPE-08-MIS-01	The vehicle shall be capable of operations in weather conditions up to Beaufort 6 wind force.	Yes	15 [m/s] gusts considered in gust loading diagram.
REQ-OPE-03-MIS-01	The vehicle's operational costs shall be significantly lower than current HEMS ($\leq 50\%$ of EC-135).	Partial	The operational cost is not 50 % lower, it is 37 % lower instead. Note that DoctAir operates for 24 hours a day compared to 12 hours for HEMS.
REQ-MAN-02-MIS-01	The target unit production cost shall enable a viable business case compared to existing HEMS solutions; this can be quantified by $\leq 50\%$ of EC-135.	Yes	Unit cost is 83 % lower than EC-135.
REQ-USR-05-MIS-01	The overall prototype development cost estimate shall not exceed (TBD/750,000) EUR (FY2025).	N/A	Further cost analysis for just prototype needed.
REQ-USR-04-MIS-01	The final design shall incorporate sustainable principles and address life cycle considerations.	Yes	See Chapter 12
REQ-OPE-01-SYS-02	The vehicle shall possess sufficient operational range to enable flight from the origin point specified in REQ-OPE-01-SYS-01 to at least two designated Trauma Centers within the Netherlands.	Yes	110 [km] range ensures this .
REQ-OPE-01-SYS-10	The vehicle shall achieve a minimum cruise speed of at least 100 km/h at Maximum Continuous Power under ISA conditions at 300 [m] altitude.	Yes	Cruise speed is 61.1 [m/s] i.e. 220 [km/h].

Requirement ID	Requirement	Compliance	Remark
REQ-REG-02-SYS-01	The vehicle external noise emissions shall comply with the standards outlined in EASA SC-VTOL and associated noise requirements documentation [Ref [66].	Partial	Max noise below 80 [dB] at 150 [m]. Further analysis into Effective Perceived Noise Level (EPNL) needed for EASA SC-VTOL.
REQ-HOS-01-SYS-01	The maximum external width of the vehicle shall not exceed 10.0 meters.	Yes	As designed
REQ-HOS-01-SYS-02	The maximum external length of the vehicle shall not exceed 10.0 meters.	Yes	As designed
REQ-OPE-01-SYS-18	The vehicle's Maximum Take-Off Weight (MTOW) shall be defined and documented.	Yes	See Chapter 9
REQ-REG-01-SYS-05	The design target for the probability of a catastrophic failure condition shall be less than $1 \cdot 10^{-9}$ per flight hour.	N/A	Further analysis needed.
REQ-REG-01-SYS-06	Redundancy shall be incorporated into flight-critical systems to mitigate failure effects.	Yes	OEI is satisfied. Battery is divided into 4 modules. Redudant electronics onboard.
REQ-SAF-01-SYS-03	Following the failure of any single propulsion unit, the vehicle shall maintain controlled flight.	Yes	OEI is satisfied (see Section 6.5)
REQ-SAF-01-SYS-04	Following the failure identified in REQ-REG-01-SYS-06, the vehicle shall be capable of reaching the intended destination (emergency site or healthcare facility).	No	Engine failure forces vehicle to land. Otherwise satisfied.
REQ-SAF-01-SYS-05	During the OEI condition specified in REQ-REG-01-SYS-06, the vehicle shall maintain level flight capability at critical altitude.	Yes	See Section 6.5.
REQ-SAF-01-SYS-01	No single failure condition within any system shall result in a catastrophic event.	Yes	OEI is satisfied. Battery is divided into 4 modules. Redudant electronics onboard.
REQ-SAF-01-SYS-02	Flight and system information presented to the pilot shall be clear, timely, and unambiguous under all operating conditions.	N/A	Further analysis needed.
REQ-REG-01-SYS-04	The vehicle shall accommodate a minimum of three occupants simultaneously.	Yes	Can accommodate 4 occupants.
REQ-REG-02-SYS-01-PPS-01	The vehicle external noise level during take-off shall not exceed 86 EPNdB at 150 meters.	Yes	Highest frequency remains below 77 [dB]
REQ-REG-01-SYS-04	The internal cabin vibration level during cruise flight shall not exceed 0.1 g RMS in critical frequency bands.	N/A	Further analysis needed.
REQ-REG-01-SYS-04	The vehicle propulsion system shall utilize sustainable energy sources during operation.	Yes	Lithium-ion NMC batteries used (see Chapter 12).
REQ-REG-01-SYS-04	The primary means of flight control shall be through manual inputs from the pilot via conventional flight controls.	Yes	Rudders and Elevons are primary control surfaces (see Section 10.3)
REQ-REG-01-SYS-04	The vehicle's dimensions and ground maneuvering capability shall allow operation on standard HEMS helipads designed for EC-135 class helicopters.	Yes	Dimensions are within hospital helipad limits. Recharging possible at hospital helipads using chargers on the market.

Requirement ID	Requirement	Compliance	Remark
REQ-REG-01-SYS-04	The vehicle shall obtain noise certification based on applicable EASA VTOL noise regulations.	Yes	Noise level below 80 [dB]

Similarly, the stakeholder requirements compliance table can be seen below. Again there are four categories when it comes to compliance: yes, no, partial, or N/A if further analysis is needed. This provides a clear overview of how well the design meets expectations of the stakeholders.

Table 18.2: *Compliance matrix for Stakeholder Requirements*

Requirement ID	Requirement Text	Compliance Status	Remark
REQ-USR-01	The project shall deliver a conceptual design for a VTOL EMS vehicle based on the provided project guide.	Yes	-
REQ-USR-02	The design process shall adhere to the Design Synthesis Exercise framework and timelines (10 weeks).	Yes	-
REQ-USR-03	The project shall be executed by 10 bachelor students.	Yes	-
REQ-USR-04	The final design shall incorporate sustainable principles and address life cycle considerations.	Yes	-
REQ-USR-05	The overall prototype development cost estimate shall not exceed 750,000 EUR (FY2025).	N/A	Further prototype cost analysis needed.
REQ-OPE-01	The vehicle shall enable rapid response times comparable to or better than current HEMS operations for critical care transport.	Yes	-
REQ-OPE-02	The vehicle shall exhibit high operational reliability and availability suitable for emergency services.	Yes	-
REQ-OPE-03	The vehicle's operational costs shall be significantly lower than current helicopter-based HEMS.	Yes	-
REQ-OPE-04	The vehicle shall seamlessly integrate standard EMS patient stretchers and critical medical equipment.	Yes	-
REQ-OPE-05	The vehicle shall have a rapid turnaround time, including energy replenishment, between missions.	Yes	-
REQ-OPE-06	The vehicle shall enable reliable external voice and/or data communication with relevant parties (ATC, hospitals, ground teams).	Yes	-
REQ-OPE-07	The vehicle shall be capable of operations during day and night.	Yes	-
REQ-OPE-08	The vehicle shall be capable of operations in weather conditions up to Beaufort 6 wind force.	Yes	-
REQ-OPE-09	The vehicle shall be capable of operations during rainfall.	Yes	-
REQ-OPE-10	The vehicle shall be capable of operating from diverse unprepared sites relevant to EMS scenarios.	Yes	-
REQ-REG-01	The vehicle design shall meet the safety and airworthiness standards defined by EASA SC-VTOL.	Yes	-
REQ-REG-02	The vehicle shall comply with applicable noise regulations for operation in urban environments (Ref. EASA Dec 2023 Spec [66]).	Yes	-
REQ-REG-03	The vehicle operations shall comply with relevant current and anticipated U-Space / Urban Air Mobility regulations.	Yes	-
REQ-REG-04	Vehicle communication systems shall comply with relevant aviation frequency allocation and usage regulations.	Yes	-
REQ-REG-05	The vehicle operations shall comply with regulations on VTOL operations and VEMS, VTOL emergency medical services, specifically COMMISSION IMPLEMENTING REGULATION (EU) 2024/1111	Yes	-
REQ-HOS-01	The vehicle shall be capable of operating from existing hospital helipads compatible with EC-135 class helicopters.	Yes	-
REQ-HOS-02	The vehicle shall facilitate efficient and safe patient transfer between the aircraft and hospital facilities.	Yes	-

Requirement ID	Requirement Text	Compliance Status	Remark
REQ-PIL-01	The vehicle shall have predictable and safe handling qualities, manageable by a single pilot in adverse conditions anticipated during EMS operations.	Yes	see Chapter 10
REQ-PIL-02	The flight deck design shall minimize pilot workload and provide clear, timely, and unambiguous situational awareness information.	Yes	-
REQ-PIL-03	The vehicle shall be primarily controlled manually by a certified pilot.	Yes	-
REQ-PIL-04	The vehicle shall possess limited, clearly defined autonomous features to assist the pilot during the cruise flight phase only.	Yes	-
REQ-MED-01	The cabin shall provide adequate space and unobstructed access for the medical crew to perform necessary patient monitoring and interventions during flight.	Yes	-
REQ-MED-02	The cabin environment (noise, vibration, climate control) shall be maintained within limits conducive to effective patient care and crew comfort/performance.	N/A	Further analysis needed.
REQ-MED-03	Reliable power source(s) and secure mounting provisions shall be available for standard critical care medical equipment.	Yes	-
REQ-PAT-01	The vehicle design and operation shall prioritize patient safety as the highest consideration in all phases of flight.	Yes	-
REQ-PAT-02	The patient transport experience shall aim to minimize physiological stress by reducing cabin noise and vibration levels compared to traditional HEMS helicopters.	N/A	Further analysis needed.
REQ-MAI-01	The vehicle shall be designed to allow for efficient, safe, and cost-effective scheduled and unscheduled maintenance procedures.	Yes	-
REQ-MAI-02	Critical components requiring regular inspection or maintenance shall be easily accessible without requiring major disassembly.	Yes	-
REQ-MAN-01	The vehicle design shall leverage materials and processes that allow for feasible and repeatable manufacturing.	Yes	-
REQ-MAN-02	The target unit production cost shall enable a viable business case compared to existing HEMS solutions.	Yes	-
REQ-PUB-01	The vehicle operation in populated areas shall pose minimal physical safety risk to non-involved persons and property on the ground.	Yes	-
REQ-PUB-02	The vehicle's perceived noise footprint during typical operations shall be minimized to a level supporting public acceptance for routine use in urban and suburban environments.	Yes	see Section 6.6
REQ-EOL-01	The vehicle design shall facilitate end-of-life disassembly and maximize the potential for material recycling or responsible disposal.	Yes	-

19

Conclusion & Recommendations

Traditional Helicopter Emergency Medical Services (HEMS) face escalating operational costs and noise restrictions that limit urban access, while ground ambulances are increasingly delayed by traffic. This report presented the development process of DoctAir, the electric Vertical Take-off and Landing (eVTOL) flying wing designed to tackle these issues and fulfill the following mission:

Ensure a faster, quieter, and more flexible emergency transportation solution to overcome challenges posed by urban congestion, limited landing space, and noise restrictions.

The key specifications of the final design are highlighted in Table 19.1 and the CAD renders are shown in Figure 19.1. The converged design features an aerodynamic configuration that combines a NACA0025 mid-section and an Eppler 186 outer-section that strikes a balance between cruise efficiency and stability. Vortex Lattice Method (VLM) simulations were validated against empirical data to within 3% error and used to perform an aerodynamic analysis of the aircraft as a whole. Propulsion is provided by four fold-away hover engines and two tilting cruise engines, each equipped with propellers that are optimized for peak performance under one-engine-inoperative (OEI) conditions. A robust power-distribution system ensures uninterrupted energy delivery to propulsion units, and avionics, while LiDAR sensors enhance obstacle awareness. Control authority and both static and dynamic stability characteristics were verified, and a PID controller enables precise handling. Model mission simulations in SUAVE confirm that DoctAir meets all performance objectives, and a sustainable end-of-life strategy ensures minimal environmental impact. Together, these features enable DoctAir to deliver faster, quieter, and more flexible emergency response in urban environments.

Table 19.1: *Final design specifications of DoctAir (ordered by importance)*

Property	**Values**
MTOW	1 788 kg
Number of occupants (incl. pilot)	4
Range	250 km
Power available	1 254 kW
Total mission energy	212.73 kWh
Battery mass	727.6 kg
Cruise lift coefficient, $C_{L_{\text{cruise}}}$	0.214
Cruise drag coefficient, $C_{D_{\text{cruise}}}$	0.014
Cruise angle of attack, α_{cruise}	5.5°
Wing area	36.9 m^2
Span	9 m
Number of engines	6
Unit cost	€ 658 322 (FY 2025)

Although the design process that was followed was elaborate, there is a degree of uncertainty to the calculations due to empirical estimations and time constraints restricting the complexity of the simulations. Hence, the next steps to be taken to arrive at a more refined design are:

1. Perform CFD using viscous methods to take into account unsteady lift phenomena, such as vortex lift. Analyze the interference of propellers on the lift distribution.
2. Perform sub-scale wind tunnel tests to arrive at a more accurate estimation of the stability and control derivatives.
3. Integrate calculations of effective perceived noise level (EPNL) for a more robust noise pollution estimation.
4. Develop a more elaborate heat analysis of the power system to ensure that all systems remain sufficiently cool.
5. Explore newer battery technologies, such as solid state batteries, as they become more readily available.
6. Perform a finite element analysis of the structure using Ansys or equivalent software.
7. Develop a robust model for transition phase simulation.
8. Implement a transition controller using control blending and a stability augmentation system.

9. Produce a more detailed manufacturing plan that include assembly procedures for specific components.
10. Identify optimal MOBs in the Netherlands using real population density data.
11. Source specific components to produce a more accurate unit cost.

(a) *Front view.*

(b) *Side view.*

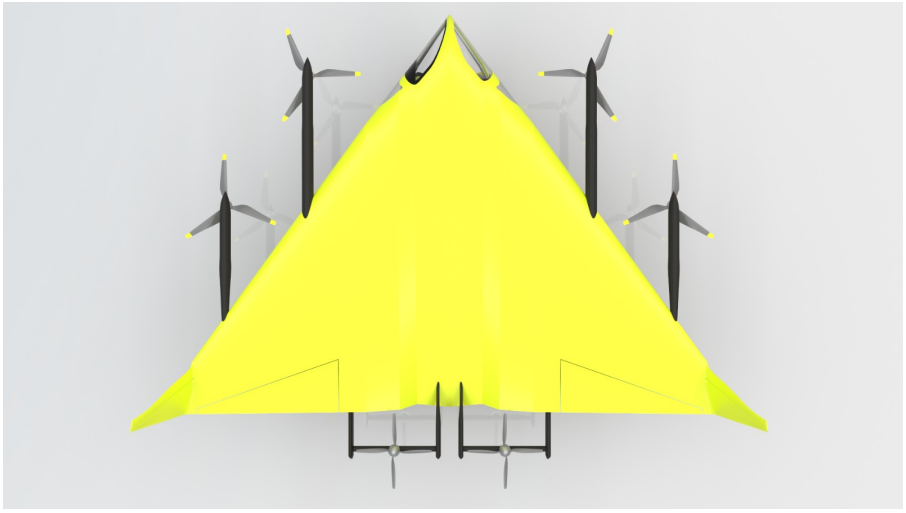

(c) *Top view.*

Figure 19.1: *CAD renders of the final design.*

References

[1] J. Röper et al. “Costing of helicopter emergency services- a strategic simulation based on the example of a German rural region”. In: *Health Economics Review* 10 (Oct. 2020).

[2] Risquez Martin. “CO2 emissions of all world countries JRC/IEA/PBL 2022 Report”. In: ISBN: 978-92-76-55802-6. DOI: 10.2760/730164. URL: https://joint-research-centre.ec.europa.eu.

[3] Emilio Botero et al. “Aerodynamic Verification and Validation of SUAVE”. In: *AIAA Science and Technology Forum and Exposition, AIAA SciTech Forum 2022*. American Institute of Aeronautics and Astronautics Inc, AIAA, 2022. ISBN: 9781624106316. DOI: 10.2514/6.2022-1929.

[4] Remco H.A. Ebben et al. *Characteristics of non-conveyance ambulance runs: A retrospective study in the Netherlands*. 2019. DOI: 10.5847/wjem.j.1920-8642.2019.04.008.

[5] Lieke Heuvelmans, Jeroen Wetzels, and Jasper Bunskoek. *Ambulance met spoed steeds langer onderweg: 'In ons dorp bijna nooit op tijd'*. Feb. 2025. URL: https://www.rtl.nl/nieuws/onderzoek/artikel/5493952/noodhulp-112-hulpdienst-aanrijtijden-wachten-ambulance.

[6] Falk Fernbach and Patrick Van. *D5.3 Comparative CBA Deliverable 5.3: Comparative CBA of manned and unmanned EMS UAM operations in comparison for traditional EMS transport 2 D5.3 Comparative CBA*. Tech. rep. 2023.

[7] A. M. K. M. Abdelrahman. “Conceptual Design Framework for Transitional VTOL Aircraft with Application to Highly-Maneuverable UAVs”. PhD thesis. Calgary, Canada: University of Calgary, Aug. 2019.

[8] NHTSA's Office of EMS. *What is EMS?* Feb. 2025.

[9] Ambulancezorg Nederland. *25 Regional Ambulance Services in the Netherlands*. URL: https://www.ambulancezorg.nl/en/themes/ambulance-care-in-the-netherlands/regional-ambulance-service/25-regional-ambulance-services-in-the-netherlands.

[10] Ministry of Justice and Security. *What happens when I call 112 for an ambulance?* URL: https://www.government.nl/topics/emergency-number-112/question-and-answer/what-happens-when-i-call-112-for-an-ambulance.

[11] Mobile Medical Team. *MMT care (Mobile Medical Team)*. Feb. 2022.

[12] ANWB MAA. *Helikopters*. URL: https://www.anwb.nl/maa/helikopters.

[13] ANWB. *Bemanning traumahelikopter*. URL: https://www.anwb.nl/maa/vliegoperatie/bemanning-traumahelikopte.

[14] Tim Nootenboom et al. “The Port of Rotterdam, a Smart Region Connected to the Randstad”. In: *2025 Smart City Symposium Prague (SCSP)*. IEEE, May 2025, pp. 1–6. ISBN: 979-8-3315-2550-7. DOI: 10.1109/SCSP65598.2025.11037683.

[15] *Study on the societal acceptance of Urban Air Mobility in Europe*. Tech. rep. 2021.

[16] Graham Jarvis. “How eVTOL aircraft could enhance emergency medical services”. In: (Aug. 2024). URL: https://www.businessairportinternational.com/features/how-evtol-aircraft-could-enhance-emergency-medical-services.html.

[17] Guy Norris. “Metro Outlines Pioneering eVTOL EMS Plan With Beta”. In: (Mar. 2025). URL: https://aviationweek.com/aerospace/advanced-air-mobility/metro-outlines-pioneering-evtol-ems-plan-beta.

[18] Joby Aviation. *Electric Aerial Ridesharing*. URL: https://www.jobyaviation.com/.

[19] ERC System. *ERC System*. URL: https://www.erc-system.com/.

[20] Paramount Business Jets. *Eurocopter EC-135-P2 Private Jet Charter*. Feb. 2022. URL: https://www.paramountbusinessjets.com/private-jet-charter/aircraft/eurocopter-ec-135-p2.

[21] Business Jet Traveler. *Airbus Helicopters H135 (T3)*.

[22] Aviamarket. *eVTOL*. URL: https://aviamarket.aero/evtol/.

[23] Mercedes-Benz. *Sprinter Panel Van Overview*. URL: https://www.mercedes-benz.com.au/vans/models/sprinter/panel-van/overview.html?srsltid=AfmBOoqOER0gHpNuk8j7Zfb82ZprobGBjz9fHsWCaMWB1X_LzR-Q2ja0.

[24] BMW. *R 1200 RT: technical data and colors*. Tech. rep. 2009.

[25] Airbus. *H135 technical information*. URL: https://www.airbus.com/en/products-services/helicopters/civil-helicopters/h135/h135-technical-information.

[26] RIVM. “Memo Beschouwing risico's benzinetankstations voor omgevingsveiligheid”. In: ().

[27] Mercedez-Benz. *Mercedes-Benz Sprinter specifications*. Tech. rep.

[28] EASA. “EC135 Data sheet”. In: ().

[29] ANWB. *Airbus Helicopter EC-135 (H135)*. URL: https://www.anwb.nl/maa/helikopters/airbus-helicopter-ec-135.

[30] ANWB. *Veiligheid*. URL: https://www.anwb.nl/maa/veiligheid.

[31] Ambulancezorg Zoetermeer. *Hoeveel mensen kunnen door de ambulance worden vervoerd?* URL: Ambulancezorg%20Zoetermeer.

[32] Rob van Werven. *Improving the response time performance of A1-priority calls for UMCG ambulancezorg*. Tech. rep. University of groningen, Sept. 2012.

[33] Robin Diederik Lokerman. “Evaluating and optimizing pre-hospital trauma triage Towards tailored decision-support”. In: (). DOI: 10.33540/2287. URL: https://doi.org/10.33540/2287.

[34] *Ambulances will soon not be allowed to drive faster than 140 during the day*. URL: https://nos.nl/artikel/2326072-ambulances-mogen-binnenkort-overdag-niet-harder-dan-140.

[35] Christine A. Chappelle et al. “Opportunities to enhance air emergency medical service scale through new vehicles and operations”. In: *2018 Aviation Technology, Integration, and Operations Conference*. American Institute of Aeronautics and Astronautics Inc, AIAA, 2018. ISBN: 9781624105562. DOI: 10.2514/6.2018-2883.

[36] Patrick Ratei et al. “Sensitivity analysis of urban air mobility aircraft design and operations including battery charging and swapping”. In: *CEAS Aeronautical Journal* (Oct. 2024). ISSN: 18695590. DOI: 10.1007/s13272-024-00725-x.

[37] Rohit Goyal and Adam Cohen. “Advanced Air Mobility: Opportunities and Challenges Deploying eVTOLs for Air Ambulance Service”. In: *Applied Sciences (Switzerland)* 12.3 (Feb. 2022). ISSN: 20763417. DOI: 10.3390/app12031183.

[38] NOTAM. *Integrated Aeronautical Information Package*. Apr. 2025. URL: https://eaip.lvnl.nl/web/2025-05-01-AIRAC/html/index-en-GB.html.

[39] *Airport regulations Heidelberglaan 100 airport in Utrecht | Planviewer, the National Location Platform*. URL: https://www.planviewer.nl/lb/381612-luchthavenregeling-luchthaven-heidelberglaan-100-te-utrecht.

[40] *Airport regulation heliport roof location Isala Clinics | Local laws and regulations*. URL: https://lokaleregelgeving.overheid.nl/CVDR714099/.

[41] *NOTAM UMCG helideck - umcg.nl*. URL: https://www.umcg.nl/notam.

[42] *Airport regulation heliport roof location Isala Clinics | Local laws and regulations*. URL: https://lokaleregelgeving.overheid.nl/CVDR714099/.

[43] *Airport regulations heliport Maastricht University Medical Center | Local laws and regulations*. URL: https://lokaleregelgeving.overheid.nl/CVDR738688.

[44] *Airport regulations heliport Maastricht University Medical Center | Local laws and regulations*. URL: https://lokaleregelgeving.overheid.nl/CVDR738688.

[45] *Heliport MCL › MCL - Medical Center Leeuwarden*. URL: https://www.mcl.nl/meer-over-mcl/over-het-mcl/heliport-mcl.

[46] R.K. Uil. “Provincie Fryslân - Luchthavenregeling voor de luchthaven van Antonius Ziekenhuis Sneek ten behoeve van medische vluchten ”. In: *PROVINCIAAL BLAD* 1.1 (Dec. 2020).

[47] J Karliner et al. “Health care’s climate footprint: the health sector contribution and opportunities for action”. In: *European Journal of Public Health* 30.Supplement_5 (Sept. 2020). ISSN: 1101-1262. DOI: 10.1093/eurpub/ckaa165.843.

[48] K. James. *International Panel on Climate Change (IPCC). AR6 synthesis report: climate change 2022*. May 2022.

[49] Gerardo Sanchez Martinez et al. *Environmentally sustainable health systems: a strategic document*. Apr. 2017.

[50] Nabil Hagag and B Hoeveler. “The feasibility of electric air taxis: balancing time-savings and co2 emissions - a joint case study of respective plans in Paris”. In: *CEAS Aeronautical Journal* (May 2025). DOI: 10.1007/s13272-025-00811-8.

[51] RIVM. *New calculation method reveals environmental impact of healthcare sector*. Oct. 2022. URL: https://www.rivm.nl/en/news/new-calculation-method-reveals-environmental-impact-of-healthcare-sector#:~:text=Total%20contribution%3A%207%25,scientific%20basis%20for%20these%20estimates..

[52] Osita Ugwueze et al. “An Efficient and Robust Sizing Method for eVTOL Aircraft Configurations in Conceptual Design”. In: *Aerospace* 10.3 (Mar. 2023), p. 311. ISSN: 2226-4310. DOI: 10.3390/aerospace10030311.

[53] John D. Anderson. *Fundamentals of Aerodynamics*. 6th. McGraw-Hill Education, 2017.

[54] R. D. Finck. *USAF (United States Air Force) Stability and Control DATCOM*. Tech. rep. MCDONNELL AIRCRAFT CO ST LOUIS MO, Apr. 1978, pp. 1–3134.

[55] Barnaby Wainfan. *Airfoil Selection, Understanding and Choosing Airfoils For Light Aircraft*. 2nd ed. 2005, pp. 33–34.

[56] Hartmut Siegmann. *Airfoil Database for Tailess and Flying Wings*. 2001.

[57] Mark Drela. “XFOIL: An Analysis and Design System for Low Reynolds Number Airfoils”. In: vol. 54. June 1989. ISBN: 978-3-540-51884-6. DOI: 10.1007/978-3-642-84010-4{_}1.

[58] Snorri Gudmundsson. *Aircraft Preliminary Design Handbook*. 2011.

[59] J.R. Gloudemans. *OpenVSP*. Washington DC, Jan. 2012.

[60] Charles N Adkins and Robert H Liebeckt. *Design of Optimum Propellers*. Tech. rep. 5. 1994, pp. 10–13.

[61] Wayne. Johnson. *Rotorcraft aeromechanics*. Cambridge University Press, 2013. ISBN: 9781107028074.

[62] Alan A. Baker and Stuart Dutton. *Composite_Materials_for_Aircraft_Structu*. AIAA 2004, Apr. 2011.

[63] Changning Chen et al. “Aerodynamic Interaction Analysis of Various Propellers on a Lift-Thrust Hybrid Configuration eVTOL Aircraft”. In: 2025, pp. 271–280. DOI: 10.1007/978-981-96-2440-9{_}26. URL: https://link.springer.com/10.1007/978-981-96-2440-9_26.

[64] Neise Wolfgang and Michel Ulf. *Aerodynamic Noise of Turbomachines*. Tech. rep. Berlin: German Aerospace Center (DLR), 1994, pp. 157–167.

[65] Haotian Qi et al. “Investigation on Aerodynamic Noise Characteristics of Coaxial Rotor in Hover”. In: *Applied Sciences (Switzerland)* 12.6 (Mar. 2022). ISSN: 20763417. DOI: 10.3390/app12062813.

[66] EASA. “ENVIRONMENTAL PROTECTION TECHNICAL SPECIFICATIONS (NOISE) APPLICABLE TO VTOL-CAPABLE AIRCRAFT POWERED BY NON-TILTING ROTORS”. In: *Regulation (EU) 2018/1139* (Dec. 2023).

[67] Jack E Made and Donald W Kurtz. *N A Review of Aerodynamic Noise From Propellers, Rofors, and Liff Fans*. Tech. rep. 1970.

[68] Nigel. *Specific Heat Capacity of Lithium Ion Cells*. Jan. 2022.

[69] EASA. *Special Condition for VTOL and Means of Compliance*.

[70] Sai Raj. *Influence of Materials Requirements on the Design of Transformational Vertical Flight Aerial Vehicles for Public Access Acknowledgements*. Tech. rep. Cleveland: NASA Glenn Research Center, Apr. 2018. URL: https://www.iea.org/publications/freepublications/publication/transport2009.pdf.

[71] Stanley. *How Electric Vehicle Light-weighting is Changing the Automotive Industry*. URL: How%20Electric%20Vehicle%20Light-weighting%20is%20Changing%20the%20Automotive%20Industry.

[72] Easa. *Easy Access Rules for Normal, Utility, Aerobatic and Commuter Category Aeroplanes (CS-23) (Initial issue)*. Tech. rep. June 2018.

[73] Suchart Siengchin. “A review on lightweight materials for defence applications: Present and future developments”. In: *Defence Technology* (2023).

[74] Gregory Szuladziński. “Performance of composites versus metals under extreme loading”. In: *International Journal of Protective Structures* 8.1 (Mar. 2017), pp. 86–108. ISSN: 2041420X. DOI: 10.1177/2041419617695963.

[75] MIT. *Stress-Strain explanation*.

[76] Qigang Han et al. “Carbon fiber reinforced epoxy composite combining superior electrochemical energy storage and mechanical performance”. In: *Chemical Engineering Journal* 437 (June 2022). ISSN: 13858947. DOI: 10.1016/j.cej.2022.135228.

[77] Texonic. *Your guide to structural fibres Fiber selection, a key component in our reinforcements*. URL: https://texonic.net/en/tableau/technical/.

[78] P. Joyce. *Resins (aka Matrices)*. Tech. rep. 2003.

[79] Honeycombpanels.eu. *Composite Panels*. URL: https://www.honeycombpanels.eu/.

[80] Ambri and Ramandeep Kaur. “Spars and Stringers - Function and Designing”. In: *International Journal of Aerospace and Mechanical Engineering* 1.1 (Sept. 2014).

[81] D. Bino Prince Raja et al. “Static structural analysis and testing of aircraft wing spar using composite material”. In: *Materials Today: Proceedings*. Vol. 64. Elsevier Ltd, Jan. 2022, pp. 416–424. DOI: 10.1016/j.matpr.2022.04.762.

[82] Daniel O Isha. *Engineering Mechanics of Composite Materials*. 2004.

[83] AE ASM. *Extra 500 Wing Box Design Design*. Tech. rep.

[84] Faserverbundwerkstoff; composite technology. “R&G mechanical properties of carbon fiber”. In: (2010).

[85] ScienceDirect. *Vinyl Ester Resin*. 2008.

[86] Shaolin Lu et al. *Molecular design and application of low dielectric bismaleimide resin*. Dec. 2024. DOI: 10.1002/pen.26973.

[87] Xinchen Ni et al. “Interlaminar reinforcement of carbon fiber composites using aligned carbon nanotubes”. In: *ICCM International Conferences on Composite Materials*. Vol. 2017-August. International Committee on Composite Materials, 2017. DOI: 10.1016/j.compositesb.2024.112098.

[88] Bruno CASTANIE, Christophe BOUVET, and Malo Ginot. *Review of composite sandwich structure in aeronautic applications*. Aug. 2020. DOI: 10.1016/j.jcomc.2020.100004.

[89] ASM International. *ASM Handbook*. Vol. 21. The Materials Information Company, 2001.

[90] M.R. Kamal. *Composite Materials and Processin*. CRC Press, 1990.

[91] Easycomposites. *4.8mm Cell 48kg Nomex Honeycomb*. URL: https://www.easycomposites.eu/5mm-48kg-nomex-honeycomb.

[92] Bradley A Newcomb et al. “Low-Density Carbon Fibers Based on Honeycomb structure”. In: Oct. 2012. URL: https://www.researchgate.net/publication/244243360_Low-Density_Carbon_Fibers_Based_on_Honeycomb_structure.

[93] Martin Herold, Sebastian Iwan, and Lothar Kroll. “Designing bended pipes under internal pressure”. In: *Technologies for Lightweight Structures (TLS)* 5.1 (Sept. 2022), pp. 161–171. DOI: 10.21935/tls.v5i1.151.

[94] SAAB AKTIEBOLAG. *LOw COst Manufacturing and Assembly of Composite and Hybrid Structures*. Aug. 2016.

[95] Biplab Chatterjee and Sumit Bhowmik. “Evolution of material selection in commercial aviation industry-a review”. In: *Sustainable Engineering Products and Manufacturing Technologies*. Elsevier, Jan. 2019, pp. 199–219. ISBN: 9780128165645. DOI: 10.1016/B978-0-12-816564-5.00009-8.

[96] Richard C Landt. *MECHANICAL FASTENERS FOR ADVANCED COMPOSITE MATERIALS*. Tech. rep.

[97] ASM Aerospace Specification Metals Inc. *Titanium Ti-6Al-4V (Grade 5), Annealed*. URL: https://asm.matweb.com/search/specificmaterial.asp?bassnum=mtp641.

[98] INC. Alloys International. *MP159 Alloy MP-159*. URL: https://alloysintl.com/inventory/nickel-and-cobalt-alloys/mp159/.

[99] Tech Steel & Materials. *Cobalt M35N*. URL: https://www.techsteel.net/alloy/cobalt/mp35n.

[100] ASM Aerospace Specification Metals Inc. *Special Metals INCONEL® Alloy 600*. URL: https://asm.matweb.com/search/SpecificMaterial.asp?bassnum=NINC30.

[101] S.J Findaly and N.D Harrison. *Why aircraftfail*. Tech. rep. Nov. 2002.

[102] Jan Roskam. *Airplane Design Part VI: Preliminary Calculation of Aerodynamic, Thrust and Power Characteristics*. DARcorporation, 2008.

[103] Peter Korba et al. “Structural design and material comparison for aircraft wing box beam panel”. In: *Heliyon* 10.5 (Mar. 2024), e27403. ISSN: 24058440. DOI: 10.1016/j.heliyon.2024.e27403.

[104] Khalid Eldwaib et al. “Design of Wing Spar Cross Section for Optimum Fatigue Life”. In: *Procedia Structural Integrity* 13 (2018), pp. 444–449. ISSN: 24523216. DOI: 10.1016/j.prostr.2018.12.074.

[105] Sascha Dähne et al. “Lightworks, a scientific research framework for the design of stiffened composite-panel structures using gradient-based optimization”. In: *Structural and Multidisciplinary Optimization* 67.5 (May 2024), p. 70. ISSN: 1615-147X. DOI: 10.1007/s00158-024-03783-1.

[106] R’ ’Vos and M’ ’Hoogreef. *Aerospace Design and Systems Engineering Elements I - Landing Gear and Empennage Design*. 2023.

[107] Serkan Özgen. *Aeronautical Engineering Design I Landing Gear Sizing and Placement*. Tech. rep. 2015.

[108] Infosys Limited. *Aircraft Lading Gear Design & Development*. Tech. rep. Bengaluru, 2018.

[109] Infosys. *How Advanced Technologies are helping to meet the challenges?* Tech. rep. 2018. URL: https://www.infosys.com/industries/communication-services/documents/landing-gear-design-and-development.pdf.

[110] ASM Aerospace Specification Metails Inc. *Aluminum 7075-T6; 7075-T651*. URL: https://asm.matweb.com/search/specificmaterial.asp?bassnum=ma7075t6.

[111] Kaizad Wadia et al. "Preliminary design and analysis of crashworthy structures for a long-range eVTOL aircraft". In: *AIAA Science and Technology Forum and Exposition, AIAA SciTech Forum 2022*. American Institute of Aeronautics and Astronautics Inc, AIAA, 2022. ISBN: 9781624106316. DOI: 10.2514/6.2022-1485.

[112] FONNOV. *7075 Aluminum Tube And 7075 Seamless Tube*. URL: https://www.fonnovaluminium.com/product/7075-aluminum-tube.

[113] Code of Federal Regulations. *Emergency Landing Conditions*. Tech. rep. July 2025. URL: https://www.ecfr.gov/current/title-14/chapter-I/subchapter-C/part-27/subpart-C/subject-group-ECFRf2515baf1391800.

[114] JPE. *Structural damping properties of mechanical systems*. URL: https://www.jpe-innovations.com/precision-point/structural-damping-properties-mechanical-systems/.

[115] FIBERMAX. "Nomex/aramid honeycomb 48 kg / 5 mm". In: (). URL: https://www.fibermax.eu/core-materials/nomex-honeycomb/nomex-aramid-honeycomb-thickness-5-mm-cell-size-3-2mm.html.

[116] US-skriptFE10. *0 Mass and Center of Gravity*. Tech. rep.

[117] J. Roskam. *Airplane Design—Part V: Component Weight Estimation*. Lawrence, Kansas: Design, Analysis and Research Corporation (DARCorporation), 2018.

[118] Quan Quan. *Introduction to multicopter design and control*. Springer Singapore, June 2017, pp. 1–384. ISBN: 9789811033827. DOI: 10.1007/978-981-10-3382-7.

[119] H.V. de Castro. *The Longitudinal Static Stability of Tailless Aircraft*. Tech. rep. Cranfield University, 2001.

[120] *Python Control Systems Library — Python Control Systems Library 0.10.1 documentation*. URL: https://python-control.readthedocs.io/en/0.10.1/.

[121] United States Air Force. "The USAF Stability And Control Digital Datcom Volume 1: Users Manual". In: *Technical Report* I.Apr 1979 (1979).

[122] Mohamed A. Mohamed et al. "Low speed aerodynamic characteristics of non-slender delta wing at low angles of attack". In: *Alexandria Engineering Journal* 61.12 (Dec. 2022), pp. 9427–9435. ISSN: 1110-0168. DOI: 10.1016/J.AEJ.2022.03.003. URL: https://www.sciencedirect.com/science/article/pii/S1110016822001703.

[123] Michael V. Cook. "Longitudinal Dynamics". In: *Flight Dynamics Principles* (2013), pp. 147–181. DOI: 10.1016/B978-0-08-098242-7.00006-7.

[124] Alberto Ruiz García et al. "Aerodynamic Model Identification of the Flying V from Sub-Scale Flight Test Data". In: *AIAA Science and Technology Forum and Exposition, AIAA SciTech Forum 2022* (2022). DOI: 10.2514/6.2022-0713.

[125] J.A. Mulder et al. *AE3202 Flight Dynamics Lecture Notes*. Tech. rep. Delft: TU Delft, Mar. 2013.

[126] Stanford University. *Stanford University Aerospace Vehicle Environment*. June 2025.

[127] Vadivelu Ponnusamy Bannari. *Material Based Structural Analysis of a Typical Landing Gear*. Tech. rep. 2017. URL: www.ijiset.com.

[128] Zahid Hasan Shuvo et al. *Comprehensive Materials Processing*. Ed. by Saleem Hashmi. 2nd ed. Vol. 13. Elsevier, 2024, pp. 303–328.

[129] Mulat Alubel Abtew et al. *Composite Structures*. Vol. 223. 2019.

[130] Jiaxuan Chi et al. *Materials Science and Engineering*. Vol. 818. 2021.

[131] Corrado Poli. *Design for Manufacturing*. Butterworth-Heinemann, 2001, pp. 231–251.

[132] M.M. Alam, M. Maniruzzaman, and M.M. Morshed. *Comprehensive Materials Processing*. Vol. 7. Elsevier, 2014, pp. 243–260.

[133] Roberto Teti Alessandra Caggiano Adelaide Marzano. "Resource Efficient Configuration of an Aircraft Assembly Line". In: *Procedia CIRP* 41 (2016), pp. 236–241.

[134] Wendy Middleton Lee H. Goldberg. *Green Electronics/Green Bottom Line*. 2000, pp. 69–82.

[135] Dassault Systemes. *Design for Disassembly in the Age of Circularity*. URL: https://www.3ds.com/sustainability/circular-economy/design-for-disassembly.

[136] Kai Meng et al. *Intelligent disassembly of electric-vehicle batteries: a forward-looking overview*. July 2022. DOI: 10.1016/j.resconrec.2022.106207.

[137] Muhammad Ateeq. "A state of art review on recycling and remanufacturing of the carbon fiber from carbon fiber polymer composite". In: *Composites Part C: Open Access* 12 (Oct. 2023). ISSN: 26666820. DOI: 10.1016/j.jcomc.2023.100412.

[138] Charles N. Eastlake and Harry W. Blackwell. "Cost estimating software for general aviation aircraft design". In: *ASEE Annual Conference Proceedings* (2000), pp. 1563–1569. ISSN: 01901052. DOI: 10.18260/1-2--8243. URL: https://www.researchgate.net/publication/344058425_Cost_Estimating_Software_For_General_Aviation_Aircraft_Design.

[139] Alex M. Stoll and Gregor Veble Mikic. "Design Studies of Thin-Haul Commuter Aircraft with Distributed Electric Propulsion". In: *16th AIAA Aviation Technology, Integration, and Operations Conference*. Reston, Virginia: American Institute of Aeronautics and Astronautics, June 2016. ISBN: 978-1-62410-440-4. DOI: 10.2514/6.2016-3765.

[140] John E. Cochran. "Aircraft Flight Dynamics and Control". In: *Journal of Guidance, Control, and Dynamics* 38.2 (Feb. 2015), pp. 356–357. ISSN: 0731-5090. DOI: 10.2514/1.G000628.

A

Functional Analysis

In this section, a functional analysis of the mission shall be presented. First, a *Functional Breakdown Structure* (FBS) is shown which lists the various functions that need to be performed during the mission in a hierarchical order. Next a *Functional Flow Diagram* (FFD) is shown in which the functions shown in the FBS are arranged in a time-sequenced manner.

A.1. Functional Breakdown Structure

From the Functional Breakdown Structure (FBS) shown on the next page, the mission can be logically divided into three major phases: Beginning-of-Life (BOL), Operations (OPS), and End-of-Life (EOL). Within each phase, there are several Level 1 functions. Level 1 functions are divided into Level 2 functions, which themselves are divided into the most elementary Level 3 functions. Level 3 functions are so elementary that they can be assigned to a single *system* that performs said function.

To maintain clarity and traceability, a consistent function identifier convention is used, as explained below:

> **Function ID format:** `<FUNC or System Acronym>-<PHASE>-ZYX`
> **Example:** `PROP-BOL-123`

Where:

- `FUNC` is used for functions that are performed by two or more systems. For Level 3 functions, `FUNC` is replaced by the acronym of the system responsible: Propulsion (PROP), Crew (CREW), Payload (PLD), Communications (COMM), Flight Control System (FCS), Ground Operations (GOPS), Energy Storage and Management (ESM), or Avionics (AVIO).
- `<PHASE>` refers to the mission phase (BOL, OPS, or EOL).
- `X` is the Level 1 function number.
- `Y` is the Level 2 function number within its parent Level 1 function (zero by default).
- `Z` is the Level 3 function number within its parent Level 2 function (zero by default).

It is worth clarifying that the crew consists of the pilot and medic when the patient is not in the vehicle. This is because the medic can perform useful functions like communicating with ground personnel etc if he/she is not tending to the patient. However, when a patient is onboard the medic joins the payload system. For instance, the function `PLD-OPS-214` is assigned to the payload system since the medic (responsible for performing this function) is now with the patient.

A.2. Functional Flow Diagram

The functions identified (and allocated to systems) in the FBS can be rearranged into time-sequenced order to obtain the FFD. The high-level functional flow, which uses only level 1 functions depicts the general top-level functional flow of the mission. Evidently, the three 3 mission phases BOL, OPS and EOL can be seen. Each level 1 function is then dissected up to its own more detailed flow comprising of elementary level 3 functions to give a detailed and comprehensive timeline of the functions performed.

The mission functional flow starts off with the project planning phase, after which the designing phase commences. Following this, the manufacturing and testing phases initiate, which are performed in-loop with the design phase to iterate and refine the product. After the final design has been manufactured, the vehicle is certified and sold to the customers. In parallel to the aforementioned, marketing is also done. This finishes the BOL phase. When the customer receives the vehicle, some first-time set-up needs to be done and the pilots need to be trained. In the operational phase, the two critical missions identified in Section 2.3 are analyzed: M1 (Emergency rescue) and M3 (Inter-facility patient transfer) with each given its own detailed functional breakdown. At the end of each mission, a check is done whether maintenance is needed. If maintenance is not needed the aircraft simply goes back to waiting for emergency calls. If it is needed, maintenance is performed. During maintenance, the fault with the aircraft can be deemed un-fixable which leads to start of the end-of-life phase. When the aircraft is at end-of-life, it is decommissioned, ferried away and disassembled.

The Future of EMS

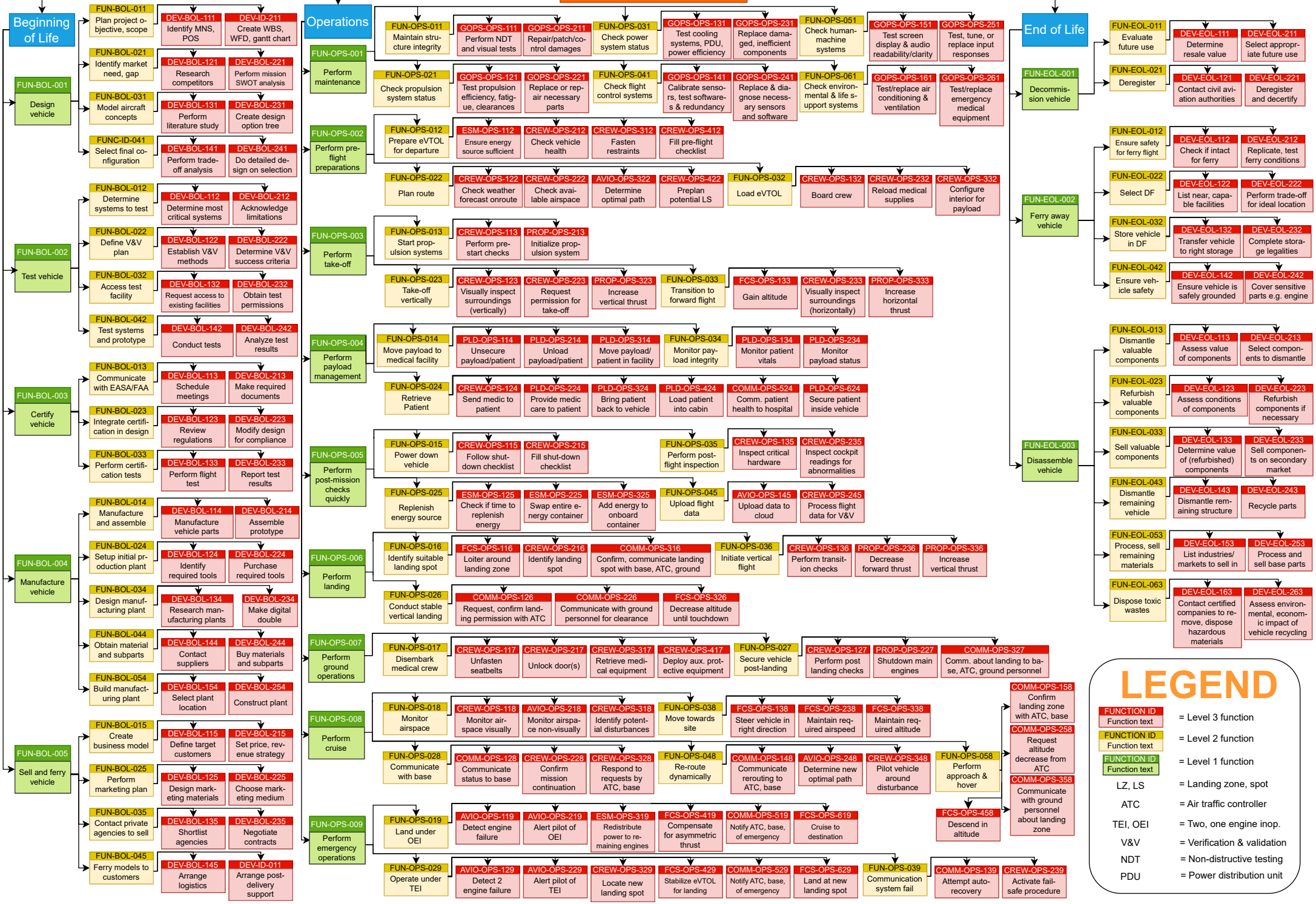

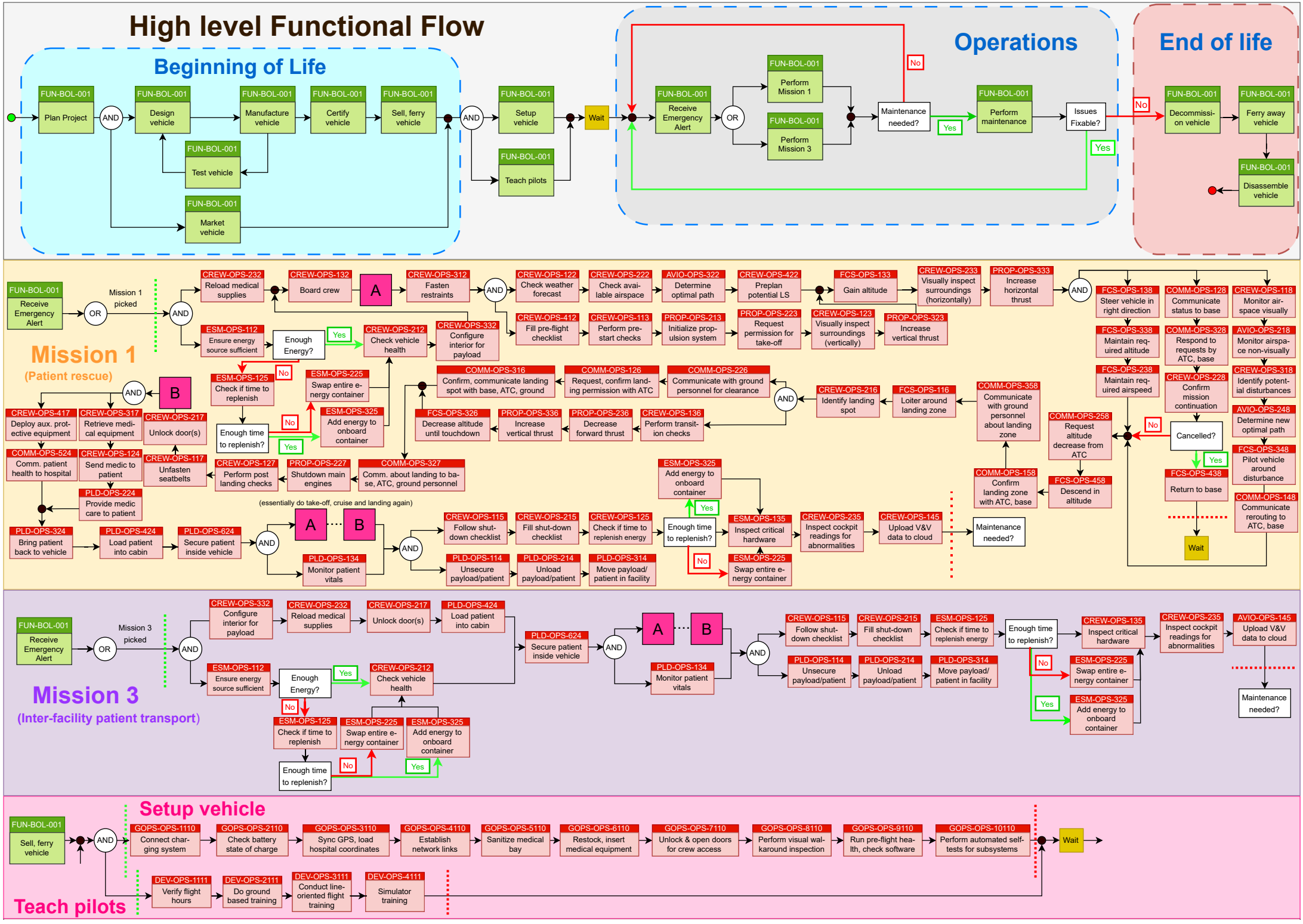
High level Functional Flow
Beginning of Life
Operations
End of life
FUN-BOL-001
Plan Project
AND
Design vehicle
Manufacture vehicle
Certify vehicle
Sell, ferry vehicle
Test vehicle
Market vehicle
Setup vehicle
Teach pilots
Wait
Receive Emergency Alert
OR
Perform Mission 1
Perform Mission 3
Maintenance needed?
No
Yes
Perform maintenance
Issues Fixable?
Decommissi-on vehicle
Ferry away vehicle
Disassemble vehicle
Mission 1
(Patient rescue)
Receive Emergency Alert
Mission 1 picked
Reload medical supplies
Board crew
A
Fasten restraints
Check weather forecast
Check avai-lable airspace
Determine optimal path
Preplan potential LS
Gain altitude
Visually inspect surroundings (horizontally)
Increase horizontal thrust
Steer vehicle in right direction
Communicate status to base
Monitor air-space visually
Ensure energy source sufficient
Enough Energy?
Check vehicle health
Configure interior for payload
Fill pre-flight checklist
Perform pre-start checks
Initialize prop-ulsion system
Request permission for take-off
Visually inspect surroundings (vertically)
Increase vertical thrust
Maintain req-uired altitude
Respond to requests by ATC, base
Monitor airspa-ce non-visually
Maintain req-uired airspeed
Confirm mission continuation
Identify potent-ial disturbances
Check if time to replenish
Swap entire e-nergy container
Add energy to onboard container
Enough time to replenish?
Confirm, communicate landing spot with base, ATC, ground
Request, confirm land-ing permission with ATC
Communicate with ground personnel for clearance
Identify landing spot
Loiter around landing zone
Communicate with ground personnel about landing zone
Request altitude decrease from ATC
Cancelled?
Determine new optimal path
Pilot vehicle around disturbance
B
Deploy aux. prot-ective equipment
Retrieve medi-cal equipment
Unlock door(s)
Comm. patient health to hospital
Send medic to patient
Unfasten seatbelts
Decrease altitude until touchdown
Increase vertical thrust
Decrease forward thrust
Perform transit-ion checks
Perform post landing checks
Shutdown main engines
Comm. about landing to ba-se, ATC, ground personnel
Provide medic care to patient
Confirm landing zone with ATC, base
Descend in altitude
Return to base
Communicate rerouting to ATC, base
Bring patient back to vehicle
Load patient into cabin
Secure patient inside vehicle
(essentially do take-off, cruise and landing again)
Monitor patient vitals
Follow shut-down checklist
Fill shut-down checklist
Check if time to replenish energy
Inspect critical hardware
Inspect cockpit readings for abnormalities
Upload V&V data to cloud
Maintenance needed?
Unsecure payload/patient
Unload payload/patient
Move payload/ patient in facility
Swap entire e-nergy container
Wait
Mission 3
(Inter-facility patient transport)
Mission 3 picked
Configure interior for payload
Reload medical supplies
Unlock door(s)
Load patient into cabin
Secure patient inside vehicle
Ensure energy source sufficient
Enough Energy?
Check vehicle health
Check if time to replenish
Swap entire e-nergy container
Add energy to onboard container
Enough time to replenish?
Follow shut-down checklist
Fill shut-down checklist
Check if time to replenish energy
Unsecure payload/patient
Unload payload/patient
Move payload/ patient in facility
Monitor patient vitals
Inspect critical hardware
Inspect cockpit readings for abnormalities
Upload V&V data to cloud
Maintenance needed?
Setup vehicle
Sell, ferry vehicle
Connect char-ging system
Check battery state of charge
Sync GPS, load hospital coordinates
Establish network links
Sanitize medical bay
Restock, insert medical equipment
Unlock & open doors for crew access
Perform visual wal-karound inspection
Run pre-flight hea-lth, check software
Perform automated self-tests for subsystems
Wait
Teach pilots
Verify flight hours
Do ground based training
Conduct line-oriented flight training
Simulator training

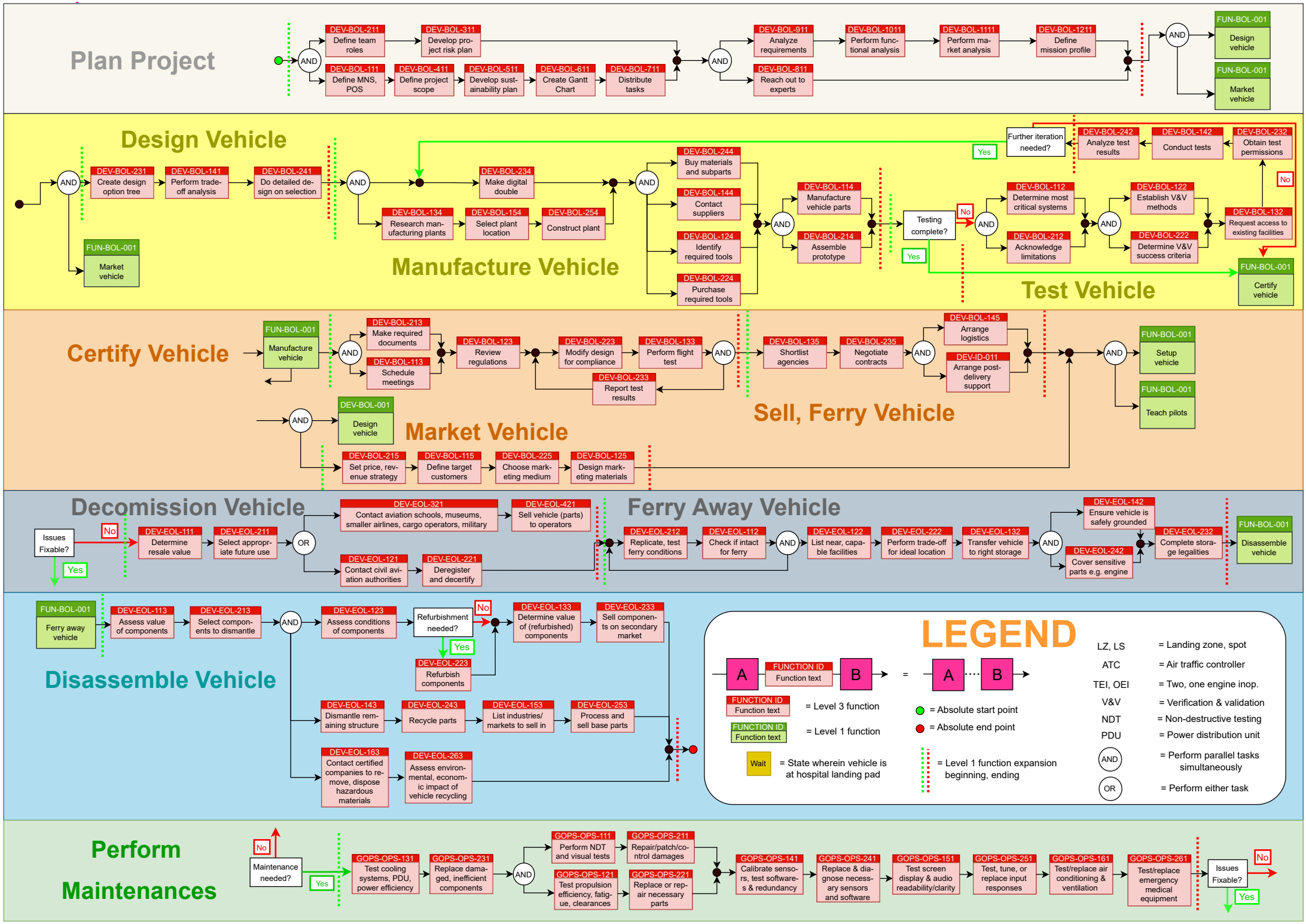
Plan Project
DEV-BOL-211 Define team roles
DEV-BOL-311 Develop project risk plan
DEV-BOL-111 Define MNS, POS
DEV-BOL-411 Define project scope
DEV-BOL-511 Develop sustainability plan
DEV-BOL-611 Create Gantt Chart
DEV-BOL-711 Distribute tasks
DEV-BOL-911 Analyze requirements
DEV-BOL-1011 Perform functional analysis
DEV-BOL-1111 Perform market analysis
DEV-BOL-1211 Define mission profile
DEV-BOL-811 Reach out to experts
FUN-BOL-001 Design vehicle
FUN-BOL-001 Market vehicle
Design Vehicle
DEV-BOL-231 Create design option tree
DEV-BOL-141 Perform trade-off analysis
DEV-BOL-241 Do detailed design on selection
FUN-BOL-001 Market vehicle
Manufacture Vehicle
DEV-BOL-134 Research manufacturing plants
DEV-BOL-154 Select plant location
DEV-BOL-254 Construct plant
DEV-BOL-234 Make digital double
DEV-BOL-244 Buy materials and subparts
DEV-BOL-144 Contact suppliers
DEV-BOL-124 Identify required tools
DEV-BOL-224 Purchase required tools
DEV-BOL-114 Manufacture vehicle parts
DEV-BOL-214 Assemble prototype
Test Vehicle
Testing complete?
Further iteration needed?
DEV-BOL-112 Determine most critical systems
DEV-BOL-212 Acknowledge limitations
DEV-BOL-122 Establish V&V methods
DEV-BOL-222 Determine V&V success criteria
DEV-BOL-132 Request access to existing facilities
DEV-BOL-242 Analyze test results
DEV-BOL-142 Conduct tests
DEV-BOL-232 Obtain test permissions
FUN-BOL-001 Certify vehicle
Certify Vehicle
FUN-BOL-001 Manufacture vehicle
DEV-BOL-213 Make required documents
DEV-BOL-113 Schedule meetings
DEV-BOL-123 Review regulations
DEV-BOL-223 Modify design for compliance
DEV-BOL-133 Perform flight test
DEV-BOL-233 Report test results
Market Vehicle
DEV-BOL-001 Design vehicle
DEV-BOL-215 Set price, revenue strategy
DEV-BOL-115 Define target customers
DEV-BOL-225 Choose marketing medium
DEV-BOL-125 Design marketing materials
Sell, Ferry Vehicle
DEV-BOL-135 Shortlist agencies
DEV-BOL-235 Negotiate contracts
DEV-BOL-145 Arrange logistics
DEV-ID-011 Arrange post-delivery support
FUN-BOL-001 Setup vehicle
FUN-BOL-001 Teach pilots
Decomission Vehicle
Issues Fixable?
DEV-EOL-111 Determine resale value
DEV-EOL-211 Select appropriate future use
DEV-EOL-321 Contact aviation schools, museums, smaller airlines, cargo operators, military
DEV-EOL-421 Sell vehicle (parts) to operators
DEV-EOL-121 Contact civil aviation authorities
DEV-EOL-221 Deregister and decertify
Ferry Away Vehicle
DEV-EOL-212 Replicate, test ferry conditions
DEV-EOL-112 Check if intact for ferry
DEV-EOL-122 List near, capable facilities
DEV-EOL-222 Perform trade-off for ideal location
DEV-EOL-132 Transfer vehicle to right storage
DEV-EOL-142 Ensure vehicle is safely grounded
DEV-EOL-242 Cover sensitive parts e.g. engine
DEV-EOL-232 Complete storage legalities
FUN-BOL-001 Disassemble vehicle
Disassemble Vehicle
FUN-BOL-001 Ferry away vehicle
DEV-EOL-113 Assess value of components
DEV-EOL-213 Select components to dismantle
DEV-EOL-123 Assess conditions of components
Refurbishment needed?
DEV-EOL-223 Refurbish components
DEV-EOL-133 Determine value of (refurbished) components
DEV-EOL-233 Sell components on secondary market
DEV-EOL-143 Dismantle remaining structure
DEV-EOL-243 Recycle parts
DEV-EOL-153 List industries/ markets to sell in
DEV-EOL-253 Process and sell base parts
DEV-EOL-163 Contact certified companies to remove, dispose hazardous materials
DEV-EOL-263 Assess environmental, economic impact of vehicle recycling
LEGEND
FUNCTION ID Function text
= Level 3 function
= Level 1 function
Wait = State wherein vehicle is at hospital landing pad
= Absolute start point
= Absolute end point
= Level 1 function expansion beginning, ending
LZ, LS = Landing zone, spot
ATC = Air traffic controller
TEI, OEI = Two, one engine inop.
V&V = Verification & validation
NDT = Non-destructive testing
PDU = Power distribution unit
AND = Perform parallel tasks simultaneously
OR = Perform either task
Perform Maintenances
Maintenance needed?
GOPS-OPS-131 Test cooling systems, PDU, power efficiency
GOPS-OPS-231 Replace damaged, inefficient components
GOPS-OPS-111 Perform NDT and visual tests
GOPS-OPS-121 Test propulsion efficiency, fatigue, clearances
GOPS-OPS-211 Repair/patch/control damages
GOPS-OPS-221 Replace or repair necessary parts
GOPS-OPS-141 Calibrate sensors, test software-s & redundancy
GOPS-OPS-241 Replace & diagnose necessary sensors and software
GOPS-OPS-151 Test screen display & audio readability/clarity
GOPS-OPS-251 Test, tune, or replace input responses
GOPS-OPS-161 Test/replace air conditioning & ventilation
GOPS-OPS-261 Test/replace emergency medical equipment
Issues Fixable?

B

Optimal Propeller Design

The methodology adopted for the optimal propeller design closely follows the work of Adkins and Liebeck [60]. In their study, a revised formulation of BEM theory is introduced to accurately design and analyze propellers under both light and moderate loading conditions. The improvements over classical methods include elimination of small-angle approximations, consistent treatment of viscous effects, and an iterative approach that ensures agreement between blade element and momentum formulations.

The foundation of the blade element theory lies in analyzing a single blade element at a radial location r along the propeller span. At this location, the local blade section encounters a relative velocity W, which is the vector sum of the axial and tangential velocity components. These are influenced by both the freestream velocity V and the propeller's angular velocity Ω, as well as by induced velocities due to the propeller loading.

The flow approaching the blade element is deflected due to induced velocities:

- The axial flow component is $V(1 + a)$, where a is the axial interference factor.
- The tangential component due to swirl is $\Omega r(1 - a')$, where a' is the rotational interference factor.

As shown in Figure B.1, the angle between the relative velocity W and the rotor plane is the inflow angle ϕ, while the blade pitch angle β is the angle between the blade chord line and the rotor plane. The difference between the pitch angle and the inflow angle gives the local angle of attack α, which directly affects the lift and drag experienced by the blade section:

$$\alpha = \beta - \phi$$

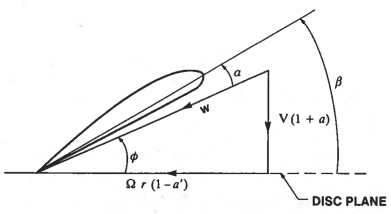

Figure B.1: *Flow geometry for blade element at radial station r[60].*

B.1. Momentum Equations

The thrust produced by a propeller can be derived from momentum theory by applying Newton's second law to a control volume surrounding the rotor. The net thrust T is given by the change in axial momentum across the control volume, i.e., $T = \dot{m}(V_{\text{exit}} - V)$, where $\dot{m}$ is the mass flow rate, V is the freestream velocity, and V_{exit} is the velocity far downstream in the propeller wake.

To apply this to a blade element, the propeller disc is divided into differential annular rings of radius r and width dr, as illustrated in Figure B.2. The differential mass flow rate through such an annulus is $d\dot{m} = 2\pi r\rho V(1+a)$, where a is the axial interference factor.

Downstream, in the slipstream, the velocity increases to $V(1 + b)$, where b is referred to as the axial slipstream factor. From momentum theory, it is known that $b = 2a$ [60]. Substituting this relation into the axial momentum balance leads to the thrust per unit radius:

$$T' = 2\pi r\rho V(1 + a)(2VaF) \tag{B.1}$$

Here, F is the loss of momentum factor, introduced to account for radial flow effects, and ρ is the air density.

A similar derivation applies to the torque, which arises from the change in angular momentum due to the swirl velocity induced in the slipstream. The torque per unit radius is expressed as:

$$\frac{Q'}{r} = 2\pi r\rho V(1 + a)(2\Omega r a' F) \tag{B.2}$$

where a' is the rotational interference factor, and Ω is the angular velocity of the propeller in radians per second.

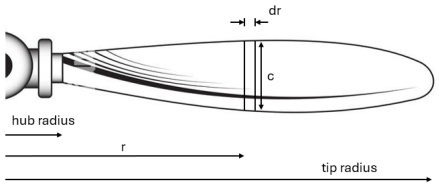

Figure B.2: *Annular ring element used in momentum analysis*

B.2. Circulation Equations

The aerodynamic forces generated by the blade section can be decomposed into:

- A lift force L' perpendicular to W
- A drag force D' aligned with W

These forces are then projected along the thrust and torque directions to compute the elemental thrust T' and torque Q'. The integration of these contributions along the blade span leads to the total thrust and torque produced by the propeller.

Looking at Figure B.3, the equations for T' and Q'/r per unit radius can be written as:

$$\begin{aligned} T' &= L' \cos\phi - D' \sin\phi \\ Q'/r &= L' \sin\phi + D' \cos\phi \end{aligned} \tag{B.3}$$

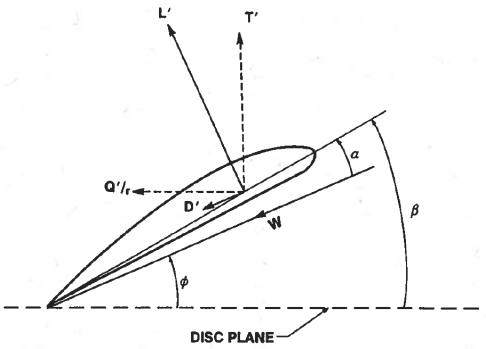

Figure B.3: *Force diagram for a blade element[60].*

An alternative formulation for computing blade forces is based on lifting-line theory and the concept of circulation. According to the Kutta–Joukowski theorem, the lift generated per unit span is equal to $\rho W \Gamma$, where Γ is the circulation around the airfoil and W is the local relative velocity. For a blade with B blades, the lift per unit radius becomes:

$$L' = B\rho W \Gamma \tag{B.4}$$

To relate the circulation to the induced velocity in the wake, Adkins and Liebeck express the total circulation shed into the wake annulus as [60]:

$$B\Gamma = 2\pi r F w_t \tag{B.5}$$

Here, w_t is the swirl velocity in the slipstream. It can be related to the vortex displacement velocity v' as $w_t = v' \sin\phi\cos\phi$. Introducing the nondimensional displacement velocity ratio $\zeta = v'/V$, this becomes $w_t = \zeta V \sin\phi\cos\phi$. Substituting this into the expression for circulation, and defining the variable $G = Fx\cos\phi\sin\phi$, where $x = \Omega r/V$, gives:

$$\Gamma = \frac{2\pi V^2 \zeta G}{B\Omega}$$

Substituting this into the lift expression and expressing thrust and torque from Equation B.3 using Γ, the final forms for thrust and torque per unit radius become:

$$\begin{aligned} T' &= \rho W \frac{2\pi V^2 \zeta G}{B\Omega} \cos\phi(1 - \epsilon \tan\phi) \\ \frac{Q'}{r} &= \rho W \frac{2\pi V^2 \zeta G}{B\Omega} \sin\phi \left(1 + \frac{\epsilon}{\tan\phi}\right) \end{aligned} \tag{B.6}$$

Here, $\epsilon = c_d/c_l$ is the drag-to-lift ratio at the given section, obtained from airfoil performance data.

Condition for Minimum Energy Loss

At this stage, to minimize induced energy losses, a key step in the Adkins and Liebeck approach is to enforce equivalence between the momentum and circulation equations [60]. Specifically, the thrust and torque expressions derived from momentum theory are equated with those from lifting-line circulation theory. This matching yields expressions for the interference factors in terms of the displacement velocity ratio ζ, the flow angle ϕ, and the local aerodynamic efficiency parameter $\epsilon = c_d/c_l$.

The axial and tangential interference factors are given by:

$$a = \frac{\zeta}{2} \cos^2\phi \, (1 - \epsilon \tan\phi) \tag{B.7}$$

$$a' = \frac{\zeta}{2x} \cos\phi \sin\phi \left(1 + \frac{\epsilon}{\tan\phi}\right) \tag{B.8}$$

Here, $x = \Omega r/V$ is the local advance ratio, and the terms involving ϵ account for viscous losses in the blade section.

By substituting these expressions for a and a' into the geometric relation for the flow angle, a simple and important result is obtained:

$$\tan\phi = (1 + \frac{\zeta}{2})/x = (1 + \frac{\zeta}{2})\frac{\lambda}{\xi} \tag{B.9}$$

where λ is the constant speed ratio $V/\Omega R$, and $\xi = r/R$ is the non-dimensional radial coordinate.

This result leads directly to Betz's condition for minimum energy loss. It implies that, for the trailing vortex sheet to form a regular and energetically optimal helical pattern the product $r \tan\phi$ must remain constant across the blade span. This means the displacement velocity ratio ζ must be constant with respect to r. This condition ensures that the induced swirl velocity in the wake does not vary radially, thus preventing unnecessary energy dissipation and maximizing propeller efficiency.

B.3. Constraint Equations Based on Specified Thrust

In the method of Adkins and Liebeck [60], constraint equations are developed to allow the design to satisfy either a specified thrust or a specified power requirement. In this study, the thrust-based formulation is used, as thrust requirements are typically known in advance for each flight phase based on aircraft weight or aerodynamic drag.

To incorporate this requirement into the circulation-based formulation, the non-dimensional thrust coefficient is introduced. It is defined as the ratio of the actual thrust to the dynamic pressure and area of the propeller disc:

$$T_c = \frac{2T}{\rho V^2 \pi R^2} \tag{B.10}$$

The nondimensional form of the differential thrust expression can be written as:

$$T_c' = I_1' \zeta - I_2' \zeta^2 \tag{B.11}$$

where ζ is the displacement velocity ratio, and I_1' and I_2' are spanwise functions given by:

$$\begin{aligned} I_1' &= 4\xi G(1 - \epsilon \tan\phi) \\ I_2' &= \lambda \left(\frac{I_1'}{2\xi}\right)(1 + \epsilon/\tan\phi)\sin\phi\cos\phi \end{aligned} \tag{B.12}$$

Once the blade span is discretized, the integrated values of I_1' and I_2' over the interval $\xi \in [\xi_0, 1]$ (from hub to tip) give the coefficients I_1 and I_2. These are substituted into the quadratic thrust constraint equation:

$$\zeta = \frac{I_1}{2I_2} - \left[\left(\frac{I_1}{2I_2}\right)^2 - \frac{T_c}{I_2}\right]^{1/2} \tag{B.13}$$

This expression provides a closed-form solution for the optimal value of ζ that yields the specified thrust while minimizing induced losses. The smaller root is selected to satisfy the Betz condition.

Once ζ is known, it can also be used to evaluate the power coefficient via:

$$P_c = J_1\zeta + J_2\zeta^2 \tag{B.14}$$

where the corresponding integrand terms are:

$$\begin{aligned} J_1' &= 4\xi G\left(1 + \epsilon/\tan\phi\right) \\ J_2' &= \left(\frac{J_1'}{2}\right)\left(1 - \epsilon\tan\phi\right)\cos^2\phi \end{aligned} \tag{B.15}$$

This power coefficient P_c can later be used to compute the efficiency of the designed propeller.

B.4. Blade Geometry

The determination of the blade geometry follows from the circulation-based formulation developed in the previous sections. As shown in Figure B.2, the blade is divided into differential elements dr at each radial station r. For each element, the chord length is denoted by c, and the local lift coefficient by c_l. The lift per unit span is defined by the standard aerodynamic relation:

$$L' = \frac{1}{2}\rho W^2 c c_l$$

where W is the local relative velocity between the air and the blade. This expression can be equated to the lift derived from the Kutta–Joukowski theorem, $\rho W\Gamma$, where the circulation Γ is obtained from the optimal circulation condition given in Equation B.5. Setting these two expressions equal and solving for Wc yields:

$$Wc = \frac{4\pi\lambda G V R\zeta}{Bc_l} \tag{B.16}$$

This equation allows the determination of the blade chord once ζ, c_l, and the inflow angle ϕ (embedded in G) are known.

Subsequently, the local Reynolds number for each blade section can be computed from:

$$Re = \frac{\rho W c}{\mu} \tag{B.17}$$

This value is required, together with the lift coefficient c_l, to determine the airfoil angle of attack α at each section.

The local flow speed W is related to the freestream velocity and the inflow angle by:

$$W = \frac{V(1+a)}{\sin\phi} \tag{B.18}$$

Thus, the blade geometry is fully determined by the local values of ϕ, a, c_l, and the design-imposed circulation and thrust constraints. These quantities are obtained iteratively during the solution process and define both the blade twist and chord distribution at the end.

B.5. Blade Design Procedure

The blade design process follows an iterative methodology based on the equations and principles established in the formulation by Adkins and Liebeck [60]. The starting point is the specification of known operating conditions: the required thrust, freestream velocity, rotational speed, number of blades, and the radial extent of the blade (hub and tip radii). The span is discretized into a finite number of stations at which the blade geometry and aerodynamic conditions will be computed. An airfoil shape must also be given as input, since the local aerodynamic coefficients are used in the design procedure.

The process begins by assuming an initial value for the displacement velocity ratio ζ, typically $\zeta = 0$. With this guess, the Prandtl tip loss factor F and the inflow angle ϕ are evaluated at each blade station. The loss factor is calculated using the expression:

$$F = \frac{2}{\pi}\arccos(e^{-f}), \quad \text{with} \quad f = \frac{B}{2}\frac{1-\xi}{\xi\sin\phi_t} \tag{B.19}$$

where $\xi = r/R$ is the nondimensional radius, B is the number of blades, and ϕ_t is the inflow angle at the blade tip. The value of ϕ_t is found using Equation B.9 by evaluating it at $\xi = 1$ (basically the tip):

$$\tan\phi_t = \lambda(1 + \zeta/2) \tag{B.20}$$

The Betz condition is enforced and the inflow angle along the span is determined by requiring $r \tan \phi$ to be constant. This leads to the relation:

$$\tan \phi = \frac{\tan \phi_t}{\xi} \tag{B.21}$$

With the inflow angle now defined at each station, the design proceeds by determining the lift coefficient c_l. This is done by giving an initial estimate of the Reynolds number and identifying the angle of attack α that minimizes the viscous loss, represented by the drag to lift ratio $\epsilon = c_d/c_l$. Minimizing ϵ ensures that each blade section operates as efficiently as possible, maximizing the lift generated for a given amount of drag.

Once c_l is selected, the product Wc and the Reynolds number can be computed using Equation B.16 and Equation B.17. With these known, the axial and tangential interference factors a and a' are calculated using Equation B.7 and Equation B.8. The local relative velocity W is then updated via Equation B.18.

The blade chord c is determined from the known value of Wc, and the blade twist angle β is obtained by summing the local angle of attack and inflow angle: $\beta = \alpha + \phi$.

At this stage, the nondimensional integrand terms I_1', I_2', J_1', and J_2' are computed (see Equation B.12 and Equation B.15) at each station. These functions are numerically integrated over the blade span from the hub radius ξ_0 to the tip ($\xi = 1$), yielding the total integrals I_1, I_2, J_1, and J_2. With these, a new value for the velocity displacement ratio ζ is computed using Equation B.13.

If this new value of ζ deviates significantly from the previous estimate, the iteration is repeated using the updated value. Convergence is typically declared when the relative change in ζ is below a predefined tolerance (e.g., 0.1%).

Once convergence is achieved, the final values of the thrust coefficient T_c and power coefficient P_c are used to compute the propeller efficiency, given by $\eta = T_c/P_c$ (see Equation B.11 and Equation B.14). Additional blade parameters such as the solidity ratio, defined as:

$$\sigma = \frac{Bc}{2\pi r} \tag{B.22}$$

can also be evaluated. The solidity is a measure of the blade area density and affects both aerodynamic loading and structural characteristics.

This design process is computationally efficient and generally converges within a few iterations. It ensures a blade geometry that satisfies thrust requirements while adhering to the optimal induced flow structure defined by the Betz condition.

B.6. Analysis of Arbitrary Designs

Once the optimal blade geometry has been determined through the design procedure, it can be evaluated under various operating conditions. This allows assessment of how the fixed geometry performs when thrust, freestream velocity, or rotational speed deviates from the design point.

The input to this analysis is the blade geometry as obtained from the design method. The freestream velocity V and rotational speed Ω are set according to the off-design flight condition of interest.

The analysis begins with an initial estimate for the inflow angle ϕ, based on Equation B.9, in which $\zeta = 0$ is assumed. An initial Reynolds number is calculated at each station using the formula $Re = \rho V c/\mu$.

The local angle of attack α is then found from $\alpha = \beta - \phi$. Using the known airfoil data, the lift coefficient c_l and drag to lift ratio c_d/c_l are interpolated based on α and the local Reynolds number. The tangential and normal force coefficients are then computed as:

$$c_y = c_l \cos \phi - c_d \sin \phi \tag{B.23}$$

$$c_x = c_l \sin \phi + c_d \cos \phi \tag{B.24}$$

Next, the local solidity is computed via $\sigma = Bc/(2\pi r)$. The intermediate quantities K and K' are calculated using:

$$K = \frac{c_y}{4 \sin^2 \phi} \tag{B.25}$$

$$K' = \frac{c_x}{4 \sin \phi \cos \phi} \tag{B.26}$$

The Prandtl tip loss factor F is determined as in Section B.5 using the tip angle ϕ_t. The axial and tangential interference factors are then calculated from:

$$a = \frac{\sigma K}{F - \sigma K} \tag{B.27}$$

$$a' = \frac{\sigma K'}{F + \sigma K'} \tag{B.28}$$

The relative wind velocity at each blade section is computed from Equation B.18. The updated flow angle ϕ is obtained from the velocity triangle:

$$\phi = \tan^{-1}\left(\frac{V(1+a)}{\Omega r(1-a')}\right) \tag{B.29}$$

This process is repeated iteratively until convergence is achieved for ϕ at all radial stations. Once convergence is reached, the thrust and torque per unit span are computed using:

$$T'(r) = \frac{1}{2}\rho W^2 B c c_y \tag{B.30}$$

$$Q'(r) = \frac{1}{2}\rho W^2 B c c_x r \tag{B.31}$$

To compute nondimensional performance coefficients, the differential thrust and power coefficients are determined using:

$$C_T' = \left(\frac{\pi^3}{4}\right)\sigma c_y \xi F^{32}\left(\frac{F + \sigma K'}{\cos\phi}\right)^{-2} \tag{B.32}$$

$$C_P' = C_T' \pi \xi \left(\frac{c_x}{c_y}\right) \tag{B.33}$$

These are integrated spanwise over $\xi \in [\xi_0, 1]$ to obtain total C_T and C_P. Finally, the propeller efficiency is just $\frac{C_T J}{C_P}$ with the advance ratio $J = \frac{V}{nD}$ where n is the rotation rate in revolutions per second and D is the propeller diameter.

C

Static Longitudinal Stability Calculations

This appendix presents the estimation of the hinge moment derivatives and the elevon control power needed for static longitudinal stability analysis. The estimations are carried out empirically using Roskam's Airplane Design Part VI [102]. For the sake of brevity, values and graphs are only presented for the converged final design. Furthermore, although DoctAir has elevons instead of a separate elevator, this appendix uses the word 'elevator' to maintain consistency with Roskam.

C.1. Hinge Moment Derivatives Estimation

In this section, the control surface hinge moment derivatives are estimated. First, the two-dimensional coefficients are calculated. They are then corrected for three-dimensional effects.

C.1.1. 2D Control Surface Hinge Moment Derivatives

Table C.1 and Table C.2 present the results of the estimation. The process of the estimation is then described.

Table C.1: *Values obtained for the 2D hinge moment derivative due to control surface deflection*

Property	Value	Unit	Reference
$\frac{t}{c}$	0.1027	-	Eppler 186 airfoil
$\frac{c_f}{c}$	0.1875	-	
Y_{90}	1.694	%	Eppler 186 airfoil
Y_{99}	0.149	%	Eppler 186 airfoil
$\tan\frac{1}{2}\Phi'_{TE}$	0.0858	-	Figure C.2a
$\frac{c_{l_\alpha}}{(c_{l\alpha})theory}$	0.89	-	Figure C.2a
$\frac{c'_{h_\delta}}{(c_{h_\delta})_{theory}}$	0.91	-	Figure C.3a
$(c_{h_\delta})_{theory}$	-0.81	rad^{-1}	Figure C.3b
c'_{h_δ}	-0.7371	rad^{-1}	Equation C.2
c''_{h_δ}	-0.7371	rad^{-1}	Equation C.3
balance ratio	0.32	-	Figure C.4
$\frac{(c_{h_\delta})_{bal}}{c''_{h_\delta}}$	0.25	-	Figure C.4a
$(c_{h_\delta})_{bal}$	-0.1843	rad^{-1}	Equation C.4
c_{h_δ}	-0.1901	rad^{-1}	Equation C.5

Table C.2: *Values obtained for the 2D hinge moment derivative due to angle of attack*

Property	Value	Unit	Reference
$\frac{c'_{h_\alpha}}{(c_{h_\alpha})_{theory}}$	0.67	-	Figure C.5b
$(c_{h_\alpha})_{theory}$	-0.4	rad^{-1}	Figure C.5a
c'_{h_α}	-0.268	rad^{-1}	Equation C.2
c''_{h_α}	-0.268	rad^{-1}	Equation C.7
$\frac{(c_{h_\alpha})_{bal}}{c''_{h_\alpha}}$	0.5	-	Figure C.4b
$(c_{h_\alpha})_{bal}$	-0.134	rad^{-1}	Equation C.8
c_{h_α}	-0.1382	rad^{-1}	Equation C.9

The procedure followed to estimate the two-dimensional hinge moment due to control surface deflection, c_{h_δ}, is as follows:

1. Verify trailing edge condition in Equation C.1. The trailing edge angles are defined graphically in Figure C.1a. Due to the assumption that the upper and lower surface lines of the control surfaces are straight, the trailing edge condition is satisfied.
$$\tan\left(\frac{\Phi'_{te}}{2}\right) = \tan\left(\frac{\Phi''_{te}}{2}\right) = \tan\left(\frac{\Phi_{te}}{2}\right) = \frac{t}{c} \tag{C.1}$$
2. Find the first estimate of the hinge moment derivative due to control surface with Equation C.2 which uses a correction for the lift curve slope ratio (given in Figure C.2a) and a theoretical value based on control surface length and the thickness-to-chord ratio of the wing.
$$c'_{h_\delta} = \frac{c'_{h_\delta}}{(c_{h_\delta})_{theory}}(c_{h_\delta})_{theory} \tag{C.2}$$
3. Since the trailing edge condition is satisfied, no correction for the curve of the airfoil surfaces is needed and $c''_{h_\delta} = c'_{h_\delta}$.
$$c''_{h_\delta} = c'_{h_\delta} \tag{C.3}$$

4. Use Equation C.4 to correct for the different control surface nose shapes and aerodynamic balance. The correction ratio is read off from Figure C.4b.

$$(c_{h_{\delta})_{bal}} = c''_{h_\delta} \frac{(c_{h_\delta)_{bal}}}{c''_{h_\delta}} \tag{C.4}$$

5. Finally, use Equation C.5 the coefficient is corrected for compressibility effects associated with the Mach number. This is the final value used for the two-dimensional hinge moment derivative due to control surface deflection.

$$(c_{h_\delta})_M = \frac{(c_{h_\delta})_{bal}}{\sqrt{1-M^2}} = c_{h_\delta} \tag{C.5}$$

The procedure for estimating the two-dimensional hinge moment derivative due to angle of attack, c_{h_α}, is equivalent but uses Equation C.6 through to Equation C.9, Figure C.4b, and Figure C.5.

$$c'_{h_\alpha} = \frac{c'_{h_\alpha}}{(c_{h_\alpha})_{theory}} (c_{h_\alpha})_{theory} \tag{C.6}$$

$$c''_{h_\alpha} = c'_{h_\alpha} \tag{C.7}$$

$$(c_{h_\alpha)_{bal}} = c''_{h_\alpha} \frac{(c_{h_\alpha)_{bal}}}{c''_{h_\alpha}} \tag{C.8}$$

$$(c_{h_\alpha})_M = \frac{(c_{h_\alpha})_{bal}}{\sqrt{1-M^2}} \tag{C.9}$$

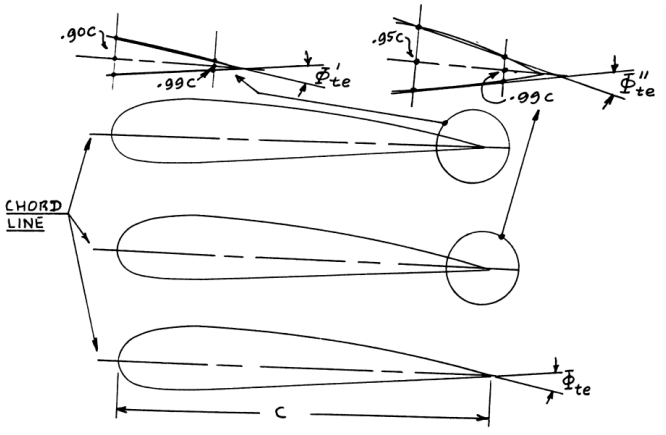

(a) *Trailing edge angles*

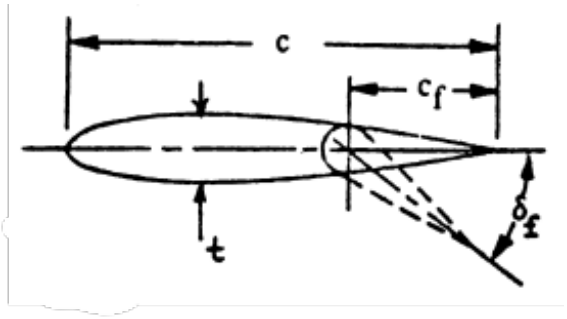

(b) *Cross-sectional parameters of a plain flap control surface*

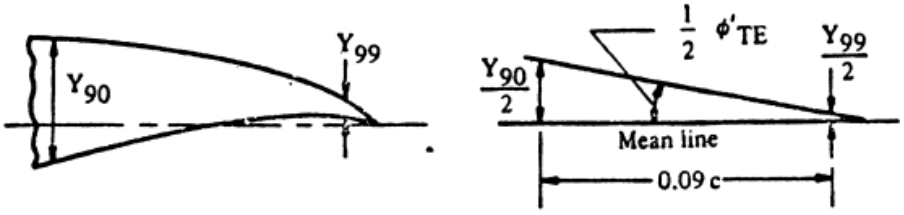

(c) *Trailing edge thicknesses*

Figure C.1: *Geometric definitions for hinge moment calculations [102]*

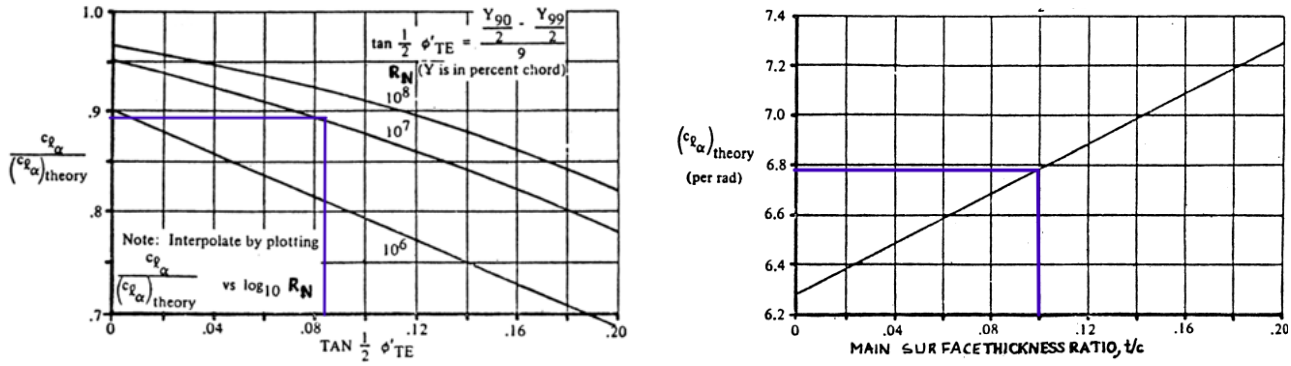

(a) *Lift curve slope correction for trailing edge dimensions*

(b) *Theoretical two-dimensional lift curve slope*

Figure C.2: *Effect of airfoil thickness and trailing edge angle on the lift curve slope [102]*

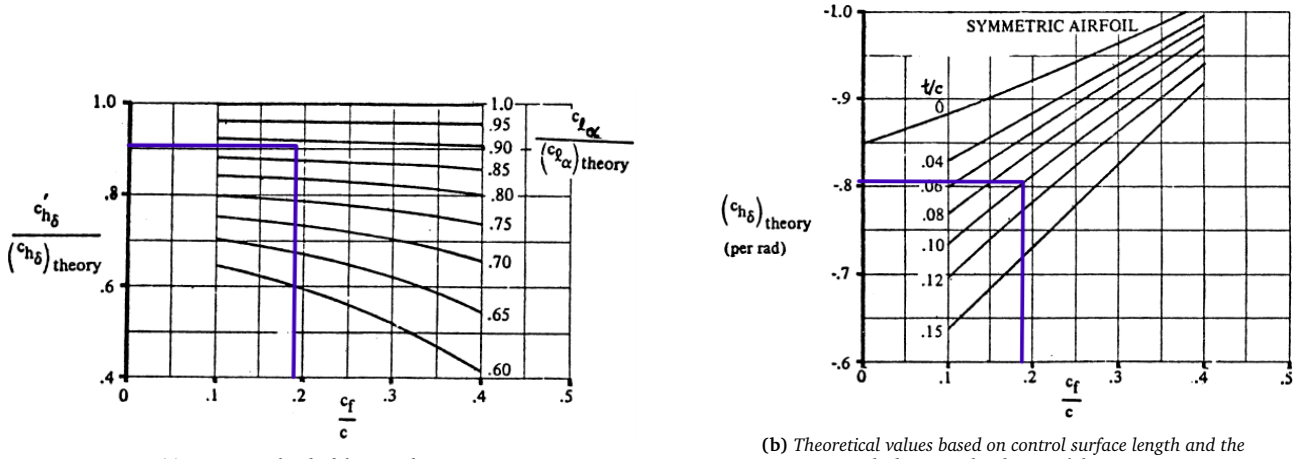

(a) *Correction for the lift curve slope ratio*

(b) *Theoretical values based on control surface length and the thickness-to-chord ratio of the wing*

Figure C.3: *Two-dimensional hinge moment derivative due to control surface deflection [102]*

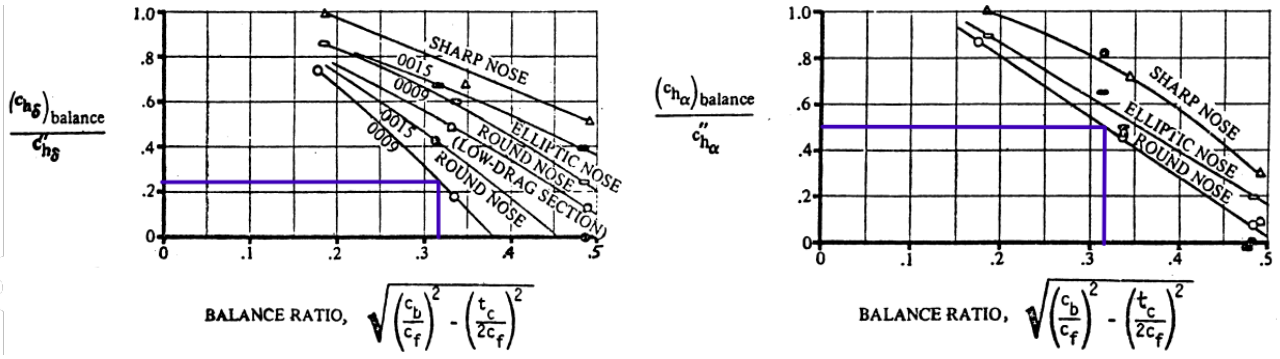

(a) *Hinge moment due to control surface deflection*

(b) *Hinge moment due to angle of attack*

Figure C.4: *Effect of nose shape and balance on the two-dimensional hinge moment derivatives [102]*

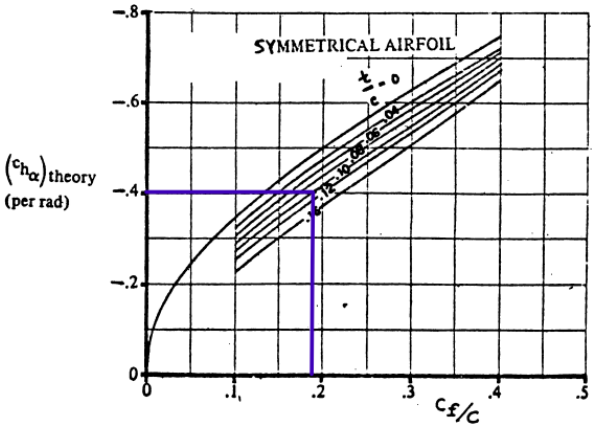

(a) *Theoretical hinge moment derivative due to angle of attack*

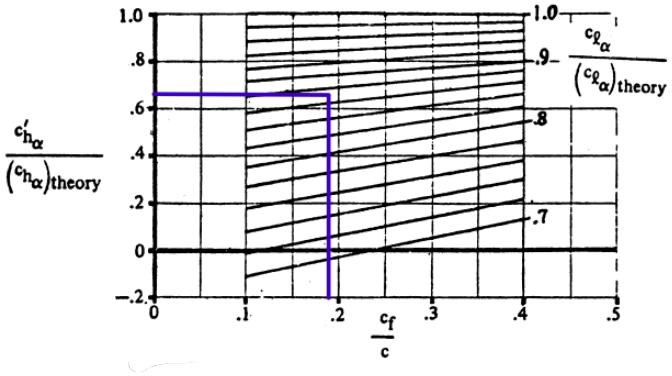

(b) *Hinge moment derivative due to angle of attack correction for lift curve slope and flap length*

Figure C.5: *Effect of control surface and wing dimensions on the two-dimensional hinge moment derivative due to angle of attack [102]*

C.1.2. 3D Control Surface Hinge Moment Derivatives

Table C.3 and Table C.4 present the results of the estimation. The process of the correction for the size and placement of the control surface, as well as other 3D effects, is described below.

Table C.3: *Values obtained for the 3D hinge moment derivative due to angle of attack*

Property	Value	Unit	Reference
A	2.4	-	
$\Lambda_{c/4}$	0.80	rad	
$\frac{\Delta C_{h_\alpha}}{c_{l_\alpha} B_2 K_\alpha \cos\Lambda_{c/4}}$	0.165	-	Figure C.6a
c_{l_α}	0.109	rad^{-1}	Figure C.2b
$\frac{c_b}{c_f}$	0.25	-	
B_2	0.72	-	Figure C.6c
η_i	0.61	-	
η_o	1	-	
K_{α_i}	2.3	-	Figure C.6b
K_{α_o}	4.3	-	Figure C.6b
K_α	2.3	-	Equation C.12
ΔC_{h_α}	1.271	rad^{-1}	Equation C.11
C_{h_α}	1.210	rad^{-1}	Equation C.10

Table C.4: *Values obtained for the 3D hinge moment derivative due to control surface deflection*

Property	Value	Unit	Reference
Λ_{hl}	0.279	rad	
α_δ	0.43	-	Figure C.8a
$\frac{\Delta C_{h_\delta}}{c_{l_\delta} B_2 K_\delta \cos\Lambda_{c/4} \cos\Lambda_{hl}}$	0.031	-	Figure C.7a
K_{δ_i}	2.1	-	Figure C.7b
K_{α_o}	4.3	-	Figure C.7b
K_δ	2.1	-	Equation C.15
c_{l_δ}	3.6	rad^{-1}	Figure C.8b
ΔC_{h_δ}	0.0113	rad^{-1}	Equation C.14
C_{h_δ}	-0.1012	rad^{-1}	Equation C.13

The three-dimensional hinge moment derivative due to angle of attack is given by Equation C.10 and Equation C.14.

$$C_{h_\alpha} = \frac{A\cos\Lambda_{c/4}}{A + 2\cos\Lambda_{c/4}} (c_{h_\alpha})_M + \Delta C_{h_\alpha} \tag{C.10}$$

$$\Delta C_{h_\alpha} = \frac{\Delta C_{h_\alpha}}{c_{l_\alpha} B_2 K_\alpha \cos\Lambda_{c/4}} c_{l_\alpha} B_2 K_\alpha \cos\Lambda_{c/4} \tag{C.11}$$

All parameters can be referenced from Table C.3, and K_α is the correction for control surface dimensions given by Equation C.12.

$$K_\alpha = \frac{(K_\alpha)_{\eta_i}(1-\eta_i) - (K_\alpha)_{\eta_o}(1-\eta_o)}{\eta_o - \eta_i} \tag{C.12}$$

To calculate K_α, the inboard and outboard stations of the elevon as a fraction of the semi-span, η_i and η_o, are used to read off $(K_\alpha)_{\eta_i}$ and $(K_\alpha)_{\eta_o}$ from Figure C.6b.

The three-dimensional hinge moment derivative due to control surface deflection is given by Equation C.13 and Equation C.11.

$$C_{h_\delta} = \cos\Lambda_{c/4} \cos\Lambda_{hl} \left[(c_{h_\delta})_M - \alpha_\delta (c_{h_\alpha})_M \frac{2\cos\Lambda_{c/4}}{A + 2\cos\Lambda_{c/4}} \right] + \Delta C_{h_\delta} \tag{C.13}$$

$$\Delta C_{h_\delta} = \frac{\Delta C_{h_\delta}}{c_{l_\delta} B_2 K_\delta \cos\Lambda_{c/4} \cos\Lambda_{hl}} c_{l_\delta} B_2 K_\delta \cos\Lambda_{c/4} \cos\Lambda_{hl} \tag{C.14}$$

All parameters can be referenced from Table C.4 and K_δ is given by Equation C.15.

$$K_\delta = \frac{(K_\delta)_{\eta_i}(1-\eta_i) - (K_\delta)_{\eta_o}(1-\eta_o)}{\eta_o - \eta_i} \tag{C.15}$$

This equation is used in the same manner as Equation C.12 but with Figure C.7b.

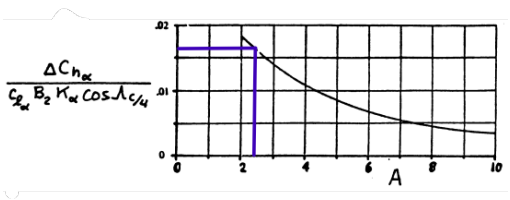

(a) *Correction for the aspect ratio of the wing*

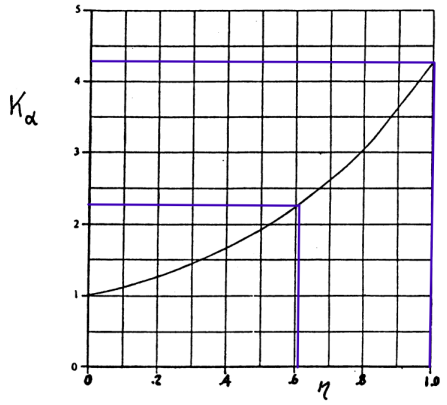

(b) *Correction for the width and position of the control surfaces*

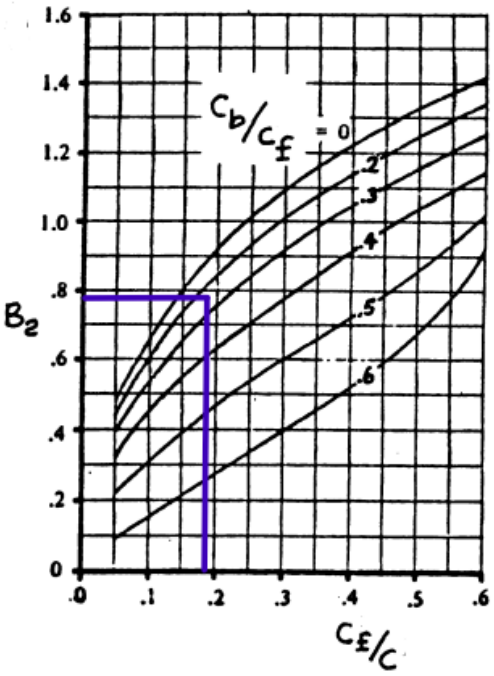

(c) *Correction for the position of the hinge line*

Figure C.6: *Three-dimensional correction factors for the control surface hinge moment derivative due to angle of attack [102]*

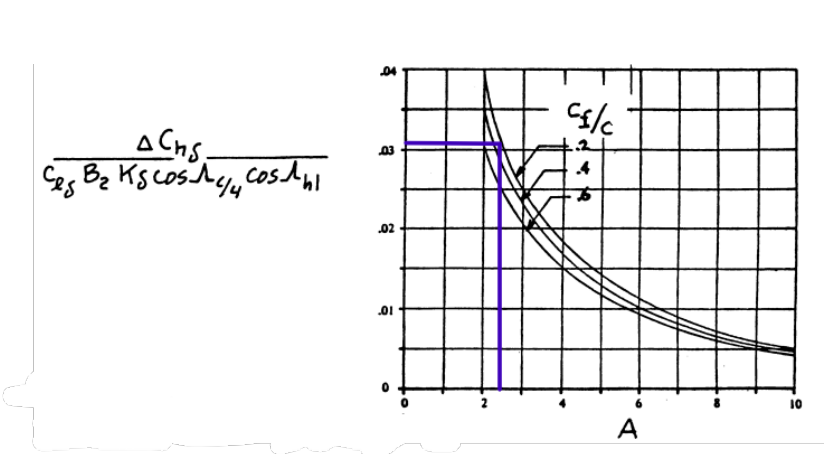

(a) *Correction for the aspect ratio of the wing*

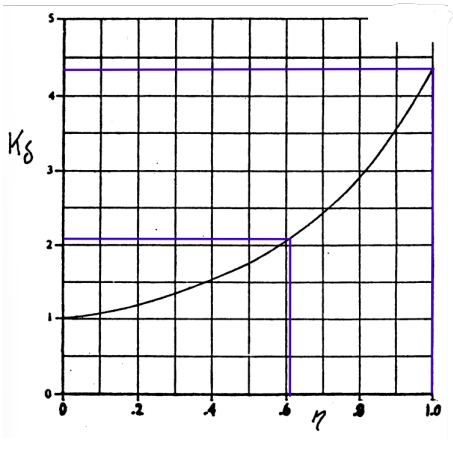

(b) *Correction for the width and position of the control surfaces*

Figure C.7: *Three-dimensional correction factors for the hinge moment derivative due to control surface deflection [102]*

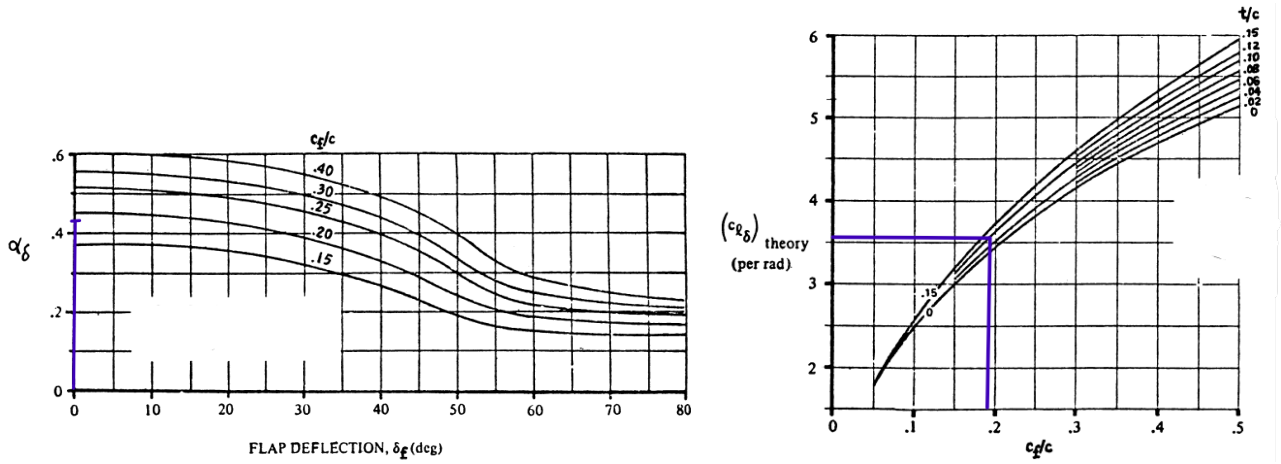

(a) *Airfoil effectiveness parameter* **(b)** *Airfoil lift curve slope due to control surface deflection [102]*

Figure C.8: *Lift effectiveness corrections*

C.2. Pitching Moment Due to Elevator Deflection Estimation

Table C.5 presents the results of the estimation. The equations used for the estimation are then presented below.

Table C.5: *Values obtained for the elevator control power*

Property	Value	Unit	Reference
λ	0.139	-	
K_b	0.23	-	Figure C.9a
$\frac{c_{l_\delta}}{(c_{l_\delta})_{theory}}$	0.82	-	Figure C.9b
k'	1	-	Linear lift curve
$c_{l_{\alpha_h}}$	0.109	deg^{-1}	From NACA0009 airfoil
$\frac{(\alpha_\delta)_{C_L}}{(\alpha_\delta)_{c_l}}$	1.14	-	Figure C.9c
α_{δ_e}	7.002	-	Equation C.17
A_e	2.88	-	
β	0.970	-	Prandtl-Glauert correction
$\Lambda_{c/2_e}$	0.197	rad	
$C_{L_{\alpha_h}}$	0.117	rad^{-1}	Equation C.19
η_h	1	-	Linear lift curve
$\bar{x}_{ac_e}$	2.065	-	
$\bar{x}_{cg}$	1.285	-	
S_e	15.73	m^2	
S	36.9	m^2	
$\bar{V}_h$	0.333	-	Equation C.20
$C_{m_{i_h}}$	-0.039	rad^{-1}	Equation C.18
$C_{m_{\delta_e}}$	-0.2731	rad^{-1}	Equation C.16

The pitching moment due to elevator deflection, $C_{m_{\delta_e}}$, also called elevator control power, is estimated using equation Equation C.16.

$$C_{m_{\delta_e}} = \alpha_{\delta_e} C_{m_{i_h}} \tag{C.16}$$

Here, α_{δ_e} is found from Equation C.17, where all parameters can be referenced from Table C.5.

$$\alpha_{\delta_e} = K_b \frac{c_{l_\delta}}{(c_{l_\delta})_{theory}} (c_{l_\delta})_{theory} \frac{k'}{c_{l_{\alpha_h}}} \frac{(\alpha_\delta)_{C_L}}{(\alpha_\delta)_{c_l}} \tag{C.17}$$

$C_{m_{i_h}}$ is found from Equation C.18, where $C_{L_{\alpha_h}}$ is estimated with Equation C.19, $\eta_h = 1$, and $\bar{V}_h$ is the equivalent horizontal tail volume coefficient found with Equation C.20. It is important to note that since DoctAir lacks a horizontal tail surface, S_h

in Equation C.20 is the equivalent horizontal tail area which represents the spanwise strip of the wing between the inboard and outboard station of the elevon, taken over the full fore-aft chord.

$$C_{m_{i_h}} = -C_{L_{\alpha_h}} \eta_h \bar{V}_h \tag{C.18}$$

$$C_{L_{\alpha_h}} = \frac{2\pi A_e}{2 + \sqrt{\frac{A_e^2 \beta^2}{c_{l_{\alpha_h}}^2}(1 + \frac{\tan^2 \Lambda_{c/2_e}}{\beta^2}) + 4}} \tag{C.19}$$

$$\bar{V}_h = \frac{\bar{x}_{ac_e} - \bar{x}_{cg}}{S_e/S} \tag{C.20}$$

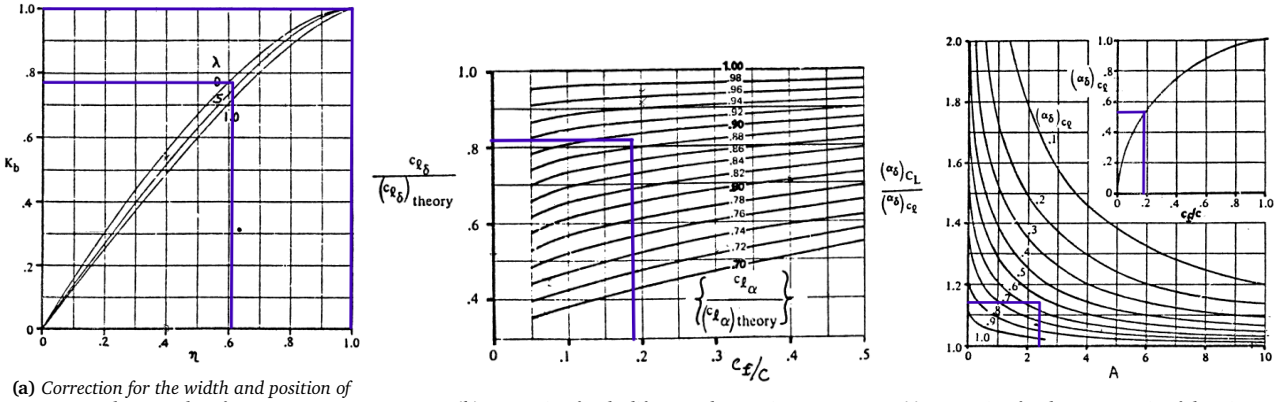

(a) *Correction for the width and position of the control surfaces*

(b) *Correction for the lift curve slope ratio*

(c) *Correction for the aspect ratio of the wing*

Figure C.9: *Corrections used in determining the control power [102]*

D

State Space System in Cruise

D.1. Assessment of Dynamic Stability in Cruise

The assessment of dynamic stability is conducted by proposing a method for modeling the aircraft dynamics, which involves the use of a state-space system. The state space is then modeled using the MATLAB control module on Python [120]. The behavior of the aircraft can then be assessed by analyzing the eigenvalues, as well as the response to inputs on the control surfaces.

D.1.1. Symmetric State Space System

The linearized equations of motion can be expressed in the form of Equation D.1.

$$\dot{x} = A \cdot x + B \cdot u \tag{D.1}$$

Where u is the input vector, hence, matrix A contains the stability derivatives, and matrix B contains the control derivatives. Now, after normalizing the equations of motion, they may be written as shown [125];

$$\left(C_{X_u} - 2\mu_c D_c\right)\hat{u} + C_{X_\alpha}\alpha + C_{Z_0}\theta + C_{X_q}\frac{\overline{q}\overline{c}}{V} + C_{X_{\delta_e}}\delta_e + C_{X_{\delta_t}}\delta_t = 0 \tag{D.2}$$

$$C_{Z_u}\hat{u} + \left[C_{Z_\alpha} + \left(C_{Z_{\dot{\alpha}}} + 2\mu_c\right)D_c\right]\alpha - C_{X_0}\theta + \left(C_{Z_q} + 2\mu_c\right)\frac{\overline{q}\overline{c}}{V} + C_{Z_{\delta_e}}\delta_e + C_{Z_{\delta_t}}\delta_t = 0 \tag{D.3}$$

$$-D_c\theta + \frac{\overline{q}\overline{c}}{V} = 0,\ C_{m_u}\hat{u} + \left(C_{m_\alpha} + C_{m_{\dot{\alpha}}}D_c\right)\alpha + \left(C_{m_q} - 2\mu_c K_Y^2 D_c\right)\frac{\overline{q}\overline{c}}{V} + C_{m_{\delta_e}}\delta_e + C_{m_{\delta_t}}\delta_t = 0 \tag{D.4}$$

This system of equations can be reorganized to produce the state-space system. This is done by moving all the derivatives of the states to one side and the rest to the other side. This leads to a system of equations that can be decomposed into systems similar to Equation D.1, which describes the state-space system. It is important to note that the trim tab contributions are ignored to simplify the design. Subsequently, the contributions from δ_t will be ignored henceforth [140].

$$\begin{bmatrix} C_{X_u} - 2\mu_c D_c & C_{X_\alpha} & C_{Z_0} & C_{X_q} \\ C_{Z_u} & C_{Z_\alpha} + (C_{Z_{\dot{\alpha}}} - 2\mu_c)D_c & -C_{X_0} & C_{Z_q} + 2\mu_c \\ 0 & 0 & -D_c & 1 \\ C_{m_u} & C_{m_\alpha} + C_{m_{\dot{\alpha}}}D_c & 0 & C_{m_q} - 2\mu_c K_y^2 D_c \end{bmatrix} \begin{bmatrix} \hat{u} \\ \alpha \\ \theta \\ \frac{qc}{V} \end{bmatrix} = \begin{bmatrix} -C_{X_{\delta_e}} \\ -C_{Z_{\delta_e}} \\ 0 \\ -C_{m_{\delta_e}} \end{bmatrix} \begin{bmatrix} \delta_e \end{bmatrix} \tag{D.5}$$

The state vector, x, is defined as $x = \begin{bmatrix} \hat{u} & \alpha & \theta & \frac{qc}{V} \end{bmatrix}^T$

The derivative of this is used in the state space equation to capture the dynamics of the aircraft. The input or control vector, u, will consist of the elevon, deflecting both surfaces in the same direction, like an elevator, and the trim deflection. This provides the groundwork for creating the state space system. A table of all parameters in the matrices is shown in Table D.1.

Table D.1: *Variable definitions for the symmetric state space system*

	$x...$	$z...$	$m...$
u	$\frac{V}{\overline{c}}\frac{C_{X_u}}{2\mu_c}$	$\frac{V}{\overline{c}}\frac{C_{Z_u}}{2\mu_c - C_{Z_{\dot{\alpha}}}}$	$\frac{V}{\overline{c}}\frac{C_{m_u} + C_{Z_u}\frac{c_{m_{\dot{\alpha}}}}{2\mu_c - C_{Z_{\dot{\alpha}}}}}{2\mu_c K_Y^2}$
α	$\frac{V}{\overline{c}}\frac{C_{X_\alpha}}{2\mu_c}$	$\frac{V}{\overline{c}}\frac{C_{Z_\alpha}}{2\mu_c - C_{Z_{\dot{\alpha}}}}$	$\frac{V}{\overline{c}}\frac{C_{m_\alpha} + C_{Z_\alpha}\frac{c_{m_{\dot{\alpha}}}}{2\mu_c - C_{Z_{\dot{\alpha}}}}}{2\mu_c K_Y^2}$
θ	$\frac{V}{\overline{c}}\frac{C_{Z_0}}{2\mu_c}$	$-\frac{V}{\overline{c}}\frac{C_{X_0}}{2\mu_c - C_{Z_{\dot{\alpha}}}}$	$\frac{V}{\overline{c}}\frac{C_{X_0}\frac{c_{m_{\dot{\alpha}}}}{2\mu_c - C_{Z_{\dot{\alpha}}}}}{2\mu_c K_Y^2}$
q	$\frac{V}{\overline{c}}\frac{C_{X_q}}{2\mu_c}$	$\frac{V}{\overline{c}}\frac{2\mu_c + C_{Z_q}}{2\mu_c - C_{Z_{\dot{\alpha}}}}$	$\frac{V}{\overline{c}}\frac{C_{m_q} + C_{m_{\dot{\alpha}}}\frac{2\mu_c + C_{Z_q}}{2\mu_c - C_{Z_{\dot{\alpha}}}}}{2\mu_c K_Y^2}$
δ_e	$\frac{V}{\overline{c}}\frac{C_{X_{\delta_e}}}{2\mu_c}$	$\frac{V}{\overline{c}}\frac{C_{Z_{\delta_e}}}{2\mu_c - C_{Z_{\dot{\alpha}}}}$	$\frac{V}{\overline{c}}\frac{C_{m_{\delta_e}} + C_{Z_{\delta_e}}\frac{c_{m_{\dot{\alpha}}}}{2\mu_c - C_{Z_{\dot{\alpha}}}}}{2\mu_c K_Y^2}$

In Table D.1, the newly defined variables in Equation D.6 are defined and shown.

$$\begin{bmatrix} \dot{\hat{u}} \\ \dot{\alpha} \\ \dot{\theta} \\ \frac{\dot{q}c}{V} \end{bmatrix} = \begin{bmatrix} x_u & x_\alpha & x_\theta & 0 \\ z_u & z_\alpha & z_\theta & z_q \\ 0 & 0 & 0 & \frac{V}{\bar{c}} \\ m_u & m_\alpha & m_\theta & m_q \end{bmatrix} \begin{bmatrix} \hat{u} \\ \alpha \\ \theta \\ \frac{qc}{V} \end{bmatrix} + \begin{bmatrix} x_{\delta_e} \\ z_{\delta_e} \\ 0 \\ m_{\delta_e} \end{bmatrix} \begin{bmatrix} \delta_e \end{bmatrix} \tag{D.6}$$

The output equation can be defined now that the state space system has been explained. To obtain outputs, new matrices must be created. The output should be in the form shown in Equation D.7.

$$y = C \cdot x + D \cdot u \tag{D.7}$$

Recall that the state, x, is $\begin{bmatrix} \hat{u} & \alpha & \theta & \frac{qc}{V} \end{bmatrix}^T$. The outputs are going to be similar; however, some modifications should be made. The desired output equation, y, is $\begin{bmatrix} \hat{u} & \alpha & \theta & q \end{bmatrix}^T$. The two vectors share a great deal of similarity; however, the last term is slightly different. This leads to the following output equation in matrix notation.

$$\begin{bmatrix} \hat{u} \\ \alpha \\ \theta \\ q \end{bmatrix} = \begin{bmatrix} 1 & 0 & 0 & 0 \\ 0 & 1 & 0 & 0 \\ 0 & 0 & 1 & 0 \\ 0 & 0 & 0 & \frac{V}{c} \end{bmatrix} \begin{bmatrix} \hat{u} \\ \alpha \\ \theta \\ \frac{qc}{V} \end{bmatrix} + \begin{bmatrix} 0 \\ 0 \\ 0 \\ 0 \end{bmatrix} \begin{bmatrix} \delta_e \end{bmatrix} \tag{D.8}$$

Equation D.8 may seem trivial as it is essentially an identity matrix with one scaling term for the pitch rate, or more accurately, it is a diagonal matrix. This can be implemented into the simulation code for the state space system. Additionally, the feedthrough matrix, or the D matrix in Equation D.7, is the zero vector, as the control inputs do not have a direct influence on the outputs. The non-dimensional inertia parameters; K_x^2, K_y^2, K_z^2, and K_{xz}^2 are defined as follows.

$$K_x^2 = \frac{I_{xx}}{mb^2} \qquad K_y^2 = \frac{I_{yy}}{m\bar{c}^2} \qquad K_z^2 = \frac{I_{zz}}{mb^2} \qquad K_{xz} = \frac{I_{xz}}{mb^2}$$

These inertia parameters are also found in the subsequent section on the asymmetric dynamics of the aircraft. Additionally, the non-dimensional mass parameters are defined as shown;

$$\mu_c = \frac{m}{\rho S \bar{c}} \qquad \mu_b = \frac{m}{\rho S b}$$

D.1.2. Asymmetric State Space System

Similar to the analysis of the symmetric equations of motion in Subsection D.1.1, the state-space system can be derived for the asymmetric state-space system. Now, the following system of equations can be found from the derivations of the equations of motion, as shown;

$$\left[C_{Y_\beta} + \left(C_{Y_{\dot{\beta}}} - 2\mu_b\right) D_b\right] \beta + C_L \varphi + C_{Y_p} \frac{p^b}{2V} + \left(C_{Y_r} - 4\mu_b\right) \frac{r^b}{2V} + C_{Y_{\delta_a}} \delta_a + C_{Y_{\delta_r}} \delta_r = 0 \tag{D.9}$$

$$-\frac{1}{2} D_b \varphi + \frac{p^b}{2V} = 0 \tag{D.10}$$

$$C_{\ell_\beta} \beta + \left(C_{\ell_p} - 4\mu_b K_X^2 D_b\right) \frac{p^b}{2V} + \left(C_{\ell_r} + 4\mu_b K_X Z D_b\right) \frac{r^b}{2V} + C_{\ell_{\delta_a}} \delta_a + C_{\ell_{\delta_r}} \delta_r = 0 \tag{D.11}$$

$$\left(C_{n_\beta} + C_{n_{\dot{\beta}}} D_b\right) \beta + \left(C_{n_p} + 4\mu_b K_X Z D_b\right) \frac{p^b}{2V} + \left(C_{n_r} - 4\mu_b K_X^2 D_b\right) \frac{r^b}{2V} + C_{n_{\delta_a}} \delta_a + C_{n_{\delta_r}} \delta_r = 0 \tag{D.12}$$

These equations can be reorganized and transformed into matrix format, leading to the following equation of matrices and vectors.

$$\begin{bmatrix} C_{Y_\beta} + \left(C_{Y_{\dot\beta}} - 2\mu_b\right) D_b & C_L & C_{Y_p} & C_{Y_r} - 4\mu_b \\ 0 & -\frac{1}{2}D_b & 1 & 0 \\ C_{\ell_\beta} & 0 & C_{\ell_p} - 4\mu_b K_X^2 D_b & C_{\ell_r} + 4\mu_b K_X Z D_b \\ C_{n_\beta} + C_{n_{\dot\beta}} D_b & 0 & C_{n_p} + 4\mu_b K_X Z D_b & C_{n_r} - 4\mu_b K_X^2 D_b \end{bmatrix} \begin{bmatrix} \beta \\ \varphi \\ \frac{pb}{2V} \\ \frac{rb}{2V} \end{bmatrix} = \begin{bmatrix} -C_{Y_{\delta_a}} & -C_{Y_{\delta_r}} \\ 0 & 0 \\ -C_{\ell_{\delta_a}} & C_{\ell_{\delta_r}} \\ -C_{n_{\delta_a}} & -C_{n_{\delta_r}} \end{bmatrix} \begin{bmatrix} \delta_a \\ \delta_r \end{bmatrix} \tag{D.13}$$

By reorganizing the terms in Equation D.13, it is possible to obtain the equation in the form $\dot{x} = Ax + Bu$, as shown in Equation D.1. This leads to the following

Table D.2: *Variable definitions for the asymmetric state space system*

	$y...$	$l...$	$n...$
β	$\frac{V}{b}\frac{C_{Y_\beta}}{2\mu_b}$	$\frac{V}{b}\frac{C_{l_\beta}K_{Z_2}^2 + C_{n_\beta}K_X z}{4\mu_b(K_X^2 K_{Z_2}^2 - K_X^2 z)}$	$\frac{V}{b}\frac{C_{l_\beta}K_X z + C_{n_\beta}K_X^2}{4\mu_b(K_X^2 K_{Z_2}^2 - K_X^2 z)}$
φ	$\frac{V}{b}\frac{C_L}{2\mu_b}$	0	0
p	$\frac{V}{b}\frac{C_{Y_p}}{2\mu_b}$	$\frac{V}{b}\frac{C_{l_p}K_{Z_2}^2 + C_{n_p}K_X z}{4\mu_b(K_X^2 K_{Z_2}^2 - K_X^2 z)}$	$\frac{V}{b}\frac{C_{l_p}K_X z + C_{n_p}K_X^2}{4\mu_b(K_X^2 K_{Z_2}^2 - K_X^2 z)}$
r	$\frac{V}{b}\frac{C_{Y_r} - 4\mu_b}{2\mu_b}$	$\frac{V}{b}\frac{C_{l_r}K_{Z_2}^2 + C_{n_r}K_X z}{4\mu_b(K_X^2 K_{Z_2}^2 - K_X^2 z)}$	$\frac{V}{b}\frac{C_{l_r}K_X z + C_{n_r}K_X^2}{4\mu_b(K_X^2 K_{Z_2}^2 - K_X^2 z)}$
δ_a	$\frac{V}{b}\frac{C_{Y_{\delta_a}}}{2\mu_b}$	$\frac{V}{b}\frac{C_{l_{\delta_a}}K_{Z_2}^2 + C_{n_{\delta_a}}K_X z}{4\mu_b(K_X^2 K_{Z_2}^2 - K_X^2 z)}$	$\frac{V}{b}\frac{C_{l_{\delta_a}}K_X z + C_{n_{\delta_a}}K_X^2}{4\mu_b(K_X^2 K_{Z_2}^2 - K_X^2 z)}$
δ_r	$\frac{V}{b}\frac{C_{Y_{\delta_r}}}{2\mu_b}$	$\frac{V}{b}\frac{C_{l_{\delta_r}}K_{Z_2}^2 + C_{n_{\delta_r}}K_X z}{4\mu_b(K_X^2 K_{Z_2}^2 - K_X^2 z)}$	$\frac{V}{b}\frac{C_{l_{\delta_r}}K_X z + C_{n_{\delta_r}}K_X^2}{4\mu_b(K_X^2 K_{Z_2}^2 - K_X^2 z)}$

Thus, the state-space system is derived similarly to the previous section on the symmetric state-space system in Subsection D.1.1.

$$\begin{bmatrix} \dot\beta \\ \dot\varphi \\ \frac{\dot p b}{2V} \\ \frac{\dot r b}{2V} \end{bmatrix} = \begin{bmatrix} y_\beta & y_\varphi & y_p & y_r \\ 0 & 0 & \frac{2V}{b} & 0 \\ l_\beta & 0 & l_p & l_r \\ n_\beta & 0 & n_p & n_r \end{bmatrix} \begin{bmatrix} \beta \\ \varphi \\ \frac{pb}{2V} \\ \frac{rb}{2V} \end{bmatrix} + \begin{bmatrix} 0 & y_{\delta_r} \\ 0 & 0 \\ l_{\delta_a} & l_{\delta_r} \\ n_{\delta_a} & n_{\delta_r} \end{bmatrix} \begin{bmatrix} \delta_a \\ \delta_r \end{bmatrix} \tag{D.14}$$

It is important to note that the state vector has been changed, as opposed to the symmetric state-space system. The input vector has also been changed, taking into account the ailerons and rudders instead. Similar to the procedure for the symmetric output equation, new matrices must be created to obtain outputs. The output should be in the form shown in Equation D.7.

Now, recall that the state, x, is $\begin{bmatrix} \beta & \varphi & \frac{pb}{2V} & \frac{rb}{2V} \end{bmatrix}^T$. The outputs are going to be similar; however, some modifications should be made. The desired output equation, y, is $\begin{bmatrix} \beta & \varphi & p & r \end{bmatrix}^T$. The two vectors share a great deal of similarity; however, the last term is slightly different. This leads to the following output equation in matrix notation.

$$\begin{bmatrix} \beta \\ \varphi \\ p \\ r \end{bmatrix} = \begin{bmatrix} 1 & 0 & 0 & 0 \\ 0 & 1 & 0 & 0 \\ 0 & 0 & \frac{2V}{b} & 0 \\ 0 & 0 & 0 & \frac{2V}{b} \end{bmatrix} \begin{bmatrix} \beta \\ \varphi \\ \frac{pb}{2V} \\ \frac{rb}{2V} \end{bmatrix} + \begin{bmatrix} 0 & 0 \\ 0 & 0 \\ 0 & 0 \\ 0 & 0 \end{bmatrix} \begin{bmatrix} \delta_a \\ \delta_r \end{bmatrix} \tag{D.15}$$

Equation D.15 seems quite trivial as it is basically an identity matrix with one term scaling the term with the pitch rate. This can be implemented into the simulation code for the state space system.

E

Unit tests for Verification

This appendix provides a list of tests that were performed using the `pytest` module to ensure that the model was implemented correctly.

Table E.1: *Unit Test Suite for Flight Envelope Verification*

Test Name	Description	Result
`test_mu_calculation`	Verifies that the mass ratio `mu` is calculated correctly.	**PASS**
`test_Kg_bounds`	Checks that the gust alleviation factor `Kg` remains within physical bounds.	**PASS**
`test_n_gust_pos`	Ensures positive gust load factor is computed correctly.	**PASS**
`test_n_gust_neg`	Ensures negative gust load factor is computed correctly.	**PASS**
`test_n_stall_pos`	Verifies positive stall load factor computation.	**PASS**
`test_n_stall_neg`	Verifies negative stall load factor computation.	**PASS**
`test_V_A_computation`	Validates that maneuver speed `V_A` satisfies stall = limit positive load.	**PASS**
`test_V_G_boundary`	Checks that gust boundary speed `V_G` satisfies gust = limit negative load.	**PASS**
`test_V_H_boundary`	Checks that stall boundary speed `V_H` satisfies stall = limit negative load.	**PASS**
`test_envelope_bounds`	Confirms flight envelope values stay within structural limits (e.g., `n_envelope`).	**PASS**
Overall Test Coverage		**99%**

Table E.2: *Unit Test Suite for Wing Structural Analysis Module*

Test Name	Description	Result
`test_calculate_chord_length`	Verifies piecewise chord length calculation across defined wing regions and at boundaries.	**PASS**
`test_calculate_chord_len_array`	Verifies vectorized chord calculation for `numpy` array inputs.	**PASS**
`test_calculate_scaling_constant`	Verifies calculation of the weight distribution scaling constant (`K`).	**PASS**
`test_calc_moment_dist_weight`	Verifies bending moment calculation from distributed wing weight, checking integration and boundary conditions.	**PASS**
`test_cal_bending_lift_moment`	Verifies bending moment calculation from distributed aerodynamic lift.	**PASS**
`test_adding_point_loads`	Verifies correct addition of concentrated point loads to distributed load diagrams.	**PASS**
`test_plot_nv_diagrams`	Verifies plotting of shear (N) and bending moment (V) diagrams with mocked `matplotlib`.	**PASS**
`test_physical_constraints`	Verifies outputs adhere to physical constraints (e.g., positive mass/lift).	**PASS**
`test_edge_case_inputs`	Verifies robustness with boundary conditions and extreme inputs (e.g., single-point arrays, dense spacing).	**PASS**
`test_load_factor_scaling`	Verifies correct scaling of aerodynamic loads with applied load factor (`n`).	**PASS**
Overall Test Coverage		**99%**

Table E.3: *Unit Test for Stress Analysis*

Test Name	Description	Result
`test_config_available_import`	Verifies successful import of configuration and dependency availability.	**PASS**
`test_performance_config_attributes`	Verifies configuration object contains necessary attributes (materials, geometry).	**PASS**

Continued on next page

Table E.3 – continued from previous page

Test Name	Description	Result
test_cross_section_parameterized	Verifies creation of parameterized cross-section geometry, checking scaling and thickness parameter handling.	PASS
test_stress_combined_loads	Verifies stress calculations (sectionproperties) under combined axial, bending, and shear loads.	PASS
test_stress_analysis_workflow	Verifies comprehensive stress analysis (von Mises, principal stresses, safety factors) and error handling for invalid inputs.	PASS
test_crit_shear_buckling_spar	Verifies critical shear buckling load calculation for spar webs.	PASS
test_crit_skin_panel_buckling	Verifies skin panel critical buckling stress calculation under combined loads.	PASS
test_crit_stringer_column_buckling	Verifies stringer critical column buckling load determination.	PASS
test_component_stress_analysis_spar	Verifies spar-specific stress calculations (web shear, flange bending).	PASS
test_component_stress_analysis_skin	Verifies skin bending stress calculations.	PASS
test_main_function_execution_modes	Verifies main analysis function in both parallel and sequential processing modes.	PASS
test_module_constants_consistency	Verifies consistency and unit compatibility of defined span and material property constants.	PASS
Overall Test Coverage		**98%**

Table E.4: *Unit Tests for Aircraft Dynamics Simulation Module*

Test Name	Description	Result
test_symmetric_ss_model	Verifies that a valid state-space system is created from A_long, B_long, C_long, D_long.	PASS
test_asymmetric_ss_model	Verifies that a valid state-space system is created from A_lat, B_lat, C_lat, D_lat.	PASS
test_symm_eigenvalues_realistic	Checks that symmetric eigenvalues have expected signs and magnitudes (e.g., phugoid, short-period). Additionally, the eigenvalues are hand-calculated and compared.	PASS
test_asymm_eigenvalues_realistic	Checks that asymmetric eigenvalues correspond to expected dynamic modes (e.g., Dutch roll, spiral). Additionally, the eigenvalues are hand-calculated and compared.	PASS
test_symmetric_forced_response	Verifies forced_response() returns expected shape for symmetric input/output.	PASS
test_asymmetric_forced_response	Verifies forced_response() returns expected shape for asymmetric multi-input case.	PASS
test_initial_input_condition	Verifies that only the initial seconds of the control input are non-zero (pulse input test).	PASS
test_output_dimension_match	Checks that time vector t matches output array shape y.shape[1].	PASS
test_output_finite_values	Verifies that all simulation outputs contain only finite values (no NaN or inf).	PASS
test_plot_function_runs	Checks that all plot functions run without error and produce a figure.	PASS
test_plot_both_simulations	Verifies combined plotting function renders all eight subplots correctly.	PASS
test_zero_input_stability	Test the system response with zero input (impulse-free) remains bounded.	PASS
test_long_time_stability	Checks that the system remains numerically stable over extended simulation time (tf > 60).	PASS
test_invalid_matrix_dimension	Checks that the system raises an error if A/B/C/D matrices are dimensionally incompatible.	PASS
Overall Test Coverage		**98%**